Studies on Energy and Environmental Applications of Ravenna Grass (*Saccharum ravennae*) Biomass

Thesis submitted in partial fulfillment of the requirements

for the degree of

DOCTOR OF PHILOSOPHY

by

Simons Dhara

Roll No.: 176107112

Department of Chemical Engineering

Indian Institute of Technology Guwahati

Guwahati 781039, India

April 2024

Studies on Energy and Environmental Applications of Ravenna Grass (*Saccharum ravennae*) Biomass

Simons Dhara

Dedicated to my Parents for their sacrifices, faith, love and support

Department of Chemical Engineering

Indian Institute of Technology Guwahati

Guwahati 781039, India

STATEMENT

I hereby declare that the content embodied in the thesis entitled "**Studies on Energy and Environmental Applications of Ravenna Grass (*Saccharum ravennae*) Biomass**" is the result of investigations carried out by me at the Department of Chemical Engineering, Indian Institute of Technology Guwahati, India, under the guidance of Prof. Mihir Kumar Purkait and Prof. Ramagopal Venkata Sai Uppaluri. In keeping with the general practice of reporting scientific observations, due acknowledgments have been made wherever the work described is based on the findings of other investigators.

Simons Dhara

Department of Chemical Engineering
Indian Institute of Technology Guwahati
Guwahati 781039, India

CERTIFICATE

It is certified that the work reported in the thesis entitled "**Studies on Energy and Environmental Applications of Ravenna Grass (*Saccharum ravennae*) Biomass**" by **Simons Dhara** has been carried out under our supervision. The work documented in this thesis has not been submitted to any other University or Institute for the award of any degree or diploma.

In our opinion, this thesis has reached the standard of fulfilling the requirements for the award of the degree of Doctor of Philosophy in accordance with the institute's regulations.

Dr. Mihir Kumar Purkait
Professor
Department of Chemical Engineering
Indian Institute of Technology Guwahati
Guwahati 781039, India

Dr. Ramagopal Venkata Sai Uppaluri
Professor
Department of Chemical Engineering
Indian Institute of Technology Guwahati
Guwahati 781039, India

Acknowledgements

This thesis becomes a reality with the kind support and help of many individuals. It is a genuine pleasure to express my deep sense of thanks and gratitude to all who helped me in the completion of this thesis.

I wish to express my deepest gratitude and appreciation to my supervisors, ***Prof. Mihir Kumar Purkait*** *and* ***Prof. Ramagopal Venkata Sai Uppaluri****, for providing me with invaluable guidance throughout the various stages of my research journey. I am indebted to them for their positive input and constant encouragement throughout my journey. I am grateful to them for their great support in every way, which helped me finish this work.*

I want to extend my sincere gratitude to my doctoral committee members, ***Prof. Bishnupada Mandal*** *(Department of Chemical Engineering),* ***Prof. Chandan Das*** *(Department of Chemical Engineering), and* ***Prof. P.K. Ghosh*** *(Department of Civil), for their valuable suggestions and constructive criticism during the project evaluations, which helped me to make necessary improvements in various stages of my research work.*

I am incredibly grateful to my ***thesis examiners, Prof. Robin K. Dutta*** *(Department of Chemical Sciences, Tezpur University) and* ***Prof. Chi-Min Shu*** *(Department of Safety, Health, and Environmental Engineering, NYUST, Taiwan) for their insightful advice that helped me improve the quality of the thesis. I would like to extend my gratitude to* ***Prof. A.T. Khan*** *(Department of Chemistry) and* ***Prof. A.K. Dasmahapatra*** *(Department of Chemical Engineering), members of my Ph.D. viva voce committee, for their invaluable insights.*

I would like to acknowledge all the centers for providing me with various facilities required for my analysis and characterization during the research work, specifically, the ***Analytical Lab Facility*** *(Department of Chemical Engineering),* ***Central Instrument Facility*** *(IITG),* ***Centre for the Environment*** *(IITG). I would also like to thank* ***Guwahati Biotech Park*** *for allowing me to conduct my analysis.*

I am also grateful to all the ***faculty*** *and* ***staff*** *members of the Department of Chemical Engineering for helping and providing me with the necessary facilities and resources.*

Acknowledgements

*I would like to thank my **senior** (Dr. Piyal Mondal) **colleagues** (Niladri, Ankush, Baite, Anweshan, Pranjal, Poushali, Nuruzamaan, and Kamal) and **Juniors** (Mukesh, Satish, and Sneha) for always being there when I need them.*

*My final words go to my family, whom I am abundantly blessed with for all their unconditional love, sacrifices, and encouragement. I am greatly indebted to my **mother (Bandana Dhara), my father (Harendra Nath Dhara),** and my younger brother **(Rimons Dhara),** whose unwavering support made it possible for me to come so far.*

Simons Dhara

Abstract

The Ph.D. thesis primarily targets the utility of *Saccharum ravennae* grass as a viable biofuel source. For this purpose, emphasis shall be upon the comprehensive utilization of all its components for various environmental applications. Bioethanol was generated from *Saccharum ravennae* with a separate hydrolysis and fermentation process. Optimization of ethanol and sugar yields involved surfactant-mediated enzymatic hydrolysis and varied pretreatment methods. Utilizing CCD-RSM for the optimization of the pretreatment process, high-purity alkaline lignin was extracted for the subsequent utility of the lignin byproduct. The lignin byproduct obtained from the pretreatment process was eventually deployed for the modification of PSf (polysulfone) membranes and was investigated for the removal of Cr(VI), Pb^{2+}, and Eosin Y dye from water.

Saccharum ravennae, known as "Ekra" in the Northeast region of India, is an elephant grass species that abundantly grows in the natural habitat of Assam. The high polysaccharide content of Ravenna grass (*Saccharum ravennae*) renders it to be a viable choice for the generation of biofuel. However, sugar conversion needs to be optimized for its economic sustainability. The pre-treatment of Ravenna grass biomass (RGB) was performed with 2% H_2SO_4(AC), 2% NaOH (AL), and subsequent H_2SO_4-NaOH (AC-AL) hydrothermal methods. Enzymatic hydrolysis of all the pre-treated samples, along with raw biomass, was conducted using cellulase from *Trichoderma reesei* with and without ionic (SDS, CTAB) and non-ionic (Tween 20) surfactants (10 mg/mL). The AC-AL-treated RGB was hydrolyzed without using surfactants, thereby, a maximum sugar yield of 624 mg/g was achieved. Regardless of the pre-treatment techniques used, adding SDS to enzymatic hydrolysis significantly decreased the sugar yield. The inclusion of CTAB in the hydrolysate also reduced the sugar yield, but only marginally. Tween 20 restricts enzyme adsorption to lignin fractions and thereby increases total sugar production for all the pre-treated samples. The cellulose and hemicellulose digestibility of AL-treated RGB significantly improved by 16.72% and 34.33%, respectively. A maximum sugar yield of 816 mg/g was obtained from the enzymatic hydrolysis of AL-treated RGB using Tween 20. The addition of Tween 20 produced 0.249 g and 0.318 g of ethanol per 1 g of AL, AC-AL treated RGB using *Saccharomyces cerevisiae* as fermenting organism. The optimized sugar yield from Ravenna

grass enhanced its prospects as a 2nd generation biofuel substrate in commercial uses and can be an alternative to sugarcane bagasse.

In the second thesis objective, deploying KOH-mediated alkaline hydrothermal pre-treatment with the oil bath method, highly pure alkaline lignin was extracted from Ravenna grass. Lignin recovery was optimized using RSM (response surface methodology) combined with a central composite model. Three process parameters, namely KOH concentration (1-3%), reaction time (50-200 minutes), and solid loading (5-15%), were varied to optimize the combined effect of these parameters. The RSM predicted a maximum lignin recovery of 15.38 g/100g of raw biomass at optimum conditions (2.4% KOH, 6.41% solid loading, 176.57 minutes). Three experimental runs were performed at optimum conditions, and 15.81±0.32 g/100g lignin recovery was obtained to infer that the predicted findings are in good agreement with the experimental findings. A maximum purity of 93.7 % purity was achieved for the extracted lignin at a different operating condition (3% KOH, 10% solid loading, 125 minutes). The commercial and extracted alkaline lignin with maximum purity was characterized with techniques such as Nuclear Magnetic Resonance (NMR), Fourier Transform Infrared Spectroscopy (FTIR), and X-ray photoelectron spectroscopy (XPS). The extracted lignin exhibits higher phenolic content and more functional groups than commercial lignin and can be used for future applications.

The extracted alkaline lignin being the second-most prevalent biomacromolecule in the world of plant biology was further utilized in the effective fabrication of lignin-based mixed matrix membranes. The influence of PSf and lignin concentration on the properties of the fabricated membranes was examined. Also, the developed membranes were assessed for surface morphology, roughness, thickness, thermal stability, functional groups, elemental composition, mechanical strength, and hydrophilicity. AFM and SEM studies demonstrated that the PSf/lignin membranes possessed rough and inconsistent morphology and comparatively greater surface porosity with respect to the corresponding properties of the Psf base membrane. The water contact angle was comparatively reduced for the 1.0 wt.% PSF/lignin membrane. Furthermore, lignin nanoparticles significantly influenced the membrane surface characteristics and lowered the Zeta potential. Under the ideal experimental scenario, M2 (0.5 wt.% lignin/PSf) and M3 (1.0 wt.% lignin/PSf) membranes

demonstrated good pure water flux values and higher removal Cr (VI) values of 98.5% and 98.75% respectively. EDX analysis of the membranes after filtration affirmed effective Cr (VI) removal from water. Owing to its low cost, green credentials, simplicity in synthesis, and remarkable efficiency, the newly developed PSf/lignin membrane is best suited for Cr (VI) removal from discharged aqueous effluents.

Further, to increase the water flux, functional property, and removal efficiency of the membranes, lignin/Graphene oxide incorporated polysulfone composite membranes were fabricated using the phase inversion method with PEG 6000 as a pore-forming agent. A series of analyses were conducted to assess the physicochemical characteristics of the nanofillers and the resulting membranes. Filtration operations were conducted with an aqueous solution containing both lead (Pb) and Eosin Y dye. Additionally, the sensitive influence of their electrostatic interactions on membrane fouling and the regeneration process was examined. The electrostatic interaction, specifically the linking effect of Pb cations between negatively charged Eosin Y molecules, resulted in the formation of larger Eosin-Pb complexes. This, in turn, led to an enhanced removal of Pb through membrane filtration. A study on the adsorption of Pb^{2+} ions in an aqueous solution was conducted using the optimized Lignin/GO membrane. The adsorption process was investigated through Langmuir and Freundlich isotherm analyses. In the adsorption studies, both the Langmuir and Freundlich isotherms exhibited a superior fit, with R^2 values of 0.977 and 0.994, respectively. According to the models' fit, it is plausible that the adsorption process involves multilayer physisorption, aligning with the principles outlined in the Langmuir and Freundlich isotherm theories.

In summary, the thesis demonstrated novelty in the following perspectives. Firstly, sugar and ethanol yields have been enhanced considerably through the deployment of surfactant-mediated enzymatic hydrolysis. Secondly, high-purity lignin extraction has been facilitated through the KOH pre-treatment process and with the CCD-RSM methodology. Thirdly, the application of lignin in the lignin-Psf mixed matrix membrane has been demonstrated for Cr (VI) removal. Finally, the application of lignin in the PSf-lignin-GO composite membrane has been demonstrated for the simultaneous removal of Eosin dye and $Pb2^{+}$. Thus, the thesis findings provide useful insights into the possible scope of the mentioned biomass in terms of sustainable process-product development research.

Research Publications

1. **Simons Dhara,** Ramagopal Venkata Sai Uppaluri, M. K. Purkait. Enhancing Bioethanol Yield from Ravenna Grass (Saccharum ravennae): Optimization of Pretreatment Strategies and Surfactant-Assisted Enzymatic Hydrolysis for Maximum Sugar Yield. **ACS Agricultural Science & Technology. https://doi.org/10.1021/acsagscitech.3c00321.**
2. **Simons Dhara,** Niladri Shekhar Samanta, R. Uppaluri, M.K. Purkait, High-purity alkaline lignin extraction from Saccharum ravannae and optimization of lignin recovery through response surface methodology. **International Journal of Biological Macromolecules. https://doi.org/10.1016/j.ijbiomac.2023.123594.**
3. **Simons Dhara,** Niladri Shekhar Samanta, Pranjal P. Das, Ramagopal Venkata Sai Uppaluri, and Mihir K. Purkait, Ravenna Grass-Extracted Alkaline Lignin-Based Polysulfone Mixed Matrix Membrane (MMM) for Aqueous Cr(VI) Removal. **ACS Applied Polymer Materials. https://doi.org/10.1021/acsapm.3c00999.**
4. **Simons Dhara,** Ankush D. Sontakke, Niladri Shekhar Samanta, Ramagopal Venkata Sai Uppaluri, Mihir K. Purkait, Biowaste-alkaline lignin and GO integrated polysulfone ultrafiltration membrane fabrication for Pb^{2+} and Eosin Y dye removal, **Separation and Purification Technology 2024**, **https://doi.org/10.1016/j.seppur.2024.126894**.

CONTENTS

LIST OF FIGURES

LIST OF FIGURES

LIST OF TABLES

Chapter 1

Introduction and Literature Review

This chapter discusses the roadmap for the utilization of Ravenna grass (Saccharum ravennae) lignocellulosic components for energy and environmental application. Section 1.1 narrates the current scenario of bioethanol consumption and a summary of the utilization of lignocellulosic components such as sugars and lignin. It also discusses alternative grass biomass options and the possible exploration of traditionally used feedstock for biofuel production. Along with this, a brief discussion of Ravenna grass has been provided. In section 1.2, the targeted perspective derived from the key features of the previous section has been discussed. In section 1.3, the available prior art has been discussed for bioethanol production and extraction of lignin from grass biomass. Thereafter, the section elaborates on the potential application of extracted alkaline lignin from softwood for the removal of heavy metals. Also, research directives for the easy development of composite membranes have been elaborated. Thereafter, in section 1.4, the possible scope for further research on the Ravenna grass for enhancing bioethanol yield, extraction of lignin, and application of lignin for heavy metals and dye removal from the water system has been discussed in detail. Furthermore, the utilization of lignin in composite membranes along with Graphene Oxide (GO) for heavy metals and dye removal has been elucidated. Finally, section 1.5 conveys the broad objectives being set to address the detailed research gaps. Finally, section 1.6 summarizes the details of the content elucidated in various chapters of the thesis.

1.1 Background and motivation

In the recent past, there has been an upsurge in demand for ethanol as a second-generation clean and sustainable biofuel. According to the statistical data published by the Renewable Fuels Association (RFA) in 2021, the US is the biggest ethanol producer and accounts for 15016 million gallons, contributing to 55% of worldwide ethanol production. Incidentally, India contributes only 3% of the worldwide ethanol production [1]. Bioethanol utilization significantly reinforces the pursuit of carbon neutrality and the

fight against climate change. Bioethanol plays a crucial role in expediting the shift towards a low-carbon economy through its capacity to reduce greenhouse gas emissions, its ability to facilitate the decarbonization of transportation, enhance energy security, foster sustainability, and foster a leap in technological progress. Also, biofuels play an essential role in biorefineries, promote sustainability, improve resource efficiency, and facilitate the shift toward a greener and more sustainable renewable energy economy. Corn and several grains are the primary substrates for ethanol production, and according to the information published by the US Department of Energy, more than 98% of gasoline in the US contains about 10% ethanol in the blend [1]. With 10% ethanol blending, the Government of India has been implementing ethanol-blended petrol (EBP) [2].

Sugarcane molasses is the primary raw substance used in India for bioethanol production. Few grass species (elephant grass species) possess plant morphology similar to that of sugarcane and can be henceforth used as an alternative 2nd generation biofuel source. Beyond its role in biofuel production, the exploration of lignocellulosic resources extends to a crucial yet unexplored component known as lignin, the second most abundantly available biopolymer on a global basis. Traditionally, lignin has been relegated as waste in the paper pulp and biofuel industries and is often utilized in combustion processes. However, unlocking the potential of lignin for environmental applications presents a transformative opportunity. Repurposing lignin in such applications not only addresses the issue of its disposal as waste but also enhances the overall feasibility and cost-effectiveness of lignocellulose as a substrate for biofuel production. This dual-purpose utilization of lignin contributes not only to waste reduction but also to the optimization of lignocellulosic resources for a more sustainable and economically viable biofuel industry.

This Ph.D. thesis research work is centered on the value-oriented exploitation of the lignocellulosic constituents that are found in the biomass of *Saccharum ravennae* grass (**Fig 1.1**). Native to South Asia, Ravenna grass (*Saccharum ravennae*) belongs to the higher classification of Saccharum, the same as sugar cane. Also known as energy grass, Ravenna grass is widely distributed across India and grows primarily in a natural profusion in the north-eastern states. Correspondingly, its presence has been confirmed

in ecologically sensitive areas such as the Grand Canyon and valleys, particularly in riparian zones and other wetland areas in the USA [3]. It can grow up to 13 m long and has a dense lignocellulosic softwood structure. With these notable cultivation characteristics, it is a worthy candidate to cultivate as a 2nd generation biofuel substrate [4]. To date, very few studies exist concerning the relevant research on *Saccharum ravennae* grass biomass. Panneerselvam et al. (2013) achieved a maximum sugar yield of 431.9 mg/g from ozonated Saccharum ravennae through enzymatic hydrolysis with 0.1 g/g Cellic® CTec2 enzyme [5]. In another study published by the same author, a maximum of ~120 mg/g glucose yield was achieved through the enzymatic hydrolysis of untreated *Saccharum ravennae* biomass [6].

Figure 1.1: Ravenna grass

1.1.1 Enhanced sugar recovery and bioethanol production from grass biomass

According to UNESCO, Grassland is defined as 'land covered with herbaceous with less than 10% tree and shrub cover'. As per this definition, it can be said that Grassland is widely spread around the world, with 52.5 million square kilometres of known area [7]. Grasses exist as major vegetation in many habitats, such as grasslands and reed swamps. However, they exist as a small part of vegetation in almost every terrestrial habitat. Among 12,000 species available in the world, only a few are edible, and among these, only a few species are used as fodder [8]. However, such non-edible grasses are an abundant source of lignocellulosic biomass and have a higher growth rate and shorter development phase. As a result, they can serve as a sustainable source of lignocellulosic biomass for biofuel production.

Lignocellulosic biomass primarily consists of cellulose (glucan), hemicellulose (xylan), and lignin [9]. The dry weight of grass biomass consists of holocellulose (60-80%) and lignin (10-30%) [10]. With the rapid growth rate of the abundant grass fields, 2nd generation biofuel production can be explored conveniently by targeting the grasses as a source of biomass. Depending on the climate conditions, the grasses are divided into two broad categories, i.e., tropical grasses or C4 grasses and Clement or C3 grasses [11]. Among these, C4 grasses are mostly studied for biofuel production. This is due to their high-yielding variety status and their ability to grow under a wide range of climate conditions [12]. Perennial grasses such as elephant grass, Napier grass, Switchgrass, Bermuda grass, and Silvergrass are among the most studied grass species for biofuel production [13]. There are 4 grass species known as elephant grass. These are Asian *Miscanthus giganteus*, *Arundo donax*, African *Pennisetum purpureum* and Eurasian *Saccharum ravennae*.

Such grass cannot be directly fermented for the production of bio-ethanol as lignocellulosic biomass could not be easily broken down due to the lignin in cell walls for the release of cellulose and hemicellulose. Therefore, pretreatment options are often explored to overcome such limitations. For the past 200 years, biomass pre-treatment for

lignocellulosic depolymerization to fermentable sugars has been studied. In such studies, the researchers targeted higher sugar production with minimal degradation to inhibitory compounds. Among alternate technologies, chemical, physicochemical, and biochemical conversions can be inferred to be the most promising technologies [14].

Microbial saccharification of delignified biomass can be performed with various bacteria and fungi that potentially hydrolyze cellulose and hemicellulose into monosaccharides. However, monosaccharides are intermediate compounds in the metabolism of cellulolytic microorganisms. Thereby, they lead to the formation of more acids, alcohols, CO_2, and H_2 and henceforth drive a reduction in the desired higher concentration of mono-saccharides [15]. Therefore, enzymatic hydrolysis is a preferable choice in which hydrolytic enzymes being extracted from the microorganisms are utilized to obtain only monosaccharides as end products. Cellulases are the key enzymes for cellulose hydrolysis. These enzymes ascertain three predominant activities, namely, exo-1,4- β-glucanase, endo-1, 4-β- glucanase, and cellobiase (also known as β-glucosidase). For the hemicellulose hydrolysis, xylanases are the primary enzymes.

Diluted sugar solutions from enzymatic saccharification further undergo fermentation for the production of bioethanol. Depending upon the most suitable microorganism, fermentation can be achieved with either bacteria or fungi. In this regard, it can be noted that three alternate fermentation types are familiar. These are lactic acid, ethanol, and acetic acid fermentation. Among anaerobic bacterial species, *Escherichia* and *Salmonella* can produce ethanol. On the other hand, *C. Shehatae*, *Pichia stipitis*, and *S. Cerevisiae* are well-known ethanol-producing fungi [16]. For ethanol fermentation, *S. Cerevisiae* (also known as baker's yeast) is a commonly used microorganism and henceforth received wider attention [17]. Alcoholic fermentation is a biological process in which sugars such as glucose, xylose, and fructose are converted into ethanol and carbon dioxide (by-products). Such fermentation is considered to be anaerobic due to the conversion taking place in the absence of oxygen. Thus, fermentation can be facilitated with yeast or bacteria.

1.1.2 Lignin extraction from biomass

The primary lignocellulosic refractory complex constituents are holocellulose (cellulose and hemicellulose) and lignin. The constituent lignin has been a significant obstacle to the effective breakdown of cellulose by enzymes. These enzymes facilitate the biochemical conversion of lignocellulose yields biofuels, notably bioethanol [18]. Lignin restricts the accessibility of substrate to the enzyme and unproductively binds to the enzyme through hydrogen bonding, electrostatic, and hydrophobic interaction [19]. Numerous pretreatment categories have been previously utilized for effectual delignification and conversion of lignocellulose to sugars that can be eventually subjected to fermentation. These methods refer to acidic, alkaline, and organosolv pre-treatment options [20], [21]. Another often ignored aspect of cost-effective bioethanol production is the utilization of lignin, a by-product of biomass pretreatments.

Lignin is a structurally heterogeneous biopolymer constituted mostly of various phenylpropane derivatives. Based on the aromatic rings with several methoxy groups, lignin can be categorized into three categories of monolignols: syringyl (S), p-hydroxyphenyl (H), and guaiacyl (G). Through oxidative coupling, lignin monomers may generate several forms of C-C and C-O-C bonds [22]. However, to accomplish total lignin removal, these conversion procedures often involve many continuous reaction stages. This translates into time-consuming, energy-intensive processes. Furthermore, the wide variety of lignin components often results in uncontrollable side reactions, color generation in water, and difficulty in the purification of the resultant product [23]. In addition, higher lignin removal enhances the susceptibility of the residual polysaccharide. To mitigate the mentioned limitation, alkaline pretreatment is promising. The technique of choice for overcoming these critical hurdles is alkaline pretreatment. Moreover, alkaline lignin can also be utilized as either a bio-based polymer or as a fuel supplement [24].

1.1.3 Lignin Applications

Extensive research endeavors deliberated to explore the potential of diverse biopolymers for a wide range of applications, such as chemical production, adsorbents, food packaging, and water treatment. The driving force behind these efforts is the imperative to substitute conventional non-biodegradable materials with environmentally and ecologically friendly resources. As the global demand for sustainable alternatives intensifies, the exploration of biopolymers as versatile solutions gains momentum across various industries. This sustained commitment to leverage biopolymers reflects upon concerted efforts to mitigate environmental impact and enhance the sustainability of the by-products, which are presently regarded as waste products.

Lignin exhibits versatile applications across industrial and biomedical dominions, encompassing sectors such as chemicals, biofuels, polymers, water treatment, and nanomaterials synthesis for drug delivery. The efficacy of these applications is dependent upon factors such as the specific source of lignin, the extent of deployed chemical modifications, and the inherent physicochemical properties of the realized material. In essence, the diverse utility of lignin in various sectors hinges on a nuanced understanding and strategic manipulation of its origin, chemical composition, and physical characteristics [25], [26].

The application of lignin in the fields of medicine and pharmaceutics holds significant promise to enhance human health. This is due to its desired antioxidant and antimicrobial properties. Moreover, lignin exhibits noteworthy biological activities, including its capacity to lower cholesterol levels by binding with the bile acids of the human intestinal system. These diverse attributes posit lignin as a promising agent to address a spectrum of diseases, including obesity, diabetes, thrombosis, viral infections, and various forms of cancers. The multifaceted therapeutic potential of lignin opens up newer avenues for innovative treatments and interventions across a range of medical conditions [27].

Also, considerable attention is paid to the deployment of adsorption and reduction techniques for the efficient elimination or reduction of metals and toxic dyes from

polluted water or industrial wastewater systems [28]. This necessitates the leveraging of biomaterials derived from environmentally friendly and cost-effective lignocellulosic sources, especially from green biomass-derived lignin and its derivatives [29]. The attention directed towards this approach underscores its potential for sustainable and effective water remediation. Through a systematic exploration of the inherent properties of lignocellulosic biomasses such as lignin, customized methodologies can profoundly contribute to environmentally conscious and economically viable strategies. Therefore, water pollution challenges can be duly addressed in an industrial domain, and the sustainable utility of the lignin product, which is regarded as a non-valuable waste product, can be sought and realized [30].

1.2 Targeted Perspectives

In the confined research area that emphasizes the utilization of *Saccharum ravennae* biomass for energy and environmental applications, this Ph.D. thesis aims to advance research and development knowledge in the following research themes:

a. Enhanced sugar recovery and bioethanol production
b. Lignin extraction from biomass
c. Value-added product development based on relevant applications of lignin

1.3 Prior art

Focusing on the customized research on the targeted perspectives, this section details the available prior art research methodology for the subsequent introspection into the possible scope for further research (to be detailed in the following section). The targeted central research theme of the Ph.D. thesis is the *Saccharum ravennae* grass biomass-based bioethanol and environmentally benign lignin production and applications of lignin for wastewater treatment. A detailed account of the prior art is provided in the following subsections.

1.3.1. Sugar recovery and bioethanol production from grass biomass

1.3.1.1 Pretreatment Strategies

The production of bioethanol from lignocellulose typically encompasses three primary steps. The initial phase involves biomass pretreatment to liberate carbohydrates and eliminate lignin. Subsequently, the second step entails hydrolysis of the delignified long-chain carbohydrates for their effective breakage into monomeric sugars. Finally, in the third step, the monomer sugar molecules undergo fermentation to ultimately yield bioethanol. Thus, the process hierarchy underscores the systematic conversion of lignocellulosic biomass into a valuable biofuel resource. To optimize bioconversion processes, a range of biomass pretreatment methods have been considered. These methods can be broadly categorized into physical pretreatment, chemical pretreatment, biological pretreatment, thermochemical pretreatment, and combined or sequential pretreatment [31], [32]. Each category represents a distinct approach to facilitate biomass preparation for subsequent conversion into valuable bio-based products. Accordingly, the alternate methods showcase deployed diverse strategies in the quest for enhanced efficiency and sustainability in the subsequent bio-conversion processes.

Among all the mentioned methods, chemical methods (acid/alkali/organosolv) have been well addressed for elephant grass pretreatment. This is due to their high lignin removal capacity. The acid pretreatment of lignocellulose relies on the vulnerability of the glucosidic bonds connecting hemicellulose and cellulose to acidic conditions. The acid catalyst produces hydronium ions, which cause the long cellulose and hemicellulose chains to break down into separate sugar monomers. To date, acid pretreatment studies with hydrochloric acid, nitric acid, phosphoric acid, and sulfuric acid have been reported for the mentioned biomass pretreatment [33]–[35]. Research findings indicate that, among various acids, sulfuric acid (H_2SO_4) is widely employed for the pretreatment of lignocellulosic biomass [36]. According to Santos et al. (2018), with increasing acid concentration, the cellulose yield increases along with a reduction in total solid recovery [37]. The authors observed that for an increase in H_2SO_4 concentration from 5% to 20%, the glucan yield increased from 36.89 to 43.13%, and the total solid recovery lowered

from 59.90% to 54.36%. In a study conducted in 2018, Sahoo et al. examined the effects of diluted acid pretreatments on the enzymatic hydrolysis of wild rice grass (*Zizania latifolia*). The findings conveyed that 163 mg of sugar/g biomass has been released for 0.4% H_2SO_4 loading upon the 10% biomass [38]. Sindhu et al. (2014) investigated the influence of dilute acid pretreatment of various Indian bamboo (*Bambusa* sp.) varieties for bioethanol production [39]. Among alternate minerals and organic acids, the H_2SO_4 emerged as the most effective pretreatment agent. Accordingly, optimized conditions of 15% (w/w) solid loading, 5% H_2SO_4, and 30 minutes of pretreatment have been realized to achieve a yield of 0.319 g/g of reducing sugars. Subsequent enzymatic saccharification and fermentation produced 1.76% (v/v) ethanol. Thus, through an optimization of the severity of acid pretreatment, high reaction rates can be attained, which potentially lead to a substantial enhancement in the hydrolysis of both hemicellulose and cellulose [40].

Pretreating lignocellulosic biomasses with organic solvents or their aqueous solutions results in the disruption of internal bonds between lignin and hemicellulose. This ultimately generates a relatively pure cellulose residue. Various organic solvents, including ethanol, methanol, acetone, organic acids, organic peracids, and ethylene glycol, or their combinations with water, have been utilized for the pretreatment of diverse lignocellulosic biomasses [36]. Typically, a catalyst is introduced during the process to either reduce the pretreatment temperature or enhance the rate of delignification. For operating temperatures above 185 °C, organic acids from the biomass are hypothesized to function as a catalyst to break the lignin-carbohydrate complex. Therefore, a catalyst is not required [41]. The ethanol organosolv pretreatment of elephant grass (Pennisetum purpureum) involved treatment with 60% ethanol containing 1.25% sulfuric acid at 180 °C for 20 minutes. This process resulted in the recovery of 72.01 wt% cellulose and 14.20 wt% hemicellulose while effectively removing the maximum lignin content, leaving only 8.65 wt% [42]. Pinewood pretreatment with the 60–80% aqueous methanol solution containing 0.2% HCl at 170°C for 45 minutes removed approximately 75% of the original lignin. In summary, delignification increased for the combined scenario of higher temperature, longer time, and increased HCl concentration up to 0.2% [43]. While organosolv pre-treatment generates pure lignin and enhances enzymatic hydrolyzable

cellulosic content, it is disadvantageous due to the expensive organic solvent and significant capital expenditures that are mandatory to handle the extremely volatile solvent system [21].

Alkali pre-treatment originates from the concept of the soda pulping process patented in the year 1854 [44]. For lignocellulose pretreatments, alkali reagents are NaOH, KOH, NH_4OH, $Ca(OH)_2$, and oxidative alkali. In comparison to the softwoods in gymnosperms that constitute lignin content greater than 26%, the alkaline pretreatment has been highly effective on hardwoods and agricultural residues in angiosperms with lower lignin content [45]. In comparison with other types of pretreatment methods, alkaline pretreatment provides several intriguing benefits, such as reduced cellulose and hemicellulose degradation, modifications in lignin structure, and effective breakdown of glycosidic linkages [46]. Bensah et al. (2019) pretreated elephant grass (*Pennisetum purpureum*) with 1% KOH (121 °C, one h) and recorded the highest delignification (67.5%) and consequently the lowest solids recovery (59.5%) [47]. In another investigation, Nascimento and Rezende (2018) subjected elephant grass (Pennisetum purpureum) to pretreatment with 5% (w/v) NaOH at a solid loading of 10%, conducted for 2 hours at 70 °C. The NaOH pretreatment successfully recovered 66.9 ± 0.4 wt% cellulose and 16.7 ± 0.3 wt% hemicellulose, concurrently removing a substantial amount of lignin. Thereby, only 12.8 ± 0.3 wt% has not been extracted [48]. Nevertheless, weak alkalis, such as $Ca(OH)_2$, exhibit limited water solubility and necessitate higher water content and extended pre-treatment durations [49]. Additionally, the removal of hemicellulose and lignin through a two-stage process involving alkali and acid reagents, as proposed by Wyman et al. [50], has been demonstrated to be efficient from the cost perspective.

Table 1.1 summarizes the key findings in the prior art in the field of alternate pretreatment strategies for elephant grass biomass.

Table 1.1: A summary of key findings in the research theme of chemical pretreatment of elephant grass biomass.

S no	Substrate	Pretreatment process	Operating conditions	Composition (pretreated)			Ref
				Cellulose	Hemi-cellulose	Lignin	
1	Elephant grass (Pennisetum purpureum)	Sulfuric acid pretreatment	1:20 w/v solid loading 20% sulfuric acid Autoclaved, at 121 °C, for 30 min	43.13 ± 2.21	10.72 ± 1.14	23.32 ± 4.62	[37]
2	Elephant grass (Pennisetum purpureum)	Organosolv pretreatment	10 % w/v solid loading 60% ethanol containing 1.25% sulfuric acid at 180 °C for 20 min	72.01	14.20	8.65	[42]
3	Elephant grass (Pennisetum purpureum)	KOH pretreatment	6 % w/v solid loading 1 % (w/v) KOH treatment at 121 °C for one h.	60.6 ± 0.6	24.1 ± 0	10.6 ± 0	[47]
4	Elephant grass (Pennisetum purpureum)	Alkali treatment	1:10 g/L solid-to-liquid ratio Mechanical stirring with 5 % (w/v) NaOH treatment at 70 °C for 2 h	66.9 ± 0.4	16.7 ± 0.3	12.8 ± 0.3	[48]

1.3.1.2 Enzymatic hydrolysis

The enzymatic hydrolysis of lignocellulose has been extensively researched as a viable method to effectively break down biomass into fermentable sugars and for their subsequent conversion into biofuels and biochemicals. Toscan et al. (2019) conducted a two-stage sequential imidazole pretreatment on Elephant grass (*Pennisetum purpureum Schum*), followed by enzymatic hydrolysis with Cellic CTec2 enzyme at a 1% solid loading. This process yielded 27 kg of glucose and 2 kg of xylose recovery [51]. Montipo et al. (2018) were also able to recover 39.29 g of sugars per 100 g of raw biomass through the enzymatic hydrolysis of steam-pretreated elephant grass (*Pennisetum purpureum*) [52]. Panneerselvam et al. (2013) investigated the effect of ozonolysis pretreatment on Saccharum ravennae. In the process, ozonolysis was effective for the removal of 59.9% lignin without cellulose degradation. The subsequent hydrolysis of pretreated solids with Cellic® CTec2 was able to recover 431.9 mg/g of total sugars [53]. However, there are still several issues and challenges in the biomass enzymatic hydrolysis method. These are excessive enzyme dosages and inadequate process performance of enzymatic hydrolysis. These lead to substantial operating expenses and impede the enhanced production of 2nd generation bioethanol [54]. To overcome the mentioned limitations, additives can be utilized to enhance the enzymatic hydrolysis process performance [55]. Surfactants being deployed in the enzymatic hydrolysis process are simple and cost-effective additives for substantial enhancement in the efficiency of the enzymatic hydrolysis process [56]. In this context, non-ionic surfactants, mainly Tween, titron, and polyethylene glycol (PEG), outperformed cationic surfactants [57], [58]. Additionally, it is hypothesized that the non-ionic surfactants might enhance enzyme stability and thereby reduce its tendency to deactivate during enzymatic hydrolysis. This, in turn, reduces the enzyme's tendency to bind ineffectively to lignin [59]. For example, Oladi and Aita (2018) observed a 36.20% enhancement in cellulose digestibility for 11.3% Tween 80 surfactant in the pretreatment case of dilute ammonia unwashed cane bagasse system [60]. On the contrary, anionic surfactants such as SDS have been reported to improve enzymatic hydrolysis between certain ranges range of concentrations [61]. According to Lou et al. (2013), polymeric anionic surfactants such as lignosulfonate improve enzymatic hydrolysis through the

minimization of ineffective cellulase adsorption [62]. The surfactant effects on enzymatic digestion of cellulosic biomass altered due to the variation in the key chemical and physical parameters such as surfactant molecular structures, temperature, pH, and ionic strength [63].

Table 1.2 presents the literature summary of the key findings of enzymatic hydrolysis for the overall recovery of total sugars from various elephant grass species.

Table 1.2: Literature data summary of enzymatic hydrolysis of elephant grass species biomass.

S no	Substrate	Enzyme	Reaction Condition	Total sugar recovery	Ref
1	Elephant grass (*Pennisetum purpureum*)	Cellic CTec2 (blend of cellulases, ß-glucosidases, and hemicellulase)	1 % w/v Solid loading Sodium azide 0.01 % (w/v). Volume makeup with sodium citrate buffer (pH 4.8, 50 mmol/L) Enzyme loading of 15 FPU/g Hydrolyzed for 48 h at 50 °C with continuous agitation of 120 rpm	29.2 kg/100 kg raw biomass	[51]
2	Elephant grass (*Pennisetum purpureum*)	Cellulolytic complex of Celluclast® (Cellulase) & Novozyme 188® (β-glucosidase)	5 %-20 % w/v Solid loading 50 mMol/L sodium citrate buffer. Cellucast & Novozyme loading of 10,15,20 and 30 FPU/g Hydrolysis was carried out at pH 4.8 and 50 °C for 24,48,72, and 96 h in a rotary shaker at 150 rpm. Sample withdrawn in every 24 h.	39.29 g/100 g raw biomass	[52]
3	*S. ravennae*	Cellic® Ctec2	8% solid loading 0.06 g enzyme protein/g dry biomass	431.9 mg/g	[53]

	0.5 M citrate buffer (pH 4.8)
	at 50 °C, 150 rpm for 72 h

1.3.2. Lignin extraction processes from biomass

Ongoing advancements in lignin recovery methods and pre-treatments convey the dynamic nature of research in this field. The traditional approaches for lignin extraction from lignocellulosic biomass closely align with the methods deployed in the paper industry (Tan et al. [64]). In general, these methods are classified into chemical or mechanical extraction, a categorization contingent upon the intended application of lignin and its co-products, cellulose and hemicellulose. The mechanical extraction methodologies can be broadly categorized into two essential processes: refiner and grinding [65]. On the other hand, chemical extraction techniques for lignin are typically classified into two main categories: sulfur and sulfur-free processes [66]. Nonetheless, alternative methodologies have been embraced to fractionate lignocellulosic biomass effectively for lignin extraction.

Refiner processes are further categorized based on pre- or post-treatment applied to lignocellulosic biomass. They are often independent of the size reduction strategies. Developed in the 1950s and industrially implemented in 1960, the refiner mechanical pulp procedure operates at atmospheric pressure and temperatures near 100 °C and without prior pretreatment [65]. Mechanisms involving cutting, shearing, and compression contribute to primary cell wall removal (shearing) and hydrogen bond disruption (compression) [32]. Such process schemes reduce biomass recalcitrance and complexity and thereby lessen the severity of pretreatment conditions. Thereby, the process enhances carbohydrate accessibility and fosters versatility for integration with other extraction methods as a preceding or subsequent step to mechanical or chemical pulping schemes.

Thermo-mechanical pulping, a widely adopted mechanical extraction method, incorporates a steam-based treatment method that was developed in the 1960s. This involves exposing lignocellulosic biomass to steam at temperatures of 140 °C to 155 °C

and pressures of 300 kPa to 500 kPa. Recognized for its potential in ethanol production and generating monomeric sugars from agro-industrial biomass, this process scheme attracted research interest. Nakagawa-Izumi et al. (2017) applied thermo-mechanical pulping (160 °C through dry-blowing) for lignin extraction from oil palm empty fruit bunches [67].

Stone groundwood, pressure groundwood, and distinct grinding processes differ in the conditions of pressure and temperature being applied during the lignocellulosic resource grinding process [68]. Stone groundwood involves grinding the biomass with a grinder that applies shear stress tangentially or radially to the surfaces. While concrete grinders were traditionally used, ceramic-based grinders are presently adapted [68]. Pressure groundwood (PGW), an industrial technique until the 1970s, enhanced the groundwood procedure by increasing pressure [44]. The process performance improvement strategies critically leverage the pressure-temperature relationship [65].

Due to its high efficiency, the Kraft method, often called the sulfate process, is widely used for lignin extraction in many paper businesses. In this method, sodium hydroxide (NaOH) and sodium sulfide (Na_2S) are used in alkaline hydrolysis in a solution called "white liquor," usually in a ratio of 1 mol/L NaOH and 0.25–0.70 mol/L Na_2S [69]. To extract lignin from *Populus alba L.*, Martín-Sampedro et al. (2019) used the Kraft pulp method in conjunction with other techniques [70]. The blend was cooked at 160 °C for 50 minutes with a liquor/wood ratio of 4:1, 16% active alkali, and 20% sulfide. This produced a yield of 89.3% and a purity of 77.2%.

The sulfite process involves reactions between a metallic sulfite and sulfur dioxide (SO_2), typically utilizing calcium sulfite ($CaSO_3$) or magnesium sulfite ($MgSO_3$). This process entails simultaneous sulfonation, hydrolysis, and condensation reactions and thereby leads to the cleavage of α- and β-ether linkages in lignin [71]. Typically being conducted at temperatures ranging from 125 °C to 150 °C and a reaction time of 3–7 hours, the resultant lignin from this procedure is known as lignosulfonates. Lignosulfonates exhibit favorable hydrophilic properties due to structural-functional groups such as carboxylic groups, phenolic hydroxyl, and sulfur-containing groups [72]. Purification steps for the

recovery of high-purity lignosulfonates involve fermentation of residual sugars to ethanol and subsequent membrane filtration to reduce metal ion content.

The soda technique is commonly used to extract lignin from non-wood precursors such as annual plants and bagasse [73]. Alkaline lignin devoid of sulfur is obtained using the soda pulping method. Such processes do not necessitate the utility of sulfur-containing chemicals. However, in comparison to the Kraft method, the lignin recovery is lower [74]. Mohamad et al. (2020) extracted soda lignin from kenaf biomass and used it as a rubber filler [75]. It involved boiling around 30% of the active alkali in an 8:1 solid/liquid ratio for three hours at 170 °C and 12-15 bar of pressure. According to their report, the procedure yielded 17.86% lignin.

Alternative lignin extraction methods, including steam explosion, ammonia treatment, deep eutectic solvents (DES), and ionic liquids, have been explored as well. Ammonia treatment involves physicochemical alkaline pretreatment with liquid ammonia at temperatures between 60 and 180 °C for 5 to 60 minutes and at a typical pressure of 0.7–4 MPa. The process has an advantage in terms of recoverable ammonia after treatment [76]. Steam explosion, a thermochemical treatment, is conducted at 180 °C–250 °C for about 1–2 minutes. The process reaches a final pressure of 4–7 MPa [44]. Deep eutectic solvents (DES) consist of solvent mixtures that demonstrate properties such as reduced melting point (approximately 50 °C) due to specific anion/cation configurations [77]. Ionic liquids (IL) serve as green solvents and accordingly enhance carbohydrate and lignin dissolution. Thereby, they mitigate lignin rigidity [78]. While IL-based treatments demonstrate increased efficiency with substantial biomass volumes, challenges such as high toxicity, pH, and cost parameters still limit their widespread use [79].

Three key requirements must be met for the lignin extraction from lignocellulosic biomass. These are quantifiability, elimination of contaminant substances, and intact structure. However, it is extremely difficult to achieve these standards with present separation technologies due to the complicated nature of lignin. Rather, the extraction methods must be modified to fit the industrial use or the ultimate goal of lignin isolation and characterization as a high-end product. The temperature, duration, pH, pressure, and extraction time together affect the obtained lignin yield and purity. For instance, Morales

et al. (2022) conducted treatments on almond and walnut shells at 121 °C for 90 minutes, using 7.5% NaOH and maintaining a liquid-to-solid ratio of 6:1 [80]. The resultant lignin purities were reported as 58.2 wt% for almond shells and 49.4 wt% for walnut shells. In contrast, an earlier study by Morales et al. (2018) demonstrated that a lower temperature (80°C), shorter treatment time (30 minutes), and 7.16% NaOH concentration, combined with a higher liquid-to-solid ratio of 10:1 for chestnut shells, resulted in a higher lignin purity of 63.5 wt% [81].

Furthermore, under similar conditions of a 10:1 liquid-to-solid ratio, Davila et al. (2017) achieved an even higher lignin purity of 89.9 wt% for the case of lignin treatment with vine shoots [82]. To do so, the authors reported 8% NaOH, 124 °C, and 168 minutes as an optimal set of process parameters. Accordingly, comparative studies underscore the importance of variant treatment parameters, such as temperature, time, NaOH concentration, and liquid-to-solid ratio, for the realization of optimal lignin extraction efficiency for alternate biomass sources.

In the field of high-purity lignin extraction from alternate biomass samples with the alkali treatment method, a summary of notable findings is presented in Table 1.3.

Table 1.3: A summary of key findings reported till date in the research theme of lignin extraction from alternate biomass systems with the alkali pre-treatment process.

S no	Substrate	Treatment condition	Reported Purity (wt%)	References
1	Almond shells	121 °C, 90 min, 7.5 % NaOH, Liquid-to-solid ratio- 6:1	58.2	[80]
2	Walnut shells	121 °C, 90 min, 7.5 % NaOH, Liquid-to-solid ratio- 6:1	49.4	[80]
3	Vine shoots	124 °C, 168 min, 8 % NaOH, Liquid-to-solid ratio- 10:1	89.9	[82]
4	Chestnut shell	80 °C, 30 min, 7.16% NaOH Liquid-to-solid ratio-10:1	63.5	[81]

1.3.3. Application of lignin for heavy metals removal

The predominant global challenges affecting the biodiversity of aquatic ecosystems, industrial processes, agricultural activities, and drinking water sources are centered around environmental and water pollution. Heavy metals, stemming primarily from human industrial activities, emerge as a crucial category of toxic substances in water resources. Consequently, international efforts have been emphasizing the regulation and treatment of heavy metals containing water. Despite these efforts, the outcomes of pollution control are not promising. Therefore, they necessitate additional endeavors to rejuvenate water resources to an acceptable quality. Depending on a number of variables, several heavy metal decontamination techniques have been proposed. These include physical, chemical, electrical, and biological approaches [83], [84]. Such alternate options pose a greater challenge to the selection of decontamination technology. In certain situations, multiple technologies may have to be adopted to realize the targeted removal efficiencies. Otherwise, one of the few alternate methods, such as chemical precipitation, ion exchange, adsorption, coagulation, electrochemical approaches, and membrane filtration, could be promising [85].

A variety of lignin surface modifications, such as carboxyl, amines, nitrates, and sulfonic groups, have been demonstrated as heavy metal absorbers with very good heavy metal adsorption rates. To date, cadmium, zinc, nickel, lead, copper, and mercury have been reported as the major heavy metal ions that can be efficiently removed with lignin [85]. Lignin sources, extraction methods, molecular weight, and functional groups all affect the receptivity of lignin to various heavy metals [86]. High Ni(II), Zn(II), and Cu(II) adsorption capacities were reported for a green composite material consisting of grafted lignin and poly(ethyleneimine). Optimal process conditions of 6.0 pH and 25 °C ensured 67.0 mg/g, 78.0 mg/g, and 98.0 mg/g adsorption capacity for Ni(II), Zn(II), and Cu(II), respectively [87]. Hydrogels made of porous lignin are an efficient heavy metal removal material [88]. It has also been observed that lignin composites, such as TiO_2/lignin and TiO_2, and SiO_2/lignin hybrids, are capable of eliminating heavy metal ions, especially cadmium and nickel (II) [89].

Due to its compatibility with synthetic polymers such as polyolefin, polyvinyl alcohol, and polyvinyl chloride, lignin interacts well with homogeneous solvents and can be henceforth deployed in various separation methods [90]. Accordingly, Yong et al. (2019) reported that the PVC/lignin ultrafiltration membrane has been effective in separating oil from water (97% oil rejection rate) [91]. According to the data statistics, enhanced lignin content increased the porosity, average pore size, and permeability of the modified membrane. In order to create a persistent hydration layer and increase the hydrophilicity of the PVC membrane, the hydrophilic groups of lignin were exposed on the membrane's upper surface. This prevented dirt from interacting with the membrane's surface. Even after oily wastewater treatment, the membrane maintained good stability and durability.

With regard to natural polymers like cellulose, lignin is not very compatible. Since lignin's hydrophilic groups are surrounded by hydrophobic chains, it is incompatible with hydrophilic carbohydrates such as cellulose. As a viable research scheme, Laura et al. (2011) used a solution-casting method to create a water-treated nanocomposite membrane with propionic acid lignin and triacetate cellulose [92]. It was employed to filter groundwater that contained elevated levels of arsenic, calcium, sodium, and magnesium. The findings indicated that the rates of membrane rejection were 15–35%, 12–42%, and 27–54% for anions, monovalent cations, and divalent cations, respectively. Furthermore, organics and ions that exist in groundwater have a sensitive influence on the membrane's ability to remove fluoride and arsenic from the groundwater system [92].

In addition to the previously mentioned polymeric materials, various lignin-based mixed membranes being created with the lignin blending with other natural polymeric substances have been reported. Duan et al. (2018) developed a novel lignin/chitin membrane with an ionic liquid, 1-butyl-3-methylimidazolium acetate, and γ-valerolactone as the solvent system [93]. This lignin/chitin membrane was applied as an adsorbent for the uptake of Fe(III) and Cu(II) cations from aqueous solutions. The findings revealed that, within 48 hours, the maximum adsorption capacity for Fe (III) was 84 wt%, and for Cu(II), it was 22 wt% [93]. Moreover, the lignin/chitin membranes demonstrated a promising ability for regeneration through the desorption of Fe(III) and Cu(II) ions. Consequently, the lignin/chitin membrane exhibited a notable capability for

the adsorption of metal ions and thereby proved to be a stable and recyclable biosorbent material.

Chromium (Cr) is placed fifth among the possibly most dangerous elements. It is carcinogenic to living creatures and poses a significant risk to the environment [94]. In stable conditions, the majority of water resources only contain the trivalent (Cr(III)) and hexavalent (Cr(VI)) forms of Cr. The literature describes several techniques for Cr removal from wastewater. Most of these are effective in removing Cr at higher concentrations. Chemical reduction, precipitation, flotation, solvent extraction, membrane separation (including ion exchange membranes, surfactant-based membranes, nanofiltration, microfiltration, hybrid membrane systems, and ultrafiltration), electrochemical treatment (electrodialysis, electrolysis, and electrocoagulation), and ion exchange are some of the conventional techniques being used for Cr removal [95]. Among these, membrane separation processes have extensive promising applications in industrial settings. Gasemloo et al. (2019) conducted a study on the fabrication of a sulfated carboxymethyl cellulose nanofiltration membrane (SCMC-GA-NF) being realized along with the glutaraldehyde (GA) crosslinked polysulfone system. For this case, the maximum removal efficiency for Cr(VI) was 79.85%, and at pH 4 and 3 bar transmembrane pressure [96]. Jo et al. (2022) developed an IP-assembled poly(acryloyl hydrazide)-branched star polymer (PAH-TFC) for Cr(VI) removal from wastewater. The advanced material demonstrated superior Cr(VI) rejection (approximately 55% at pH 3) in comparison to similar water-permeable commercial reverse osmosis membranes [97]. In summary, membrane separation can be affected by a variety of factors, including material, membrane pore size, and content. To date, membrane filtration has not received enough attention for Cr removal due to its lower removal capacity. Thereby, altered membrane characteristics through the utilization of catalysts have been targeted.

Polysulfone (PSf) is a frequently employed material in the production of membranes utilized for membrane separation applications, such as wastewater treatment. Because of its exceptional film-forming qualities, chemical inertness, strong mechanical strength, thermal stability, programmable pore size, and reliably repeatable features, the polymer makes membrane fabrication easy [98]. Efficient separation of heavy metal ions requires

membrane modification. Such a scheme addresses limitations in rejecting or adsorbing small molecules and overcomes the inherent hydrophobic nature of the membrane. This can be achieved through the incorporation of organic/inorganic compounds or nano-materials as a third component in the membrane casting solution. Habibi et al. (2015) reported that SiO_2 nanoparticles and polydopamine (PDA) integrated PSf membrane demonstrated enhanced hydrophilicity, stable water flux of 13 L/m^{2}h, and 94% Cr (VI) removal at pH 3 [98]. According to a 2019 study by Jacob et al., [99] PSf with 1% TiO_2 performed better and demonstrated a flow rate of 75.714 L/m^{2}h and an impressive 94.045% rejection of Cr (VI) ions. Further, better antifouling characteristics have been reported. Similarly, Nayak et al. (2020) investigated TiO_2 grafted PSf membrane, which removed 88% Cr (VI) with a 69 times lower pressure differential [100].

Shah et al. (2013) enhanced heavy metal removal through the utilization of functionalized multi-walled carbon nanotube/polysulfone (MWNT/PSf) composite membranes [101]. The authors discovered that the higher nanotubes percentage led to better results, especially under high pressure (0.49 MPa) acidic conditions (pH 2.6). Membranes with amide-functionalized nanotubes achieved an impressive 94.2% removal of Cr(VI). Thereby, they surpassed the performance of plain polysulfone membranes, which could only manage Cr (VI) 10.2% removal. In a study conducted by Mahajan and colleagues in 2021, the authors aimed to enhance the performance of polysulfone (PSf) membranes for chromium (Cr) removal from water [102]. The optimization involved the utility of polyethylene glycol (PEG) as a porogen. Further, ZnO was used as an additive to enhance the membrane's capabilities for Cr(VI) removal from contaminated water systems. With HCl-treated ZnO, the authors achieved an impressive maximum of 80% Cr (VI) removal. Furthermore, the incorporation of a porogen led to a substantial increase in the pure water flux and eventually reached a high transmembrane water flux of 302 L/m^{2}h. Jacob et al. (2020) explored the utility of nano clay and about 3% montmorillonite clay (MMT) as a nanofiller for the enhancement of the surface properties of PSf membranes [103]. The authors concluded that the incorporation of MMT in the PSf matrix enabled the removal of 94% of Cr(VI) in a cross-flow filtration system. Additionally, the introduction of polyvinylpyrrolidone (PVP) as a porogen led to a notable increase in PWF. Typically, a

polysulfone (PSf) membrane without any porogen tends to have lower pure water flux (PWF). In a study conducted by Xu et al. in 2014, the authors synthesized a PSf hollow fiber membrane through the grafting with 10% 2-acrylamido-2-methylpropane sulfonic acid (AMPS) [104]. Despite achieving a high removal efficiency of 95.1% for Cr(VI), the pure water flux remained relatively low at 23.8 L/m^2h.

Table 1.4 summarizes the best outcomes of the PSf-based membranes for the treatment of Cr (VI) containing aqueous systems.

Table 1.4: Literature data summary of PSf-based membranes for Cr (VI) removal from aqueous systems.

S no	Membrane	Filtration condition	PWF (L/m^2h)	Cr (VI) Removal (%)	Ref.
1	One wt.% Amide functionalized carbon nanotube/PSf composite membrane	UF test cell setup (0.49 MPa) at pH 2.6	210	94.2	[101]
2	PSf/PEG/HCl treated ZnO membrane	Dead-end cell (2 bar)	302	80	[102]
3	PSf/PVP/1% TiO_2	Cross-flow filtration unit (69 bar)	75.714	94.045	[99]
4	PSf/SiO2/PDA (polydopamine) membrane	Dead-end filtration apparatus (2 bar) at pH 3	13	94	[98]
5	PSf/3% mMMT (modified montmorillonite clay) MMM	Cross-flow filtration unit (2 bar)	271	95	[103]
6	10% 2-acrylamido-2-methylpropane sulfonic acid (AMPS) grafted PSf hollow fiber membrane	Home-built cross-flow filtration apparatus (4 bar) at pH 9.0	23.8	95.1	[104]
7	2.5% ABA-PVC (4-aminobenzoic acid-polyvinyl chloride)/PSf/TiO_2 (300 mg) composite membrane	Stainless steel dead-end filtration unit (100 kPa) at pH 4	6.5	88	[100]

1.3.4. Application of lignin in membrane modification for the simultaneous removal of heavy metal and dye

Water contaminated with dye or heavy metals is a serious environmental issue, and significant research has been devoted to removing them effectively and affordably. The extreme toxicity, nonbiodegradability, and accumulation of these pollutants in humans, animals, and plants render them the two most paramount contaminants in wastewater [105]. Prolonged exposure to heavy metal ions, such as lead (Pb^{2+}), can result in illness, neurological disorders, kidney and liver disease, anemia, cardiovascular inadequacies, lung problems, bone damage, hypertension, and cancer [106]. The maximum permitted lead concentration in drinking water is 0.01 mg/L as per the World Health Organisation recommendation and 0.015 mg/L as per the US Environmental Protection Agency recommendations [107]. Hence, lead pollution in aqueous systems is a global concern that requires concerted efforts to efficiently remove the ions from polluted water systems.

Among various contaminants, dyes are one of the most toxic substances that have been released into the environment. In several industries, including food, leather, printing, plastic, paper, and textile, dyes are used as colorants. Dyes have complex aromatic structures that are not biodegradable and are carcinogenic. Eosin Y, also commercially known as Acid red 87, is an anionic dye, highly water soluble, and belongs to the group of triaryl methane dyes. Due to its red color and powerful absorption by RBC (red blood cells), Eosin Y is often used in bacterial Gram staining. Also, as a heterocyclic dye, it finds industrial applications, including fluorescent pigments, painting, dying, printing, and leather industries [108]. Such industrial usage of Eosin Y dye might seriously irritate the skin and eyes. It has several harmful consequences when ingested or inhaled, especially on the liver, kidney, and lungs. Through obliteration of the retinal ganglion, Eosin Y also causes the eye to suffer irreversible damage [108].

Due to the toxicity and adverse effects of Pb^{2+} and Eosin Yellow, it is essential to devise a simple and cost-effective technique for their removal from wastewater. Previously, many procedures have been explored to eliminate lead ions from wastewater. These include systems such as membrane electrodialysis, ion exchange, solvent extraction,

filtration, adsorption, chemical precipitation, and electrocoagulation [109], [110]. Despite being economical, adsorption processes involve extended timeframes without an external source of energy. Membrane technologies are generally efficient, clean, low-cost, and ecological in efficiently separating heavy metals [111]–[113]. Compared to nanofiltration, reverse osmosis, and microfiltration, ultrafiltration is a favorable alternative for industrial heavy metals and dye removal. This is due to its balanced selectivity, reduced fouling tendency, energy efficiency, and water quality preservation [114], [115].

Lignin stands out as a significant and easily accessible renewable resource. Due to its structure, characterized by a wealth of aromatics and phenolic hydroxyls, lignin has become the focus of exploration for numerous innovative applications. Numerous studies have documented the diverse applications of lignin as an adsorbent for the removal of heavy metals and dyes [116]. Zhang et al. (2020) employed the cross-linking method to create the lignosulfonate biosorbent (CLLS), which demonstrated the capability to concurrently adsorb Pb^{2+} and methylene blue (MB) [117]. The highest adsorption capacities for Pb^{2+} and MB in a single system were 358.4 mg/g and 100.9 mg/g, respectively. Chen et al. (2020) also developed a fully degradable lignin adsorbent (SLS) through the suspension cross-linking method. The system exhibited effective removal of Pb^{2+} and MB [118]. In the adsorption study, the maximum capacity for Pb^{2+} and MB was determined to be 80 mg/g and 70 mg/g, respectively. In a one-step process, An et al. (2020) employed silanization and amination on sulfate lignin to create double-modified lignin (SAL) for the adsorption studies of Congo red and Cu^{2+} [119]. Accordingly, the maximum adsorption capacities were determined to be 74.4 mg/g for Congo red and 17.8 mg/g for Cu^{2+}, respectively. While the developed lignin adsorbents exhibit the capability to adsorb dyes and heavy metal ions, there exists a significant disparity in their adsorption effectiveness. Additionally, certain adsorbents display a lower adsorption capacity. Even though the formulated lignin-based adsorbent can achieve the simultaneous adsorption of heavy metal ions and dyes, variations exist. Certain adsorbents demonstrate effectiveness in removing dyes, while others prove to be efficient in removing metal ions [116].

Lignin, a key component of lignocellulose biomass, has a three-dimensional structure and an abundance of oxygen-containing groups such as phenolic hydroxyls. Hence, it can serve as a possible blending material for membrane fabrication [120]. Lignin-based adsorbents have been used extensively to remove organic dyes and heavy metal ions [121], [122]. However, innovative lignin-incorporated membranes for dye and heavy metals removal have not been investigated. Also, it is crucial to develop multifunctional materials to effectively remove heavy metals and organic dyes due to the complexity of wastewater composition. Due to its distinct structure of functional groups, including carboxylic acid, hydroxyl, and epoxide groups, Graphene oxide (GO) was typically extensively researched in terms of its potential in the industrial sector as an excellent adsorbent for wastewater remediation and heavy metal removal. However, the membranes modified with GO are prone to fouling, and regeneration does not ensure a return to the initial conditions due to electrostatic interactions with heavy metals [123].

Till now, there has not been a dedicated study addressing the simultaneous removal of Pb^{2+} ions and Eosin Y dye from aqueous solutions. This gap in the existing research suggests an opportunity for further investigation into the potential of lignin-GO incorporated membranes that could effectively address the concurrent removal of both contaminants. Existing studies have explored effective methods for removing Pb^{2+} or Eosin Y dye independently, but the specific challenges and potential synergies associated with the concurrent removal of both contaminants remain unexplored. Zhang et al. (2022) have recently created an effective thin-film nanofibrous composite (TFNC) membrane [124]. This membrane is made up of polyacrylonitrile (PAN) and UiO-66-$(COOH)_2$. By incorporating calcium alginate (CaAlg) into the membrane, the research group demonstrated the capability to treat wastewater containing single lead ions up to 7659 L/m^2, meeting the WHO drinking water standard. In their efforts to eliminate lead ions from water, Alfalahy and Al-Jubouri (2022) developed a polyethersulfone ultrafiltration membrane with NaX zeolite [125]. The authors achieved a 97% removal of Pb^{2+} ions using a membrane containing 0.9 weight percent zeolite and at process conditions of 6 pH, 25 ^oC, and 1.6 bar transmembrane pressure.

In a 2023 study reported by Parveen et al. [126], the authors found that a commonly available material called the commercial anion exchange membrane BI (AEM BI) can work really well to remove Eosin yellow dye from wastewater. The authors deployed only 0.15 g of the adsorbent. Thereby, in the first cycle of 120 minutes, the adsorbent removed 88% of the dye from a solution containing 50 mg/L dye. Surprisingly, after the third cycle, the adsorbent was even more effective and removed up to 94% of the dye. In a study conducted in 2018, Kuvarega et al. [127] developed a novel photocatalytic membrane through the addition of N, Pd-doped TiO_2 into the PSf matrix. Upon exposure to the sunshine, the membrane was expected to degrade the Eosin yellow dye. Thereby, for exposure to visible light for four hours, up to 97% of the Eosin yellow dye was eliminated.

Table 1.5 summarises the important findings reported in the field of membrane-based removal of Pb^{2+} and Eosin Y dye.

Table 1.5: A summary of key findings reported in the literature for the composite membrane-based Pb^{2+} and Eosin yellow removal from aqueous systems.

S no	Membrane	Operating setup	PWF (L/m^2h)	Contaminant	Removal /rejection (%)	Ref.
1	CaAlg/PAN-UiO-66-$(COOH)_2$ TFNC (thin film nanofibrous composite) membrane (UiO-66-$(COOH)_2$: PAN=2)	Using a dead-end filtration system (M8010, Millipore, USA)- at 0.1 MPa	50	Pb^{2+}	≥90%	[124]
2	NaX zeolite (0.9 %)/ PES (Polyethersulfone) ultrafiltration mixed matrix membrane	Cross-flow system- at 1.6 bar	88.05	Pb^{2+}	97%	[125]

3	Commercial anion exchange membrane BI (quaternized poly 2,6-dimethyl-1,4-phenylene oxide and polyvinyl alcohol).	Adsorption study- 0.15 g membrane in 50mg/mL Eosin Y solution (tap water) for 60 minutes (1st cycle)	NA	Eosin Y	94%	[126]
4	N,Pd codoped TiO_2 (7%) /PSf membrane	The photocatalytic degradation- 3 cm × 3 cm membrane in 100 mL of 100 PPM EY solution under visible light irradiation for 4 h	NA	Eosin Y	97%	[127]

1.4 Possible scope for further research

1.4.1 Enhance sugar yield from Ravenna grass for maximizing bioethanol yield

The effectiveness of pretreatment methods depends upon the characteristics of the deployed biomass. Based on literature findings, both H_2SO_4 (sulfuric acid) and alkalis such as NaOH can be inferred to be superior choices for biomass pretreatment in terms of the maximum yield of the reducing sugars [39], [128]. Further, Ravenna grass can be analyzed as the least studied biofuel substrate among various elephant grass species. The literature only documents the exploration and documentation of the ozone pretreatment for the mentioned grass species [6]. Panneerselvam et al. (2013) obtained a peak sugar yield of 431.9 mg/g from enzymatic hydrolysis of ozonated *Saccharum ravennae* [5].

In the presence of surfactants, the enzymatic breakdown of cellulosic substrates is more effective. Surfactants play a crucial role in preventing the thermal denaturation of enzymes during hydrolysis. This is valid even under elevated temperatures. Additionally, it has been noted that surfactants may adsorb onto the lignin fraction of lignocellulosic

biomass through hydrophobic interactions during the conversion of cellulose to glucose [129]. Thereby, the adsorption helps to prevent the binding of enzymes to lignin and ultimately enhances the breakage into glucose. The influence of the ionic strength of various surfactants on the alternate pretreated substrate systems during enzymatic hydrolysis can provide a deeper understanding of the system's efficacy in terms of the desired output. Additionally, it can help to build a more affordable yet successful method in terms of improved sugar yields.

The existing literature suggests that in order to make Ravenna grass a viable lignocellulosic substrate for second-generation biofuel production, there is a need to enhance the theoretical sugar yield. Currently, it is challenging to directly compare various pretreatment procedures due to their distinct characteristics, differences in approaches, and the use of different substrates. Specifically, the effects of acid, alkali, and two-stage acid-alkali pretreatment on the composition of Saccharum ravennae biomass have not been investigated. Furthermore, the synergistic impact of different pretreatment methods and surfactants on the enzymatic hydrolysis of Ravenna grass biomass remains unexplored. Understanding how these factors interact and influence the efficiency of enzymatic hydrolysis is crucial for optimizing the overall bioethanol production process using this particular substrate. These shall be addressed as the first objective of this Ph.D. thesis.

1.4.2 High-purity alkaline lignin extraction

As elucidated in the preceding section 1.3.2 and as detailed in Table 1.3, alkaline pretreatment with sodium hydroxide (NaOH) has been superior and effective for lignin extraction in conjunction with the alternative chemical pretreatment methods. Using an 8% NaOH solution, Dávila et al. (2017) recovered 89.8% pure lignin from vine shoots and demonstrated its efficacy for selective lignin removal [82].

Despite conveying the capability of both NaOH and KOH to dissolve Kraft lignin, the reported findings did not deliberate upon the meticulous investigation of potassium

hydroxide (KOH) for lignin extraction in comparison with the sodium hydroxide (NaOH). The potential advantages of KOH, such as its stronger basicity due to weaker K-O bonds compared to Na-O bonds, have not been thoroughly explored in the context of lignin extraction. While Melro et al. (2020) demonstrated the ability of both NaOH and KOH to dissolve Kraft lignin, there is a need for more in-depth investigations into the specific mechanisms and efficiency of lignin extraction using KOH and for the mentioned elephant grass system[130]. The reported substantial weight percentage of dissolved lignin (40 wt.%) provides a promising starting point but warrants further exploration to optimize extraction conditions. Therefore, it is important to understand and explore the full potential of KOH as a lignin extraction agent. Moreover, the study by Fierro et al. (2007) highlighted the chemical activation of kraft lignin with KOH. This resulted in the generation of extremely microporous materials. However, a research gap exists in the direct comparison of materials deduced through either KOH or NaOH, especially in terms of surface areas and micropore volumes. [131]. A useful insight into the alterations in the activation outcomes of these two alternate bases could provide inferences for the consolidation of the application domain of the unique properties of the resultant materials.

In summary, the research gap conveys the need for a more comprehensive exploration of potassium hydroxide (KOH) for lignin extraction. A comparative framework for the NaOH base system shall be explored in the context of the realized materials and their properties in terms of the surface areas and micropore volumes. Addressing such gaps could contribute to the optimization of lignin extraction processes to thereby enhance the properties of activated materials for various applications. These shall be addressed as the second objective of this Ph.D. thesis.

1.4.3 Lignin-based mixed matrix membrane preparation for heavy metal removal

The antecedent scientific literature underscores the modification of lignin as a pivotal avenue for heavy metal adsorption applications [85], [89]. Lignin has been established as a promising adsorbent for hexavalent chromium ions (Cr(VI)). The modification of lignin

for chromium adsorption studies over the last decade reflects the ongoing efforts that targeted the optimization and enhancement of the adsorption properties of lignin-based materials [132], [133]. Additionally, lignin-based hydrogels exhibited a proclivity for the effective separation of oil from aqueous environments [134]. However, it is worth noting that there is a marked dearth of research on lignin-based membrane development for heavy metal removal. In a recent study conducted by Peredija et al. (2021), a bio-membrane was developed with modified cellulose, lignin, and tannic acid for the removal of heavy metals. Despite ascertaining promising adsorption performance, it shall be noted that the procured materials were commercial and henceforth enhanced the cost of the material synthesis and operation [135]. According to the literature, commercially available lignin has been the most frequently used material for investigations targeting lignin-based membranes for water treatment applications [92], [135], [136]. Such applications do not ensure relevant confidence levels for the utilization of lignin from spent or waste resources. Thus, lignin generated from the waste grassland can be explored as a viable option for the fabrication of cost-effective membranes. Further, due to its poor removal ability, membrane filtration did not receive significant attention for Cr removal.

From the provided literature, several research gaps emerge. Firstly, there is a notable absence of studies utilizing biowaste-generated lignin for the removal of hexavalent chromium from aqueous systems. This suggests an untapped potential for the deployment of lignin derived from biowaste sources in environmental remediation efforts. Secondly, explorations of the incorporation of lignin into the polysulfone membrane matrix have not been reported to date. The absence of research in this area leaves unaddressed questions in terms of lignin integration and its influence on the membrane performance characteristics. Lastly, the potential impact of lignin on membrane performance has not been thoroughly investigated. Understanding how lignin interacts within the polysulfone membrane matrix and its consequences for membrane properties and efficacy is a crucial aspect that remains unexplored. In conclusion, a formidable research gap exists in terms of the utilization of biowaste-generated lignin for Cr(VI) removal, the incorporation of lignin into polysulfone membranes, and the subsequent study of its effects on membrane performance. Exploring these aspects could contribute to economically feasible and

sustainable environmental remediation methods, particularly in the context of chromium removal using membrane filtration. These shall be addressed as the third objective of this Ph.D. thesis.

1.4.4 Lignin-based composite membrane development for heavy metal and dye removal

As delineated in the prior art, a multitude of investigations posit lignin as a judicious material for the formulation of adsorbents tailored for the sequestration of heavy metals and dyes. In a notable instance, Zhang et al. (2020) employed a cross-linking methodology to fabricate a lignosulfonate biosorbent. This biosorbent exhibited its ability to concurrently adsorb Pb^{2+} ions and methylene blue [117]. In an alternate investigation, An et al. (2020) utilized silanization and amination on sulfate lignin. This resulted in the development of double-modified lignin [119]. The modified lignin was then employed in adsorption experiments involving Congo red and Cu^{2+}. While the modified lignin-based adsorbent demonstrates concurrent adsorption capabilities for heavy metal ions and dyes, some adsorbents exhibit diminished adsorption capacities. Specific adsorbents excel in the removal of dyes, whereas others ensure highly efficient extraction of metal ions [116]. Lead is employed in the textile industry in different forms, such as lead acetate for dyeing textiles, lead chloride for preparing lead salts, and lead molybdate for pigments used in dyestuffs. Additionally, Eosin Y, a water-soluble dye commonly known as eosin, is a red crystalline powder extensively utilized in textile dyeing and ink manufacturing. The coexistence of both Eosin Y dye and lead metal ions in textile industry effluents is, therefore, high. Based on the literature discussed, there appears to be a gap in research, as no studies have been conducted on the simultaneous removal of Eosin Y and Pb^{2+} ions. This underscores the need for further investigation and research in this specific area to better understand and address the potential challenges associated with the coexistence of Eosin Y dye and lead (Pb^{2+}) ions in various contexts, such as industrial effluents.

Lignin-based adsorbents have been used extensively to remove organic dyes and heavy metal ions [121], [122]. However, innovative lignin-incorporated membranes for dye and heavy metals removal have not been investigated. Also, it is important to develop

multifunctional materials to effectively remove heavy metals and organic dyes due to the complexity of wastewater composition. There is currently a lack of research on the synergistic effect of the coexistence of alkaline lignin and graphene oxide in the polysulfone membrane matrix for contaminants removal. Future studies in this area could explore how the presence of alkaline lignin and graphene oxide influences the properties and performance of the polysulfone membrane, especially in terms of heavy metals and dye removal.

For the above-mentioned reasons, the Ph.D. thesis research work attempts to improve PSf membrane performance through the inclusion of lignin and GO at variant membrane constitutions for efficient membrane performance. The goal was twofold: first, to improve the membrane's ability to absorb Pb^{2+} and, second, to enhance its dye rejection capabilities as an ultrafiltration membrane. Utilizing the unique functional groups and intrinsic qualities of both Lignin and GO, it is possible to overcome the inherent constraints that exist to fabricate a highly effective, regenerable, and superior membrane. Also, to make the process eco-friendly and economically feasible, the filler substances shall be extracted from waste sources. Thereby, commercial procurement can be avoided to enhance sustainability in process development research studies. These shall be addressed as the fourth objective of the Ph.D. thesis.

1.5 Objectives of thesis work

Based on the prior art review and detailed scope of possible work, the objectives of the Ph.D. thesis work have been stated as follows:

- Studies on the chemical pretreatment and surfactant-mediated enzymatic hydrolysis of *Saccharum ravennae* grass biomass for enhanced sugar and bioethanol yield.
- KOH pretreatment based high purity alkaline lignin extraction from *Saccharum ravennae* grass and its characterization.

- Preparation and characterization of mixed matrix membrane for Cr(VI) removal with the alkaline lignin extracted from Ravenna grass.
- Preparation and characterization of PSf-GO-alkaline lignin ultrafiltration composite membrane for Pb^{2+} and Eosin Y dye removal.

1.6 Organization of the Thesis

Chapter 1 discusses the background of the problems undertaken in this work, i.e., the associated gap in the field of the extraction and utilization of lignocellulosic components of Ravenna grass (*Saccharum ravennae*) biomass. Subsequently, the objectives of the thesis have been stated.

Chapter 2 gives a detailed account of the procedures adopted for the enhancement of sugar yield and bioethanol from *Saccharum ravennae* grass biomass using chemical pre-treatment and surfactant-mediated enzymatic hydrolysis methods. A detailed account of the targeted investigations that delineate the effects of acid, alkali, and subsequent acid/alkali pre-treatment, and cationic, anionic, and non-ionic surfactant-mediated enzymatic hydrolysis on total sugar recovery has been presented. Accordingly, the hydrolysates with optimized sugar content were fermented with *S. cerevisiae* to produce bioethanol.

Chapter 3 describes the extraction of highly pure lignin from *Saccharum ravennae* lignocellulosic biomass through alkali-mediated hydrothermal pre-treatment. An optimization study of lignin extraction with various parameters such as temperature, KOH concentration, solid loading, and reaction temperature was conducted via ANOVA (analysis of variance) of the central composite design-response surface methodology (CCD-RSM). Thereby, conditions favoring the highest lignin recovery efficiency have been identified. Through acid hydrolysis, the impurities of the lignin samples (i.e., acid-soluble lignin and sugars) were removed and quantified along with the produced alkaline lignin. Additionally, the total phenolic content (TPC) of lignin has also been measured. The morphology, crystallinity, and presence of the functional group in the extracted lignin

were examined. The resultant highly pure lignin sample was compared with commercial-grade alkaline lignin through several analytical processes to assess its purity.

Chapter 4 details upon the optimality of Cr (VI) removal through the incorporation of alkaline lignin extracted from Ravenna (*Saccharum ravennae*) grass into the PSf mixed matrix membrane. The influence of lignin at its variant concentrations was assessed in terms of the membrane structure and functionality. The effective lignin doping in the PSf MMMs was assessed to examine the concomitant morphological changes. Also, water flux and contact angle analysis enabled an examination of the enhanced hydrophilicity of the membranes. The influence of various lignin concentrations on Cr (VI) removal was examined, and the findings were corroborated with the analysis undertaken in terms of the energy dispersive x-ray spectroscopy (EDX) study of the spent membranes. Further, antifouling tests were conducted, and elongation and tensile strength were measured to assess better the functionality of the PSf/lignin mixed matrix membranes.

Chapter 5 details upon the findings of the utilization of membrane performance. These were realized through the synthesis of GO and alkaline lignin into the PSf matrix at variant concentrations and with the phase inversion method. The assessment of incorporated functional groups, membrane crystallinity, composition, and distinct chemical bonds within the produced membranes was conducted. The sensitive influence of lignin and GO on the hydrophilicity and antifouling properties of membranes was explored. Finally, the newly developed ultrafiltration membranes' ability to handle simulated wastewater containing a mixture of Eosin Y dye and Pb^{2+} solution was thoroughly examined.

Chapter 6 summarizes the inferences drawn from the conducted works. Thereafter, it details upon few suggestions for future research.

References:

[1] "Annual Ethanol Production." [Online]. Available: https://ethanolrfa.org/markets-and-statistics/annual-ethanol-production. [Accessed: 18-Jul-2023].

[2] M. Saini, N. Garg, A. SINGH, A. Tyagi, U. Niyogi, and R. Khandal, "Ethanol Blended Fuel in India: An Overview," *J. Biofuels*, vol. 1, Jul. 2010, doi: 10.5958/j.0976-3015.1.2.026.

[3] N. Pasiecznik, "Saccharum ravennae (ravenna grass)," *CABI Compendium*. CABI Compendium, 03-Nov-2023, doi: 10.1079/cabicompendium.109359.

[4] "Ravennagrass | All Species Wiki | Fandom." [Online]. Available: https://allspecies.fandom.com/wiki/Ravennagrass. [Accessed: 03-Oct-2023].

[5] A. Panneerselvam, R. R. Sharma-Shivappa, P. Kolar, D. A. Clare, and T. Ranney, "Hydrolysis of ozone pretreated energy grasses for optimal fermentable sugar production," *Bioresour. Technol.*, vol. 148, pp. 97–104, 2013, doi: https://doi.org/10.1016/j.biortech.2013.08.119.

[6] A. Panneerselvam, R. R. Sharma-Shivappa, P. Kolar, T. Ranney, and S. Peretti, "Potential of ozonolysis as a pretreatment for energy grasses," *Bioresour. Technol.*, vol. 148, pp. 242–248, 2013, doi: https://doi.org/10.1016/j.biortech.2013.08.129.

[7] R. File:///C:/Users/simons/Downloads/citation-333825249.risfile:///C:/Users/simons/Downloads/citation-333825249.ris *et al.*, "World resources, 2000-2001: people and ecosystems; the fraying web of life," *Choice Rev. Online*, vol. 38, no. 08, pp. 38-4430-38–4430, 2001, doi: 10.5860/choice.38-4430.

[8] M. J. M. CHRISTENHUSZ and J. W. BYNG, "The number of known plants species in the world and its annual increase ," *Phytotaxa; Vol 261, No 3 20 May 2016DO - 10.11646/phytotaxa.261.3.1* , May 2016.

[9] S. Mohapatra, S. S. Mishra, P. Bhalla, and H. Thatoi, "Engineering grass biomass for sustainable and enhanced bioethanol production," *Planta*, vol. 250, no. 2, pp. 395–412, 2019, doi: 10.1007/s00425-019-03218-y.

[10] A. Agarwal, M. Rana, and J.-H. Park, "Advancement in technologies for the depolymerization of lignin," *Fuel Process. Technol.*, vol. 181, pp. 115–132, 2018, doi: 10.1016/j.fuproc.2018.09.017.

[11] S. Mohapatra, C. Mishra, S. S. Behera, and H. Thatoi, "Application of pretreatment, fermentation and molecular techniques for enhancing bioethanol production from grass biomass – A review," *Renew. Sustain. Energy Rev.*, vol. 78, pp. 1007–1032, Oct. 2017, doi: 10.1016/J.RSER.2017.05.026.

[12] J. E. Mullet, "High-biomass C4 grasses—Filling the yield gap," *Plant Sci.*, vol. 261, pp. 10–17, 2017, doi: https://doi.org/10.1016/j.plantsci.2017.05.003.

[13] T. Weijde *et al.*, "The potential of C4 grasses for cellulosic biofuel production ," *Frontiers in Plant Science* , vol. 4. 2013.

[14] H. Rabemanolontsoa and S. Saka, "Various pretreatments of lignocellulosics," *Bioresour. Technol.*, vol. 199, pp. 83–91, 2016, doi: https://doi.org/10.1016/j.biortech.2015.08.029.

[15] L. R. J., L. J. H., and S. T. M., "file:///C:/Users/simons/Downloads/B9780128137666000035.ris," *Appl. Environ. Microbiol.*, vol. 54, no. 5, pp. 1216–1221, May 1988, doi: 10.1128/aem.54.5.1216-1221.1988.

[16] S. K. Mohanty and M. R. Swain, "Chapter 3 - Bioethanol Production From Corn and Wheat: Food, Fuel, and Future," R. C. Ray and S. B. T.-B. P. from F. C. Ramachandran, Eds. Academic Press, 2019, pp. 45–59.

[17] L. C. Basso, H. V de Amorim, A. J. de Oliveira, and M. L. Lopes, "Yeast selection for fuel ethanol production in Brazil," *FEMS Yeast Res.*, vol. 8, no. 7, pp. 1155–1163, Nov. 2008, doi: 10.1111/j.1567-1364.2008.00428.x.

[18] Y. Zeng, S. Zhao, S. Yang, and S.-Y. Ding, "Lignin plays a negative role in the biochemical process for producing lignocellulosic biofuels," *Curr. Opin. Biotechnol.*, vol. 27, pp. 38–45, 2014, doi: https://doi.org/10.1016/j.copbio.2013.09.008.

[19] H. Liu, J. Sun, S.-Y. Leu, and S. Chen, "Toward a fundamental understanding of cellulase-lignin interactions in the whole slurry enzymatic saccharification process," *Biofuels, Bioprod. Biorefining*, vol. 10, no. 5, pp. 648–663, Sep. 2016, doi: https://doi.org/10.1002/bbb.1670.

[20] Y.-A. Chen, Y. Zhou, Y. Qin, D. Liu, and X. Zhao, "Evaluation of the action of Tween 20 non-ionic surfactant during enzymatic hydrolysis of lignocellulose: Pretreatment, hydrolysis conditions and lignin structure," *Bioresour. Technol.*, vol. 269, pp. 329–338, 2018, doi: https://doi.org/10.1016/j.biortech.2018.08.119.

[21] A. A. Vaidya, K. D. Murton, D. A. Smith, and G. Dedual, "A review on organosolv pretreatment of softwood with a focus on enzymatic hydrolysis of cellulose," *Biomass Convers. Biorefinery*, vol. 12, no. 11, pp. 5427–5442, 2022, doi: 10.1007/s13399-022-02373-9.

[22] A. Azarpira, J. Ralph, and F. Lu, "Catalytic Alkaline Oxidation of Lignin and its Model Compounds: a Pathway to Aromatic Biochemicals," *BioEnergy Res.*, vol. 7, no. 1, pp. 78–86, 2014, doi: 10.1007/s12155-013-9348-x.

[23] W.-J. Liu, H. Jiang, and H.-Q. Yu, "Thermochemical conversion of lignin to functional materials: a review and future directions," *Green Chem.*, vol. 17, no. 11, pp. 4888–4907, 2015, doi: 10.1039/c5gc01054c.

[24] J. S. Kim, Y. Y. Lee, and T. H. Kim, "A review on alkaline pretreatment

technology for bioconversion of lignocellulosic biomass," *Bioresour. Technol.*, vol. 199, pp. 42–48, 2016, doi: https://doi.org/10.1016/j.biortech.2015.08.085.

[25] S. Gillet *et al.*, "Lignin transformations for high value applications: towards targeted modifications using green chemistry," *Green Chem.*, vol. 19, no. 18, pp. 4200–4233, 2017, doi: 10.1039/C7GC01479A.

[26] S. Beisl, A. Miltner, and A. Friedl, "Lignin from Micro- to Nanosize: Production Methods.," *Int. J. Mol. Sci.*, vol. 18, no. 6, Jun. 2017, doi: 10.3390/ijms18061244.

[27] M. P. Vinardell and M. Mitjans, "Lignins and Their Derivatives with Beneficial Effects on Human Health.," *Int. J. Mol. Sci.*, vol. 18, no. 6, Jun. 2017, doi: 10.3390/ijms18061219.

[28] C. Yu, F. Wang, C. Zhang, S. Fu, and L. A. Lucia, "file:///C:/Users/simons/Downloads/scopus.risfile:///C:/Users/simons/Downloads/scopus.risof a lignin-based hydrogel for remediation of cationic dye-contaminated effluent," *React. Funct. Polym.*, vol. 106, pp. 137–142, 2016, doi: https://doi.org/10.1016/j.reactfunctpolym.2016.07.016.

[29] L. Liu, M. Qian, P. Song, G. Huang, Y. Yu, and S. Fu, "Fabrication of Green Lignin-based Flame Retardants for Enhancing the Thermal and Fire Retardancy Properties of Polypropylene/Wood Composites," *ACS Sustain. Chem. Eng.*, vol. 4, no. 4, pp. 2422–2431, 2016, doi: 10.1021/acssuschemeng.6b00112.

[30] S. Sangon, A. J. Hunt, T. M. Attard, P. Mengchang, Y. Ngernyen, and N. Supanchaiyamat, "file:///C:/Users/simons/Downloads/10.1007_s13399-022-02373-9-citation.ris of highly effective carbon based adsorbents for dyes removal," *J. Clean. Prod.*, vol. 172, pp. 1128–1139, 2018, doi: https://doi.org/10.1016/j.jclepro.2017.10.210.

[31] V. B. Agbor, N. Cicek, R. Sparling, A. Berlin, and D. B. Levin, "Biomass pretreatment: Fundamentals toward application," *Biotechnol. Adv.*, vol. 29, no. 6, pp. 675–685, 2011, doi: https://doi.org/10.1016/j.biotechadv.2011.05.005.

[32] S. M. Kim, B. S. Dien, and V. Singh, "Promise of combined hydrothermal/chemical and mechanical refining for pretreatment of woody and herbaceous biomass," *Biotechnol. Biofuels*, vol. 9, no. 1, p. 97, 2016, doi: 10.1186/s13068-016-0505-2.

[33] S. Zu *et al.*, "Pretreatment of corn stover for sugar production using dilute hydrochloric acid followed by lime.," *Bioresour. Technol.*, vol. 152, pp. 364–370, 2014, doi: 10.1016/j.biortech.2013.11.034.

[34] I. Kim, Y. H. Seo, G.-Y. Kim, and J.-I. Han, "Co-production of bioethanol and biodiesel from corn stover pretreated with nitric acid," *Fuel*, vol. 143, pp. 285–289, 2015, doi: https://doi.org/10.1016/j.fuel.2014.11.031.

[35] R. B. Nair, M. Lundin, T. Brandberg, P. R. Lennartsson, and M. J. Taherzadeh,

"Dilute phosphoric acid pretreatment of wheat bran for enzymatic hydrolysis and subsequent ethanol production by edible fungi Neurospora intermedia," *Ind. Crops Prod.*, vol. 69, pp. 314–323, 2015, doi: https://doi.org/10.1016/j.indcrop.2015.02.038.

[36] J. Baruah *et al.*, "Recent Trends in the Pretreatment of Lignocellulosic Biomass for Value-Added Products ," *Frontiers in Energy Research* , vol. 6. 2018.

[37] C. C. Santos, W. de Souza, C. Sant 'Anna, and M. Brienzo, "Elephant grass leaves have lower recalcitrance to acid pretreatment than stems, with higher potential for ethanol production," *Ind. Crops Prod.*, vol. 111, pp. 193–200, 2018, doi: https://doi.org/10.1016/j.indcrop.2017.10.013.

[38] D. Sahoo, S. B. Ummalyma, A. K. Okram, A. Pandey, M. Sankar, and R. K. Sukumaran, "Effect of dilute acid pretreatment of wild rice grass (Zizania latifolia) from Loktak Lake for enzymatic hydrolysis," *Bioresour. Technol.*, vol. 253, pp. 252–255, Apr. 2018, doi: 10.1016/J.BIORTECH.2018.01.048.

[39] R. Sindhu, M. Kuttiraja, P. Binod, R. K. Sukumaran, and A. Pandey, "Bioethanol production from dilute acid pretreated Indian bamboo variety (Dendrocalamus sp.) by separate hydrolysis and fermentation," *Ind. Crops Prod.*, vol. 52, pp. 169–176, 2014, doi: https://doi.org/10.1016/j.indcrop.2013.10.021.

[40] Y. Sun and J. Cheng, "Hydrolysis of lignocellulosic materials for ethanol production: a review," *Bioresour. Technol.*, vol. 83, no. 1, pp. 1–11, 2002, doi: https://doi.org/10.1016/S0960-8524(01)00212-7.

[41] S. J. B. Duff and W. D. Murray, "Bioconversion of forest products industry waste cellulosics to fuel ethanol: A review," *Bioresour. Technol.*, vol. 55, no. 1, pp. 1–33, 1996, doi: https://doi.org/10.1016/0960-8524(95)00122-0.

[42] X. Lu *et al.*, "Enzymatic sugar production from elephant grass and reed straw through pretreatments and hydrolysis with addition of thioredoxin-His-S," *Biotechnol. Biofuels*, vol. 12, no. 1, p. 297, 2019, doi: 10.1186/s13068-019-1629-y.

[43] K. Shimizu and K. Usami, "Enzymatic hydrolysis of wood. III. Pretreatment of woods with acidic methanol-water mixture," *Mokuzai Gakkaishi;(Japan)*, vol. 24, no. 9, 1980.

[44] P. Bajpai, "Chapter 12 - Pulping Fundamentals," P. B. T.-B. H. of P. and P. (Third E. Bajpai, Ed. Elsevier, 2018, pp. 295–351.

[45] J. Nystrom, "'Pfile:///C:/Users/simons/Downloads/Citation.ris'.," *Biotechnol. Bioeng. Symp.*, vol. 219, no. 5, pp. 221–224, 1975.

[46] N. Mosier *et al.*, "Features of promising technologies for pretreatment of lignocellulosic biomass," *Bioresour. Technol.*, vol. 96, no. 6, pp. 673–686, 2005, doi: https://doi.org/10.1016/j.biortech.2004.06.025.

[47] E. C. Bensah, Z. Kádár, and M. Y. Mensah, "Alkali and glycerol pretreatment of West African biomass for production of sugars and ethanol," *Bioresour. Technol. Reports*, vol. 6, pp. 123–130, 2019, doi: https://doi.org/10.1016/j.biteb.2019.02.013.

[48] S. A. Nascimento and C. A. Rezende, "Combined approaches to obtain cellulose nanocrystals, nanofibrils and fermentable sugars from elephant grass," *Carbohydr. Polym.*, vol. 180, pp. 38–45, Jan. 2018, doi: 10.1016/J.CARBPOL.2017.09.099.

[49] "Physical and Chemical Properties of Quicklime," in *Lime and Limestone*, 1998, pp. 117–123.

[50] C. E. Wyman, B. E. Dale, R. T. Elander, M. Holtzapple, M. R. Ladisch, and Y. Y. Lee, "Coordinated development of leading biomass pretreatment technologies," *Bioresour. Technol.*, vol. 96, no. 18, pp. 1959–1966, 2005, doi: https://doi.org/10.1016/j.biortech.2005.01.010.

[51] A. Toscan, R. C. Fontana, J. Andreaus, M. Camassola, R. M. Lukasik, and A. J. P. Dillon, "New two-stage pretreatment for the fractionation of lignocellulosic components using hydrothermal pretreatment followed by imidazole delignification: Focus on the polysaccharide valorization," *Bioresour. Technol.*, vol. 285, p. 121346, 2019, doi: https://doi.org/10.1016/j.biortech.2019.121346.

[52] S. Montipó *et al.*, "Integrated production of second generation ethanol and lactic acid from steam-exploded elephant grass," *Bioresour. Technol.*, vol. 249, pp. 1017–1024, 2018, doi: https://doi.org/10.1016/j.biortech.2017.11.001.

[53] A. Panneerselvam, R. R. Sharma-Shivappa, P. Kolar, T. Ranney, and S. Peretti, "Potential of ozonolysis as a pretreatment for energy grasses," *Bioresour. Technol.*, vol. 148, pp. 242–248, Nov. 2013, doi: 10.1016/J.BIORTECH.2013.08.129.

[54] Z. X. Zhou Yan Liu Dehua, "file:///C:/Users/simons/Downloads/10.1007_s12155-011-9125-7-citation.ris Hydrolysis of Lignocellulose and Corresponding Mechanism," *Progress in Chemistry*, vol. 27, no. 11. pp. 1555–1565.

[55] R. Huang, R. Su, W. Qi, and Z. He, "file:///C:/Users/simons/Downloads/S0141022902001345.ris," *BioEnergy Res.*, vol. 4, no. 4, pp. 225–245, 2011, doi: 10.1007/s12155-011-9125-7.

[56] T. Eriksson, J. Börjesson, and F. Tjerneld, "Mechanism of surfactant effect in enzymatic hydrolysis of lignocellulose," *Enzyme Microb. Technol.*, vol. 31, no. 3, pp. 353–364, 2002, doi: https://doi.org/10.1016/S0141-0229(02)00134-5.

[57] A. Alhammad, P. Adewale, M. Kuttiraja, and L. P. Christopher, "Enhancing enzyme-aided production of fermentable sugars from poplar pulp in the presence of non-ionic surfactants," *Bioprocess Biosyst. Eng.*, vol. 41, no. 8, pp. 1133–1142, 2018, doi: 10.1007/s00449-018-1942-z.

[58] M. Yang, A. Zhang, B. Liu, W. Li, and J. Xing, "Improvement of cellulose

conversion caused by the protection of Tween-80 on the adsorbed cellulase," *Biochem. Eng. J.*, vol. 56, no. 3, pp. 125–129, 2011, doi: https://doi.org/10.1016/j.bej.2011.04.009.

[59] S. Okino, M. Ikeo, Y. Ueno, and D. Taneda, "Effects of Tween 80 on cellulase stability under agitated conditions," *Bioresour. Technol.*, vol. 142, pp. 535–539, 2013, doi: https://doi.org/10.1016/j.biortech.2013.05.078.

[60] S. Oladi and G. M. Aita, "Interactive effect of enzymes and surfactant on the cellulose digestibility of un-washed and washed dilute ammonia pretreated energy cane bagasse," *Biomass and Bioenergy*, vol. 109, pp. 221–230, 2018, doi: https://doi.org/10.1016/j.biombioe.2017.12.005.

[61] X. Lin, H. Lou, Q. Xueqing, Y. Pang, and D. Yang, "file:///C:/Users/simons/Downloads/S0960852413011838.ris," *Cellulose*, vol. 24, Feb. 2017, doi: 10.1007/s10570-016-1186-5.

[62] H. Lou *et al.*, "Reducing non-productive adsorption of cellulase and enhancing enzymatic hydrolysis of lignocelluloses by noncovalent modification of lignin with lignosulfonate," *Bioresour. Technol.*, vol. 146, pp. 478–484, 2013, doi: https://doi.org/10.1016/j.biortech.2013.07.115.

[63] Y. Jiang, T. Geng, Q. Li, G. Li, and H. Ju, "Influences of temperature, pH and salinity on the surface property and self-assembly of 1:1 salt-free catanionic surfactant," *J. Mol. Liq.*, vol. 199, pp. 1–6, 2014, doi: https://doi.org/10.1016/j.molliq.2014.07.045.

[64] S. S. Y. Tan *et al.*, "Extraction of lignin from lignocellulose at atmospheric pressure using alkylbenzenesulfonate ionic liquid," *Green Chem.*, vol. 11, no. 3, pp. 339–345, 2009, doi: 10.1039/B815310H.

[65] J. Blechschmidt and S. Heinemann, "Mechanical Pulping Processes," in *Handbook of Pulp*, 2006, pp. 1079–1111.

[66] S. Laurichesse and L. Avérous, "Chemical modification of lignins: Towards biobased polymers," *Prog. Polym. Sci.*, vol. 39, no. 7, pp. 1266–1290, 2014, doi: https://doi.org/10.1016/j.progpolymsci.2013.11.004.

[67] A. Nakagawa-Izumi, Y. Y. H'ng, L. T. Mulyantara, R. Maryana, V. T. Do, and H. Ohi, "Characterization of syringyl and guaiacyl lignins in thermomechanical pulp from oil palm empty fruit bunch by pyrolysis-gas chromatography-mass spectrometry using ion intensity calibration," *Ind. Crops Prod.*, vol. 95, pp. 615–620, 2017, doi: https://doi.org/10.1016/j.indcrop.2016.11.030.

[68] M. Ragnar, G. Henriksson, M. E. Lindström, M. Wimby, J. Blechschmidt, and S. Heinemann, "Pulp," in *Ullmann's Encyclopedia of Industrial Chemistry*, 2014, pp. 1–92.

[69] R. Rinaldi *et al.*, "Paving the Way for Lignin Valorisation: Recent Advances in

Bioengineering, Biorefining and Catalysis," *Angew. Chemie Int. Ed.*, vol. 55, no. 29, pp. 8164–8215, Jul. 2016, doi: https://doi.org/10.1002/anie.201510351.

[70] R. Martín-Sampedro, J. I. Santos, Ú. Fillat, B. Wicklein, M. E. Eugenio, and D. Ibarra, "Characterization of lignins from Populus alba L. generated as by-products in different transformation processes: Kraft pulping, organosolv and acid hydrolysis," *Int. J. Biol. Macromol.*, vol. 126, pp. 18–29, 2019, doi: https://doi.org/10.1016/j.ijbiomac.2018.12.158.

[71] B. Saake and R. Lehnen, "Lignin," in *Ullmann's Encyclopedia of Industrial Chemistry*, 2007.

[72] D. Areskogh, J. Li, G. Gellerstedt, and G. Henriksson, "Structural modification of commercial lignosulphonates through laccase catalysis and ozonolysis," *Ind. Crops Prod.*, vol. 32, no. 3, pp. 458–466, 2010, doi: https://doi.org/10.1016/j.indcrop.2010.06.016.

[73] A. Nadif, D. Hunkeler, and P. Käuper, "Sulfur-free lignins from alkaline pulping tested in mortar for use as mortar additives," *Bioresour. Technol.*, vol. 84, no. 1, pp. 49–55, 2002, doi: https://doi.org/10.1016/S0960-8524(02)00020-2.

[74] P. Azadi, O. R. Inderwildi, R. Farnood, and D. A. King, "Liquid fuels, hydrogen and chemicals from lignin: A critical review," *Renew. Sustain. Energy Rev.*, vol. 21, pp. 506–523, 2013, doi: https://doi.org/10.1016/j.rser.2012.12.022.

[75] N. A. Mohamad Aini, N. Othman, M. H. Hussin, K. Sahakaro, and N. Hayeemasae, "Effect of extraction methods on the molecular structure and thermal stability of kenaf (Hibiscus cannabinus core) biomass as an alternative bio-filler for rubber composites," *Int. J. Biol. Macromol.*, vol. 154, pp. 1255–1264, 2020, doi: https://doi.org/10.1016/j.ijbiomac.2019.10.280.

[76] J. J. Liao, N. H. A. Latif, D. Trache, N. Brosse, and M. H. Hussin, "Current advancement on the isolation, characterization and application of lignin," *Int. J. Biol. Macromol.*, vol. 162, pp. 985–1024, 2020, doi: https://doi.org/10.1016/j.ijbiomac.2020.06.168.

[77] Q. Ji, X. Yu, A. E.-G. A. Yagoub, L. Chen, and C. Zhou, "Efficient removal of lignin from vegetable wastes by ultrasonic and microwave-assisted treatment with ternary deep eutectic solvent," *Ind. Crops Prod.*, vol. 149, p. 112357, 2020, doi: https://doi.org/10.1016/j.indcrop.2020.112357.

[78] A. Ovejero-Pérez, V. Rigual, J. C. Domínguez, M. V. Alonso, M. Oliet, and F. Rodriguez, "Acidic depolymerization vs ionic liquid solubilization in lignin extraction from eucalyptus wood using the protic ionic liquid 1-methylimidazolium chloride," *Int. J. Biol. Macromol.*, vol. 157, pp. 461–469, 2020, doi: https://doi.org/10.1016/j.ijbiomac.2020.04.194.

[79] Q. Zhou *et al.*, "Quantitative structures and thermal properties of Miscanthus ×

giganteus lignin after alcoholamine-based ionic liquid pretreatment," *Ind. Crops Prod.*, vol. 147, p. 112232, 2020, doi: https://doi.org/10.1016/j.indcrop.2020.112232.

[80] A. Morales, J. Labidi, and P. Gullón, "Impact of the lignin type and source on the characteristics of physical lignin hydrogels," *Sustain. Mater. Technol.*, vol. 31, p. e00369, 2022, doi: https://doi.org/10.1016/j.susmat.2021.e00369.

[81] A. Morales, B. Gullón, I. Dávila, G. Eibes, J. Labidi, and P. Gullón, "Optimization of alkaline pretreatment for the co-production of biopolymer lignin and bioethanol from chestnut shells following a biorefinery approach," *Ind. Crops Prod.*, vol. 124, pp. 582–592, 2018, doi: https://doi.org/10.1016/j.indcrop.2018.08.032.

[82] I. Dávila, P. Gullón, M. A. Andrés, and J. Labidi, "Coproduction of lignin and glucose from vine shoots by eco-friendly strategies: Toward the development of an integrated biorefinery," *Bioresour. Technol.*, vol. 244, pp. 328–337, 2017, doi: https://doi.org/10.1016/j.biortech.2017.07.104.

[83] F. A. Caliman, B. M. Robu, C. Smaranda, V. L. Pavel, and M. Gavrilescu, "Soil and groundwater cleanup: benefits and limits of emerging technologies," *Clean Technol. Environ. Policy*, vol. 13, no. 2, pp. 241–268, 2011, doi: 10.1007/s10098-010-0319-z.

[84] D. Del Buono, E. Pannacci, M. L. Bartucca, L. Nasini, P. Proietti, and F. Tei, "Use of two grasses for the phytoremediation of aqueous solutions polluted with terbuthylazine," *Int. J. Phytoremediation*, vol. 18, no. 9, pp. 885–891, Sep. 2016, doi: 10.1080/15226514.2016.1156633.

[85] H. Sadeghifar and A. Ragauskas, "Lignin as a bioactive polymer and heavy metal absorber- an overview," *Chemosphere*, vol. 309, p. 136564, 2022, doi: https://doi.org/10.1016/j.chemosphere.2022.136564.

[86] H. Sadeghifar and A. Ragauskas, "Perspective on Technical Lignin Fractionation," *ACS Sustain. Chem. Eng.*, vol. 8, no. 22, pp. 8086–8101, Jun. 2020, doi: 10.1021/acssuschemeng.0c01348.

[87] L. Qin, Y. Ge, B. Deng, and Z. Li, "Poly (ethylene imine) anchored lignin composite for heavy metals capturing in water," *J. Taiwan Inst. Chem. Eng.*, vol. 71, pp. 84–90, 2017, doi: https://doi.org/10.1016/j.jtice.2016.11.012.

[88] J. Domínguez-Robles, M. S. Peresin, T. Tamminen, A. Rodríguez, E. Larrañeta, and A.-S. Jääskeläinen, "Lignin-based hydrogels with 'super-swelling' capacities for dye removal," *Int. J. Biol. Macromol.*, vol. 115, pp. 1249–1259, 2018, doi: https://doi.org/10.1016/j.ijbiomac.2018.04.044.

[89] Ł. Klapiszewski, K. Siwińska-Stefańska, and D. Kołodyńska, "Preparation and characterization of novel TiO2/lignin and TiO2-SiO2/lignin hybrids and their use as functional biosorbents for Pb(II)," *Chem. Eng. J.*, vol. 314, pp. 169–181, 2017,

doi: https://doi.org/10.1016/j.cej.2016.12.114.

[90] Y. Li, F. Li, Y. Yang, B. Ge, and F. Meng, "Research and application progress of lignin-based composite membrane," vol. 41, no. 4, pp. 245–258, 2021, doi: doi:10.1515/polyeng-2020-0268.

[91] M. Yong, Y. Zhang, S. Sun, and W. Liu, "Properties of polyvinyl chloride (PVC) ultrafiltration membrane improved by lignin: Hydrophilicity and antifouling," *J. Memb. Sci.*, vol. 575, pp. 50–59, 2019, doi: https://doi.org/10.1016/j.memsci.2019.01.005.

[92] L. Manjarrez Nevárez *et al.*, "Biopolymers-based nanocomposites: Membranes from propionated lignin and cellulose for water purification," *Carbohydr. Polym.*, vol. 86, no. 2, pp. 732–741, 2011, doi: https://doi.org/10.1016/j.carbpol.2011.05.014.

[93] Y. Duan, A. Freyburger, W. Kunz, and C. Zollfrank, "Lignin/Chitin Films and Their Adsorption Characteristics for Heavy Metal Ions," *ACS Sustain. Chem. Eng.*, vol. 6, no. 5, pp. 6965–6973, May 2018, doi: 10.1021/acssuschemeng.8b00805.

[94] A. Zhitkovich, "Chromium in Drinking Water: Sources, Metabolism, and Cancer Risks," *Chem. Res. Toxicol.*, vol. 24, no. 10, pp. 1617–1629, Oct. 2011, doi: 10.1021/tx200251t.

[95] K. E. Ukhurebor *et al.*, "Effect of hexavalent chromium on the environment and removal techniques: A review," *J. Environ. Manage.*, vol. 280, p. 111809, 2021, doi: https://doi.org/10.1016/j.jenvman.2020.111809.

[96] H. Liu *et al.*, "Plant-mediated biosynthesis of iron nanoparticles-calcium alginate hydrogel membrane and its eminent performance in removal of Cr(VI)," *Chem. Eng. J.*, vol. 378, p. 122120, 2019, doi: https://doi.org/10.1016/j.cej.2019.122120.

[97] H. Ozaki, K. Sharma, and W. Saktaywin, "Performance of an ultra-low-pressure reverse osmosis membrane (ULPROM) for separating heavy metal: effects of interference parameters," *Desalination*, vol. 144, no. 1, pp. 287–294, 2002, doi: https://doi.org/10.1016/S0011-9164(02)00329-6.

[98] S. Habibi, A. Nematollahzadeh, and S. A. Mousavi, "Nano-scale modification of polysulfone membrane matrix and the surface for the separation of chromium ions from water," *Chem. Eng. J.*, vol. 267, pp. 306–316, 2015, doi: https://doi.org/10.1016/j.cej.2015.01.047.

[99] L. Jacob, T. Moses, S. Joseph, L. Varghese, and S. Nalinakshan, "Study on the Effective Removal of Chromium VI via Polysulfone/TiO2 Nanocomposite Membranes and Its Antifouling Property," 2019, pp. 157–166.

[100] V. Nayak, K. Soontarapa, R. G. Balakrishna, M. Padaki, V. Y. Zadorozhnyy, and S. D. Kaloshkin, "Influence of TiO2 charge and BSA-metal ion complexation on retention of Cr (VI) in ultrafiltration process," *J. Alloys Compd.*, vol. 832, p.

153986, 2020, doi: https://doi.org/10.1016/j.jallcom.2020.153986.

[101] P. Shah and C. N. Murthy, "Studies on the porosity control of MWCNT/polysulfone composite membrane and its effect on metal removal," *J. Memb. Sci.*, vol. 437, pp. 90–98, 2013, doi: https://doi.org/10.1016/j.memsci.2013.02.042.

[102] P. Mahajan-Tatpate, S. Dhume, and Y. Chendake, "Recovery of chromium using membrane containing charged material," *IOP Conf. Ser. Mater. Sci. Eng.*, vol. 1146, no. 1, p. 12022, 2021, doi: 10.1088/1757-899X/1146/1/012022.

[103] L. Jacob, S. Joseph, and L. A. Varghese, "Polysulfone/MMT Mixed Matrix Membranes for Hexavalent Chromium Removal from Wastewater," *Arab. J. Sci. Eng.*, vol. 45, no. 9, pp. 7611–7620, 2020, doi: 10.1007/s13369-020-04711-3.

[104] H. Xu, J. Wei, and X. Wang, "Nanofiltration hollow fiber membranes with high charge density prepared by simultaneous electron beam radiation-induced graft polymerization for removal of Cr(VI)," *Desalination*, vol. 346, pp. 122–130, 2014, doi: https://doi.org/10.1016/j.desal.2014.05.017.

[105] L. Hu *et al.*, "Fabrication of hyperbranched polyamine functionalized graphene for high-efficiency removal of Pb(II) and methylene blue," *Chem. Eng. J.*, vol. 287, pp. 545–556, 2016, doi: https://doi.org/10.1016/j.cej.2015.11.059.

[106] S. Ghorai, A. K. Sarkar, and S. Pal, "Rapid adsorptive removal of toxic Pb2+ ion from aqueous solution using recyclable, biodegradable nanocomposite derived from templated partially hydrolyzed xanthan gum and nanosilica," *Bioresour. Technol.*, vol. 170, pp. 578–582, 2014, doi: https://doi.org/10.1016/j.biortech.2014.08.010.

[107] S. J. Ebrahimi, A. Eslami, and L. Ebrahimzadeh, "Evaluation of heavy metals concentration in the drinking water distribution network in Kurdistan villages in the year 2012," *Res. J. Pharm. Biol. Chem. Sci.*, vol. 6, pp. 55–61, Jan. 2015.

[108] A. T., S. K. P., and S. K. K., "Synthesis of nano-sized chitosan blended polyvinyl alcohol for the removal of Eosin Yellow dye from aqueous solution," *J. Water Process Eng.*, vol. 13, pp. 127–136, 2016, doi: https://doi.org/10.1016/j.jwpe.2016.08.003.

[109] M. Kamali, A. Ebrahimi, and V. Vatanpour, "New dithiocarbamate-based polymer (DTCP) as an additive to improve microporous polysulfone membrane efficiency in lead and dye removal," *J. Environ. Manage.*, vol. 339, p. 117925, 2023, doi: https://doi.org/10.1016/j.jenvman.2023.117925.

[110] P. P. Das, S. Dhara, and M. K. Purkait, "Hybrid Electrocoagulation and Ozonation Techniques for Industrial Wastewater Treatment BT - Sustainable Industrial Wastewater Treatment and Pollution Control," M. P. Shah, Ed. Singapore: Springer Nature Singapore, 2023, pp. 107–128.

[111] Deepti, Anweshan, S. Dhara, and M. K. Purkait, "Membrane and Disinfection Technologies for Industrial Wastewater Treatment BT - Industrial Wastewater Reuse: Applications, Prospects and Challenges," M. P. Shah, Ed. Singapore: Springer Nature Singapore, 2023, pp. 89–112.

[112] S. S. Hosseini, E. Bringas, N. R. Tan, I. Ortiz, M. Ghahramani, and M. A. Alaei Shahmirzadi, "Recent progress in development of high performance polymeric membranes and materials for metal plating wastewater treatment: A review," *J. Water Process Eng.*, vol. 9, pp. 78–110, 2016, doi: https://doi.org/10.1016/j.jwpe.2015.11.005.

[113] S. Dhara, P. P. Das, R. Uppaluri, and M. K. Purkait, "Chapter 3 - Phosphorus recovery from municipal wastewater treatment plants," M. P. B. T.-D. in W. T. R. and P. Shah, Ed. Elsevier, 2023, pp. 49–72.

[114] R. Singh, "Chapter 1 - Introduction to Membrane Technology," R. B. T.-M. T. and E. for W. P. (Second E. Singh, Ed. Oxford: Butterworth-Heinemann, 2015, pp. 1–80.

[115] S. Dhara, P. P. Das, R. Uppaluri, and M. K. Purkait, "12 - Biological approach for energy self-sufficiency of municipal wastewater treatment plants," M. Sillanpää, A. Khadir, and K. B. T.-R. R. in M. W. W. Gurung, Eds. Elsevier, 2023, pp. 235–260.

[116] Z. Zhang, Y. Chen, D. Wang, D. Yu, and C. Wu, "Lignin-based adsorbents for heavy metals," *Ind. Crops Prod.*, vol. 193, p. 116119, 2023, doi: https://doi.org/10.1016/j.indcrop.2022.116119.

[117] X. Zhang, A. Lu, D. Li, L. Shi, Z. Luo, and C. Peng, "Simultaneous removal of methylene blue and Pb2+ from aqueous solution by adsorption on facile modified lignosulfonate," *Environ. Technol.*, vol. 41, no. 13, pp. 1677–1690, Jun. 2020, doi: 10.1080/09593330.2018.1544666.

[118] R. Chen, J. Cai, Q. Li, X. Wei, H. Min, and Q. Yong, "Coadsorption behaviors and mechanisms of Pb(ii) and methylene blue onto a biodegradable multi-functional adsorbent with temperature-tunable selectivity," *RSC Adv.*, vol. 10, no. 59, pp. 35636–35645, 2020, doi: 10.1039/D0RA07139K.

[119] L. An, C. Si, J. H. Bae, H. Jeong, and Y. S. Kim, "One-step silanization and amination of lignin and its adsorption of Congo red and Cu(II) ions in aqueous solution," *Int. J. Biol. Macromol.*, vol. 159, pp. 222–230, 2020, doi: https://doi.org/10.1016/j.ijbiomac.2020.05.072.

[120] S. Dhara, N. S. Samanta, R. Uppaluri, and M. K. Purkait, "High-purity alkaline lignin extraction from Saccharum ravannae and optimization of lignin recovery through response surface methodology," *Int. J. Biol. Macromol.*, vol. 234, p. 123594, 2023, doi: https://doi.org/10.1016/j.ijbiomac.2023.123594.

[121] P. Santander, B. Butter, E. Oyarce, M. Yáñez, L.-P. Xiao, and J. Sánchez, "Lignin-based adsorbent materials for metal ion removal from wastewater: A review," *Ind. Crops Prod.*, vol. 167, p. 113510, 2021, doi: https://doi.org/10.1016/j.indcrop.2021.113510.

[122] C. Jiang *et al.*, "Construction of magnetic lignin-based adsorbent and its adsorption properties for dyes," *J. Hazard. Mater.*, vol. 369, pp. 50–61, 2019, doi: https://doi.org/10.1016/j.jhazmat.2019.02.021.

[123] H. Namdar, A. Akbari, R. Yegani, and H. Roghani-Mamaqani, "Influence of aspartic acid functionalized graphene oxide presence in polyvinylchloride mixed matrix membranes on chromium removal from aqueous feed containing humic acid," *J. Environ. Chem. Eng.*, vol. 9, no. 1, p. 104685, 2021, doi: https://doi.org/10.1016/j.jece.2020.104685.

[124] T. Zhang, P. Li, S. Ding, and X. Wang, "High-performance TFNC membrane with adsorption assisted for removal of Pb(II) and other contaminants," *J. Hazard. Mater.*, vol. 424, p. 127742, 2022, doi: https://doi.org/10.1016/j.jhazmat.2021.127742.

[125] H. Alfalahy and S. Al-Jubouri, "Preparation and application of polyethersulfone ultrafiltration membrane incorporating NaX zeolite for lead ions removal from aqueous solutions," *Desalin. Water Treat.*, vol. 248, Mar. 2022, doi: 10.5004/dwt.2022.28072.

[126] K. Parveen, S. Zafar, M. Khan, R. Anwer, and A. Shanableh, "Removal of eosin yellow from wastewaters by the commercial anion exchange membrane BI," *Desalin. Water Treat.*, vol. 287, pp. 245–253, Apr. 2023, doi: 10.5004/dwt.2023.29368.

[127] A. T. Kuvarega, N. Khumalo, D. Dlamini, and B. B. Mamba, "Polysulfone/N,Pd co-doped TiO2 composite membranes for photocatalytic dye degradation," *Sep. Purif. Technol.*, vol. 191, pp. 122–133, 2018, doi: https://doi.org/10.1016/j.seppur.2017.07.064.

[128] Z. Talha, W. Ding, E. Mehryar, M. Hassan, and J. Bi, "Alkaline Pretreatment of Sugarcane Bagasse and Filter Mud Codigested to Improve Biomethane Production," *Biomed Res. Int.*, vol. 2016, p. 8650597, 2016, doi: 10.1155/2016/8650597.

[129] K. Li, J. Wan, X. Wang, J. Wang, and J. Zhang, "Comparison of dilute acid and alkali pretreatments in production of fermentable sugars from bamboo: Effect of Tween 80," *Ind. Crops Prod.*, vol. 83, pp. 414–422, 2016, doi: https://doi.org/10.1016/j.indcrop.2016.01.003.

[130] E. Melro *et al.*, "Dissolution of kraft lignin in alkaline solutions," *Int. J. Biol. Macromol.*, vol. 148, pp. 688–695, 2020, doi: https://doi.org/10.1016/j.ijbiomac.2020.01.153.

[131] V. Fierro, V. Torné-Fernández, and A. Celzard, "Methodical study of the chemical activation of Kraft lignin with KOH and NaOH," *Microporous Mesoporous Mater.*, vol. 101, no. 3, pp. 419–431, 2007, doi: https://doi.org/10.1016/j.micromeso.2006.12.004.

[132] A. B. Albadarin, A. H. Al-Muhtaseb, N. A. Al-laqtah, G. M. Walker, S. J. Allen, and M. N. M. Ahmad, "Biosorption of toxic chromium from aqueous phase by lignin: mechanism, effect of other metal ions and salts," *Chem. Eng. J.*, vol. 169, no. 1, pp. 20–30, 2011, doi: https://doi.org/10.1016/j.cej.2011.02.044.

[133] A. H. S. B. Lalvani T. S. Wiltowski, "Chromium Adsorption by Lignin," *Energy Sources*, vol. 22, no. 1, pp. 45–56, Jan. 2000, doi: 10.1080/00908310050014207.

[134] Z. Tan, L. Hu, D. Yang, D. Zheng, and X. Qiu, "Lignin: Excellent hydrogel swelling promoter used in cellulose aerogel for efficient oil/water separation," *J. Colloid Interface Sci.*, vol. 629, pp. 422–433, 2023, doi: https://doi.org/10.1016/j.jcis.2022.08.185.

[135] J. Perendija *et al.*, "Bio-membrane based on modified cellulose, lignin, and tannic acid for cation and oxyanion removal: Experimental and theoretical study," *Process Saf. Environ. Prot.*, vol. 147, pp. 609–625, 2021, doi: https://doi.org/10.1016/j.psep.2020.12.027.

[136] H. W. Kwak, H. Woo, E. H. Kim, and K. H. Lee, "Water-resistant Lignin/Poly(vinyl alcohol) Blend Fibers for Removal of Hexavalent Chromium," *Fibers Polym.*, vol. 19, no. 6, pp. 1175–1183, 2018, doi: 10.1007/s12221-018-8052-z.

Chapter 2

Studies on the chemical pretreatment and surfactant-mediated enzymatic hydrolysis of *Saccharum ravennae* grass biomass for enhanced sugar and bioethanol yield

This chapter gives a complete description of the experimentation involved and the results of the surfactant-mediated enzymatic hydrolysis and ethanol yield from Saccharum ravennae grass biomass using thermochemical pretreatment methods. The pretreatments were performed with H_2SO_4, NaOH, and subsequent H_2SO_4-NaOH hydrothermal methods. Enzymatic hydrolysis of all the pretreated samples, along with raw biomass, was conducted using cellulase from Trichoderma reesei with and without ionic (SDS, CTAB) and non-ionic (Tween 20) surfactants. The background of this work, details of the literature, and the scope of work are elaborated in Chapter 1, Section 1.1.1, 1.3.1, and Section 1.4.1, respectively. This work has been scientifically acknowledged in the ACS Agricultural Science & Technology.

2.1 Materials and Methods

2.1.1 Materials

Ravenna grass was collected from the IIT Guwahati campus in India (N 26° 11' 13.9992", E 91° 41' 30.0012"). Grass biomass was washed, dried, ground, and then sieved to 150 microns. Sulfuric acid (98%), Nitric acid (70%) and SDS (≥90%), Ammonium sulfate (99.5%), Potassium dihydrogen phosphate (98%), and Peptone were procured from Merck Life Science. Sodium hydroxide pellet (97%) was collected from Finar Chemicals India. Citric acid (99.8%) was purchased from Otto Chemie, India. Tween 20 (1.10 g/mL) and CTAB (99%) were purchased from SRL India. Cellulase from *Trichoderma reesei* (≥ 700 units/g) was procured from Sigma Aldrich. Premium grade Ethanol (100%) was purchased from Hayman Speciality Products, UK. To prepare standard sugar calibration curve D-(+)-Glucose (99.50%), D-(+)-Xylose (99%),

D-(+)-Galactose (99%), D-(+)-Mannose (98%), D-(+)-Cellobiose (98%), and L (+) Arabinose (99%) were purchased from HIMedia Laboratories, India. The commercial *S. cerevisiae* was bought from the local market in Guwahati, India. Magnesium Sulphate Heptahydrate (99%) was collected from CDH Fine Chemical, India.

2.1.2 Pretreatment of Ravenna Grass

The RGB was treated independently with acid and alkali and sequentially with both. The RGB was pretreated with diluted acid with 2.0 % (w/v) H_2SO_4 in a 500 mL conical flask and autoclaved for 60 minutes at 121°C with 10% (w/v) solid loading. Similarly, RGB was treated with 2.0 % (w/v) NaOH for alkaline treatment under the same operational conditions mentioned above. To perform the sequential two-stage pretreatment, initially, The RGB was pretreated with 2.0 % (w/v) H_2SO_4 at 121°C for 60 min and a fixed choice of the solid-to-liquid ratio of 1:10. The acid-pretreated biomass was water-washed to the point the pH was neutral. A hot air oven was used to dry the recovered solid until it reached a consistent weight. Further, in the second stage, the dried biomass was pretreated with 2.0 % (w/v) NaOH using the same experimental conditions. After the pretreatments were over, all the solids were separated from the black liquor generated during pretreatments using vacuum filtrations, followed by a thorough water wash with deionized water. The black liquor separated specifically from 2% NaOH pretreated solvent was further treated with 6M HNO_3 solution to precipitate acid-insoluble lignin (AIL). The collected AIL was centrifuged (Model No. :2-16P, Maker: Sigma, Germany), washed, oven-dried, and stored for further pH and ζ potential analysis.

2.1.3 Characterization of raw and pretreated biomass samples

By employing analytical techniques designed by the National Renewable Energy Laboratory (NREL), raw and processed RGB were characterized for their structural carbohydrates and lignin component, total solids, ash, and extractives [1], [2].

Scanning electron microscopic images were taken at magnification 1000X for raw and pretreated biomass using Gemini 300 field emission scanning electron microscope (ZEISS, Germany) to study the morphological changes in biomass.

ATR-FTIR spectra were studied using Spectrum two-PerkinElmer instrument (Singapore). It offers insights into the molecular framework and bonding between molecules in the biomass samples before and after pretreatment. The spectra were acquired in the 4000-400 cm^{-1} region with a resolution of 4 cm^{-1} using a standard of 25 scans. The Smartlab 9KW Powder XRD System from Rigaku Technologies (Japan) was used to analyze X-ray diffraction patterns. At an average pace of 10°/min, all biomass substrates were scanned at 2θ angles ranging between 5 to 50° at the ambient temperature. The substrate crystallinity was determined using a method developed by Segal et al. (1959)[3]. The crystallinity% was determined with the following expression:

$$\%\ Crystallanity = \frac{(I_{002} - I_{AM})}{I_{002}} \times 100 \quad (1)$$

where I_{002} was the 002-peak intensity, and I_{AM} was the minimum peak intensity between 002 and 101 peaks.

Thermal degradation curves were obtained from a TG209 F1 NETZSCH TGA instrument using alumina crucibles. On average, each run utilized 15 mg of biomass samples. These tests were conducted with a continuous nitrogen flow rate of 40 mL/min and a temperature ramp adjusted to 10°C/min. The weight loss of samples was tracked from 25 to 800°C. The tests were carried out twice for confirmation.

The raw and pretreated RGB samples were evaluated using X-ray photoelectron spectroscopy. The samples were examined using a PHI 5000 VersaProbe III Photoelectron Spectrometer (ULVAC-PHI, Inc., Japan). At intervals of 1.0 eV, survey spectra (1200 to 2 eV) were collected using 200 eV pass energy. With 55 eV pass energy at 0.05 eV intervals in the 281-292 eV and 525-540 eV regions, the high-resolution spectra of C_{1S} and O_{1S} have been acquired.

2.1.4 DLS and ζ potential study of surfactants and cellulase enzyme

The Litesizer 500 Particle Analyzer (Anton Paar) equipment was utilized to figure out the particle size distribution and zeta potential of the aqueous enzyme (15 µL/mL) solution and surfactants (10% w/v) in the aqueous media. Additionally, studies were made on how cellulase affected the hydrodynamic diameter and zeta potential of surfactants. A glass cuvette was used for DLS measurement, and zeta potential was measured using an Anton Paar omega cuvette. All the samples were analyzed at 25℃.

2.1.5 Enzymatic Hydrolysis of raw and pretreated RGB

Sodium citrate buffer (0.1 M) was used for enzymatic hydrolysis for all the biomass samples. The biomass (5% w/v) was initially loaded in a buffer solution at pH 4.8. Hydrolysis reactions were executed in a shaker incubator (Orbitek, Scigenics Biotech, India) at 50 ℃ temperature for 72 h at 110 rpm. 1.5% (v/v) Cellulase enzyme from *Trichoderma reesei* (700 Endoglucanase units/gm, 20 FPU/mL) was used to hydrolyze the polysaccharides present in the biomass. The enzymatic hydrolysis studies were conducted through a fixed choice of enzyme loading with different pretreated RGB with various cellulose content. Accordingly, the effectiveness of various pretreatment techniques under similar conditions has been compared in a fair and relevant manner. For surfactant-mediated enzymatic saccharification, biomass samples were loaded with surfactants (0.2 g/g of biomass) individually in sodium citrate buffer and incubated at 50℃ temperature for one hour at 110 rpm. After one hour of incubation, 1.5% (v/v) enzyme was added to the surfactant-containing hydrolysis solutions. All the hydrolysis tests were conducted in duplicates. 2 mL of the liquid hydrolysate fraction was taken after 6, 12, 24, 48, and 72 hours of the enzymatic hydrolysis process being started. Collected samples were centrifuged (Model No. :2-16P, Make: Sigma, Germany) at 10000 rpm for 5 minutes. The supernatants from the centrifuged samples were pipetted out, and a 2-factor dilution was performed with Mili-Q water. Diluted hydrolysates were stored at 4 ℃ for further analysis.

2.1.6 Determination of sugar yield

The sugars in the enzymatic hydrolysates were measured employing a high-performance liquid chromatography (HPLC) (Prominence, Shimadzu, Singapore) instrument

connected to a refractive index detector (RID) and Aminex (BIO-RAD) HPX-87P HPLC column. The mobile phase was a 0.01 M H_2SO_4 solution, and the flow rate was adjusted at 0.6 mL/min. The temperature in the column was kept constant at 60℃. Prior to hydrolysate analysis, HPLC-grade sugar standards were used for calibration. The enzymatic digestibility of cellulose and hemicellulose was measured using the following equations.

$$Enzymatic\ digestibility\ of\ Cellulose\ (\%) = \frac{Glu_h}{Cel_s \times 1.11} \times 100\% \quad (2)$$

$$Enzymatic\ digestibility\ of\ Hemicellulose\ (\%) = \frac{Xyl_h}{Hcel_s \times 1.136} \times 100\% \quad (3)$$

Glu_h and Xyl_h are the glucose and xylose content in the enzymatic hydrolysate quantified by HPLC. Cel_s and $Hcel_s$ are the cellulose and hemicellulose content in the initial substrate of enzymatic hydrolysis. 1.11 and 1.136 are the cellulose-to-glucose and hemicellulose-to-xylose conversion factors, respectively.

2.1.7 Fermentation of RGB hydrolysates

A separate hydrolysis and fermentation (SHF) approach was implemented for the fermentation process. The hydrolysates of the optimized pretreatment and enzymatic hydrolysis procedure were used for fermentation. The hydrolysates were filtered through 0.25µm filters prior to fermentation. The pH of the optimized hydrolysate was assessed and neutralized to 7, followed by the addition of 5 g/L yeast extract, 1 g/L $(NH_4)_2SO_4$, 2 g/L KH_2PO_4, and 1 g/L $MgSO_4 \cdot 7H_2O$ to prepare fermentation medium. The prepared fermentation medium was inoculated with 5% (v/v) *S. cerevisiae* pre-inoculated solution. The samples were incubated in a shaker incubator for 72 hours at 35 ° C and 110 rpm. After 72 hours of incubation, samples were centrifuged (Model No. :2-16P, Maker: Sigma, Germany) for 5 minutes at 10,000 rpm to separate the supernatants, which were then used for estimating ethanol yield using the HPLC-RID instrument.

The ethanol conversion efficiency was calculated using the following equation:

$$Ethanol\ conversion\ efficiency = \frac{Et_{OH(HPLC)}}{0.51 \times Glu_f} \times 100\ \% \quad (4)$$

Where $ET_{OH(HPLC)}$ was the ethanol concentration detected by HPLC, 0.51 was the conversion factor from glucose to ethanol, and Glu_f was the glucose concentration in the fermentation medium.

2.2 Results and Discussion

2.2.1 Analysis of biomass substrates

2.2.1.1 Compositional analysis

The composition of the raw RGB was initially analyzed (**Table 2.1**) to examine the composition differences between raw and pretreated RGB. Carbohydrates comprised 57.53% wt/wt of the dry biomass and contained cellulose (36.68%) and hemicellulose (20.85%). The lignin and ash contents were 28.9 % and 6.85 %, respectively. The lignin fraction was divided into acid-soluble (ASL-4.54 %) and acid-insoluble (AIL-24.36 %) lignin. The raw biomass contains some moisture (5.45%) and extractives (4.84 %). The evaluated carbohydrates and lignin content in raw RGB biomass were in agreement with the data published by Panneerselvam et al. (2013) [4].

2% sulfuric acid pretreatment (AC) of RGB exhibits better solid recovery (52.3%) but low delignification (38.76%). However, the removal percentage of ASL was higher compared to alkaline pretreatment. Furthermore, during AC treatment, the breakdown and reorganization of lignin structures under acidic conditions result in the formation of Pseudo lignin, a complex and typically non-native lignin-like compound. This phenomenon is responsible for the observed enhancement in the weight percentage of AIL wt.%. Dilute acid pretreatment is an old method well-known for separating hemicellulose from the primary substrate [5]. Studies have demonstrated the covalent bonding between lignin and hemicelluloses leads to carbohydrate-lignin complexes [6]. On the other hand, cellulose and hemicellulose are linked through hydrogen bonds because of the existence of suitable hydrogen bonding sites in these polysaccharides [7]. AC treatment effectively dissociates hydrogen bonds and covalent bonds and removes around 69.25 % of the total hemicellulose content.

In a study conducted by Panneerselvam et al. (2013), the ozonolysis technique was applied to treat S. ravennae biomass. The study investigated a range of ozone concentrations, varying from 40 to 58 mg/L, and explored two distinct flow configurations: uniflow and reverse flow. Notably, with the reverse flow configuration and an ozone concentration of 50 mg/L, the study achieved the recovery of a maximum of 43.3 ± 1.19% cellulose and 20.1 ± 0.27% hemicellulose from the treated biomass[8]. In another study, when S. ravennae biomass was subjected to treatment with 1% NaOH at 121°C for a duration of 1 hour, the maximum achieved delignification was reported to be 53.6%[4]. In contrast, in this article, a 2% NaOH pretreatment has been reported, which resulted in a significantly higher maximum delignification of 87.71%. Additionally, good cellulose and hemicellulose recovery rates of 54.2 ± 0.86% and 25.93 ± 0.64%, respectively, were achieved. These findings demonstrate the enhanced effectiveness of the 2% NaOH pretreatment method. The 2% NaOH-mediated alkaline pretreatment (AL) drastically changed the composition of the RGB. The cellulose loss in this pretreatment was higher than in AC pretreatment (Cellulose loss in AC- 29.32%, and AL- 35.48 %). The loss rates were unaffected by the pretreatment conditions. In contrast, the degradation and removal of hemicellulose were much less compared to AC treatment. However, alkali pretreatment was mainly employed to separate lignin from the lignocellulose matrix for better substrate availability to enzymatic hydrolysis. According to a report published by Jin et al. (2006), cellulose molecules are covalently (molecularly) attached to more than 50% of the lignin units in softwoods [6]. NaOH solution damages the linkages of lignin with polysaccharides in crystalline as well as in the amorphous region, causing the separation of hemicellulose in tiny amounts. While Na^+ ions interact with lignin to generate sodium phenolate, $O\text{-}H^-$ ions from NaOH denatured the bonds that formed lignin's fundamental framework. This salt of phenol can be dissolved. The solution had a black color, indicating the presence of dissolved lignin. [9]. A maximum of 87.71 % delignification was achieved through AL pretreatment. However, an unusual phenomenon was observed in this work. The filtration and washing of NaOH-treated biomass were difficult and time-consuming due

to small insoluble fragments and undegraded hemicellulose fragments in the NaOH-treated solution.

Utilizing 2% H_2SO_4 in the initial step and 2% NaOH in the following stage, the two-stage pretreatment (AC-AL) of the RGB completed its course. The observed overall cellulose recovery was 57 %, and a maximum delignification of 92.07 % was achieved. Considering the outcomes, AC-AL pretreated biomass composition improved and was suitable for high-yielding enzymatic hydrolysis.

Table 2.1: Compositional analysis of raw and pretreated RGB

Sample	Cellulose	Hemi-cellulose	Lignin		De-lignification	Moisture	Ash	Extractives	Solid recovery
			ASL	AIL					
RB	36.68 ±0.55	20.85 ±0.78	4.54 ± 0.22	24.36 ±0.61	-	5.45 ± 0.29	6.85 ±0.27	4.84 ±0.21	-
AC	49.57 ±1.01	6.41 ±0.38	1.53 ±0.04	32.4 ±0.57	38.76%	3.21 ±0.09	3.72 ±0.14	2.12 ±0.32	52.3%
AL	54.2 ±0.86	25.93 ±0.64	2.62 ±0.05	5.56 ±0.1	87.71%	3.45 ±0.11	3.48 ±0.21	1.54 ±0.17	43.66%
AC-AL	84.58 ±0.41	0	1.17 ±0.03	8.1 ±0.17	92.07 %	4.45 ±0.24	0.49 ±0.08	0.98 ±0.13	24.74%

2.2.1.2 SEM analysis

Scanning electron microscopy (SEM) analysis provided valuable insights into the profound morphological changes in the RGB that underwent different pretreatment procedures. The SEM images of raw and pretreated biomass are shown in **Fig. 2.1**. The raw biomass (RB) morphology exhibits a complete lignocellulosic framework with a comparably smoother surface without cavities and a robust, dense fiber composed of parallel contrasting stripes merely coated with extractives. The comparatively high hemicellulose and lignin percentages of Ravenna grass could develop a tight fiber structure, reducing cellulose exposure to enzymes and negatively impacting hydrolysis productivity.

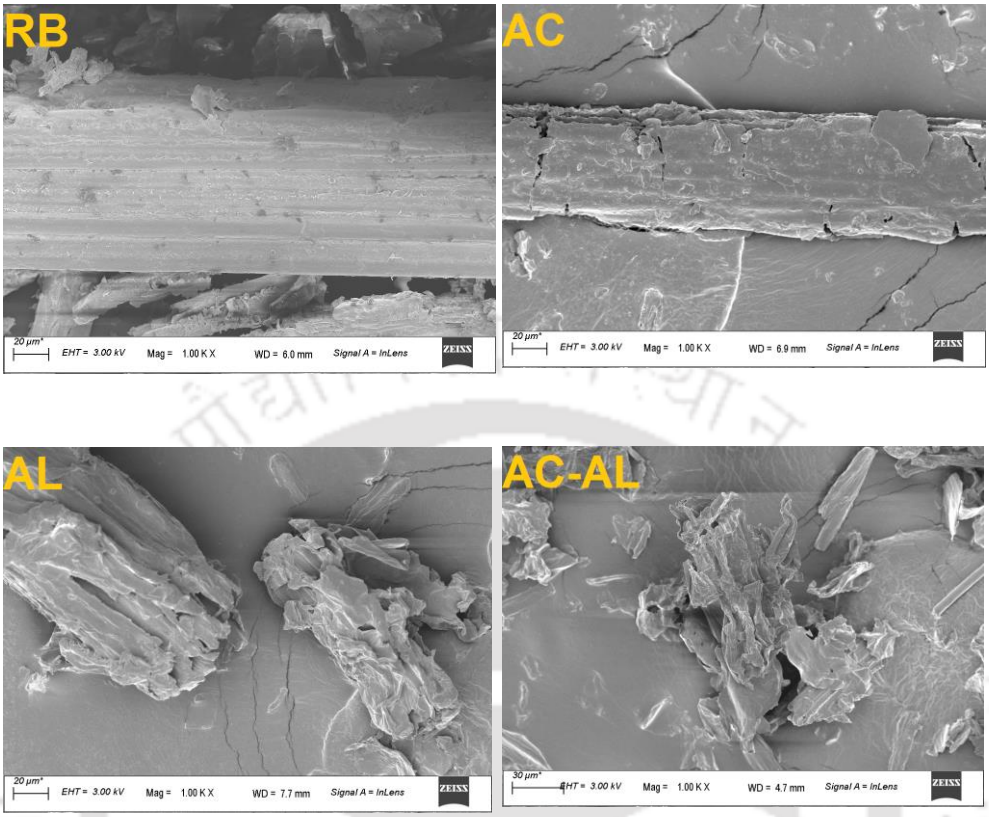

Figure 2.1: Changes in surface morphology of RGB after acid (AC), alkali (AL), and subsequent acid/alkali (AC-AL) pretreatment

The prolonged subjecting of biomass to harsh pretreatment conditions (high temperature and pressure) with dilute acid (AC) (2% H_2SO_4) results in the degradation of hemicellulose, which changes the exterior of the RB tissues and forms a loose framework. This reflects the elimination of its amorphous hemicellulose part, but the undissolved lignin is still present. Pretreatment with dilute alkali (AL) 2% NaOH successfully facilitated the elimination of lignin, demonstrating the structural disintegration of the fiber that caused the sudden rupture. The AL pretreatment primarily eliminated 84.81% of the total lignin content, ultimately making the cellulose more accessible to enzymatic activity. Sequential acid-base pretreatment (AC-AL) leads to a severe degree breakdown in the biomass fibers and the total elimination of hemicellulose, making the cellulose available and fiber-free. The fragmented fibers

were visible in the SEM image of the AC-AL biomass, illustrating how the removal of the lignin (92.07 %) and hemicellulose (100%) severely ruptured the biomass. Ascencio et al. (2020) showed comparable morphological outcomes for consecutive acid-base treatments [10].

2.2.1.3 FTIR Analysis

The presence and characteristics of functional groups in raw and pretreated RGB substrates were analyzed through ATR-FTIR analysis (**Fig. 2.2)**. Two significant absorption regions exist between the 3500–2000 cm^{-1} range, notably the stretching vibration of the hydroxyl O-H at 3343 cm^{-1} and bending vibration of the C-H of the CH_2 and CH_3 groups at a double peak region of 2917 and 2847 cm^{-1} (asymmetric and symmetric stretches), which are prevalent in the carbohydrates, and lignin molecular chains [11]. The hydroxyl peak intensity of the RB was the weakest in the graph, and the impact of chemical hydrothermal pretreatment on the alteration of hydroxyl absorption peak magnitude was apparent. With an increased percentage of cellulose, the hydroxyl peak became more intense. According to research conducted by Ben et al. (2018), cellulose contains maximum hydroxyl groups (18.52 mmol/g) followed by hemicellulose (7.21 mmol/g) and lignin (5.29 mmol/g), which explained the maximum hydroxyl peak intensity in AS-AL spectra [12].

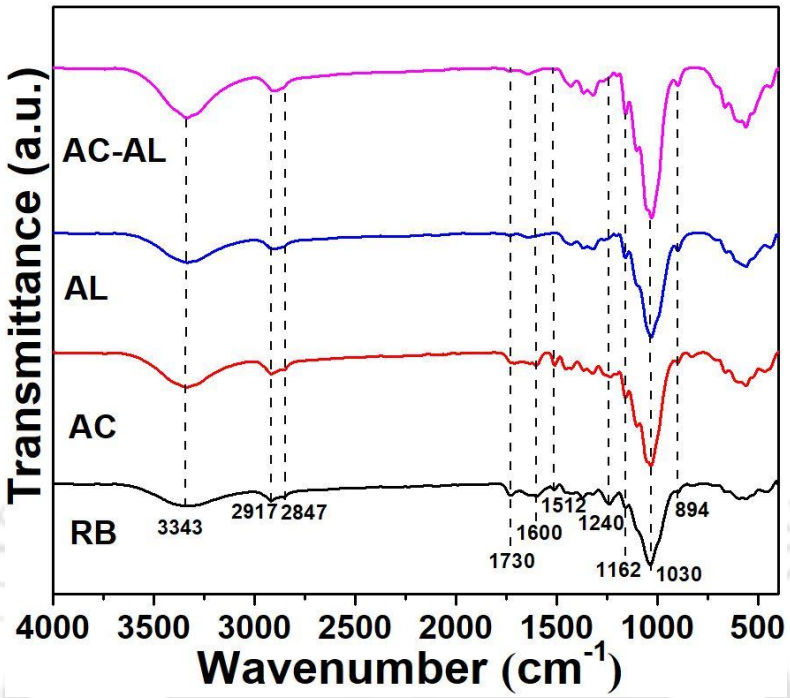

Figure 2.2: ATR-FTIR spectra of raw and pretreated RGB

The acetyl ester stretching vibrations at 1240 cm^{-1} were primarily due to hemicellulose, a distinct element easily distinguishable from other components. These peak values were lessened in AC-treated biomass compared to raw biomass and absent in AL and AC-AL-treated biomass. This is because hemicellulose content in AC-AL treated biomass was zero, and AL treatment degraded hemicellulose-branched chains. The significant characteristic peaks for lignin were located at 1600 cm^{-1} and 1512 cm^{-1}, which indicated C=C groups where the benzene ring structural vibration occurred. Ester bonds involving lignin and hemicellulose were thought to be responsible for the peak occurring at 1730 cm^{-1} [13]. Transmittance in pretreated RGBs at 1730 cm^{-1} demonstrated a successful breakage of ester bonds within lignin and hemicellulose. The reduced intensity of these bonds in AL and AC-AL treated biomass indicated a higher degree of delignification. Peaks of C-O-C, C-O stretching in cellulose and hemicellulose, and C-O-C stretching at the β-glucosidic linkages in cellulose and hemicellulose were recorded at 1162 cm^{-1}, 1030 cm^{-1}, and 894 cm^{-1}, respectively, and the intensities increased in the pretreated biomass samples.

2.2.1.4 XRD Analysis

To understand the crystallization behavior of RGB, raw and pretreated substrates were examined using the X-ray diffraction (XRD) technique, and the results are depicted in **Fig. 2.3**. These substrate spectra displayed expected peaks for the standard cellulose-I structure, which was located at 2θ = 16º and 22.2º and 34.7º. The distinct identities of the cellulose crystals were 101, 002, and 040 crystalline peaks, respectively [14]. The RB substrate was estimated to have a crystallinity of 31%, whereas the AC substrate had a higher crystallinity of 37.7% (since the amorphous hemicellulose fraction was removed). AL-substrate notably exhibited higher crystallinity (49.2%), mainly as a result of extensive disintegration of amorphous subject matter, particularly lignin. A maximum of 51.7% crystallinity was calculated for AC-AL treated biomass, where the remaining amorphous content was removed. These XRD crystallinity degree values exhibit an analogous pattern to the findings of the compositional analysis, where crystallinity increased with the increase in cellulose content in biomass.

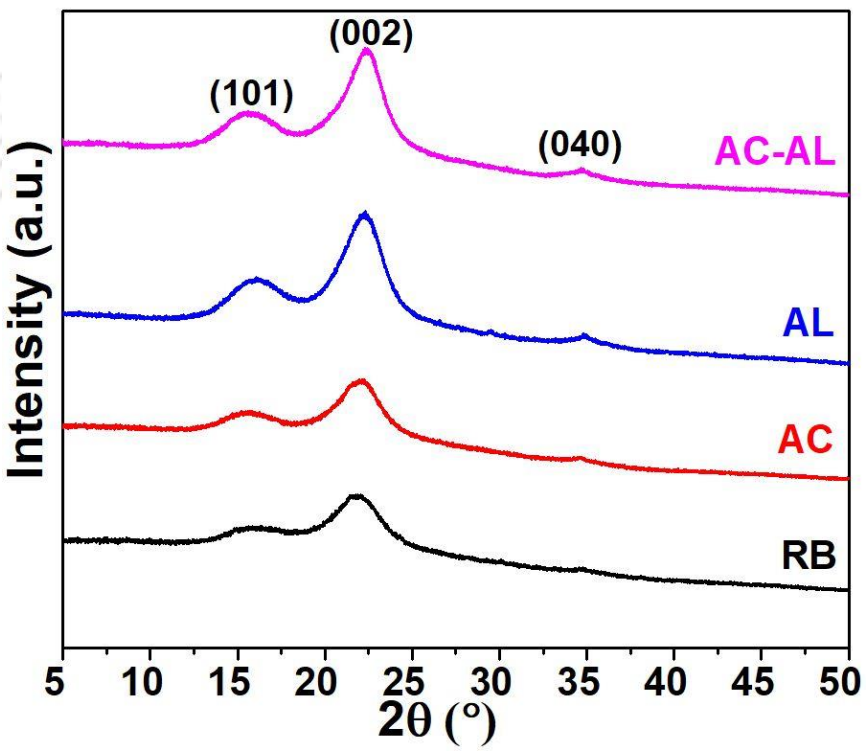

Figure 2.3: X-ray diffraction spectra of raw and pretreated RGB

2.2.1.5 Thermogravimetric Analysis

A comparison study of the thermal behavior and characteristics of RGB substrate before and after chemical hydrothermal pretreatment was conducted. The thermogravimetric (TG) curves of the biomass substrates are presented in **Fig. 2.4**. The thermal degradation of biomass samples could be divided into three main parts: removal of light volatile components and moisture (<95°C), degradation of carbohydrates (hemicellulose followed by cellulose) (200-380°C), and lignin pyrolysis at higher temperature (>400°C).

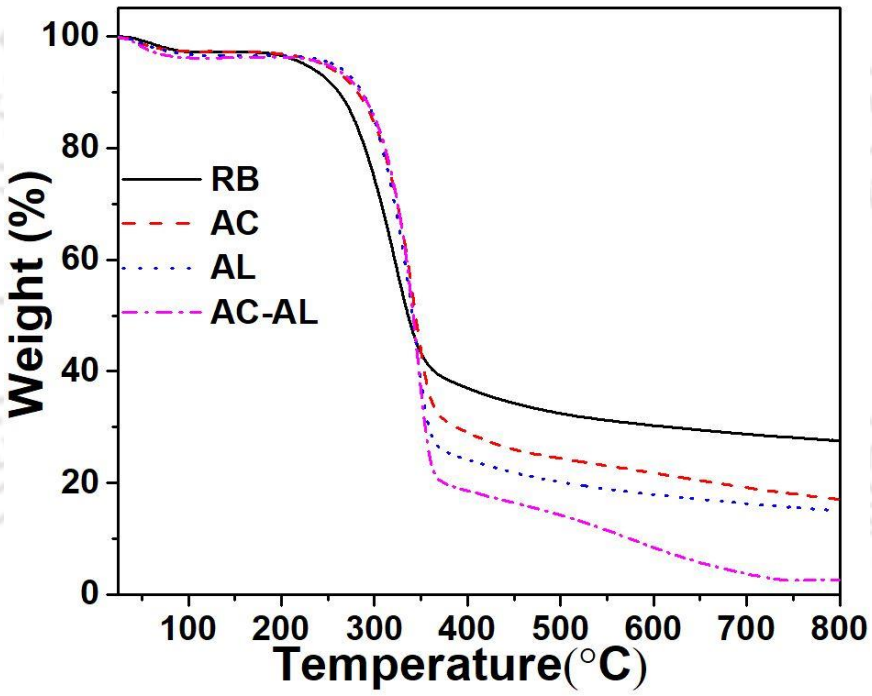

Figure 2.4: Thermogravimetric graph of raw and pretreated RGB

The degradation of carbohydrates in the RB sample started at a lower temperature compared to other pretreated samples as the weak hydrogen and covalent bonds between carbohydrates and lignin started to break at lower temperatures. For the pretreated samples, the curve of thermal degradation of carbohydrates changed significantly, the degradation degree increased, and the temperature range shortened. This might be due to the breakdown of the lignocellulose matrix during pretreatment, which resulted in unbound polysaccharides in the samples. The extended carbohydrate

degradation range in the AC-AL sample indicates the higher cellulose content in the biomass. The residual char contents in RB, AC, AL, and AC-AL samples were 27.5%, 17%, 15%, and 3%, respectively. Biomass with higher lignin content ended up with higher residual char, as high molecular weight fractions of lignin did not get degraded at 800°C.

2.2.1.6 XPS Analysis

An X-ray photoelectron spectroscopy (XPS) analysis was conducted to ascertain the composition of the raw and pretreated RGB elements. The survey and high-resolution C 1s and O 1s spectra of biomass samples are shown in **Fig. 2.5**. While the N 1s peak was not prominent in the XPS spectrum of the raw biomass, the derived atomic composition table from the spectra showed 0.57 % of nitrogen indicates the presence of protein fraction in the raw biomass. The predominant elemental peaks observed in the biomass spectrum were C 1s and O 1s. Deconvolution of the C 1s spectra, as seen in **Fig. 2.5b**, produced three peaks, each with an integrating binding energy of 284.60±0.20 eV for C-C and C-H species, 285.80 eV for C-N species, and 286.50±0.20 eV for C-OH and C-O-C species [15][16]. Due to the breakdown of carbon-carbon and carbon-hydrogen bonds between lignin and carbohydrates during pretreatment, the content of C-C and C-H species decreased from 49.94% to 33.21%, whereas the content of C-OH and C-O-C increased significantly from 28.85 % to 66.78 % as the concentration of cellulose in the biomass increased after pretreatments.

As shown in **Fig. 2.5c**, the O1s spectrum showed three peaks that corresponded to the C=O (531.75±0.48 eV), C-O-C/C-OH (532.73±0.21 eV), and H_2O (335.3 eV) groups in the AC biomass sample[15][17]. In contrast, RB, AL, and AC-AL biomass had two peaks corresponding to C=O and C-O-C/C-OH groups. Carbonyl groups are a significant component of lignin, and the group's presence in the biomass sample indicates a higher lignin concentration. The surface composition of functional groups changed due to the pretreatment process. Particularly, the number of carbonyl groups (C=O) was found to have significantly decreased, while the number of ether linkages (C-O-C/C-OH) had increased considerably. Collectively, these findings point to a

change in the binding arrangement of the surface, with a predominance of single bonds combining carbon (C) and oxygen (O) atoms and a perceived decline in the frequency of double bonds. The pretreatment technique changed the oxidation state of carbon in the biomass as the number of carbonyl groups (C=O) decreased. The delignification mechanism involved in the pretreatment, which significantly lowers the lignin concentration in the biomass, is responsible for the decrease in the intensity of the C=O peak. This is especially noteworthy because lignin generally has more carbonyl groups than other components. Because of the higher cellulose concentration over the pretreatment process and the increased amount of oxygen-containing functional groups in the biomass, the area of the ether linkages increased. According to the outcomes of the aforementioned analysis, carbonyl groups were lost while ether linkages increased during pretreatment. These findings were in line with those of the XRD and compositional studies.

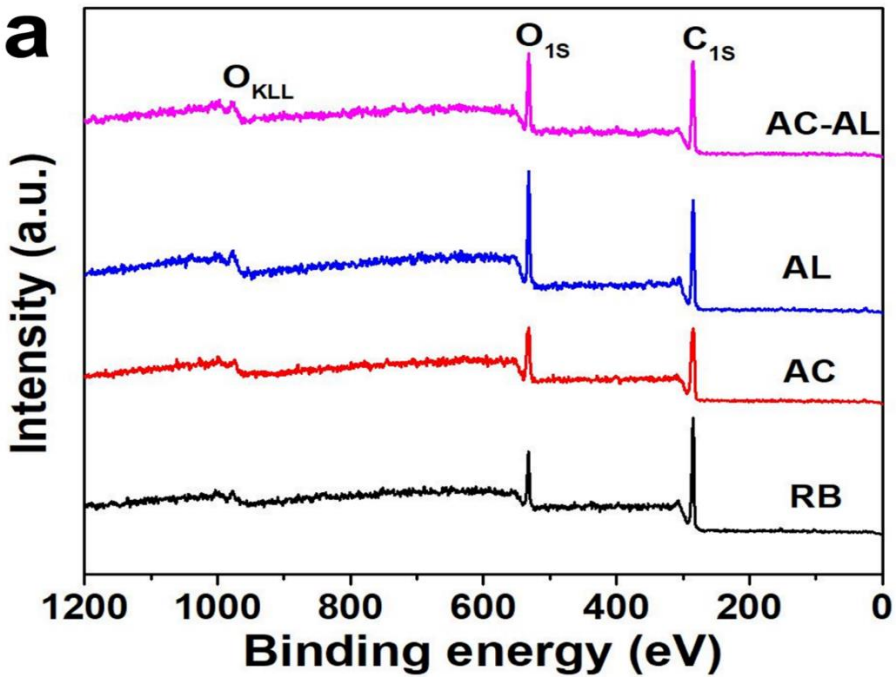

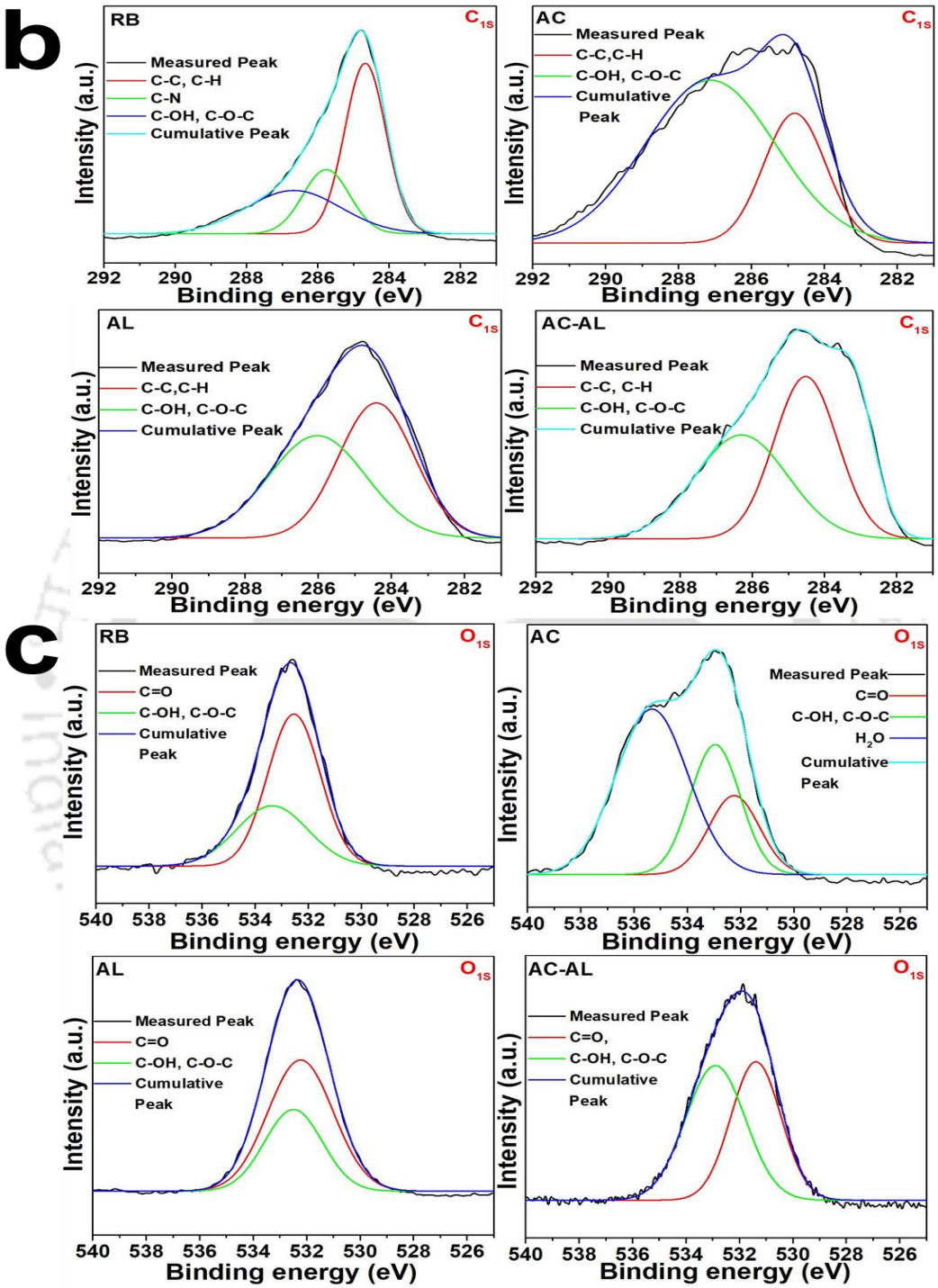

Figure 2.5: XPS **(**a) survey spectra, (b) C_{1s} spectra, and (c) O_{1s} spectra of raw and pretreated RGB

2.2.2 Particle size distribution and zeta potential of surfactants and Cellulase enzyme

Driven by the mitigation of aggregation and enhanced dispersion, the surfactants play a vital role in controlling enzyme particle size. Additionally, factors such as solvent choice, temperature, and concentration influence the particle size of the system. Furthermore, a modification of the pH levels, selection of appropriate buffer solutions, and inclusion of surfactants can all lead to alterations in the zeta potential of aqueous enzyme solutions. Dynamic light scattering analysis has been used to identify changes in cellulase size brought on by surfactants, as depicted in **Table 2.2**. The unfolding and refolding caused by surfactant interaction or the complexation of surfactant with cellulase can cause changes in cellulase size. Cellulase from *Trichoderma reesei* exhibits a hydrodynamic diameter (D_h) of 7.24 nm in a stabilization form. Similar findings were reported by Gong et al. (2021), who observed an average particle size of cellulase to be approximately 10 nm[18]. These consistent results from different studies suggest that the cellulase complex in the analyzed samples exhibits a similar nanoscale size range. For the 10% aqueous SDS solution, two peaks at D_h ~1.95 nm and Dh ~232.4 nm appeared in the particle size distribution curve, where the former peak represented the micelle peak, and the latter corresponded to vesicle formation. Aqueous CTAB solution followed a similar pattern and exhibited a micelle peak (0.85 nm) and a peak of vesicular systems (201.5 nm). In the presence of SDS, the D_h of cellulase increases from 7.24 to 8.47 nm, which indicates cellulase unfolding in certain concentrations of SDS. The cellulase unfolding was electrostatically induced by the SDS ion site-specific adherence to positively charged amino acid regions on the protein surface [19]. Contrarily, cellulase hydrodynamic diameter decreases to 6.39 nm due to folding caused by CTAB. It has also been observed that the size of SDS and CTAB vesicles increased in response to cellulase from 232.4 and 201.5 nm to 323.7 and 280.3 nm, respectively. These data strongly suggest the possibility that cellulase got adsorbed in the bilayer or on the surface of the vesicle, which causes the vesicles to inflate. In surfactant-protein chemistry, the shared vesicle area is referred to as the maximal protein destabilization region because of enhanced hydrophobic interactions among

surfactant vesicles and the various cellulase protein units[20]. No vesicle formation was observed in the aqueous Tween 20 solution. A D_h of 7.65 nm was noticed with a polydispersity of 7.1%, indicating Tween 20 was monodispersed.

Table 2.2: DLS and ζ potential data of enzyme and surfactants

Aqueous Sample	Particle size distribution peak(nm)	Standard Deviation (nm)	Polydispersity Index (PDI)	Solution pH	ζ potential (mV)
Cellulase (15 µL/mL)	7.24	1.63	0.05	4.6	-1.3± 0.1
SDS (10% w/v)	1.95	0.56	0.08	9.5	-26.3± 1.4
	232.4	66.62	0.08		
CTAB (10% w/v)	0.85	0.22	0.06	4.5	+49.2± 1.7
	201.5	54.94	0.07		
Tween 20 (10% w/v)	7.65	2.07	0.07	5.9	-8.4 ±0.3
Cellulase (15 µL/mL) + SDS (10% w/v)	8.47	6.92	0.66	6.5	-26.8± 1.1
	323.7	165.98	0.26		
Cellulase (15 µL/mL) + CTAB (10% w/v)	6.39	2.43	0.14	3.47	+20.4± 0.4
	280.3	92.93	0.10		
Cellulase (15 µL/mL) + Tween 20 (10% w/v)	8.85	2.45	0.07	4.56	-1.8± 0.1

ζ potential of the surfactant vesicles with ionic strength influenced the enzyme-surfactant system by immobilizing the enzyme. The aqueous pH of cellulase was around 4.6 and had a ζ potential value of -1.3 mV. The addition of ionic surfactant (SDS, CTAB) alters the pH and ζ potential value of the enzyme as per their ionic nature. Tween 20, a non-ionic surfactant, exhibits a slightly negative ζ potential value in aqueous media with a concentration far exceeding its CMC (critical micelle concentration) value. As no adsorption occurred in the Tween 20 surface, the pH and

the ζ potential of cellulase did not change much in the presence of the non-ionic surfactant.

2.2.3 Enzymatic hydrolysis

2.2.3.1 Effect of Pretreatment on Enzymatic Hydrolysis

Pretreatment is primarily used to release polysaccharides from the lignocellulose matrix before enzymatic hydrolysis to increase sugar production. As demonstrated in **Table 2.3**, the enzymatic digestibility of raw biomass (RB) yielded negligible sugars. The cellulose enzyme from *Trichoderma reesei* contained eight endo-β-1,4-glucanase (EG), seven β-glucosidases, components, and two cellobiohydrolases (CBH I and II) (exocellulase) components [21]. The high lignin content in RB irreversibly gets bound to the enzyme, which mainly deactivates the enzyme and lowers overall sugar production. β-Glucosidase and CBH I had the highest affinity towards lignin adsorption [22], [23]. The preference of EG towards amorphous cellulose and affinity of CBH II towards cellobiose fragments present in the non-reducing end of cellulose resulted in glucose and a small amount of cellobiose in the hydrolysate of RB [24], [25].

After dilute acid (AC) pretreatment, the maximum amount of hemicellulose in raw RGB was removed as expected. The overall sugar yield of AC was limited to 273.8 mg/g of pretreated biomass despite the substantial disintegration of hemicellulose throughout the pretreatment process. The leading cause of the comparatively low enzyme digestibility of the AC substrate was possibly due to the lignin fragment present in the solid AC-pretreated substrate. This can prevent the cellulose from being accessed and adsorb the cellulase through ineffective binding. D-xylopyranose, the backbone of free hemicellulose residues in the AC biomass, is linked by β (1→3, 1→4) glycosidic bonds, which were digested by β-glucosidases enzyme and produce xylose fraction in the AC hydrolysate.

Table 2.3: Sugar yield of different pretreated biomass hydrolysates

Biomass Sample	Time (h)	Glucose g/L	Xylose g/L	Cellobiose mg/L	Total sugar yield (mg/g of initial hydrolysate biomass sample)
RB.	6	2.30±0.06	-	6.00±0	46.12
	12	2.62±0.01	-	5.00±0	52.50
	24	2.93±0.07	-	4.30±0.20	58.68
	48	3.20±0.05	-	4.00±0.14	64.08
	72	3.34±0.06	-	3.85±0.10	66.87
AC	6	5.86±0.02	0.81±0.01	-	133.40
	12	7.95±0.07	1.03±0.01	-	179.60
	24	9.60±0.06	1.11±0.01	-	214.20
	48	12.40±0.04	1.20±0.01	-	273.40
	72	12.42±0.02	1.27±0.01	-	273.80
AL	6	8.90±0.13	4.75±0.03	-	273.00
	12	12.22±0.20	5.76±0.05	-	359.60
	24	16.00±0.20	7.03±0.04	-	460.60
	48	19.10±0.28	7.98±0.06	-	541.60
	72	20.97±0.40	9.13±0.12	-	602.00
AC-AL	6	10.38±0.17	-	-	206.40
	12	14.90±0.20	-	-	298.00
	24	21.06±0.31	-	-	421.20
	48	24.70±0.44	-	-	494.00
	72	31.20±0.42	-	-	624.00

In a study conducted by Panneerselvam et al. (2013), a remarkable achievement was reported. The authors attained a maximum sugar yield of 431.9 mg/g from the enzymatic hydrolysis of ozone-treated *S. ravennae* grass biomass. For this purpose, the authors deployed Cellic® CTec2 enzyme with an enzyme loading of 0.1 g/g of biomass

[4]. In this work, the maximum sugar yield of AL and AC-AL hydrolysates was 602 mg/g and 624 mg/g, respectively. These values underscore the effectiveness of the acid-alkali pretreatment method in facilitating enzymatic hydrolysis for sugar production from *S. ravennae* biomass. The AC-AL solid substrate has no hemicellulose segment. The entirety of the amount of sugar was synthesized in the form of glucose. Meanwhile, xylose makes up 30% of the sugar in the AL hydrolysate, and glucose makes up the remaining 70%. Due to the low lignin content in both hydrolysates, the enzyme actively digested polysaccharides into monosaccharides without generating any cellobiose intermediates.

2.2.3.2 Effect of anionic surfactant (SDS) on enzymatic hydrolysis

The effects of anionic surfactant (SDS) on the cellulase treatment of raw and pretreated RGB were investigated. The total amount of sugar generated for each enzymatic process is shown in **Fig. 2.6**. It is evident that the overall sugar yield drastically decreased for all four biomass substrates during enzymatic hydrolysis with SDS. The sugar yield was already low during the enzymatic digestion of RB and AC without surfactant, as high lignin content inhibits the enzymatic conversion of sugars by interaction with the cellulase enzyme in an ineffective way. The addition of SDS further reduced the rate of polysaccharides to monosaccharides conversion. Several studies have shown that ionic surfactants firmly bind to proteins in contrast to non-ionic surfactants and that such contact could allow proteins to become denaturized [20][26]. SDS, an anionic surfactant, interacts with most proteins below its CMC (10 mM at >40°C). In this study, the concentration of SDS was above its CMC (34.7 mM). Thereby, the SDS was cooperatively attached to the enzyme and enabled the cluster formation on its surface. In this regard, it shall be noted that the bindings involved electrostatic interactions at both low and high SDS concentrations. The SDS electrostatic interaction involved its effective binding with the positively charged surface residue of the enzyme. After the SDS-Cellulase binding content surpassed a particular level, the surfactant molecules electrostatically repelled other molecules. This enabled the destruction of the cellulase spatial structure and decreased its cellulase activity [27]. With SDS addition, the zeta

potential of the cellulase solution reduced from -1.3 mV to -26.8 mV (**Table 2.2**). This further demonstrated the electrostatic repulsion between cellulase and SDS.

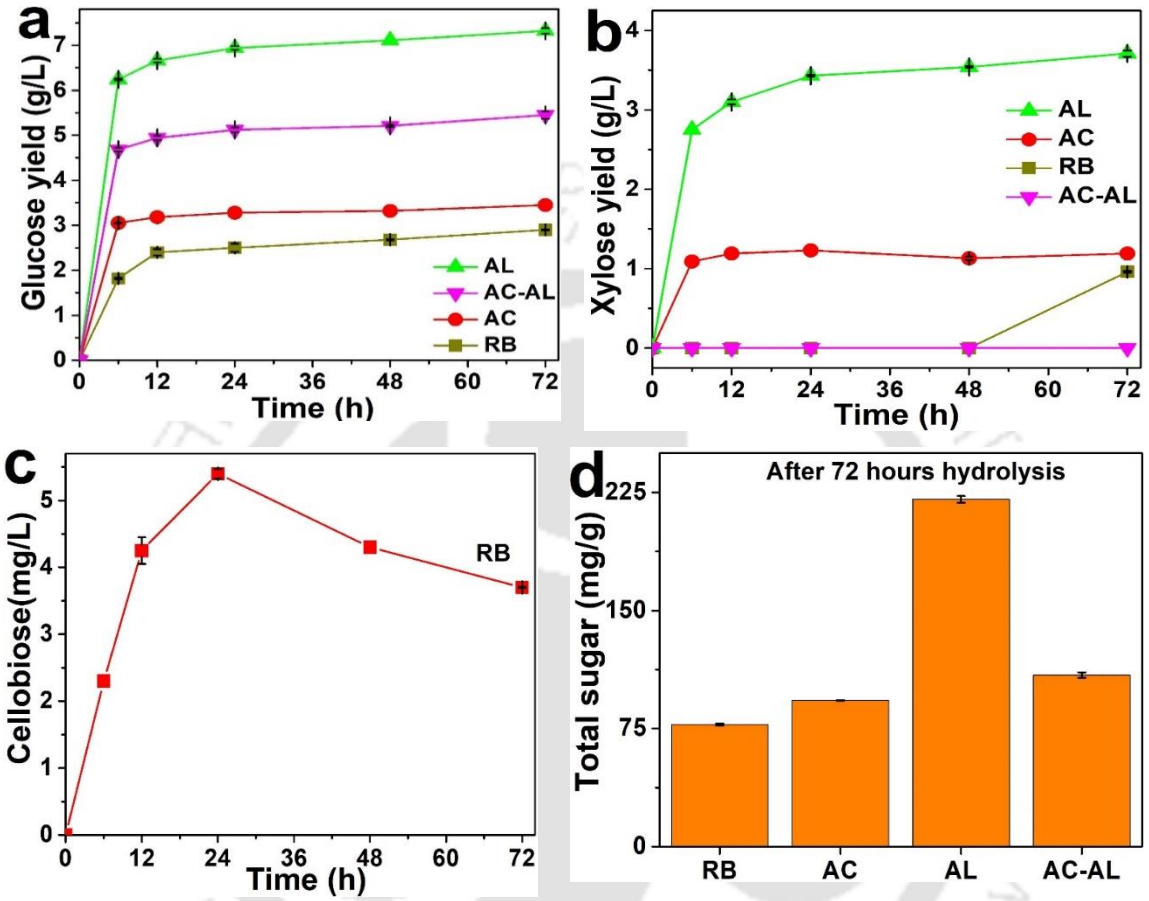

Figure 2.6: Effect of SDS on (a) Glucose yield, (b) Xylose yield, (c) Cellobiose concentration, and (d) total sugar yield.

Contrary to the enzymatic hydrolysis without surfactant, the glucose yield in the presence of SDS was higher for AL biomass than AC-AL. According to the studies conducted by Vitha et al. (1996), the micellar environments of water-solubilized SDS have strong hydrogen bond donating ability (α = 0.87) and moderate hydrogen bond accepting ability (β = 0.40) [28]. The strong electrophiles, such as carbonyl and hydroxyl groups in the cellulose, attach to the hydrophilic head (SO_4^{2-}) of the SDS micelles. Since the AC-AL sample did possess lesser lignin content and no hemicellulose content, the absorbance of the cellulose substrate was maximum. This led to a lesser cellulose-to-glucose conversion and reduced total sugar yield.

2.2.3.3 Effect of cationic surfactant (CTAB) on enzymatic hydrolysis

The effect of CTAB (cationic surfactant) on the enzymatic hydrolysis of different pretreated RGB is depicted in **Fig. 2.7**. As cellulase exhibited a negative charge density profile in the aqueous media **(Table 2.2)**, an electrostatic interaction of cationic CTAB with globular proteins in cellulase was expected. Due to a greater number of negatively charged aspartic (Asp) and glutamic acid (Glu) regions on the enzyme surface, the CTAB-cellulase electrostatic interactions are more plausible. Consequently, such interactions reduced β-glucosidase activity. This resulted in increased cellobiose concentration in the hydrolysates of RGB samples.

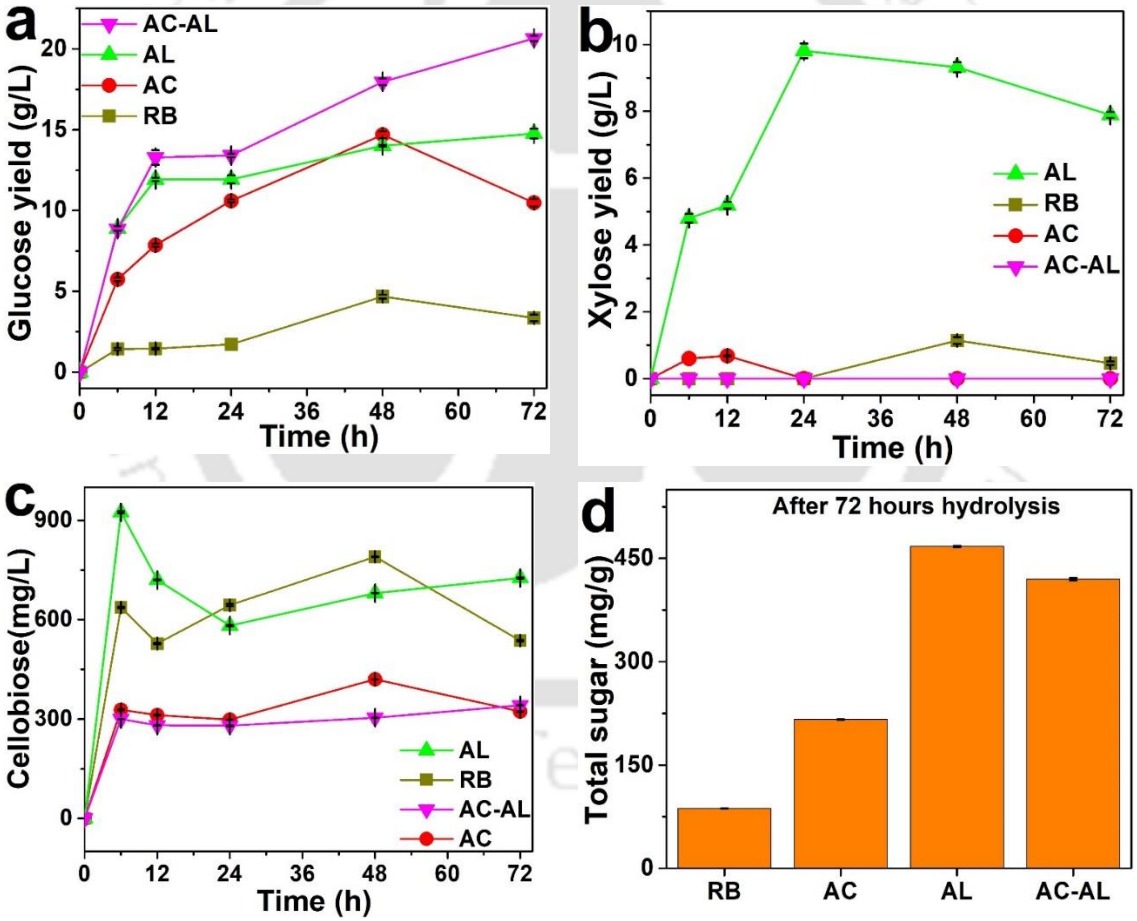

Figure 2.7: Effect of CTAB on (a) Glucose yield, (b) Xylose yield, (c) Cellobiose concentration, and (d) total sugar yield.

β-glucosidase, on the other hand, not only hydrolyzes disaccharides and transglycosylates them and converts monosaccharides to disaccharides. This may also cause cellobiose in hydrolysates [29]. CTAB interacted with carboxylic groups of aspartic (Asp) and glutamic acid (Glu) constituents of the cellulase [30]. In a broader sense, the electrostatic interaction is probably less significant than the hydrophobic interaction. The hydrophobic tails of CTAB enabled it to enter the CBH I binding tunnel in cellulase and attach to the active site. Such a mechanism leads to the inactivation of the enzyme. Because of that, compared to the controlled (without surfactant) enzymatic digestion of RGB, the sugar yield decreased during CTAB-mediated enzymatic hydrolysis.

However, after 48 h of hydrolysis, the glucose yield from RB and AC samples was 4.68 g/L and 14.7 g/L, which were 46% and 18% better than controlled enzymatic hydrolysis. This was due to the higher lignin content in the RB and AC samples. The higher carboxylic and phenolic groups present in the lignin resulted in higher negative charge density even in the acidic pH. At higher concentrations (27.4 mM), CTAB bounded cooperatively and formed clusters on the protein. This caused the formation of the bigger vesicles. Accordingly, the hydrolysis suspension exhibited a strong positive charge density (**Table 2.2**). However, the enzymatic hydrolysis suspension should have a marginal negative charge for a favorable outcome. Initially, the negatively charged lignin gets bound to the positively charged CTAB. This affected the enzyme activity in a positive manner. However, with the progression of hydrolysis, the glucose yield in the hydrolysate of RB and AC samples gradually decreased. The hydrogen bond water network was ruptured by the CTAB surfactant. Intermolecular hydrogen bonding with water partly compensated for the higher glucose yield. This, in turn, reduced hydrophobic interaction by heavily aggregating the hydrophilic part of CTAB. As a result, the aggregation number (N) of CTAB decreased [31]. The CTAB monomers bound to the glucose molecules decreased glucose yield in the hydrolysate (72 h) of RB and AC samples [32]. Similarly, RB, AC, and AL hydrolysate showed an initial rise followed by a gradual decrease in xylose yield.

2.2.3.4 Effect of non-ionic surfactant (Tween 20) on enzymatic hydrolysis

The findings of Tween 20-added enzymatic hydrolysis are given in **Fig. 2.8**. Tween 20 significantly enhanced the enzymatic hydrolysis of raw and pretreated RGB substrates. The glucose yields grew steadily as the hydrolysis period was extended. As the hydrolysis period approached 72 hours, the glucose yields of RB, AC, AL, and AC-AL samples were 4.92 ± 0.14 g/L, 13.29 ± 0.56 g/L, 26 ± 0.21 g/L, and 32.31 ± 0.33 g/L, respectively, and that exceeded the glucose yield of enzymatic hydrolysate with and without of SDS, and CTAB. The RGB samples containing hemicellulose fraction also showed enhanced xylose yield (RB- 1.4 ±0.03 g/L, AC-1.49 ± 0.01 g/L, AL-14.8 ± 0.03 g/L) after 72 h of hydrolysis with Tween 20.

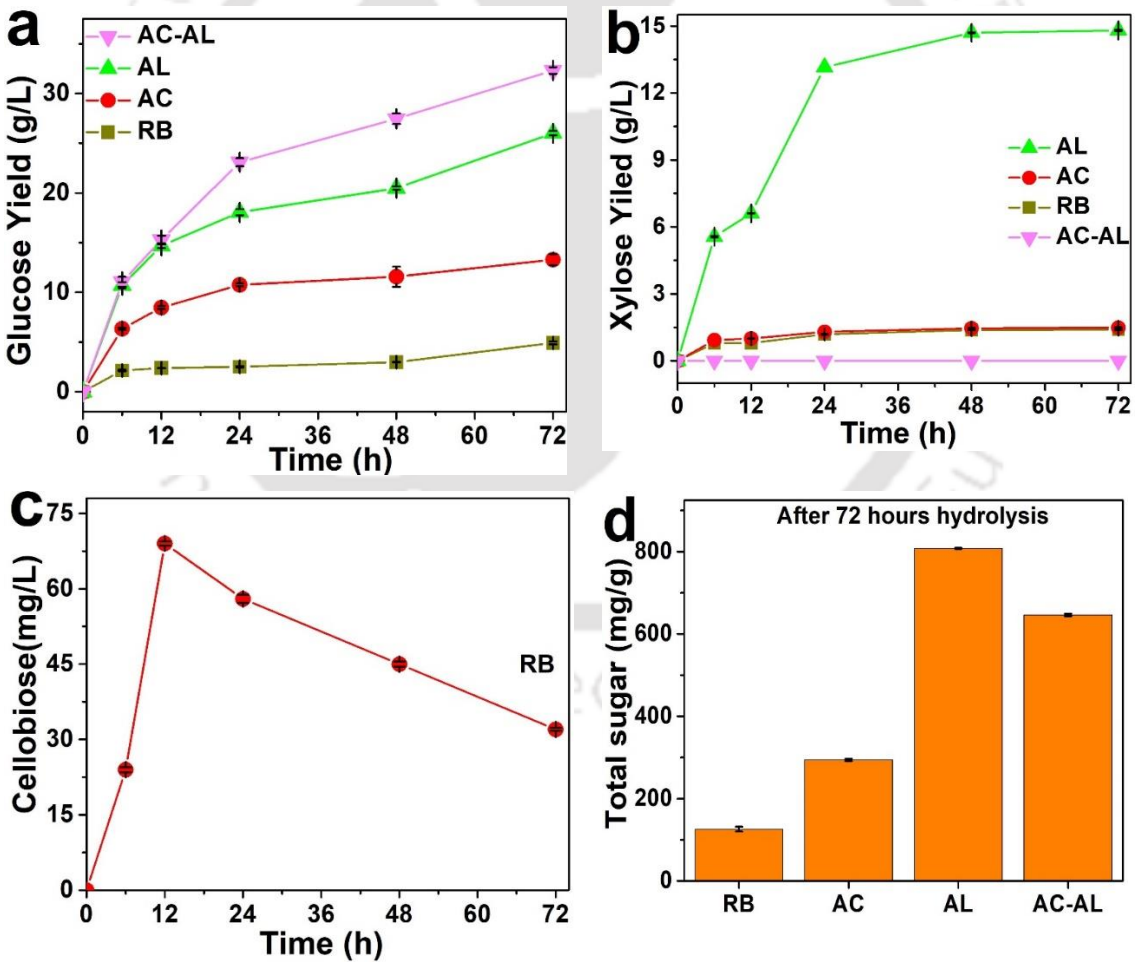

Figure 2.8: Effect of Tween 20 on (a) Glucose yield, (b) Xylose yield, (c) Cellobiose concentration, and (d) total sugar yield

The maximal increase in enzymatic digestibility of cellulose and hemicellulose with Tween 20 was over 16% and 34%, respectively (**Table 2.4**). The results indicated that the pretreatment strategies had a significant impact on the degree to which Tween 20 boosted the enzymatic hydrolysis of RGB substrates. However, no intermediate cellobiose was formed during the enzymatic digestion of pretreated biomass samples. There was a noticeable rise in performance for dilute alkali (AL- 2% NaOH) pretreated substrates. At the same time, Tween 20 seemed not so practical in improving the sugar yield of subsequent acid-alkali (AC-AL) pretreated substrates. According to some studies at higher non-ionic surfactant concentrations, pretreated lignocellulosic biomass performed better than pure cellulose regarding the total sugar yield [33], [34]. This was due to the higher crystallinity of pure cellulose. With increased substrate crystallinity, the specific surface area decreases, which might influence the interaction between cellulase and cellulose [33], [34]. The increased cellulose crystallinity of subsequent acid-alkali (AC-AL) processed biomass might be a limiting factor for reduced sugar output.

Table 2.4: Cellulose and Hemicellulose digestibility

Digestibility (%)	**Surfactant in Enzymatic Hydrolysis**	**Biomass sample**			
		RB	**AC**	**AL**	**AC-AL**
Cellulose Digestibility	Without surfactant	16.40 %	45.14 %	69.71 %	66.46 %
	SDS	14.24 %	12.54 %	24.33 %	11.61 %
	CTAB	16.45 %	38.09 %	49.06 %	44.00 %
	Tween 20	24.17 %	48.30 %	86.43 %	68.83 %
Hemicellulose Digestibility	Without surfactant	0.00 %	35.70 %	63.44 %	_
	SDS	8.10 %	32.68 %	25.20 %	_
	CTAB	3.88 %	0.00	53.57 %	_
	Tween 20	11.31 %	39.00 %	97.77 %	_

The amount of lignin in the biomass substantially influenced the surfactant action because non-ionic surfactants interacted with the lignin fraction of pretreated substrates to lessen the unproductive protein adsorption. Regardless of how much residual lignin was present, the enhancement achieved by Tween 20 was also constrained for the dilute acid-pretreated (AC-2% H_2SO_4) substrates. Although raw biomass and substrate processed with diluted acid often contained substantially greater quantities of lignin, Tween 20 could not significantly increase its enzymatic digestibility. This finding revealed that lignin concentration could not be the only element influencing the improved performance of Tween 20 and that lignin structure, which was strongly related to the pretreatment procedure, could be equally crucial. Also, pH significantly affects the enzymatic activity on cellulosic substrates. The pH of all the hydrolysates was measured. The RB, AC, and AC-AL substrate hydrolysates had pHs of 3.45, 3.4, and 3.7, respectively. Meanwhile, the AL substrate hydrolysate with Tween 20 had a pH of 4.2. The optimum working pH of Cellulase from Trichoderma ressei had been reported between pH 4-5, and also below its isoelectric point, cellulase possessed a slightly negative charge, which have a positive impact on enzymatic digestibility [35]. AL substrate hydrolysate had a pH beyond the isoelectric point of cellulase (PI-4.8), which would result in a slight negative charge on the protein and also falls under the optimum working pH range of the enzyme, which contributed to the increased enzymatic digestibility of AL-treated substrate in the presence of Tween 20.

2.2.4 Ethanol Yield

The final hydrolysate (72h) from the Tween 20-mediated enzymatic hydrolysis of AL (40.83±0.15 g/L sugar with 26±0.21 g/L glucose) and AC-AL (32.31±0.33 g/L sugar with 100% glucose) biomass was used for ethanol fermentation. Hydrolysates of AL (30.1±0.74 g/L sugar with 20.97±0.4 g/L glucose) and AC-AL (31.20±0.42 g/L sugar with 100% glucose) without surfactant were also fermented to understand the effects of Tween 20 further. Due to its abilities for fermentation and tolerance of ethanol, *Saccharomyces cerevisiae* has traditionally been utilized for the synthesis of 2nd generation bioethanol. However, since it lacks the aptitude to use pentose sugars, xylose could not be utilized. The ethanol production and conversion yield from hydrolysate of

AL and AC-AL treated biomass were 8.73±0.12 g/L and 86%, and 13.45±0.15 g/L and 89%, respectively. The ethanol production and conversion efficiency rose to 11.82±0.19 g/L and 15.11±0.25 g/L, and 94% and 96.5%, respectively, when Tween 20 was added to the enzymatic hydrolysis solution of AL and AC-AL treated biomass. The results indicated that by utilizing Tween 20 in enzymatic hydrolysate, 0.249 and 0.318 g of ethanol could be generated from 1 g of AL and AC-AL treated RGB, respectively.

A thorough comparison was conducted, encompassing an investigation of the data recorded in pertinent literature sources, to contextualize and analyze the outcomes achieved from the fermentation process in the current study. **Table 2.5** provides a detailed summary of the important statistics and patterns encountered across numerous research, summarising the key findings of this comparative evaluation.

Table 2.5: Literature comparison for bioethanol yield

S. no	Substrate	Pretreatment	Enzymatic hydrolysis and fermentation conditions	Ethanol yield	Reference
1	*Pennisetum purpureum* grass	Acid-Alkali (100 mg H_2SO_4 / g, 0.5M NaOH)	Semi-Simultaneous Saccharification and Fermentation: 20 FPU cellulase, 0.5 g/L of *Scheffersomyces shehatae* UMFG-HM 52.2, with 0.3 mL Tween. 96 h	4.98 g/L, 0.30-0.40 g/g biomass, Conversion efficiency-83%	[36]
2	Napier grass	Wih 3% sulfuric acid at 190 °C for 30-min	Liquefaction and fermentation: liquefaction with 10 FPU/g- cellulase (Novozymes Cellic CTec2) at 50 °C for 2 h. fermentation with 2 mL of 500 g-wet cells/L yeast (*S. cerevisiae*) at 35 °C for	13.2 g/L, 0.26 g/g biomass	[37]

			70 h		
3	Kans grass (*Saccharum spontaneum*)	8-stage fractional hydrolysis process (H_2SO_4 concentrations: 1, 2, 5, 10, 15, 20, 25, 30%)	Co-culture fermentation: Xylose-rich fraction fermented with 10% v/v *S. shehatae* at 150 rpm, 30 °C for 48 h, sequentially Glucose-rich fraction with 10% v/v *Z. mobilis*	25.0 g/L, Conversion efficiency-78.6 %	[38]
4	Napier grass (*Pennisetum purpureum Schumach*)	With 2 M NaOH at 96 °C for 1 h and 56 min	Hydrolysis: 40 FPU/g cellulase Cellic® CTec2 with 50 mM citrate buffer (pH 5.0) at 50 °C for 5 days. SHF: with Autolyzed yeast powder 2 g/L, 10% *Saccharomyces cerevisiae* inoculum at 30 °C and 100 rpm for 48 h.	30.6 g/L	[39]
5	Silver grass (*Miscanthus sacchariflorus*)	With 1% (w/v) sulfuric acid at 121 °C for 30 min	Hydrolysis: with Celtic CTec2 enzyme (Novozyme) (128 FPU/mL) at 50 °C, 200 rpm for 72 h. Fermentation: with 5% *Saccharomyces cerevisiae* inoculum at 30 °C and 200 rpm for 144 h.	~13 g/L, 0.04 g/g of biomass	[40]
6	Eragrostis airoides Nees grass	With 5% sulphuric acid at 121 °C, 15 psi for 20 min	Hydrolysis: with cellulase from *Trichoderma reesei* at 50 °C, 75 rpm for 4 days. Fermentation: with *Saccharomyces cerevisiae*	17.56 g/L	[41]

			inoculum at 35 °C, 75 rpm, 72 h.		
7	Amur Silvergrass	With 4% NaOH at 1:6 solid-to-liquid ratio at 100 °C for 15 min	Simultaneous Saccharification and Fermentation: With 20 U/g cellulase and 0.03% (w/v) dry angel yeast at 34 °C, 100 rpm, 96 h.	~18 g/L, Conversion efficiency-78.3%	[42]
8	Ravenna grass (*Saccharum ravennae*)	Two-stage acid-alkali treatment at 10% solid loading with 2% H_2SO_4 and 2% NaOH at 121 °C for 1 h under 15 psi pressure	Hydrolysis: 5% solid loading and with cellulase from *Trichoderma reesei* and Tween 20 (0.2 g/g) at 50 °C, 75 rpm for 72 hours. Fermentation: with 5% (v/v) *Saccharomyces cerevisiae* inoculum at 35 °C, 110 rpm, for 72 h.	15.11±0.25 g/L, Conversion efficiency-96.5%, 0.318 g/g of biomass	This work

Saccharomyces cerevisiae consistently sticks out as the preferred microbe for the production of 2nd generation bioethanol due to its previous achievements of extraordinary fermentation efficiency and remarkable tolerance to ethanol. The capacity of this yeast to produce ethanol from a variety of carbohydrates, especially hexose sugars, has been broadly utilized to generate biofuel. However, a crucial drawback of *S. cerevisiae* is that it cannot metabolize pentose sugars, particularly xylose, which is loaded in lignocellulosic biomass and is a crucial feedstock for the industrial production of 2nd generation bioethanol. The use of certain yeast or bacterial strains capable of effectively digesting pentose carbohydrates like xylose is one potential approach to overcome the constraint. These specialized microbes are able to effectively transform pentose sugars into ethanol simply due to their enzymatic pathway, allowing them to use a broader range of sugars found in lignocellulosic biomass. Additionally, the field of

genetic engineering has become a powerful tool for solving the difficulty of pentose utilization. *S. cerevisiae* strains with enhanced capacities can effectively metabolize both hexose and pentose carbohydrates. As a result, formerly useless carbohydrates may now be converted into ethanol with the help of crucial enzymes and regulatory components.

2.2.5 Future prospective

Optimizing the conversion of Ravenna grass biomass into bioethanol offers substantial benefits. Given its renewable and organic origins, the reduction of carbon emissions and diminished human reliance on oil are some notable outcomes. The carbon fixation rate through photosynthesis in the Ravenna grass and its carbon concentration considerably varied with the cultivated time (years) of biomass-producing species. Based on a 2018 research study conducted by the USDA-ARS (U.S. Department of Agriculture - Agricultural Research Service), the carbon concentration in Ravenna grass biomass fluctuated between 430 and 470 grams per kilogram over a span of five years [43]. The critical environmental advantage of bioethanol production from Ravenna grass biomass lies in its potential to achieve carbon neutrality throughout its lifecycle. The carbon dioxide (CO_2) emitted when utilizing bioethanol is offset by CO_2 absorption in the atmosphere during the growth phase of the Ravenna grass species.

Alkaline pretreatment (2% NaOH) of Ravenna grass biomass (RGB) resulted in a decent solid recovery percentage of 43.66% containing 54.2% cellulose, 26 % hemicellulose and causing 87.71% delignification. When Tween 20 was added, the overall sugar yield of alkali-treated RGB substrates increased by around 34% to 816 mg/g from 602 mg/g **(Fig. 2.9)**. Cellulose and hemicellulose conversion into glucose and xylose had a cumulative contribution to the enhanced sugar yield. However, xylose, the primary pentose sugar in hydrolysates of lignocellulosic biomass, cannot be fermented by the majority of yeast and bacteria. To ensure the economic feasibility of the bioethanol conversion of lignocellulose biomass, the total sugar yield as well as the ethanol conversion yield from sugar, shall be optimized. The conducted work reported in this article effectively enhanced the sugar yield of RGB substrate through enzymatic

digestion with Tween 20. However, all deployed chemicals were of laboratory-grade quality, and the enzyme used was procured commercially. This can lead to an elevated overall cost of ethanol production. To circumvent such higher production costs, cost-saving measures such as bulk purchase of commercial chemicals, in-house enzyme production, and the implementation of optimized pretreatment and Tween 20-assisted enzymatic hydrolysis processes can be explored to reduce the production costs of ethanol.

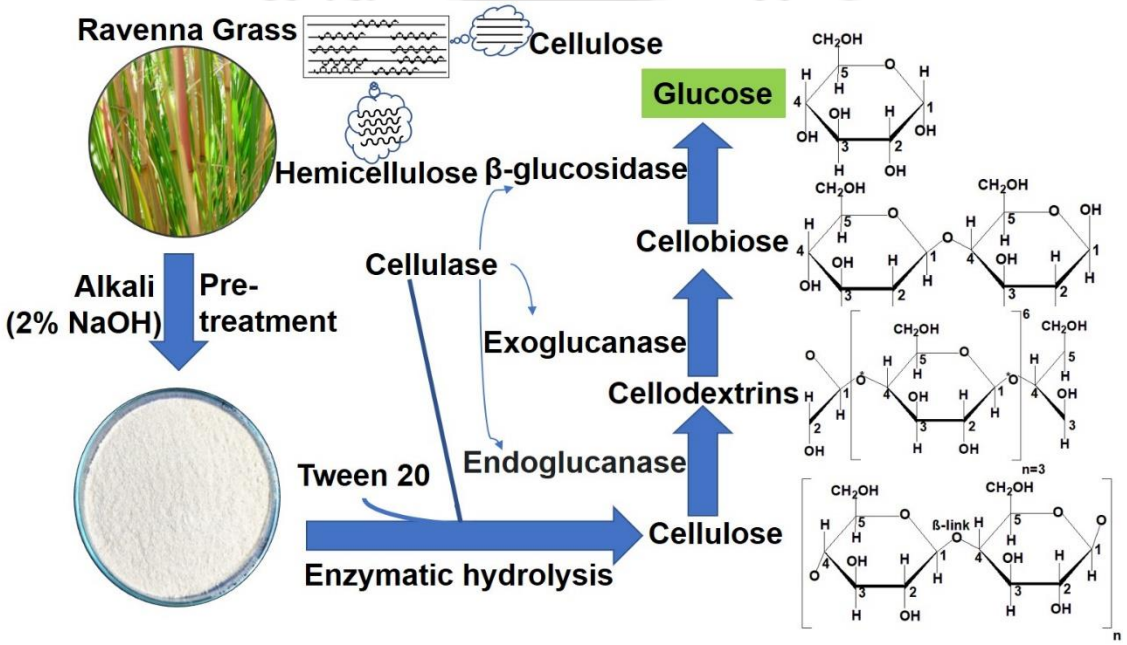

Figure 2.9: Enzymatic hydrolysis mechanism of Ravenna Grass Biomass

Several studies conveyed that the genetic modification of yeasts such as *Saccharomyces cerevisiae* and *Pichia stipitis* can foster xylose utilization for ethanol production [44], [45]. Also, bacterium species like *Zymobacter palmae* with genetic modifications have been reported to ferment a combination of xylose and glucose simultaneously and with 95% theoretical ethanol yield [46]. Another aspect of cost-effective bioethanol production is the utilization of lignin, the byproduct of alkaline pretreatment of RGB. In the earlier investigations, highly pure alkaline lignin was successfully extracted from RGB. Such a product can be utilized in specialized aromatic chemical development, packaging, heavy metals removal, and thermal combustion [47]. To summarize, alkaline

pretreatment followed by non-ionic surfactant-mediated enzymatic hydrolysis with fermentation by genetically modified microorganisms can enhance the ethanol yield and utilization of pretreatment byproducts. Thereby, such interventions can enable bioethanol production on a cost-competitive basis.

2.3 Summary

In this study, several pretreatments have been conducted, and the acid-alkali method proved effective in achieving nearly complete hemicellulose removal and maximum delignification (92.07%). However, it resulted in a low solid recovery (24.74%). Alkali treatment, on the other hand, outperformed in terms of solid recovery, delignification, and hemicellulose retention. Cellulase from Trichoderma reesei successfully digested cellulose and hemicellulose, boosting the total sugar yield. The addition of SDS significantly reduced enzymatic digestibility by deactivating the enzyme. CTAB also had a negative impact on sugar conversion, primarily by binding to β-glucosidase and reducing its activity, leading to cellobiose formation and hindering endoglucanase activity. Conversely, Tween 20 played a positive role in maintaining enzyme activity by stabilizing pH within the optimal range and preventing non-productive enzyme adsorption into the lignin matrix. For AL and AC-AL treated RGB, the highest sugar yields were achieved with the addition of Tween 20, totaling 816 mg/g and 646.2 mg/g, respectively. However, the impact of Tween 20 on AC-AL treated RGB was not significant, resulting in only a 3.5% increase in sugar yield and a 12.3% increase in ethanol yield. Overall, the presence of Tween 20 improved glucose-to-ethanol conversion efficiency by 7.5-8%.

In conclusion, it is advised to integrate AC-AL pretreatment with Tween 20-mediated enzymatic hydrolysis for higher ethanol output if the fermenting organism cannot convert pentose sugars into ethanol. However, AL pretreatment coupled with Tween 20-mediated enzymatic hydrolysis is preferable for the highest possible sugar production. The ethanol output from RGB can be significantly increased by using genetically modified fermenting microorganisms with the ability to use pentose sugar, and it will pave the way for Ravenna grass to be utilized commercially as a biofuel substrate.

References:

[1] A. Sluiter *et al.*, "Determination of structural carbohydrates and lignin in biomass. National Renewable Energy Laboratory," *Natl. Renew. Energy Lab. (NREL), Golden CO*, 2008.

[2] J. B. Sluiter, R. O. Ruiz, C. J. Scarlata, A. D. Sluiter, and D. W. Templeton, "Compositional Analysis of Lignocellulosic Feedstocks. 1. Review and Description of Methods," *J. Agric. Food Chem.*, vol. 58, no. 16, pp. 9043–9053, Aug. 2010, doi: 10.1021/jf1008023.

[3] L. Segal, J. J. Creely, A. E. Martin, and C. M. Conrad, "An Empirical Method for Estimating the Degree of Crystallinity of Native Cellulose Using the X-Ray Diffractometer," *Text. Res. J.*, vol. 29, no. 10, pp. 786–794, Oct. 1959, doi: 10.1177/004051755902901003.

[4] A. Panneerselvam, R. R. Sharma-Shivappa, P. Kolar, D. A. Clare, and T. Ranney, "Hydrolysis of ozone pretreated energy grasses for optimal fermentable sugar production," *Bioresour. Technol.*, vol. 148, pp. 97–104, 2013, doi: https://doi.org/10.1016/j.biortech.2013.08.119.

[5] Z. Zhang, "Chapter 5 - Waste pretreatment technologies for hydrogen production," Q. Zhang, C. He, J. Ren, and M. B. T.-W. to R. B. Goodsite, Eds. Academic Press, 2021, pp. 109–122.

[6] Z. Jin, K. S. Katsumata, T. B. T. Lam, and K. Iiyama, "Covalent linkages between cellulose and lignin in cell walls of coniferous and nonconiferous woods," *Biopolymers*, vol. 83, no. 2, pp. 103–110, Oct. 2006, doi: https://doi.org/10.1002/bip.20533.

[7] X. Zhang, W. Yang, and W. Blasiak, "Modeling study of woody biomass: Interactions of cellulose, hemicellulose, and lignin," *Energy and Fuels*, vol. 25, no. 10, pp. 4786–4795, 2011, doi: 10.1021/ef201097d.

[8] A. Panneerselvam, R. R. Sharma-Shivappa, P. Kolar, T. Ranney, and S. Peretti, "Potential of ozonolysis as a pretreatment for energy grasses," *Bioresour. Technol.*, vol. 148, pp. 242–248, 2013, doi: https://doi.org/10.1016/j.biortech.2013.08.129.

[9] D. Andhika, A. Kasim, A. Asben, and Y. Yusniwati, "Delignification of Lignocellulosic Biomass," *World J. Adv. Res. Rev.*, vol. 12, pp. 462–469, Nov. 2021, doi: 10.30574/wjarr.2021.12.2.0618.

[10] J. J. Ascencio, A. K. Chandel, R. R. Philippini, and S. S. da Silva, "Comparative study of cellulosic sugars production from sugarcane bagasse after dilute nitric acid, dilute sodium hydroxide and sequential nitric acid-sodium hydroxide pretreatment," *Biomass Convers. Biorefinery*, vol. 10, no. 4, pp. 813–822, 2020, doi: 10.1007/s13399-019-00547-6.

[11] N. S. Samanta, P. P. Das, P. Mondal, U. Bora, and M. K. Purkait, "Physico-

chemical and adsorption study of hydrothermally treated zeolite A and FAU-type zeolite X prepared from LD (Linz–Donawitz) slag of the steel industry," *Int. J. Environ. Anal. Chem.*, pp. 1–23, May 2022, doi: 10.1080/03067319.2022.2079082.

[12] H. Ben *et al.*, "Characterization of Whole Biomasses in Pyridine Based Ionic Liquid at Low Temperature by 31P NMR: An Approach to Quantitatively Measure Hydroxyl Groups in Biomass As Their Original Structures," *Front. Energy Res.*, vol. 6, p. 13, Mar. 2018, doi: 10.3389/fenrg.2018.00013.

[13] D. Haldar and M. K. Purkait, "Thermochemical pretreatment enhanced bioconversion of elephant grass (Pennisetum purpureum): insight on the production of sugars and lignin," *Biomass Convers. Biorefinery*, vol. 12, no. 4, pp. 1125–1138, 2022, doi: 10.1007/s13399-020-00689-y.

[14] S. Park, J. O. Baker, M. E. Himmel, P. A. Parilla, and D. K. Johnson, "Cellulose crystallinity index: measurement techniques and their impact on interpreting cellulase performance," *Biotechnol. Biofuels*, vol. 3, no. 1, p. 10, 2010, doi: 10.1186/1754-6834-3-10.

[15] S. Dhara, N. Shekhar Samanta, P. P. Das, R. V. S. Uppaluri, and M. K. Purkait, "Ravenna Grass-Extracted Alkaline Lignin-Based Polysulfone Mixed Matrix Membrane (MMM) for Aqueous Cr(VI) Removal," *ACS Appl. Polym. Mater.*, Jul. 2023, doi: 10.1021/acsapm.3c00999.

[16] X. Xu, L. Xia, Q. Huang, J.-D. Gu, and W. Chen, "Biosorption of cadmium by metal-resistant filamentous fungus isolated from chicken manure compost," *Environ. Technol.*, vol. 33, pp. 1661–1670, Jul. 2012, doi: 10.1080/09593330.2011.641591.

[17] N. S. Samanta, Anweshan, P. Mondal, U. Bora, and M. K. Purkait, "Synthesis of precipitated calcium carbonate from LD-slag using CO2," *Mater. Today Commun.*, vol. 36, p. 106588, 2023, doi: https://doi.org/10.1016/j.mtcomm.2023.106588.

[18] Z. Gong *et al.*, "Understanding the promoting effect of non-catalytic protein on enzymatic hydrolysis efficiency of lignocelluloses," *Bioresour. Bioprocess.*, vol. 8, Dec. 2021, doi: 10.1186/s40643-021-00363-9.

[19] P. Bharmoria, M. J. Mehta, I. Pancha, and A. Kumar, "Structural and Functional Stability of Cellulase in Aqueous-Biamphiphilic Ionic Liquid Surfactant Solution," *J. Phys. Chem. B*, vol. 118, no. 33, pp. 9890–9899, Aug. 2014, doi: 10.1021/jp506211b.

[20] D. Otzen, "Protein–surfactant interactions: A tale of many states," *Biochim. Biophys. Acta - Proteins Proteomics*, vol. 1814, no. 5, pp. 562–591, 2011, doi: https://doi.org/10.1016/j.bbapap.2011.03.003.

[21] K. Sakka, T. Kimura, S. Karita, and K. Ohmiya, "Molecular breeding of cellulolytic microbes, plants, and animals for biomass utilization.," *J. Biosci.*

Bioeng., vol. 90, no. 3, pp. 227–233, 2000.

[22] J. K. Ko, E. Ximenes, Y. Kim, and M. R. Ladisch, "Adsorption of enzyme onto lignins of liquid hot water pretreated hardwoods.," *Biotechnol. Bioeng.*, vol. 112, no. 3, pp. 447–456, Mar. 2015, doi: 10.1002/bit.25359.

[23] H. Palonen, F. Tjerneld, G. Zacchi, and M. Tenkanen, "Adsorption of Trichoderma reesei CBH I and EG II and their catalytic domains on steam pretreated softwood and isolated lignin.," *J. Biotechnol.*, vol. 107, no. 1, pp. 65–72, Jan. 2004, doi: 10.1016/j.jbiotec.2003.09.011.

[24] C. Schiano-di-Cola *et al.*, "Systematic deletions in the cellobiohydrolase (CBH) Cel7A from the fungus Trichoderma reesei reveal flexible loops critical for CBH activity," *J. Biol. Chem.*, vol. 294, no. 6, pp. 1807–1815, 2019, doi: https://doi.org/10.1074/jbc.RA118.006699.

[25] S. A. Teter, K. B. Sutton, and B. Emme, "7 - Enzymatic processes and enzyme development in biorefining," K. B. T.-A. in B. Waldron, Ed. Woodhead Publishing, 2014, pp. 199–233.

[26] T. W. Randolph and L. S. Jones, "Surfactant-protein interactions.," *Pharm. Biotechnol.*, vol. 13, pp. 159–175, 2002, doi: 10.1007/978-1-4615-0557-0_7.

[27] C. Cai *et al.*, "Using temperature-responsive zwitterionic surfactant to enhance the enzymatic hydrolysis of lignocelluloses and recover cellulase by cooling," *Bioresour. Technol.*, vol. 243, pp. 1141–1148, 2017, doi: https://doi.org/10.1016/j.biortech.2017.07.058.

[28] M. F. Vitha, J. D. Weckwerth, K. Odland, V. Dema, and P. W. Carr, "Study of the Polarity and Hydrogen Bond Ability of Sodium Dodecyl Sulfate Micelles by the Kamlet−Taft Solvatochromic Comparison Method," *J. Phys. Chem.*, vol. 100, no. 48, pp. 18823–18828, Jan. 1996, doi: 10.1021/jp962129u.

[29] M. Suto and F. Tomita, "Induction and catabolite repression mechanisms of cellulase in fungi," *J. Biosci. Bioeng.*, vol. 92, no. 4, pp. 305–311, 2001, doi: https://doi.org/10.1016/S1389-1723(01)80231-0.

[30] K. Holmberg, "Interactions between surfactants and hydrolytic enzymes," *Colloids Surfaces B Biointerfaces*, vol. 168, pp. 169–177, 2018, doi: https://doi.org/10.1016/j.colsurfb.2017.12.002.

[31] T. Afrin, S. Karobi, M. Rahman, M. Mollah, and M. Susan, "Water Structure Modification by Sugars and Its Consequence on Micellization Behavior of Cetyltrimethylammonium Bromide in Aqueous Solution," *J. Solution Chem.*, vol. 42, Aug. 2013, doi: 10.1007/s10953-013-0050-6.

[32] P. K. Sen, J. K. Midya, S. Bysakh, and B. Pal, "Kinetic and mechanistic studies on the oxidation of d-glucose by MnO2 nanoparticles. Effect of microheterogeneous environments of CTAB, Triton X-100 and Tween 20," *Mol. Catal.*, vol. 440, pp. 75–86, 2017, doi:

https://doi.org/10.1016/j.mcat.2017.07.009.

[33] Y. Zhou, H. Chen, F. Qi, X. Zhao, and D. Liu, "Non-ionic surfactants do not consistently improve the enzymatic hydrolysis of pure cellulose," *Bioresour. Technol.*, vol. 182, pp. 136–143, 2015, doi: https://doi.org/10.1016/j.biortech.2015.01.137.

[34] W. Yang *et al.*, "Synergistic effect of ionic liquid and surfactant for enzymatic hydrolysis of lignocellulose by Paenibacillus sp. LLZ1 cellulase," *Biomass and Bioenergy*, vol. 142, p. 105760, 2020, doi: https://doi.org/10.1016/j.biombioe.2020.105760.

[35] T. Kogo *et al.*, "Production of rice straw hydrolysis enzymes by the fungi Trichoderma reesei and Humicola insolens using rice straw as a carbon source," *Bioresour. Technol.*, vol. 233, Feb. 2017, doi: 10.1016/j.biortech.2017.01.075.

[36] F. A. F. Antunes, P. E. M. Machado, T. M. Rocha, Y. C. S. Melo, J. C. Santos, and S. S. da Silva, "Column reactors in fluidized bed configuration as intensification system for xylitol and ethanol production from napier grass (Pennisetum Purpureum)," *Chem. Eng. Process. - Process Intensif.*, vol. 164, p. 108399, 2021, doi: https://doi.org/10.1016/j.cep.2021.108399.

[37] K. S. K. Ismail *et al.*, "Pretreatment of extruded Napier grass by hydrothermal process with dilute sulfuric acid and fermentation using a cellulose-hydrolyzing and xylose-assimilating yeast for ethanol production," *Bioresour. Technol.*, vol. 343, p. 126071, 2022, doi: https://doi.org/10.1016/j.biortech.2021.126071.

[38] A. Mishra and S. Ghosh, "Saccharification of kans grass biomass by a novel fractional hydrolysis method followed by co-culture fermentation for bioethanol production," *Renew. Energy*, vol. 146, pp. 750–759, 2020, doi: https://doi.org/10.1016/j.renene.2019.07.016.

[39] M. B. Kongkeitkajorn, R. Yaemdeeka, I. Chaiyota, K. Hamsupo, A. Oraintara, and A. Reungsang, "Bioethanol from Napier grass employing different fermentation strategies to evaluate a suitable operation for batch bioethanol production," *Energy Convers. Manag. X*, vol. 12, p. 100143, 2021, doi: https://doi.org/10.1016/j.ecmx.2021.100143.

[40] P. H. N. Tran, J. H. Jung, J. K. Ko, G. Gong, Y. Um, and S.-M. Lee, "Co-production of ethanol and polyhydroxybutyrate from lignocellulosic biomass using an engineered Saccharomyces cerevisiae," *Renew. Energy*, vol. 212, pp. 601–611, 2023, doi: https://doi.org/10.1016/j.renene.2023.05.080.

[41] Y. D. Singh, "Cellulosic bioethanol production from Eragrostis airoides Nees grass collected from Northeast India," *SN Appl. Sci.*, vol. 1, no. 8, p. 889, 2019, doi: 10.1007/s42452-019-0952-z.

[42] F. Gao *et al.*, "Dilute Alkali Pretreatment and Subsequent Enzymatic Hydrolysis of Amur Silvergrass for Ethanol Production," *Bioresour. Vol 15, No 3*, 2020.

[43] T. L. Springer, "Variation of Agronomic Traits of Ravenna Grass and Its Potential as a Biomass Crop," *Agronomy*, vol. 8, no. 5. 2018, doi: 10.3390/agronomy8050070.

[44] A. Matsushika, H. Inoue, T. Kodaki, and S. Sawayama, "Ethanol production from xylose in engineered Saccharomyces cerevisiae strains: current state and perspectives," *Appl. Microbiol. Biotechnol.*, vol. 84, no. 1, pp. 37–53, 2009, doi: 10.1007/s00253-009-2101-x.

[45] J. N. Nigam, "Bioconversion of water-hyacinth (Eichhornia crassipes) hemicellulose acid hydrolysate to motor fuel ethanol by xylose–fermenting yeast," *J. Biotechnol.*, vol. 97, no. 2, pp. 107–116, 2002, doi: https://doi.org/10.1016/S0168-1656(02)00013-5.

[46] Y. Hideshi, S. Dai, Y. Keiko, M. Saori, Y. Sho, and O. Kenji, "Genetic Engineering of Zymobacter palmae for Production of Ethanol from Xylose," *Appl. Environ. Microbiol.*, vol. 73, no. 8, pp. 2592–2599, Apr. 2007, doi: 10.1128/AEM.02302-06.

[47] S. Dhara, N. S. Samanta, R. Uppaluri, and M. K. Purkait, "High-purity alkaline lignin extraction from Saccharum ravannae and optimization of lignin recovery through response surface methodology," *Int. J. Biol. Macromol.*, vol. 234, p. 123594, 2023, doi: https://doi.org/10.1016/j.ijbiomac.2023.123594.

Chapter 3

KOH pretreatment based high purity alkaline lignin extraction from *Saccharum ravennae* grass and its characterization

In this chapter, the extraction of high-purity alkaline lignin using a KOH-mediated alkaline hydrothermal pretreatment using the oil bath technique is discussed. Lignin recovery was optimized using RSM (response surface methodology) combined with a central composite model. Three process parameters, namely KOH concentration, reaction time, and solid loading, varied to optimize the combined effect of these parameters. The extracted alkaline lignin with the highest purity was characterized using Nuclear Magnetic Resonance (NMR), Fourier Transform Infrared Spectroscopy (FTIR), and X-ray photoelectron spectroscopy (XPS), and the results were compared to commercially obtained alkaline lignin. The background, state-of-the-art literature, and the scope of this research have been described in Chapter 1, Section 1.1.2, 1.3.2, and Section 1.4.2., respectively. This work has been published in the International Journal of Biological Macromolecules.

3.1. Materials and methods

3.1.1 Materials

Saccharum ravennae grass was harvested from the Indian Institute of Technology, Guwahati campus. Raw grass was thoroughly washed to remove mud and soil particles and dried at 75^{o}C in a hot air oven for 36 hours. Dried biomass was ground, sieved (particle size ≤ 150 μm), and stored in a BOPP bag at ambient temperature for further study.

Potassium hydroxide flakes (M.W. -56.11 g/mol), Nitric acid (69%), Dimethyl sulfoxide (99%), and sodium carbonate anhydrous (M.W. – 105.99 g/mol) were procured from Merck Life Science. Sigma-Aldrich, USA supplied Dimethyl sulfoxide-d6. D(+)Glucose, D(+) Xylose, D(+) Galactose, D(+) Cellobiose, L(+) Arabinose, and

Sulfuric acid pure (97%) were purchased from HIMedia Laboratories. Lignin (alkaline) was supplied by TCI Chemicals, Japan. Gallic Acid (3,4,5- Trihydroxy benzoic acid, 99%) was purchased from Sisco Research Laboratories, and the FCP reagent was bought from Spectrochem, India.

3.1.2 Lignin extraction

The delignification was carried out using 1-3% KOH solution where solid loading was varied from 5-15% at 100^{o}C oil bath for 50-200 minutes. After pretreatment, at ambient temperature, samples were allowed to cool. The pretreated solution was vacuum-filtered using the Buchner funnel and Grade-1 Whatman filter paper. The delignified retentate solid was washed with deionized water until pH 7 was achieved. Collected filtrate (black liquor) treated with 6M HNO_3 solution to precipitate lignin. Lignin begins to precipitate at pH 2. The deposited lignin mixture was centrifuged at 10000 rpm for 5 minutes, washed with warm water, and again centrifuged at the same condition. Centrifuged samples were dried at 60^{o}C until a constant weight was attained. Dried lignin samples were powdered and stowed at ambient temperature.

3.1.3 Experimental design

The influence of independent factors on the intended dependent variables was evaluated through experiments with the Design-Expert program (Version 7.0.0) utilizing a CCD face-centered model. A few exploratory experiments were conducted to regulate the upper and lower limits of the specified process parameters. To shorten the pretreatment time, the highest time limit was established. Similarly, the highest limit for KOH concentration was set so that the leaching of hemicellulose could be prevented. The ideal KOH concentration must exceed the upper limit value. However, owing to the unwanted leaching of hemicellulose, any additional KOH concentration increase is not considered practical. Furthermore, the experimental design is built on the basis of solid loading (wt%) of the biomass in the KOH solution. The experimental design allows for a limited number of runs with values that exceed the defined upper and lower value boundary limitations. This is a significant benefit of the CCD-based RSM [1].

The independent variables range was defined using the face-centered central composite design of experiments (1-3% KOH concentration, 50-200 min for the duration, and 5-15 % solid loading wt.%) (**Table 3.1**).

Table 3.1- Central Composite Design (CCD) of 15 sets matrix of alkaline pretreatment and their responses.

Sl no	Independent variables			Dependent variables	
	KOH concentration wt.%	Solid loading wt.%	Pretreatment time (min)	Solid recovery wt.%	Lignin recovery (g/100g of raw biomass)
S1	1	15	50	77.46	0.72
S2		15	200	74.43	0.75
S3		10	125	64.68	6.24
S4		5	50	57.75	10.01
S5		5	200	52.15	13.576
S6	2	15	125	58.38	7.57
S7		10	50	51.88	12.07
S8		10	125	51.01	14.20
S9		10	200	48.1	13.36
S10		5	125	45.34	14.175
S11	3	15	50	49.75	13.18
S12		15	200	51.24	9.668
S13		10	125	45.59	15.297
S14		5	50	46.55	13.652
S15		5	200	42.11	14.317

The upper and lower process parametric ranges were varied in terms of +1 or -1 levels, as mentioned in **Table 3.2**. The analysis of variance (ANOVA), statistical regression analysis, and 3D model graphs were performed using the Design-Expert 7.0 software to assess the model's suitability, the significance of the variables under study, and the variable interactions in regard to lignin recovery. RSM was used to optimize lignin extraction from alkali pretreatment and solid recovery at the same time after getting data

from all the response variables and subsequent fitting of acceptable models. The design expert software explored alternative cubic, two-factor interaction, linear, two-factor interaction, and quadratic models. The best alternative model has been established on the F-value (most desired) and p-value (least preferred).

Table 3.2- The real and coded independent variables used in CCD optimization

Symbol	Variables	Levels		
		-1	**0**	**+1**
A	**KOH Concentration (%)**	1	2	3
B	**Reaction time (min)**	50	125	200
C	**Solid loading (%)**	5	10	15

3.1.4 Characterization of Extracted Lignin

3.1.4.1 Purity of extracted lignin

A modified version of the technique used by Davila et al. (2017) was used to measure the content of sugars, acid-soluble lignin (ASL), and alkaline lignin present in extracted lignin samples [2]. Alkali-extracted lignin contains monosaccharides and acid-soluble lignin as impurities. Two stages of acid hydrolysis were done to compute ASL. 500 mg of extracted lignin was subjected to 5 ml of 72% (w/w) H_2SO_4 solution for 1 hour at 30^oC during the first stage. In the second stage, the H_2SO_4 solution was watered down to 12% (w/w) using deionized water and autoclaved at 121^oC for an hour. Samples were hydrolyzed, cooled to ambient temperature, and vacuum-filtered. Retained solid phase after filtration is recognized as AIL (acid-insoluble lignin), indicating the purity of alkaline lignin. Spectrophotometry was used to quantify acid-soluble lignin (ASL) (at 205 nm). In 1M H_2SO_4, filtrate samples were diluted until the absorbance ranged from 0.1 to 1.0. (UV-2600, Shimadzu, Singapore). Eq. (1) was used to compute the absorption, where VF is the filtrate volume, DF stands for dilution factor, Abs250 nm is the absorption, and at 205 nm, the value of lignin extinction coefficient ε is 110 Lcm/g. Prior to acid hydrolysis, the sample weight (g as 100% dry weight) is denoted as DM_i.

$$\%ASL = \frac{Abs_{250nm} \times DF \times VF}{\epsilon \times DM_i} \times 100 \quad (1)$$

The concentration of disaccharides (cellobiose) and monosaccharides in the hydrolysis filtrate was quantified by HPLC (Prominence, Shimadzu, Singapore). The mobile phase (flow rate of 0.6mL/min) was 0.01 M H_2SO_4 produced with deionized water. High-purity standard sugars from Himedia were utilized for calibration.

3.1.4.2 Total Phenolic content

Through the Folin-Ciocalteau (F-C) technique with DMSO (dimethyl sulfoxide) as the solvent and gallic acid as a reference component, the total phenolic content (TPC) of the lignin samples was measured. Six distinct concentrations (10–100 mg/L) of gallic acid in DMSO were used to generate the calibration curve. Lignin solutions of 2g/L in DMSO were made to quantify the total phenolic content. Prepared lignin samples were diluted with DMSO solution until the absorbance was between 0.1-1. 500 µL of each diluted lignin sample was assimilated into 2.5 mL F-C reagent (10% v/v) and 2 mL Na_2CO_3 solution (20% w/v). The solutions were kept in the dark at ambient temperature for two hours. The absorbance of lignin at 750 nm was noted against the blank with the same solvent. TPC in lignin was calculated as % of gallic acid. The concentration of gallic acid in lignin samples (C_{GA}) was stated as mg/L of dissolved gallic acid.

$$C_{GA} = \frac{A_{750}}{M_{cal}} \times \text{DF} \quad (2)$$

A_{750} represents the absorbance at 750 nm, while M_{cal} represents the slope of the calibration curve, and DF is the dilution factor. Total phenolic content was also calculated by comparing the gallic acid concentration in the dried lignin sample (percent GAC on a dry basis) to the lignin content (CL_{sample}) in the sample solution (reported as g/L).

$$GAC = \frac{C_{GA}}{CL_{sample}} \times 100 \quad (3)$$

3.1.4.3 Analytical Procedures

Compositional analysis of raw (RB) and pretreated (PTB) biomass was performed according to the National Renewable Energy Laboratory (NREL) protocols [3]. CHNS elemental analyzer Eurovector EA3000 was used to obtain the elemental composition of biomass and lignin samples in mass %. The proportion of oxygen in the samples was obtained by deducting the contents of C, H, N, and S in mass % from 100.

The surface morphology of raw biomass significantly changes as lignin is removed from the lignocellulosic matrix. Untreated, pretreated biomass, extracted lignin, and commercial lignin were subjected to a scanning electron microscope (SEM) by placing them on stubs using non-conducting carbon tape. Before analysis, all the samples were dried overnight. SEM images were obtained using Gemini 300 Field Emission Scanning Electron Microscope (Carl Zeiss). Palladium was sputter coated onto samples to increase conductivity.

Thermogravimetric analysis of raw biomass, delignified biomass, extracted lignin, and commercial lignin was carried out using TG 209 F1 Libra TGA/SDTA analyzer (M/s Netzsch, Germany). The mass loss characteristic of the samples during the thermal degradation process was evaluated (25-800 °C) in an N_2 atmosphere(10 °C/min heating rate).

The FTIR analysis of biomass samples, extracted, and commercial lignin was carried out using Shimadzu IR Affinity-1. A ceramic infrared (IR) source is embedded in the device. Spectra were recorded with a maximum resolution of 0.5 cm^{-1} in the 4000-400 cm^{-1} scanning range.

The X-ray powder diffraction was performed in a Smartlab 9KW Powder X-Ray Diffraction System (Rigaku Technologies, JAPAN) with Cu-kαl filter radiation (λ = 1.5406Å). The samples were analyzed at a scanning rate of 6º/min, with 2θ ranging from 4º to 60º at room temperature.

Variations in the structure of extracted lignin and commercial lignin were evaluated by ^{13}C and ^{1}H NMR analyses. In DMSO-d6, the samples of lignin were dissolved. The

spectra were recorded on an AVANCE III HD 600 MHz NMR Spectrometer at 25 °C and 125 MHz. Glycin with a carbonyl peak concentration of 176 ppm was used to indirectly calibrate ^{13}C chemical shifts. With DMSO serving as an internal standard, the chemical shifts of the ^{1}H NMR spectra were calibrated. For the ^{13}C dimensions, the spectral width was 25,000 Hz, whereas for ^{1}H, it was 10,000 Hz.

X-ray Photoelectron Spectroscopy was used to assess the purity and hydroxyl content of lignin samples. Extracted and commercial lignin sample was analyzed using PHI 5000 VersaProbe III Photoelectron Spectrometer (ULVAC-PHI, Inc, Japan). 200 eV pass energy was used to acquire survey spectra with binding energies ranging from 1200 to 2 eV at intervals of 1.0 eV. C1s and O1s high-resolution region spectra were obtained using an analyzer pass energy of 55 eV at 0.05 eV intervals in the 281-292 eV and 528-540 eV ranges, respectively.

3.2 Results and Discussion

3.2.1 Elemental analysis of biomass and lignin samples

The biomass was characterized before and after alkali pretreatment (3% KOH, 10% solid loading, 125 minutes) to determine cellulose, hemicellulose, lignin, extractives, and ash content. Wt. % of these constituents are given in **Table 3.3.** After pretreatment, the composition changes are primarily due to the removal of lignin and hydrolysis of cellulose and hemicellulose fractions, resulting in a low solid recovery percentage. After pretreatment, cellulose content in biomass increased significantly due to the partial hydrolysis of hemicellulose and removal of lignin. Due to the impact of the alkali on the ester linkages and glycosidic chains, the KOH pretreatment enabled a high lignin removal. The enhanced porosity of the biomass and the cellulose accessibility have been associated with this effective lignin removal.

Table 3.3. Composition of raw (RB) and alkali pretreated (PTB) Ravenna grass biomass (wt.%).

Sample	Cellulose	Hemicellulose	Lignin	Extractives	Ash	Moisture
RB	33.68±0.55	19.85 ±0.77	27.43±0.61	4.74±0.21	6.91±0.22	6.45±0.29
PTB	48.54±1.01	25.17±0.82	5.7±0.36	1.70±0.37	5.31±0.14	7.87±0.63

The Elemental analysis of raw *Saccharum ravennae* grass biomass (RB) and lignin fractions reflects their chemical composition (**Table 3.4**). Elemental analysis shows that the RB has high carbon (46.228%) and oxygen (40.391%) content. The hydrogen concentration of biomass ranges typically from 3% to 11% (6.3% on average), which is greater than the fossil fuel average (5.4%) [4]. With a calorific value more significant than that of carbon, hydrogen is the 2_{nd} most abundant combustible element. The *Saccharum ravennae* grass biomass had a hydrogen content of 12.556%, increasing the calorific value of the biomass. The presence of nitrogen (0.825%) in the biomass implies that it has relatively little protein. During the delignification process, the proteins that were typically linked to lignin in the raw plant material were also removed. On the other hand, the absence of sulfur in the RB makes it suitable for clean biofuel production.

Table 3.4 also represents the elemental compositions of the commercial (CL) and extracted (EL) lignin. It can be observed that the amount of carbon was almost the same in both the lignin samples. However, the amount of oxygen is lower in CL samples, resulting in a low O/C ratio (0.41) compared to the EL sample (0.61). A Low O/C ratio indicates a less calorific value of the lignin samples as a fuel. However, EL has a significant portion of nitrogen (3.472%), whereas the CL sample has a very tiny amount of nitrogen (0.050%), probably because the HNO_3 solution was used to precipitate lignin fractions from alkali pretreated black liquor filtrate, and also have protein residues. The CL sample has 3.096% sulfur, resulting from the acid hydrolysis or extraction process of CL. It is also possible that the source biomass of CL has a high amount of sulfur.

Table 3.4- Elemental composition of raw biomass and lignin samples

Element	RB	EL	CL
Carbon (wt%)	46.228	52.310	54.947
Oxygen(wt%)	40.391	32.00	22.829
Hydrogen(wt%)	12.556	12.218	9.778
Nitrogen(wt%)	0.825	3.472	0.050
Sulfur (wt%)	–	–	3.096

3.2.2 Experimental design of alkaline pretreatment

The Central composite design matrix comprising 15 trials is shown in **Table 3.1**, together with the statistical responses of the three dependent variables. ANOVA was used to assess the fit of each model. The model is competent, as evidenced by the high coefficient of determination values (0.9828-0.9983) for the examined responses. For the assessed variables, predicted vs. actual plots are shown in **Fig. 3.1**. A good model fit is indicated by the rectangles clustering around the diagonal line. The model was statistically significant, as demonstrated by the F-values of 318.52 for solid yield and 31.76 for delignification, respectively. A second-order polynomial equation predicted the connections among the variables and the response of solid and lignin recovery in the response surface model:

$$Y_1 = 50.49 - 9.12A - 1.54B + 6.74C + 0.71AB - 3.71AC + 1.06BC + 4.78A^2 - 0.37B^2 + 1.50C^2 \quad (4)$$

$$Y_2 = 12.95 + 3.48A + 0.20B - 3.38C - 0.81AB + 2.12AC - 0.96BC - 1.86A^2 + 0.083B^2 - 1.76C^2 \quad (5)$$

Where Y_1 and Y_2 are predictive responses (solid and lignin recovery), A, B, and C represent KOH concentration, reaction time, and solid loading. The negative and positive signs ahead of the variables denote antagonistic and synergistic impacts, indicating the effect of independent factors on responses [5].

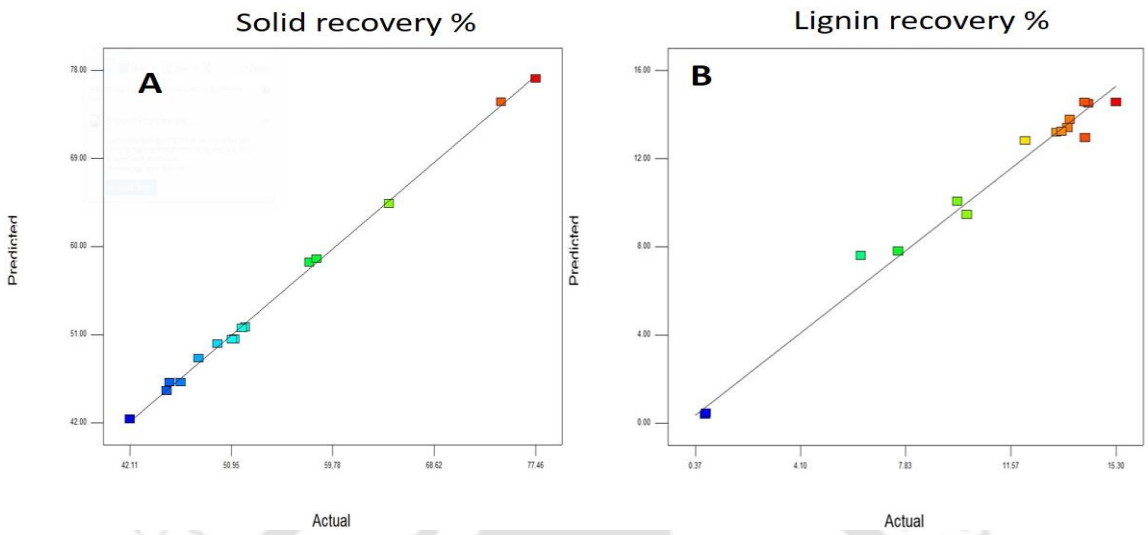

Figure 3.1: Comparison of predicted vs. actual experimental data corresponding to (A) Solid recovery and (B) Lignin recovery.

3.2.2.1 Impact of Independent variables on the solid recovery

Solid recovery varied from 77.46% (S1) to 42.11% (S15), as shown in **Table 3.1**. High KOH concentration during pretreatment solubilizes lignin, hemicellulose, and extractives, causing lower solid recovery. As a result, at 3% KOH concentration (S11-15), maximum delignification and less solid recovery were observed. Alkaline pretreatment mainly removes acid-insoluble compounds from lignocellulosic biomass. Still, it also promotes swelling of cellulose and partial loss of it along with hemicellulose and a small amount of acid-soluble lignin.

Considering the linear and interaction effects of the reaction time, solid loading, and the KOH concentration, the quadratic effect of all three variables significantly influenced the solid recovery. The findings of this work did not coincide with those of Morales et al. (2018) [6] and Noor et al. (2020) [5]. They found that retention time and solid loading were insignificant parameters compared to the alkaline percentage concerning the solid recovery. The influence of two variables when the third variable was set to the midpoint value is displayed in **Fig. 3.2**.

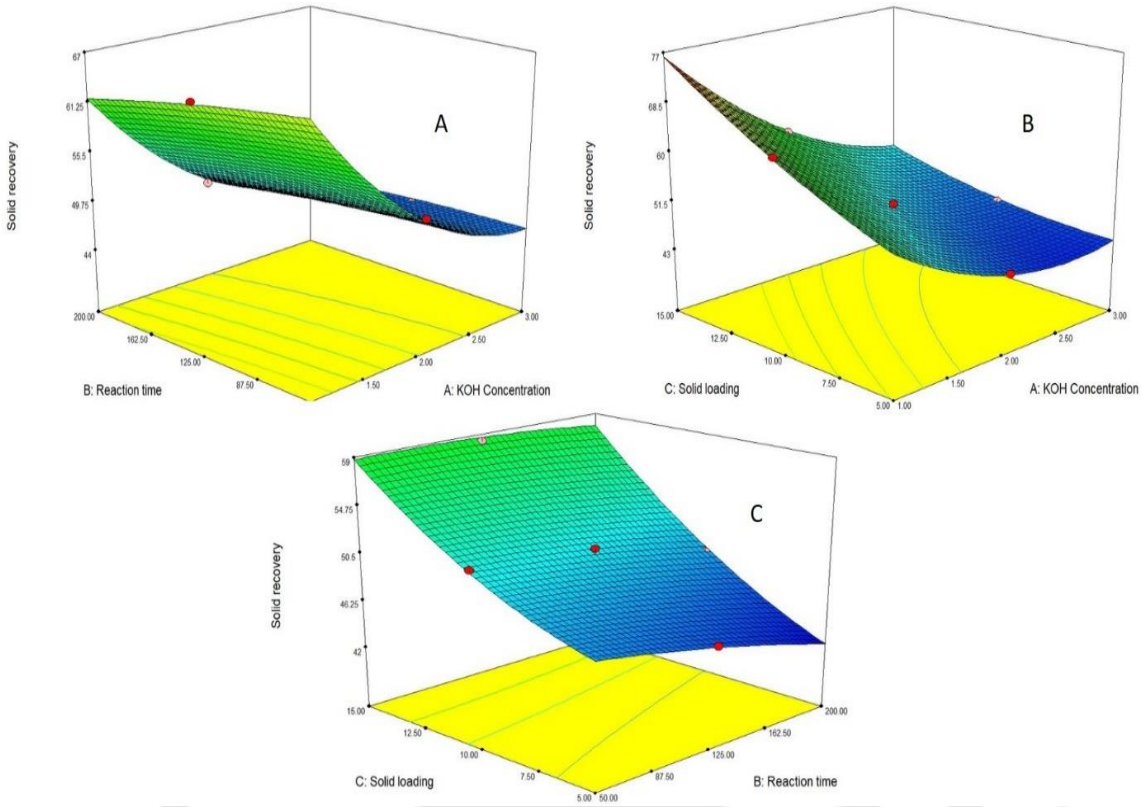

Figure 3.2. 3-dimensional analysis of the combined effect of (A) KOH concentration vs. Reaction time at a fixed solid loading (10%), (B) KOH Concentration vs. Solid loading at a fixed reaction time of 125 minutes, and (C) Solid loading vs. Reaction Time at a fixed 2% KOH concentration on the solid recovery.

With increasing reaction time, KOH concentration, and decreasing solid loading, the solid yield decreased dramatically. The ability to solubilize the structural constituents of the raw biomass was enhanced drastically under harsh pretreatment conditions. Consequently, it follows that the mildest operational condition of the model was able to generate the highest solid yield.

3.2.2.2 Impact of Independent variables on Lignin recovery

The amount of delignifying agent employed will significantly impact the lignin removal process. Given the complexity of lignin, significant effort must be put into breaking down the complex bonds. For that, different percentages of KOH were used to treat the

Saccharum ravennae grass biomass in the current study. With an increase in KOH %, lignin recovery from raw biomass increased. As the alkaline concentration rose from 1% to 3%, the rate of lignin recovery increased progressively. Degradation in the biomass texture was severe after pretreatment with a 3% KOH solution, which indicates lignin was removed from the lignocellulose matrix. The lignin recovery from 5% solid loading decreased by almost half when it increased to 10%. Nevertheless, the rise in solid loading to 15% resulted in nearly six times a fall in lignin recovery during 1 % KOH treatment. Different energy collisions occur between solvent and substance in different solid loading percentages. At low solid loading concentrations, surface interaction increases between particles, resulting in a higher lignin recovery. Biomass is subjected to thermal and non-thermal impacts during hydrothermal pretreatment, which causes an explosive reaction in the biomass particles, disrupting the surface of the lignocellulose matrix and rupturing the bonds between the lignin-hemicellulose matrix. As shown in **Fig. 3.3B**, at a fixed reaction time and with an increasing KOH concentration, lignin recovery will increase if the solid loading percentage decreases. However, at 3% KOH treatment, maximum lignin recovery was observed with 10% solid loading. Further fall in solid loading percentage resulted in a decrement of lignin recovery. The summary of the data shows that a solid loading of 10% is adequate to recover a significant amount of lignin.

The breakdown of complicated bonds and their elimination depend greatly on the reaction time, in addition to KOH concentration and solid loading. As seen in **Fig. 3.3A**, the administered concentration of KOH steadily accelerated the rate of removal percentage of lignin from biomass as the reaction time increased. This could be because as contact time gradually increases, the delignifying agent has more opportunity to break more lignin bonds without altering the concentration of KOH, creating proportionally larger cavities on the biomass surface. It has been previously noted that as reaction time increases, the alkali tends to have more chances to interact with lignin [7].

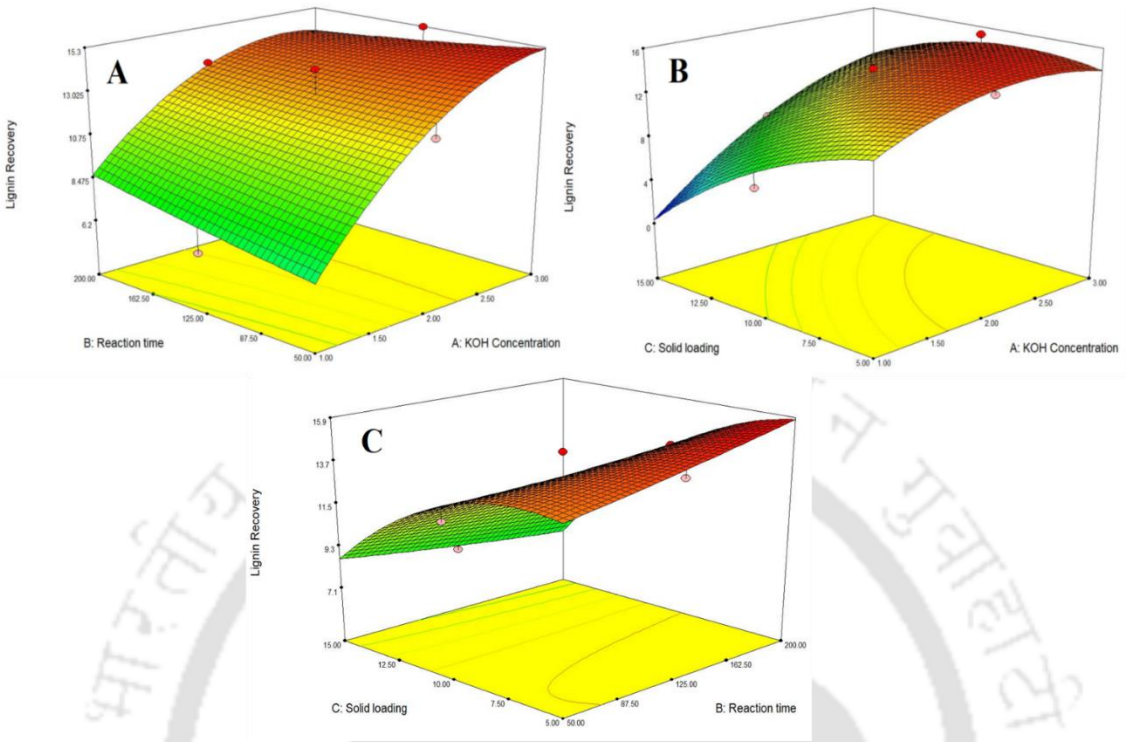

Figure 3.3: 3-dimensional analysis of the combined effect of (A) KOH concentration vs. Reaction Time at a fixed solid loading (10%), (B) KOH Concentration vs. Solid loading at a fixed reaction time of 125 minutes, and (C) Solid loading vs. Reaction Time at a fixed 2% KOH concentration on the lignin recovery.

3.2.2.3 Statistical analysis

Table 3.5 provides an overview of the ANOVA statistics for the quadratic model for lignin recovery. To better comprehend the connection and impact of the various factors on the response, all of the data in Table 1 were further evaluated (Y). The model F value of 31.76 in Table 5 indicates that the quadratic model was significant. There is a mere 0.07% possibility that a "Model F-value" this big could exist due to noise. If the p-value of the variable model is less than 0.05, the variable model is deemed significant. Additionally, it was shown that the linear terms of KOH Concentration (A) and Solid Loading (C) had substantial effects on lignin recovery, with respective F-values of

110.08 and 104. With an F-value of 0.38, reaction time (B) does not substantially affect the lignin recovery. The lignin recovery is unaffected by the interaction between factors AB. However, the variable interactions AC and BC have a substantial impact, with a p-value below 0.05.

Table 3.5: Statistical analysis for computed lignin recovery from *Saccharum ravennae* grass biomass

ANOVA for quadratic equation model developed for lignin recovery						
Source	**Sum of Squares**	**df**	**Mean Square**	**F Value**	**p-value Prob > F**	
Model	314.76	9	34.97	31.76	0.0007	significant
A-KOH Concentration	121.23	1	121.23	110.08	0.0001	
B-Reaction time	0.42	1	0.42	0.38	0.5658	
C-Solid loading	114.53	1	114.53	104.00	0.0002	
AB	5.19	1	5.19	4.71	0.0821	
AC	36.10	1	36.10	32.78	0.0023	
BC	7.44	1	7.44	6.75	0.0483	
A^2	8.93	1	8.93	8.11	0.0359	
B^2	0.018	1	0.018	0.016	0.9040	
C^2	7.96	1	7.96	7.23	0.0434	
Residual	5.51	5	1.10			
Cor Total	320.27	14				

With an F-value of 8.11, 0.016, and 7.23, respectively, the quadratic terms of KOH Concentration (A^2), reaction duration (B^2), and solid loading (C^2) had negligible influence on the recovery of lignin. From the overall observations, KOH Concentration (A) and solid loading (C) were the most significant variables for the effective lignin recovery, owning to their high F value (110.8 and 104) and low p-value (0.0001 and 0.0002).

Table 3.6: Statistics related to the developed quadratic model for lignin recovery

Std. Dev.	1.05	**R-Squared**	0.9828
Mean	10.59	**Adj R-Squared**	0.9519
C.V. %	9.91	**Pred R-Squared**	0.8831
PRESS	37.44	**Adeq Precision**	16.573

The regression equation and the determination coefficient (R^2) were examined to see if the model was fit for its purpose. The sample variance of 98.28 % lignin recovery was ascribed to the independent variables, according to the determination coefficient value (R^2= 0.9828), and the model could not describe only 1.72% of the overall variation. The "Pred R-Squared" of 0.8831 and the "Adj R-Squared" of 0.9519 are reasonably in agreement. (**Table 3.6**). The high adjusted determination coefficient value supports the high significance of the model. The signal-to-noise ratio is measured using "Adeq Precision." A ratio of at least four is preferred. An effective signal is indicated by a ratio of 16.573. One can utilize this model to explore the design space. To demonstrate the repeatability of the model, the coefficient of variation value (CV) was used to depict the standard error of estimate to mean response value ratio [5]. The model was highly replicable and dependable, as the CV value is less than 10% (C.V.- 9.91%).

3.2.2.4 Optimization of pretreatment conditions for lignin recovery and validation of the model

In this study, response optimization was focused on identifying the delignification settings that would optimize the amount of lignin recovered. The optimum parameters predicted for maximum lignin recovery were at 6.41 % solid loading, a reaction time of 176.57 minutes, and 2.4 % KOH concentration, resulting in 43.041 % solid recovery and lignin recovery of 15.3869 g/100g of raw biomass. Three tests were carried out under optimum conditions to test the validity of the model. **Table 3.7** shows the predicted and experimental outcomes. These experimental values indicate the accuracy and suitability of optimum conditions generated through the central composite design

model of Design Expert software, as it was pretty consistent with the predicted outcomes.

Table 3.7: Predicted and experimental results at optimal conditions of lignin recovery.

	Solid recovery (wt. %)	Lignin recovery (g/100g of raw biomass)
Predicted value	43.041	15.3869
Experimented value	41.92 ±0.44	15.81±0.32

Mean ± standard deviation (SD) of three experimental replications.

3.2.3 Purity of Extracted Lignin Samples

Quantitative acid hydrolysis was used to measure lignin purity and the quantity of contaminants present in the samples to analyze the selectivity of the lignin extraction techniques. Klason lignin (acid-insoluble lignin) was taken into consideration while calculating the measured purities for the derived lignins. The lignin that was successfully extracted under the optimum delignification parameters (3%KOH, 10%solid loading, 125 minutes reaction time) contained 93.7% Klason lignin, 0.99% acid soluble lignin, 1 % cellobiose, 1.02 % xylose, and 0.75% arabinose as depicted in **Table 3.8.** At the mild pretreatment condition (1% KOH_15% solid loading_50 minutes reaction time), recovered lignin has the highest impurities in the form of cellobiose. Cellobiose is a subunit produced by the hydrolysis of cellulose and is soluble in alkali solutions at a given pH range (10.5-13.5) [8]. In mild pretreatment conditions, the pH of the pretreatment solution is low (10-11), where Z of cellobiose is almost zero [8], and it aggregates on the lignin matrix. Increasing KOH concentration or decreasing the solid loading leads to a higher pH value of the pretreatment solution. At high pH levels, cellobiose behaves as an acid and dissociates by deprotonating the OH groups, resulting in a drop in Z to a negative value and an increase in cellobiose solubility. Extracted lignins from harsh pretreatment conditions (High KOH concentration and low solid

loading) have less cellobiose content as solubilized cellobiose gets separated during lignin precipitation through acid treatment and centrifugation.

Table 3.8: Purity, ASL, and sugar content of extracted lignin samples

Sample	Purity (wt.%)	Impurities (wt.%)				
	AIL	ASL	glucose	xylose	cellobiose	arabinose
S1	64.42	1.91	-	-	28.57	-
S2	66.14	2.19	0.17	-	27.91	-
S3	78.53	1.06	1.45	2.75	4.30	1.45
S4	79.11	1.21	-	2.64	4.50	1.54
S5	79.47	1.13	-	1.94	4.91	1.35
S6	80.24	1.04	-	1.8	4.43	1.14
S7	83.06	0.9	-	0.57	5.35	0.23
S8	83.95	1.06	-	0.4	5.10	0.25
S9	88.94	0.66	-	0.25	4.81	0.1
S10	80.13	1.08	0.72	2.39	4.67	1.38
S11	79.08	1.05	-	2.85	4.71	1.41
S12	87.12	1.12	-	2.36	2.76	1.13
S13	93.70	0.99	-	1.02	1.00	0.75
S14	82.44	0.75	-	3.07	3.87	1.51
S15	81.76	0.58	-	3.36	4.19	1.75
OC*	84.02±0.36	1.07±0.07	-	2.55±0.1	4.83±0.29	1.32±0.17

OC*- optimized condition obtained through RSM (176.57 minutes, 6.41 % solid loading, and 2.4 % KOH); Mean ± standard deviation (SD) of three experimental replications.

According to Ana et al. (2013), lignin extracted from olive tree pruning through alkaline pretreatment is impure to a great extent (4.5% ASL) and contains a high amount of

total sugars [9]. A comparable outcome was attained by Morales et al. (2018), where chestnut shells were treated with NaOH solution. Lignin recovered under the optimal delignification condition, comprising 63.5% AIL, 2.13% ASL, and 19.6% sugars (**Table 3.9**) [6]. In another study, Morales et al. (2022) extracted lignin from almond shells with 7.5 % NaOH solution at 121^{o}C, where the purity was less than 59%. However, after autohydrolysis, the purity of the same lignin sample increased to 88.2% [10]. Under alkaline (12% NaOH, 105 min, and 124 °C) conditions, Davila et al. (2017) also investigated the impact of autohydrolysis on the lignin removal from vine shoots [2]. The purity of the obtained lignin was around 90%, but the delignification was lower (67.7%) than in this present study. As the S13 lignin sample shows maximum purity, this lignin fraction was used in the subsequent characterization and analysis processes.

Table 3.9: Literature comparison on extracted lignin purity

Sl no	Substrate	Treatment condition	Reported Purity (wt.%)	References
1	Almond shells	121 °C, 90 min, 7.5 % NaOH, Liquid-to-solid ratio- 6:1	58.2	[10]
2	walnut shells	121 °C, 90 min, 7.5 % NaOH, Liquid-to-solid ratio- 6:1	49.4	[10]
3	vine shoots	124 °C, 168 min, 8 % NaOH, Liquid-to-solid ratio- 10:1	89.9	[2]
4	Chestnut shell	80 °C, 30 min, 7.16% NaOH Liquid-to-solid ratio-10:1	63.5	[6]
5	Ravenna grass	100 °C, 125 min, 3% KOH Liquid-to-solid ratio-10:1	93.7	This study

3.2.4 Total Phenolic content (TPC) of lignin samples

The TPC of the commercial (CL) and all the extracted lignin samples (S1-S15) quantified by the F-C technique are reported in **Table 3.10**. TPC varied from 20.61-54.44 wt.% in the extracted lignin samples, whereas CL exhibits only 11.85%. Extracted lignin showed higher TPC than CL may be due to a more condensed form of

lignin fraction present in CL. Mild alkaline condition (1% KOH) exhibits a fair amount of phenolic groups in lignin samples. A slight increase in KOH concentration (2%) resulted in higher phenolic content in lignin samples, whereas decreasing solid loading (15%- 5%) and prolonging reaction time had a negative effect on TPC.

Table 3.10: Total phenolic content of different lignin samples

Sample name	Pretreatment Condition			C_{GA} mg/L	%GAC
	KOH concentration (wt. %)	Solid loading (wt. %)	Reaction time (min)		
CL	–	–	–	237	11.85
S1	1	15	50	643	32.15
S2		15	200	650.5	32.52
S3		10	125	871	43.55
S4		5	50	917.2	45.86
S5		5	200	740.4	37.02
S6	2	15	125	1088.8	54.44
S7		10	50	952.4	47.62
S8		10	125	941.2	47.06
S9		10	200	933.2	46.66
S10		5	125	866	43.3
S11	3	15	50	735.6	36.78
S12		15	200	767.4	38.37
S13		10	125	786	39.3
S14		5	50	628.8	31.44
S15		5	200	412.2	20.61

But further increment in alkaline percentage (3%) causes a reduction in phenolic amount in lignin. Extreme pretreatments (very alkaline conditions, extended reaction times, and reduced solid loading) accelerated the dissolution of additional components from the raw material, which led to samples of lignin-containing higher levels of contaminants and lower levels of phenolics. Different studies have shown that lignin

derived from alkaline pretreatment contains low phenolic groups [11][12]. On the contrary, in this work, a maximum of 54.44% TPC was achieved without performing any purification process (acid hydrolysis), which might increase the TPC content even further. The lower TPC of the CL sample correlates to lesser phenolic protons in the NMR spectrum. Therefore, compared to the CL sample, the lignin recovered utilizing the alkali treatment may be described as of better quality in terms of functional groups (FT-IR and NMR) and TPC presence.

3.2.5 SEM Analysis

The fiber framework had significant degradation, and the cell walls were swollen, according to SEM pictures of raw biomass and pretreated biomass samples (**Fig. 3.4A, 3.4B**). This suggests that part of the hemicellulose and lignin molecules have been broken down, increasing the cellulose surface area. The pretreatment of the fiber morphology causes the disintegration of the lignin-hemicellulose matrix inside the cell wall. The loss of lignin causes morphological changes in the cell wall, resulting in increased pore diameters at the surface of the biomass fibers. The ether linkages of the lignin-cellulose complex can be damaged by lignin and hemicellulose degradation, which promotes the separation of lignin from the cellulose matrix fibers [13]. Commercial lignin (CL) contains agglomerates and has a wide-ranging particle size distribution, with an average size of 16.5 µm. The extracted lignin (EL) particles had a broad particle size distribution and were spherical in shape, and the size varies from 25 nm to 1 µm. The average particle size of EL was calculated to be 220 nm. There were also some agglomerates consisting of small lignin spheres with smooth surfaces.

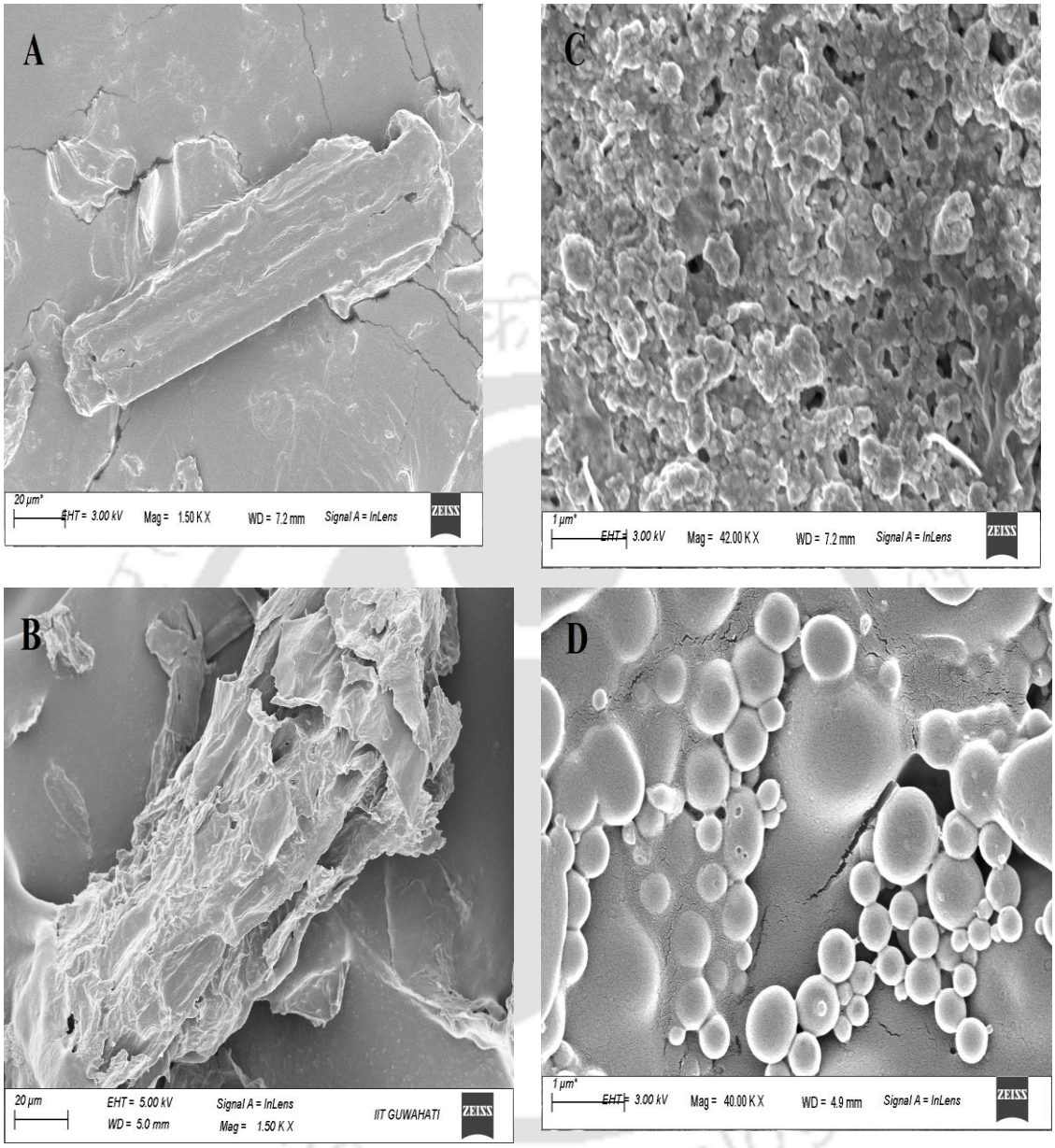

Figure 3.4: SEM images of A) Raw biomass, B) pretreated biomass (3% KOH, 10% solid loading, 125 minutes), C) commercial lignin, D) extracted lignin (3% KOH, 10% solid loading, 125 minutes)

3.2.6 TGA analysis

The thermal stability of lignin is another crucial quality to consider, particularly given its usage in the fabrication of composite materials, polymeric membranes, and thermochemical conversion into chemicals and energy. Therefore, the samples of lignin

and biomass were thermogravimetrically assessed to investigate and understand the thermal degradation of chemical structures. **Fig. 3.5** shows the thermogravimetric curves of commercial and extracted (3% KOH, 125 min, 10% solid loading) lignin and biomass samples. There are four major phases to the thermal decomposition of the lignocellulose samples.: (1) In this stage, moisture and very light volatile components removal occur below 110 °C. Raw biomass loses 3% mass in the form of moisture, whereas the Pretreated biomass sample loses 4.5 % mass in terms of moisture and volatile components produced during the pretreatment of biomass. (2) Degradation of hemicellulose takes place in this stage (220–300 °C for RB, 240–330 °C for PTB); (3) cellulose and lignin decomposition (RB-300–370 °C, PTB-330–395 °C) and (4) lignin degradation (> 410 °C). Between 300–400 °C, PTB loses almost 54 wt.% as lignin has been removed through pretreatment, whereas RB loses only 36% weight as it contains more lignin than PTB, and lignin is thermally more stable than cellulose.

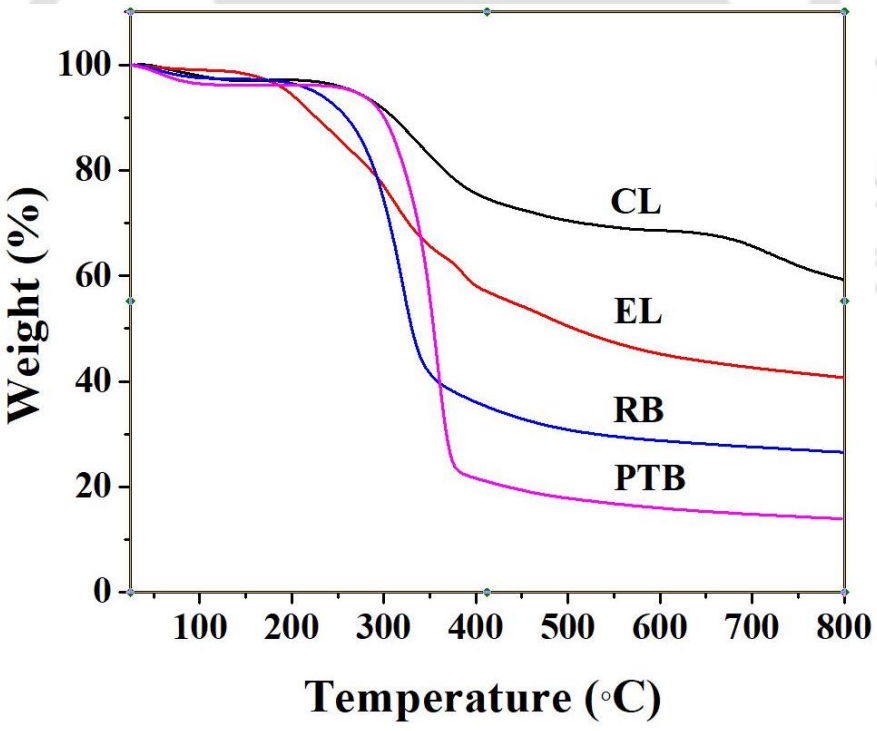

Figure 3.5: Thermogravimetric analysis graph of RB-raw biomass, PTB- pretreated biomass, EL-extracted lignin, CL-commercial lignin

The functional groups of lignin impact the rate of lignin thermo-decomposition [14]. Accordingly, increased initial decomposition (200–400 °C) might be linked to the bending of the weaker linkages in the β-O-4 structure. Afterward, breakdowns are related to the side-chain oxidation of lignin. Degradation may occur over 500 °C due to lignin C-C bond breaking. Alkali lignin undergoes only two thermal degradation stages: dehydration and lignin breakdown. The lignin samples had an early stage of weight loss of 2–3% below 130 °C, which was caused by the water and low molecular weight volatiles evaporation from the sample. Then, the second stage of deterioration between 200 and 500 °C was noticed, which was related to severe lignin degradation. In this temperature range, it was anticipated that most of the ether bonds would cleave. In the second stage, side-chain oxidation and dehydrogenation of lignin, along with carboxylation and carbonylation of aliphatic hydroxyl groups, took place [15]. The final stage occurred after 500 °C, which involved C-C bond breakdown and the cleaving of the methoxy groups. Concurrently, the aromatic ring breakdown takes place. Small quantities of char remnants are eventually generated. The remnant char contents of CL and EL alkali lignins, as shown in **Fig. 3.5**, were 59% and 41%, respectively, which is somewhat connected to the G/S unit ratio of alkali lignin. Because G is more thermally stable compared to the remaining lignin monomers, the higher the fraction of G, the more char that persists. However, the difference between the remnant char concentration of CL and EL is very high, probably due to degraded lignin fractions present initially in the CL sample. Between 600–700 °C, a small mass gain can be seen in the CL sample, where the condensation reaction of aromatic rings occurs.

3.2.7 FTIR Analysis

The structural differences between extracted and commercial lignin and the structural alterations in lignocellulosic material following pretreatment with KOH were determined using the FTIR analysis. FTIR observations can offer qualitative and quantitative statistics for compositional analysis of lignin and biomass samples. The peak intensity drop indicates the modified or disturbed functional groups. The IR absorption spectra of extracted and commercial lignin, the raw and pretreated biomass components recorded within the range of 4000-400 cm^{-1} [16], are shown in **Fig. 3.6**.

The wide band in the biomass samples around 3342 cm^{-1} reflected the hydrogen bonding and stretching vibration of the hydroxyl group [17]. The bands at 2853 and 2921 cm^{-1} were associated with C-H stretching vibrations in methylene and methyl groups, respectively. The absence of these peaks indicated most of the syringyl and guaiacyl methoxy groups in the commercial lignin were broken. C-H bending vibrations in the same groups mentioned earlier made up the band at 1456 cm^{-1}. A very weak band at 2360 cm^{-1} can be seen for C-H aldehyde stretching [18].

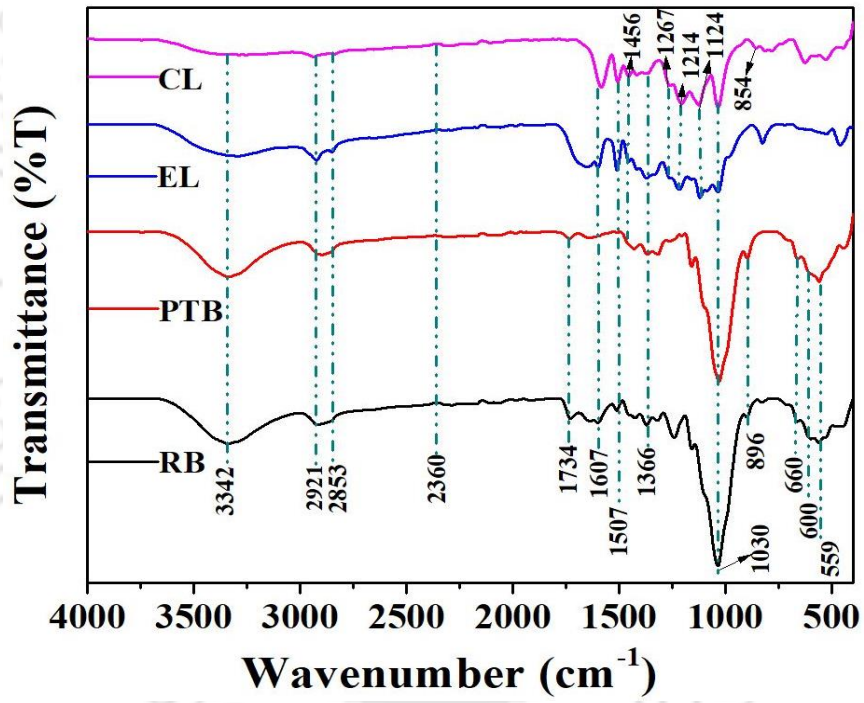

Figure 3.6: FTIR spectra of CL-commercial lignin, EL- EL-extracted lignin, PTB-pretreated biomass, RB- raw biomass

The C=O vibration in hemicellulose or the acetyl and p-coumaroyl groups in lignin was mainly attributable to the band at 1734 cm^{-1}, showing that ester bonds were disrupted in lignin. The non-appearance of this band in the commercial lignin (CL) sample suggests an absence of hemicellulose impurity. The C=C stretching and the ring stretching of the lignin benzene ring skeleton are visible at 1607 and 1507 cm^{-1}, respectively. The

diminution in the strength of those absorption bands in the PTB sample suggested that free radicals degraded the benzene ring structure of lignin [19]. After KOH treatment, a lessening of the intensity of the In-plane deformation vibration of the phenolic hydroxyl group and the CH_3 peak (1366 cm^{-1}) of the biomass samples occurs. Only in the lignin samples spectrum does the band at 1267 cm^{-1} exist, linked to the C-O stretching of the guaiacyl ring. When depolymerization occurs, the -C-O-C bonds break, as can be seen by carefully observing that the band intensity at 1214 cm^{-1} caused by alkoxy groups has diminished in the PTB spectrum. The existence of C-H bond vibrations in the syringyl ring is shown at 1124 cm^{-1} in the CL and EL spectrum despite its low intensity. The C-O stretching vibration in lignin, hemicellulose, and cellulose is associated with a sharp peak at 1030 cm^{-1}. It could also correspond to the in-plane C-H stretching vibration of the guaiacyl ring [20]. Bands between 900 and 820 cm^{-1} were related to the out-of-plane C-H bending deformation of S and G units [6]. C-O-C stretching at the β-glucosidic bonds in cellulose and hemicellulose induces the intensity of the bands at 896 cm^{-1} of RB and PTB. The small bands between 660 and 559 cm^{-1} correspond to the C–OH bending and C–H stretch vibration of the cellulose and lignin matrix [21].

3.2.8 XRD Analysis

The XRD spectra of the raw (RB) and pretreated biomass (PTB) are shown in **Fig. 3.7**. The crystalline structures of cellulose I (101) and (002) were responsible for the primary diffraction peaks of 15.92° and 22.08°, respectively [19]. The crystallinity index of pretreated (3%KOH, 10% solid loading, 125 minutes) biomass was 41%, higher than the raw biomass (35%). The Crystallinity % was calculated using the equation given below.

$$\%\ Crystallinity = \frac{Area\ of\ all\ the\ Crystalline\ peaks}{Area\ of\ all\ the\ Crystalline\ and\ amorphous\ peaks} \times 100 \qquad (6)$$

The amount of crystalline cellulose increased because of the fractional breakdown of amorphous lignin and hemicellulose extraction upon pretreatment, enhancing the crystallinity of the PTB sample. In comparison to the extracted lignin (EL), the XRD pattern of commercial lignin (CL) exhibits high intensity with a large, amorphous area

(2θ = 22.9°), indicating that the EL particles have a lower crystallization degree than the CL sample. It is most likely owing to the smaller particle size of nanoparticles and plasticization instigated by moisture sorption from the environment. The sharp peaks at 21° in the EL samples are responsible for the crystalization phase of the alkaline lignin. In contrast, intense signals at 19, 23, 31, and 35° are a feature of the crystalline regions of cellulose [10] and hemicelluloses [22], which confirms the presence of impurities in the EL sample.

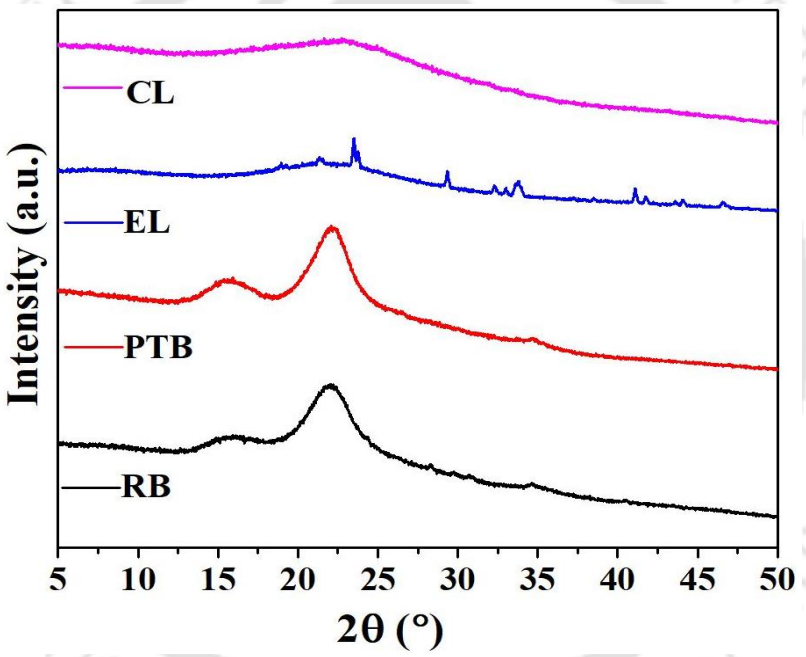

Figure 3.7: XRD analysis of biomass and lignin samples

CL- commercial lignin**, EL**- extracted lignin**, PTB**- pretreated biomass**, RB**-raw biomass

3.2.9 ^{1}H and ^{13}C-NMR Analysis

^{1}H and ^{13}C analyses were performed to study the structural differences between extracted and commercial alkaline lignin. ^{1}H spectrums of both the lignin samples are

shown in **Fig. 3.8**, where the signals between 10-8 ppm account for H in the aldehyde and hydroxyl groups [23]. DMSO-d6 and H_2O produced the two signals at δ_H 2.53 and 3.49 ppm, respectively. The aromatic cations in G and S units in lignin were exhibited by peaks between 8 ppm and 6.5 ppm. In the extracted lignin sample, signals ranging from 6.8 ppm to 6.2 ppm corresponded to syringyl-propane and guaiacyl-propane units. The most frequent bond between lignin units, the β-O-4 ether bond, only displayed a faint resonance around 4.33 ppm in the EL spectra. It implied some degree of breakdown in the separated lignin from black liquor. Whereas, in CL spectra, Hα and Hβ protons of β-O-4 linkages are absent, which might be due to the complete breakdown of those bonds during acid hydrolysis. The aromatic rings containing aliphatic protons in their side chains are thought to be responsible for the peak between 4.2 and 6.2. Methoxyl protons in both the lignin fractions cause significant changes between 4.0 and 3.5 ppm [23]. The relative abundance of acetylated phenolic hydroxyl and alcoholic hydroxyl group signals ranged from 1.7 to 2.4 ppm, attributable to the release of some of them during lignin breakdown via ether linkage breaking [24]. Protons in the methyl and methylene side chains of lignin contributed signals ranging from 1.6 ppm to 0.7 ppm. EL and CL spectra demonstrate almost similar peaks, but the intensity of the signals is higher for EL sample spectra. The intensity of NMR signals is proportional to the molar concentration of the sample. The integrated intensity of a signal in a ^1H NMR spectrum gives a ratio for the number of hydrogens that give rise to the signal. It indicates that although both lignin samples have similar functional groups, the extracted lignin has a higher number of functional groups than the commercial alkaline lignin. This result signifies the higher TPC content of the extracted lignin sample.

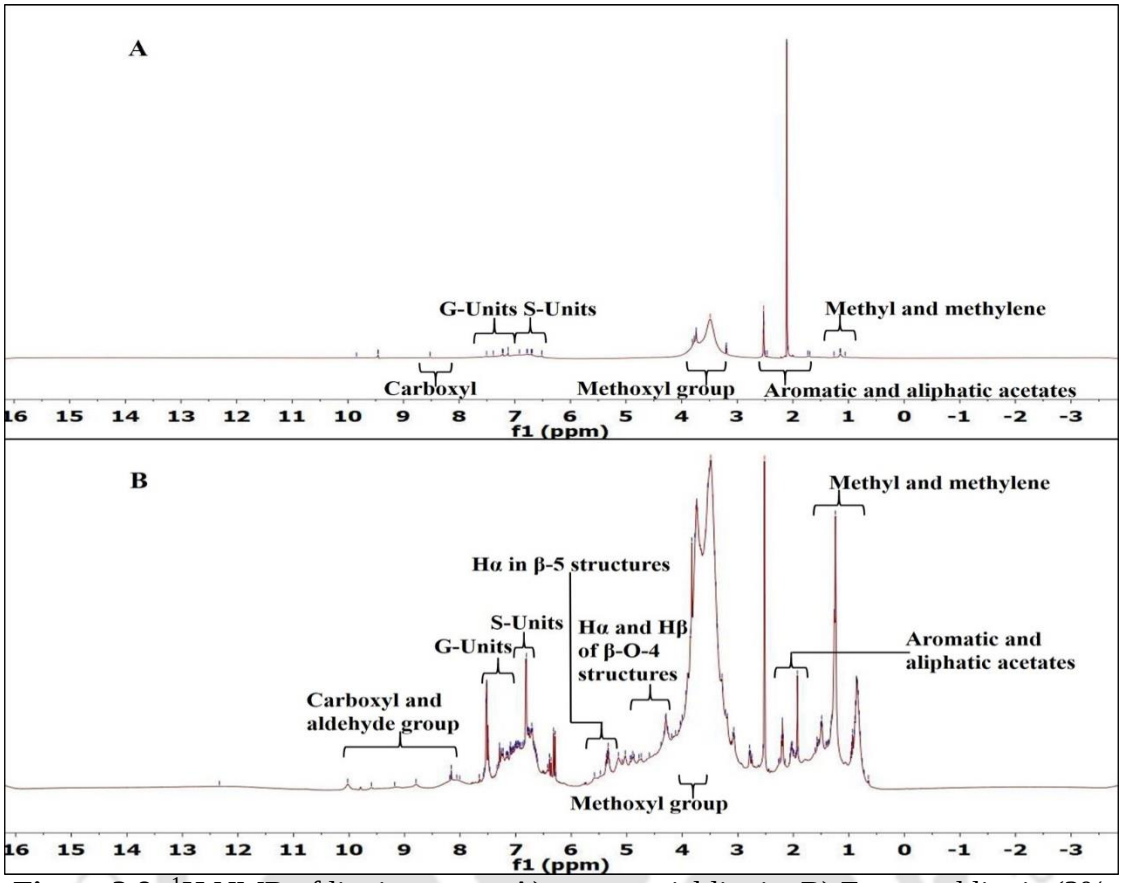

Figure 3.8: ^{1}H NMR of lignin spectra A) commercial lignin, B) Extracted lignin (3% KOH, 125 min, 10% solid loading)

As can be seen in **Fig. 3.9**, ^{13}C NMR was also utilized to examine the chemical composition of lignin fragments. Spectra appeared at 207 ppm in the commercial lignin sample, indicating the presence of carbonyl groups. Aliphatic COOR is responsible for signals in extracted lignin spectra between 177 and 168 ppm. S, G, and H units were shown to be prevalent signals in the aromatic area between 100 and 160 ppm linked to the lignin-forming units that can only be seen in extracted lignin samples. The C_3 and C_4 etherified carbon of G units gave signals at 148 and 149 ppm, whereas peaks at 145.2 and 144.7 indicate the presence of C_4 of G-CH_2 and C_α of the p-coumarate (PCA) unit, respectively [25][26]. Peaks between 127-130 ppm are responsible for $C_{2,6}$ of p-hydroxyphenyl units. At 125 and 123 ppm, signals for C_5 of the guaiacyl and C_6 of ferulate (FA) units have emerged. Three distinct signals around 116 ppm are referred to as C_3 and C_5 in the p-coumarate unit and C_5 of the guaiacyl ring. The lignin sample

contamination with polysaccharides is linked to signals between 90 and 105 ppm [5]. In the β-O-4 bonds of S units, the α and β carbons were identified in intensities of 70 and 75 ppm, respectively. The methoxyl carbon side chains of the G and S units were thought to be responsible for the specific peak at 55 ppm. α and β-methylene and γ-methyl groups present in the n-propyl side chains of lignin are specifically responsible for the signals between 15-34 ppm [27].

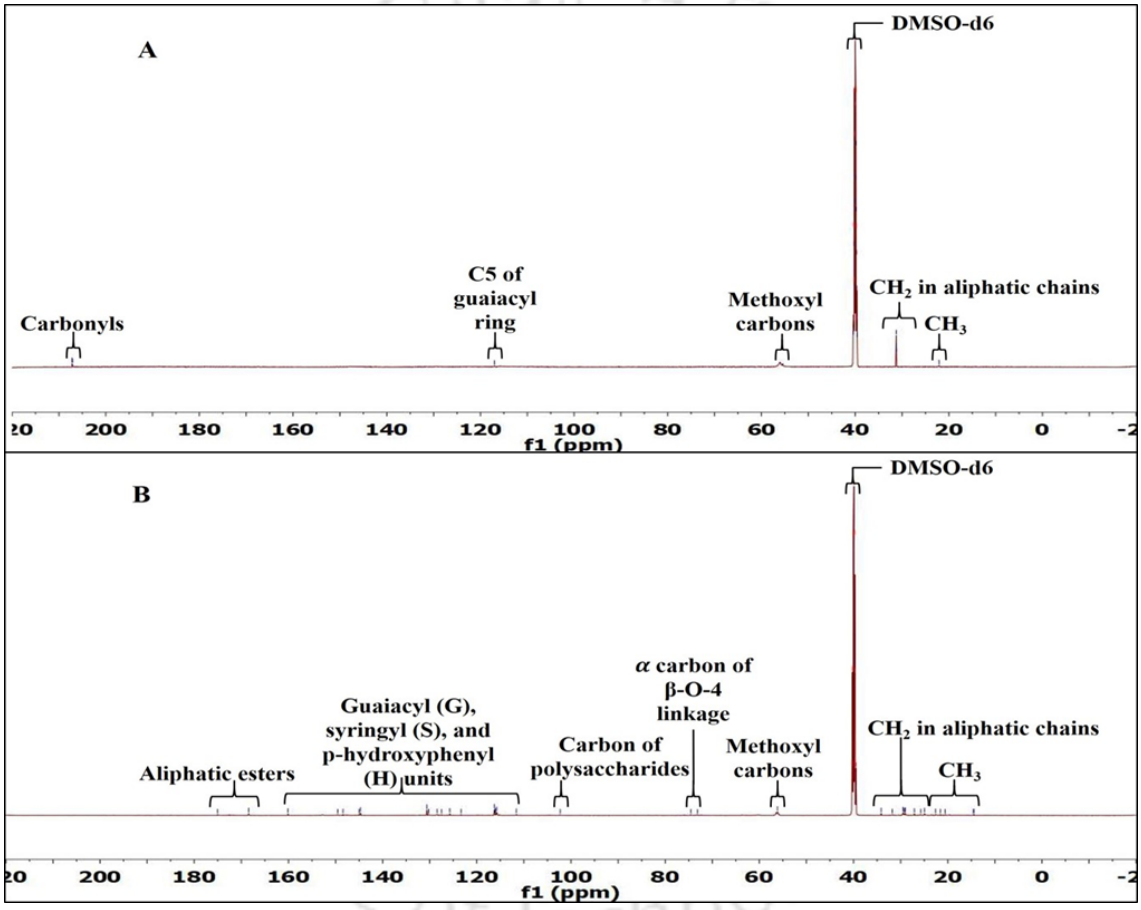

Figure 3.9: ^{13}C NMR of lignin spectra A) commercial lignin, B) Extracted lignin (3% KOH, 125 min, 10% solid loading)

3.2.10 XPS Analysis

To determine the elemental composition of the commercial (CL) and extracted (EL) lignin, an X-ray photoelectron spectroscopy (XPS) study was carried out. The XPS

survey spectrum of the CL sample exhibits the presence of C 1s, O 1s, O KLL, Na 1s, Na KLL, S 2s, and S 2p core levels (**Fig. 3.10**). The presence of Si 2p in the CL sample is due to the 3M scotch tape used in the XPS analysis, as it contains silicone. The commercial lignin is contaminated with Na (9.3 %) and S (2.92 %), presumably resulting from its pretreatment and purification process. On the contrary, extracted lignin (EL) does not contain K (pretreated with KOH instead of NaOH) and S, as, after pretreatment, lignin was washed thoroughly with warm water to remove all the alkaline residues. However, a small amount of N_2 was detected in EL. It was shown by the typical N1s peak at 400 eV.

The chemical valences of the building elements were further investigated using a high-resolution XPS scan. Four types of carbon atoms were identified from the carbon spectrum. The 284.3-284.7 eV peak is responsible for carbon bonds (C-C, C=C) and hydrocarbon bonds (C-H). Peaks between 285.5-286 eV binding energy indicate the presence of carbon bonds with nitrogen and noncarbonyl oxygen atoms (C-OH, C-N, C-O-C). Peaks appeared in the range of 286.5-286.7 eV binding energy, indicating the presence of aldehyde ketones and carbonyl groups (C=O). The peak indicates that carboxyl and esters groups (O-C=O) arose between 288.2-288.7 eV. Three different high-resolution O1s spectra have been identified. Each band consists of different oxygen bonds within a close binding energy range. These bands are labeled as PO1 (531.2-532.4 eV), PO2 (532.6- 533.2 eV), and PO3 (533.5-533.7 eV). The probable constituent of PO1 is C=O*−O (aliphatic, aromatic) and C=O (aliphatic and aromatic carbonyl group). PO2 consists of C-OH (aliphatic alcohol), C-O-C, and C=O-O* (aromatic) bonds, and the PO3 band is responsible for aromatic OH and C=O-O* (aliphatic bonds). After studying all the elements of C and O, it can be seen that hydrocarbons and carbonyl groups are major components of C1s in CL, whereas, in EL, all four bands of C1s are present within a small range of difference. PO1 was the main type in O_2 for CL, while PO2 was the major contributor to the EL sample. It indicated that oxygen was the predominant element present in extracted lignin C-O bonds, which also explains the high phenolic content of the EL sample.

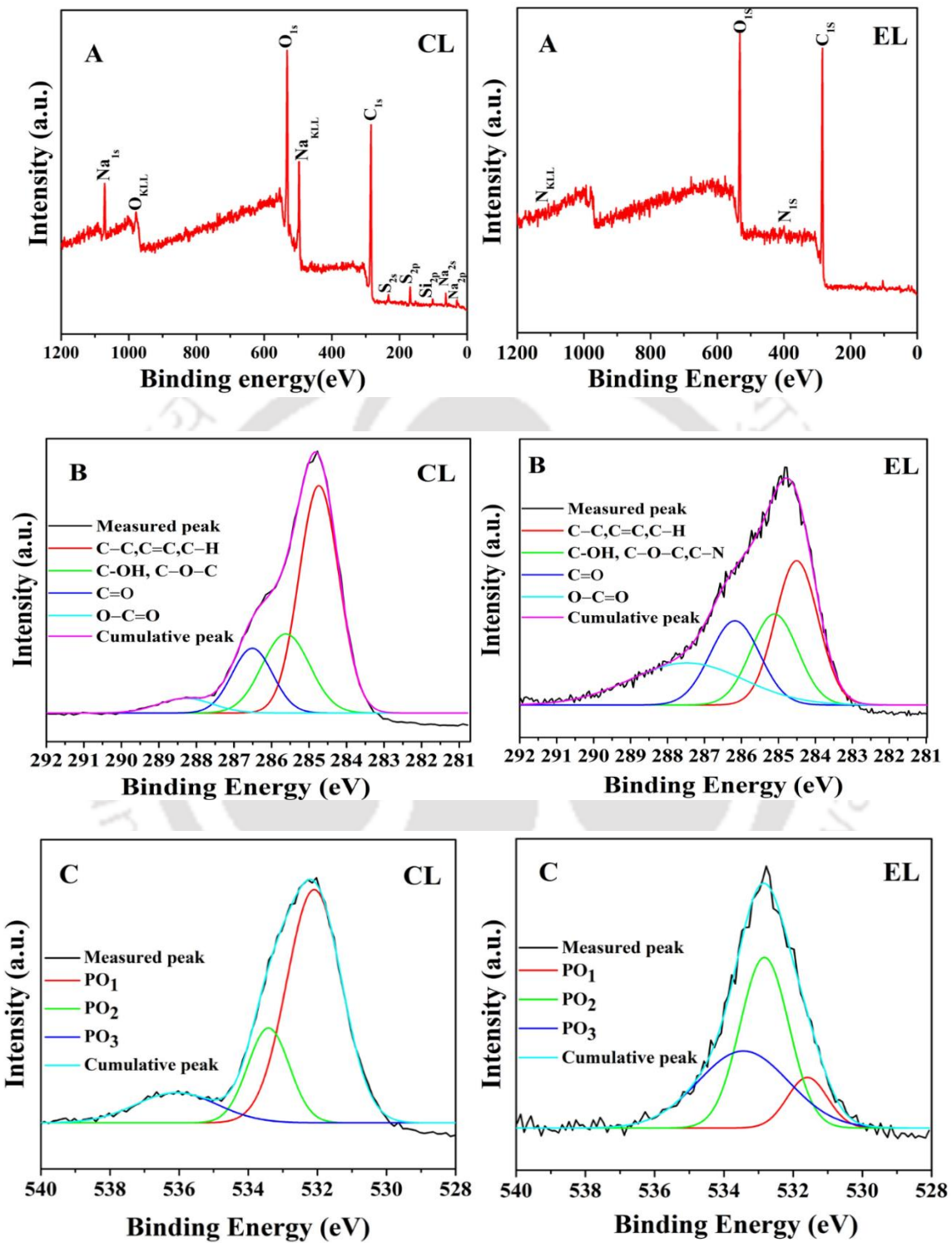

Figure 3.10: XPS A) Survey spectrum, B) High-resolution C1s spectra, and C) High-resolution O1s spectra of Commercial (CL) and Extracted (EL) lignin.

3.3. Summary

KOH-mediated alkaline pretreatment of *Saccharum ravennae* grass biomass for lignin recovery was carried out using process optimization with CCD application based on Research surface methodology. A minimum dose of 2.4% KOH was able to remove 15.81 g/100 g of lignin with a solid loading of 6.41% over a reaction time of 176.57 min at 100 °C as preoptimized reaction temperature. The lignin recovery process was simulated and optimized using CCD. It was discovered that the concentration of KOH and solid loading percentage had a comparatively larger influence than reaction time. According to the purity test results of the lignin samples through acid hydrolysis, a maximum of 93.7% purity was achieved by the S13 sample (3% KOH,10% solid loading,125 minutes). The folin-Ciocalteu method reveals that extracted lignin samples (20.61-54.44%) contain more phenolic groups than commercial lignin (11.85%). According to the outcomes of the instrumental analysis, the alkaline treatment was capable of removing lignin from the grass biomass, which contains more functional groups, G and S units of lignin, compared to commercially available alkaline lignin. Although a small fraction of sugar impurities are present in the lignin sample, they can be easily removed through acid hydrolysis. Thus, the lignin extracted through alkaline pretreatment was deemed effective in its profuse commercial utility as an aromatic biopolymer.

References

[1] P.P. Das, M. Sharma, M.K. Purkait, Recent progress on electrocoagulation process for wastewater treatment: A review, Sep. Purif. Technol. 292 (2022) 121058. https://doi.org/10.1016/j.seppur.2022.121058.

[2] I. Dávila, P. Gullón, M.A. Andrés, J. Labidi, Coproduction of lignin and glucose from vine shoots by eco-friendly strategies: Toward the development of an integrated biorefinery, Bioresour. Technol. 244 (2017) 328–337. https://doi.org/https://doi.org/10.1016/j.biortech.2017.07.104.

[3] J.B. Sluiter, R.O. Ruiz, C.J. Scarlata, A.D. Sluiter, D.W. Templeton, Compositional Analysis of Lignocellulosic Feedstocks. 1. Review and Description of Methods, J. Agric. Food Chem. 58 (2010) 9043–9053. https://doi.org/10.1021/jf1008023.

[4] A. Adamovics, R. Platace, I. Gulbe, S. Ivanovs, The content of carbon and hydrogen in grass biomass and its influence on heating value, 2018. https://doi.org/10.22616/ERDev2018.17.N014.

[5] R.M. Noor, M.M. Salleh, A. Yahya, H. Hussin, A.I. Galadima, Optimization of microwave pretreatment conditions for maximum lignin recovery from rice husk using central composite design (CCD) by response surface methodology (RSM), Res. J. Adv. Sci. 1 (2020) 61–83.

[6] A. Morales, B. Gullón, I. Dávila, G. Eibes, J. Labidi, P. Gullón, Optimization of alkaline pretreatment for the co-production of biopolymer lignin and bioethanol from chestnut shells following a biorefinery approach, Ind. Crops Prod. 124 (2018) 582–592. https://doi.org/https://doi.org/10.1016/j.indcrop.2018.08.032.

[7] A. Mukherjee, S. Banerjee, G. Halder, Parametric optimization of delignification of rice straw through central composite design approach towards application in grafting, J. Adv. Res. 14 (2018) 11–23. https://doi.org/https://doi.org/10.1016/j.jare.2018.05.004.

[8] E. Bialik, B. Stenqvist, Y. Fang, A. Ostlund, I. Furo, B. Lindman, M. Lund, D. Bernin, Ionization of Cellobiose in Aqueous Alkali and the Mechanism of Cellulose Dissolution, J. Phys. Chem. Lett. 7 (2016). https://doi.org/10.1021/acs.jpclett.6b02346.

[9] T. Ana, X. Erdocia, L. Serrano, J. Labidi, Influence of Extraction Treatment on Olive Tree (Olea europaea) Pruning Lignin Structure, Environ. Prog. Sustain. Energy. (2013). https://doi.org/10.1002/ep.11725.

[10] A. Morales, J. Labidi, P. Gullón, Impact of the lignin type and source on the characteristics of physical lignin hydrogels, Sustain. Mater. Technol. 31 (2022) e00369.

https://doi.org/https://doi.org/10.1016/j.susmat.2021.e00369.

[11] N. Ratanasumarn, P. Chitprasert, Cosmetic potential of lignin extracts from alkaline-treated sugarcane bagasse: Optimization of extraction conditions using response surface methodology, Int. J. Biol. Macromol. 153 (2020) 138–145. https://doi.org/https://doi.org/10.1016/j.ijbiomac.2020.02.328.

[12] E. Cequier, J. Aguilera, M. Balcells, R. Canela-Garayoa, Extraction and characterization of lignin from olive pomace: a comparison study among ionic liquid, sulfuric acid, and alkaline treatments, Biomass Convers. Biorefinery. 9 (2019) 241–252. https://doi.org/10.1007/s13399-019-00400-w.

[13] X. Li, E. Ximenes, Y. Kim, M. Slininger, R. Meilan, M. Ladisch, C. Chapple, Lignin monomer composition affects Arabidopsis cell-wall degradability after liquid hot water pretreatment, Biotechnol. Biofuels. 3 (2010) 27. https://doi.org/10.1186/1754-6834-3-27.

[14] J.-L. Wen, B.-L. Xue, S.-L. Sun, R.-C. Sun, Quantitative structural characterization and thermal properties of birch lignins after auto-catalyzed organosolv pretreatment and enzymatic hydrolysis, J. Chem. Technol. Biotechnol. 88 (2013) 1663–1671. https://doi.org/https://doi.org/10.1002/jctb.4017.

[15] J. Ke, D. Singh, X. Yang, S. Chen, Thermal characterization of softwood lignin modification by termite Coptotermes formosanus (Shiraki), Biomass and Bioenergy. 35 (2011) 3617–3626. https://doi.org/https://doi.org/10.1016/j.biombioe.2011.05.010.

[16] P.P. Das, A. Anweshan, M.K. Purkait, Treatment of cold rolling mill (CRM) effluent of steel industry, Sep. Purif. Technol. 274 (2021) 119083. https://doi.org/10.1016/j.seppur.2021.119083.

[17] N.S. Samanta, P.P. Das, P. Mondal, U. Bora, M.K. Purkait, Physico-chemical and adsorption study of hydrothermally treated zeolite A and FAU-type zeolite X prepared from LD (Linz–Donawitz) slag of the steel industry, Int. J. Environ. Anal. Chem. 00 (2022) 1–23. https://doi.org/10.1080/03067319.2022.2079082.

[18] H. Yanti, W. Syafii, N.J. Wistara, F. Febrianto, N.H. Kim, Effect of Biological and Liquid Hot Water Pretreatments on Ethanol Yield from Mengkuang (*Pandanus artocarpus* Griff), J. Korean Wood Sci. Technol. 47 (2019) 145–162. https://doi.org/10.5658/WOOD.2019.47.2.145.

[19] K. Zhang, M. Si, D. Liu, S. Zhuo, M. Liu, H. Liu, X. Yan, Y. Shi, A bionic system with Fenton reaction and bacteria as a model for bioprocessing lignocellulosic biomass, Biotechnol. Biofuels. 11 (2018) 31. https://doi.org/10.1186/s13068-018-1035-x.

[20] N.I. Haykir, E. Bahcegul, N. Bicak, U. Bakir, Pretreatment of cotton stalk with ionic liquids including 2-hydroxy ethyl ammonium formate to enhance biomass digestibility, Ind. Crops Prod. 41 (2013) 430–436. https://doi.org/https://doi.org/10.1016/j.indcrop.2012.04.041.

[21] N.S. Samanta, S. Banerjee, P. Mondal, Anweshan, U. Bora, M.K. Purkait, Preparation and characterization of zeolite from waste Linz-Donawitz (LD) process slag of steel industry for removal of Fe3+ from drinking water, Adv. Powder Technol. 32 (2021) 3372–3387. https://doi.org/10.1016/j.apt.2021.07.023.

[22] L. Cong, Z. Li, Z. Guanqun, X. Jianguo, L. Zhang, Characterization and components separation of corn stover by alkali and hydrogen peroxide treatments, Polish J. Chem. Technol. 17 (2015). https://doi.org/10.1515/pjct-2015-0035.

[23] Y. Wang, W. Liu, L. Zhang, Q. Hou, Characterization and comparison of lignin derived from corncob residues to better understand its potential applications, Int. J. Biol. Macromol. 134 (2019) 20–27. https://doi.org/https://doi.org/10.1016/j.ijbiomac.2019.05.013.

[24] Z. Tian, L. Zong, R. Niu, X. Wang, Y. Li, S. Ai, Recovery and characterization of lignin from alkaline straw pulping black liquor: As feedstock for bio-oil research, J. Appl. Polym. Sci. 132 (2015). https://doi.org/https://doi.org/10.1002/app.42057.

[25] C. Huang, H. Juan, R. Narron, Y. Wang, Q. Yong, Characterization of Kraft Lignin Fractions Obtained by Sequential Ultrafiltration and Their Potential Application as a Biobased Component in Blends with Polyethylene, ACS Sustain. Chem. Eng. 5 (2017). https://doi.org/10.1021/acssuschemeng.7b03415.

[26] K.P. Kringstad, R. Mörck, 13C-NMR Spectra of Kraft Lignins, in: 1983.

[27] A. García, M. González Alriols, G. Spigno, J. Labidi, Lignin as natural radical scavenger. Effect of the obtaining and purification processes on the antioxidant behaviour of lignin, Biochem. Eng. J. 67 (2012) 173–185. https://doi.org/https://doi.org/10.1016/j.bej.2012.06.013.

Chapter 4

Preparation and characterization of mixed matrix membrane for Cr(VI) removal with the alkaline lignin extracted from Ravenna grass

This chapter has covered the comprehensive process for developing a lignin-based MMM using polysulfone (PSf) as the base material. The influence of PSf and lignin concentration on the properties of the fabricated membranes was examined. Also, the developed membranes were assessed for surface morphology, roughness, thickness, thermal stability, functional groups, elemental composition, mechanical strength, and hydrophilicity. AFM and SEM studies showed that the PSf/lignin membranes possessed rough and inconsistent morphology and comparatively greater surface porosity. The background of this work, recent literature, and the scope of this work have been discussed in Chapter 1, Section 1.4, and Section 1.5.3, respectively. This work has been published in ACS Applied Polymer Materials.

4.1 Methodology

4.1.1 Materials

Ravenna grass was collected from Guwahati, northeast India. HNO_3 (69%), KOH pallets, and polysulfone (average M_W 30,000Da, PDI-1.36) were purchased from Merck Life Science, India. NMP (N-Methyl-2-Pyrrolidone, 99.5%) was bought from SRL, India.

4.1.2 Lignin sample preparation

Harvested grass biomass was thoroughly washed and dried in a hot air oven. The dried biomass was ground up and passed through a 150-micron sieve. The lignin was extracted from dried powder biomass by adopting optimized lignin extraction conditions reported in an earlier investigation [1]. First, the powdered biomass was suspended in a 3 wt% KOH solution with a solid loading ratio of 10%. The solution was

then pre-treated at 100 ^{o}C for 125 minutes in an oil bath. Following pre-treatment, the resulting solution was subjected to vacuum filtration using grade 1 Whatman filter paper after being momentarily cooled. The filtrate black liquor was collected and stored separately. The separated black liquid was mixed with a 2% nitric acid solution drop by drop, and this process was maintained until coagulation began at a pH of around 2. The resulting semi-coagulated lignin solution was centrifuged at 10,000 rpm for five minutes. The precipitate after centrifugation was washed with warm water (at 50 ^{o}C), and the centrifugation step was repeated to remove residual acid from the lignin precipitate. The final solid lignin residues were oven-dried for 12 hours at 60 ^{o}C. The dried lignin was then ground using a mortar pestle and kept in an air-tight container for further analysis and application.

4.1.3 Fabrication of PSf/Lignin Mixed Matrix Membrane

The fabrication of the PSf/Lignin mixed-matrix membrane was carried out with the phase inversion technique [2]. Phase inversion is a method of demixing that divides a homogenous polymer solution into two phases by submerging it in a coagulation bath. There are four main methods for phase conversion, illustrated in **Fig. 4.1**. Among these techniques, immersion precipitation phase inversion provides ease of use, adaptability, the ability to control membrane morphology, high porosity, scalability, and the possibility of membrane customization. Because of these advantages, immersion precipitation phase inversion was utilized in this study to fabricate membranes efficiently (**Fig. 4.2**). Initially, lignin nanoparticles were added to the NMP solvent and ultrasonicated (50 Hz and 120 Watts) for 45 minutes to form a homogeneous mixture. After ultrasonication, 20 wt.% PSf beads were dissolved in the homogenous lignin-NMP solution. PSf beads were dissolved in lignin-NMP solution at a 1:4 weight ratio to formulate the membrane casting solution. The final mixture was heated and stirred at 60 ^{o}C for 6 h at 110 rpm on a hot plate-magnetic stirrer. After heating for six hours, the PSf beads were dissolved entirely and formed a thick, homogenous casting solution. Finally, air bubbles in the casting solution were removed by keeping it at 60 °C in a hot air oven for six hours.

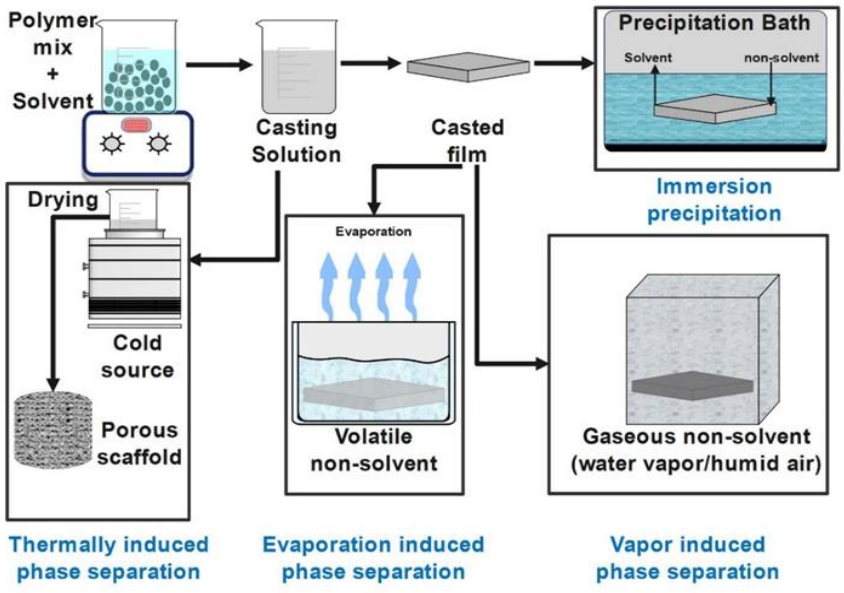

Figure 4.1: Different phase inversion methods

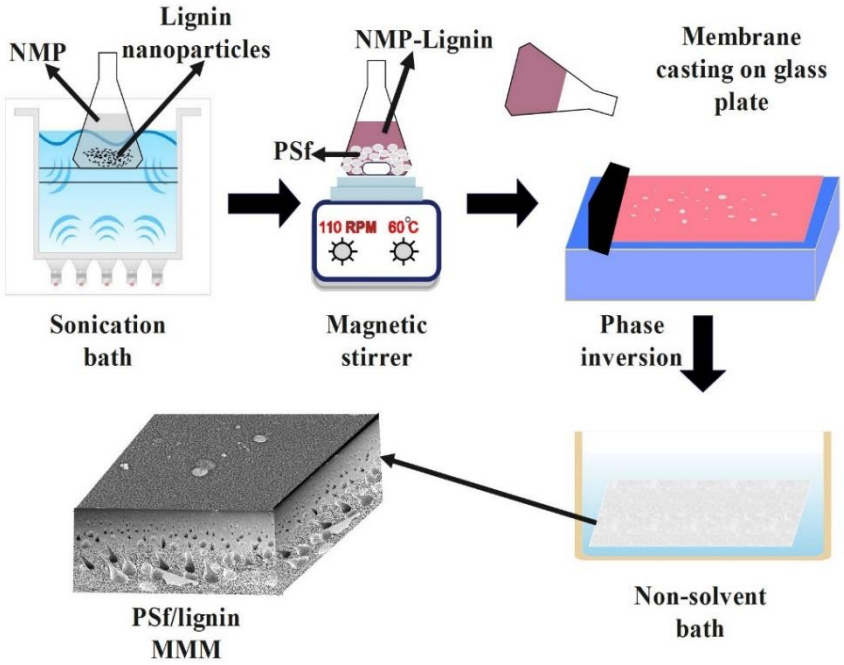

Figure 4.2: PSf/lignin MMM preparation through immersion precipitation

After degassing, the casting solution was hand-cast with a casting knife on an untainted glass sheet. The height of the casting knife from the glass sheet was maintained at 350 µm. The effective membrane casting area on the glass sheet was 11 cm in width and 21 cm in length. The freshly formed membrane on the glass sheet was subsequently solidified by submerging it in a deionized water bath. The immersion process was allowed for 24 hours to achieve complete solidification and solvent elimination. The solidified membranes were then air-dried at room temperature. Concentrations of alkaline lignin were varied (0-1 wt.% of the overall solution weight) to fabricate multiple PSf/lignin MMMs. **Table 4.1** displays the constituents and their constitutions in each membrane formulation.

Table 4.1: Constituents and their constitutions in each membrane casting formulation

Membrane	PSf (wt.%)	NMP (wt.%)	Lignin (wt.%)
M0	**20**	**80**	**NA**
M1	**20**	**79.75**	**0.25**
M2	**20**	**79.5**	**0.5**
M3	**20**	**79**	**1**

4.1.4 Lignin characterization

Scanning electron microscope (SEM) images of lignin particles were captured with a Sigma 300 instrument (Zeiss, Germany). The sample for SEM analysis was prepared using the drop-casting method. For this, powdered lignin was dissolved in an organic solvent. The sample was gold coated before analysis, and the image was taken at 3 kV and 150kX magnification. The pertinent phases of the lignin powder sample were evaluated using Field emission transmission electron microscopy (FETEM) 2100F (JEOL, Japan) [3]. For the TEM analysis, lignin was dissolved in DMSO solvent. The suspension was pipetted and dropped onto a 300-mesh carbon-coated copper grid. The droplet grid was kept overnight for drying before TEM imaging at 60 kX magnification. Anton Paar LitesizerTM 500 device was used to measure the zeta potential of the extracted alkaline lignin. Adding 50 mg of lignin sample to 20 mL of deionized water

and varying the pH levels (pH 2-11) facilitated the sample preparation. With the help of 0.1 M NaOH and HCl solutions, the pH of the solvents was changed. For comparison, the reported characterization data of the extracted lignin (elemental analysis, total phenolic content, FTIR, XRD, XPS, and NMR) was used from the previous Chapter 3 [1].

4.1.5 Membrane Characterization

The strength of interaction between PSf and alkali lignin polymer was estimated through the interaction parameter (χ) defined by the Flory-Huggins theory [4]. The parameter was obtained using Hildebrand solubility parameters, as shown below.

$$\chi = \frac{V_R(\delta_L - \delta_P)^2}{RT} \quad (1)$$

δ_L and δ_P were the solubility parameters of alkali lignin and PSf. V_R stands for "reference volume," where "V_R" was measured as 100 cm^3, "R" was "universal gas constant," and "T" was "absolute temperature"[5]. The average Hildebrand solubility δ_h of polysulfone is 21.2 $MPa^{1/2,}$ and the solubility parameter of alkaline lignin at 60 °C was reported as 24.27 $MPa^{1/2}$ [6]. The interaction parameter was computed at 60 °C.

The FTIR analysis of fabricated membranes was carried out with Spectrum two-PerkinElmer (Singapore). With a 4000-400 cm^{-1} scanning spectral range, the ATR-FTIR spectra were obtained with 0.5 cm^{-1} optimal resolution.

Smartlab 9KW Powder XRD System (Rigaku Technologies, Japan) was used to carry out X-ray diffraction analysis. With 2θ varying from 3° to 70° at the ambient temperature, each sample was scanned with a 10°/min tempo.

The constructed membranes and extracted lignin were subjected to a thermal degradation test using the TG209 F1 NETZSCH TGA instrument. A 20 mL/min flow rate of nitrogen gas was used to purge the instrument, and a 40 mL/min flow rate was used for analysis. Alumina crucibles were used for sample analysis. The analysis temperature was set between 25 and 800 °C at a heating rate of 10 °C per minute [7].

Atomic force microscopy (AFM) Cypher S (Oxford Instruments, UK) was used to assess the surface roughness of the membranes. Small square-shaped membranes were cut and adhered with carbon tape onto the surface of the magnetic metal specimen support. Thereafter, scanning was conducted.

The surface morphology of the produced membranes was analyzed with a Zeiss FESEM Sigma 300, and the membrane cross-sections were investigated with a Zeiss FESEM Gemini 300. All the samples were gold-coated before analysis. The surface images were captured at 100kx magnification, and cross-sectional images were taken at 700x magnification. The extra high-tension (EHT) voltage was the same (5 kV) for both analyses.

Using the Anton Paar LitesizerTM 500, the zeta potential of the constructed membrane surfaces was measured. The membranes were cut into smaller pieces and immersed in deionized water with a pH of 7. Thereafter, the sample was kept aside for 12 hours. Prior to the analysis, 30 minutes of sonication was performed.

The porosity (ε) of the synthesized membranes was estimated with the gravimetric method and with the expression [8]:

$$\varepsilon = (\omega 1 - \omega 2)/(A \times l \times \rho) \quad (2)$$

Where ω1, ω2 represents the weight of wet and dry membranes (kg), A (m^2) denotes the effective membrane area, l (m) denotes the membrane thickness, and ρ (998 kg/m^3) denotes water density.

The sessile drop procedure was used to determine the water contact angle on the membrane surface. To do so, the membranes were cut to an appropriate size. Then both ends of the membrane samples were taped to a clear slide. Consequently, using a micro syringe, a tiny drop of deionized water was placed on the dry membrane surface. The water contact angle micrograph was acquired and studied with Holmarc's contact angle meter (Model No: HO-ED-M-01).

Using a 5KN electromechanical universal testing machine (UTM) Z005TNProline (Zwick Roell, Austria), the elongation and tensile strength of the membranes at the breakpoint were assessed prior to and after three filtration cycles. For the mechanical assessment, each sample was cut into rectangular pieces, and the analysis was performed at a 5 mm/min speed.

4.1.6 Membrane-based Cr (VI) removal studies

The potassium dichromate ($K_2Cr_2O_7$) was desiccated after drying at 100°C for 60 minutes. A 283 mg of $K_2Cr_2O_7$ was dissolved in 100 mL deionized water to achieve a 1000 ppm Cr(VI) solution. One mL of 1000 ppm solution was diluted to 100 mL for a standard 10 ppm Cr(VI) stock solution. The following concentrations of Cr(VI) standards were made for the calibration curves using the stock solution: 10, 8, 6, 4, 2, 1, 0.5, 0.1, 0.05, and 0.0 ppm.

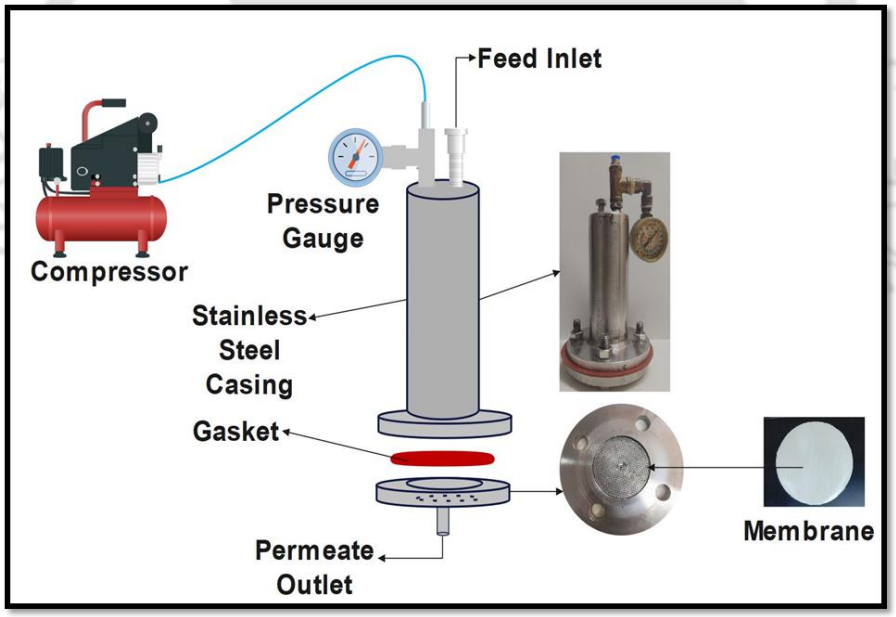

Figure 4.3: Filtration setup

A rudimentary dead-end filtration device was fabricated to assess the fouling properties, permeation flux, and rejection of the membranes (**Fig. 4.3**). Initially, 3 bar pressure was

applied for 30 minutes to avoid compaction ramifications. The PWF was calculated at 2 bar pressure and was denoted as J_0 (L/m^{2}h).

Following PWF measurement, the effectiveness of prepared membranes was assessed over the course of three filtration cycles. A 2 ppm Cr (VI) solution (pH-7) was used for filtration. The filtration was performed over three cycles. Each cycle duration was 120 minutes, operated under 2 bar transmembrane pressure. After every cycle, PWF was measured and denoted as J_1, J_2, and J_3, respectively. The spent membranes were regenerated with HCl solution (pH-3) and water for 20 minutes after completing the 3rd cycle. After that, regenerated fouled membrane flux J_F was measured. Using J_0, J_1, J_2, J_3, and J_F flux values, the flux recovery and fouling parameters were determined with the following expressions [9] :

$$FR_n = J_n/J_{n-1} \quad (3)$$

$$TFR = (J_0 - J_3)/J_0 \quad (4)$$

$$RFR = (J_f - J_3)/J_0 \quad (5)$$

$$IFR = (J_0 - J_f)/J_0 \quad (6)$$

where FR, TFR, RFR, and IFR refer to flux recovery, total, reversible, and irreversible fouling ratios, respectively, and n denotes the cycle number. The removal percentage of Cr was determined with the expression:

$$Cr\ removal\ (\%) = (1 - C_f/C_i) \times 100 \quad (7)$$

C_i and C_f refer to the amounts of Cr (VI) in the initial feed and filtrate streams. These were determined with atomic absorption spectroscopy (AAS, AA240- Varian, Netherlands) and at a wavelength of 357.9 nm.

After filtration, the spent membranes were subjected to the Energy dispersive X-ray (EDX) microanalysis to confirm the presence of Cr(VI) on the membrane surfaces. Field Emission Scanning Electron Microscope (FESEM) with element EDS detector (Make: Zeiss, Model: Sigma 300) was used for EDX analysis with a maximum resolution of 15Kx.

4.2 Result and Discussion

4.2.1 Characterization of extracted lignin

The morphology of extracted lignin was investigated by SEM (**Fig. 4.4a)**. The figure conveys that the particles possessed diameters of 25 to 170 nm and emerged as aggregates. Such an effect was due to the hydrodynamic radius of colloidal lignin suspension in the organic solvent, which can be affected by several elements, like pH, temperature, and concentration. Most lignin particle agglomerates were within the size range of 100–1200 nm. The variation in the particle size suggested that the lignin underwent degradation due to alkaline treatment. This conclusion was further supported by the TEM images (**Fig. 4.4b**), where most particles had poor dispersibility and were asymmetric in their shape characters. During TEM analysis, lignin particles were dissolved in the DMSO solution, thereby ensuring better particle size distribution of lignin particles. With a spherical shape, the particles possessed an average particle size of 55±30 nm. **Fig. 4.4c** depicts the SAED pattern of lignin and the white ring-shaped pattern that confirms the amorphous nature of lignin particles.

The zeta potential distribution curve of alkaline lignin fails to reach the isoelectric point (IEP) (**Fig. 4.4d**). However, based on its shape, it could reach the IEP at a pH of about 0.5. The value of the isoelectric point, which eventually became apparent, was significantly influenced by the prevalent functional groups in the lignin subunits. The zeta potential value of alkaline lignin was negative in the entire pH range. The ionization of phenolic functional groups on the lignin subunits was the primary source of the -ve charge. Functional groups such as -OH, -COOH, and C=O that exist on the particle surfaces got substantially scattered in the aqueous environment. Thus, their degree of association influenced the surface charge. It is evident from the conducted research and prior art data that the alkaline lignin had a substantial constitution of carboxyl and phenolic groups (among other types of groups) on its surface. The H^+ and OH^- ions were, without a doubt, the potential-forming ions in the studied dispersive structure, as seen by the considerable variations in zeta potential as a function of solution pH [10].

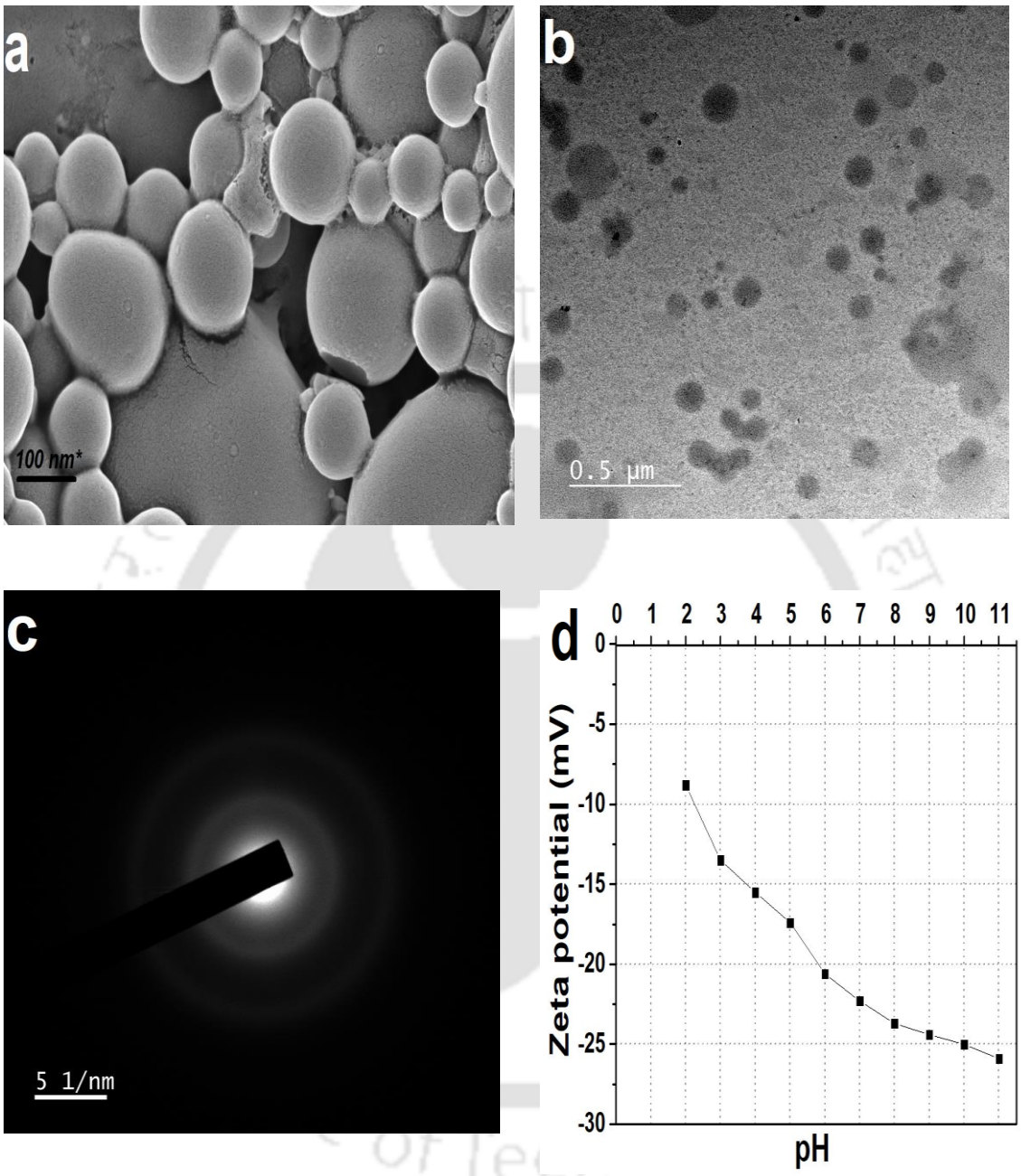

Figure 4.4: a) SEM image of lignin, b) TEM image of lignin, c) SAED pattern of lignin, d) Zeta potential distribution of lignin particles.

4.2.2 Characterization of membranes

The computed value of the Flory-Huggins interaction parameter (χ) between PSf and alkaline lignin was 0.34, indicating a favorable interaction between the two materials. A

positive χ value suggests that the two polymers interact favorably and can combine or blend together in a homogenous solution. This could be the result of intermolecular forces, such as hydrogen bonds, dipole-dipole interactions, or other forces, between PSf and alkaline lignin. Compared to systems with negative or zero χ values, the positive value signifies that the mixture or solution may show increased miscibility and perhaps enhanced characteristics. However, it is essential to understand that the specific value of the Flory-Huggins interaction parameter could differ based on parameters such as blending composition, temperature, and the individual qualities or compositions of PSf and alkaline lignin [11][12].

FTIR spectra of pure and lignin-doped PSf membranes were obtained and analyzed to study and identify associated chemical linkages in the structure of various samples. **Fig. 4.5** illustrates the FTIR spectra of pure PSf membrane and PSf/Lignin membranes. Two distinct and significant absorption bands could be seen at 1582 cm^{-1} and 1490 cm^{-1} wavelengths. These corroborate with the stretching of C=C bonds within the lignin benzene ring skeleton and the polysulfone group. The spectra at 1148, 1297, and 1325 cm^{-1} represent O=S=O sulfone group stretching vibration [13][14]. The C-O-C stretching can be detected at 1240 cm^{-1}.

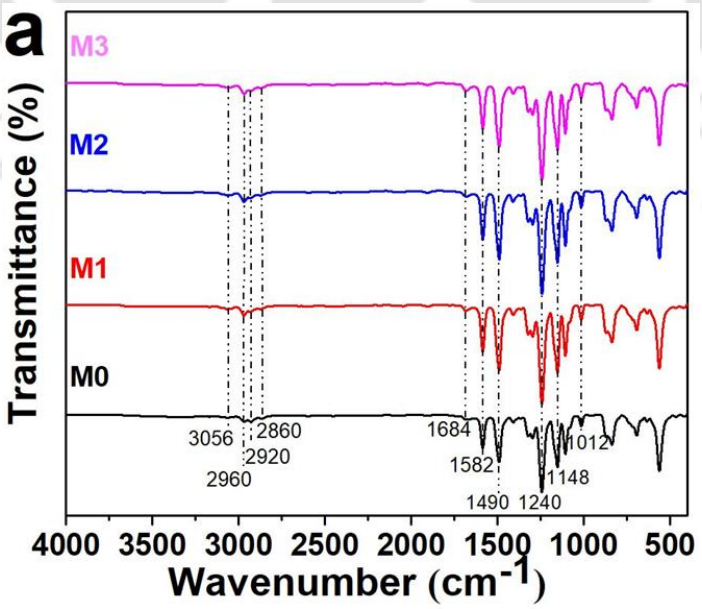

Figure 4.5: FTIR spectra of fabricated membranes

Also, an increase in the peaks of the PSf/Lignin membrane spectra affirms the existence of alkoxy groups of the lignin guaiacyl ring. The vibrational bonding of =C-H of the polysulfone aromatic ring is responsible for the peak at 3056 cm^{-1} [14]. C-H stretching vibrations in the methylene and methyl groups of lignin and polysulfone polymer were responsible for the bands between 2860 and 2960 cm^{-1} [14][15]. The peak at 1684 cm^{-1} was primarily accounted for by the C=O vibration of the acetyl and p-coumaroyl groups in the lignin. A strong band at 1012 cm^{-1} can be linked to the C-O stretching vibration in the lignin and polysulfone structure.

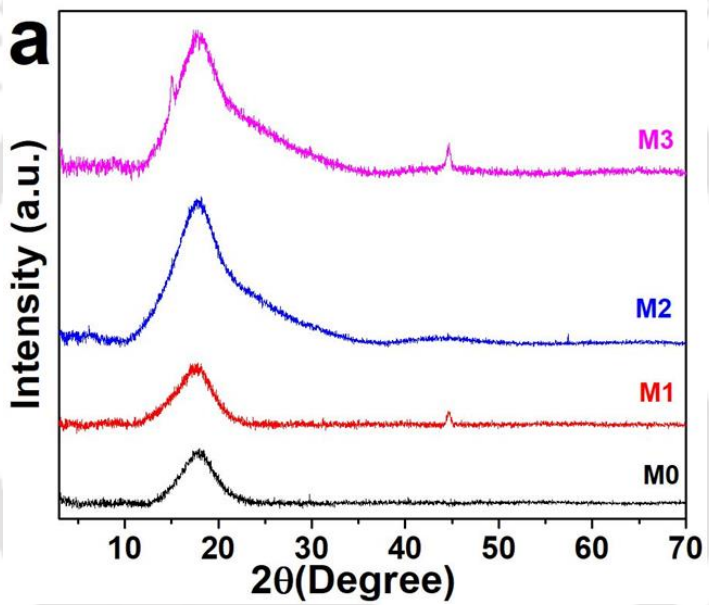

Figure 4.6: XRD spectra of (a) fabricated membranes

Fig. 4.6 depicts the X-ray diffraction patterns of polysulfone and polysulfone-lignin mixed matrix membranes in the 2θ range of 3° to 70°. All samples affirmed a single peak at a 2θ value of 18°, the standard peak for lignin and PSf. Thus, the evaluated samples were all amorphous. The peak width of the PSf/lignin membranes conveyed its enhancement. Thus, the irregularities arose in the polymer chain structure and were enhanced due to the inclusion of lignin in the PSf framework. In other words, the PSf structure underwent significant modifications.

The peak location in the XRD spectra of PSf/lignin mixed matrix membranes altered towards lower angles. This occurred due to polymer-polymer interaction. Another

medium pattern at about the value of 2θ 44.7º was observed in the PSf/lignin membrane spectra. This was possibly due to the lignin. The emergence of a small shoulder peak at 15.1° in the PSf/lignin-1wt.% spectra indicated the expansion of the lattice. This occurred due to the expansion of the cellulose matrix impurity that exists in the deployed lignin sample.

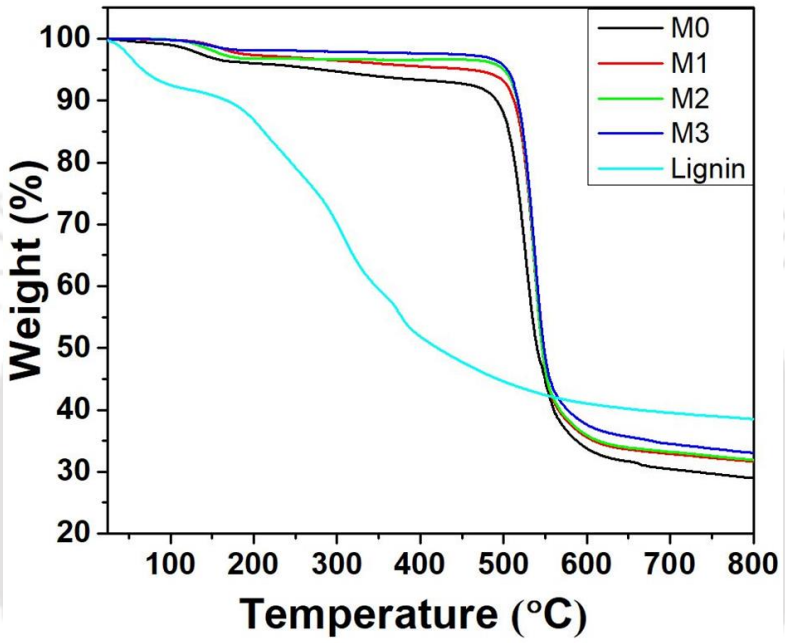

Figure 4.7: TGA thermogram of extracted lignin and fabricated membranes

TGA accomplished thermal analysis of the developed membranes, and the data were compared to the data reported for the extracted alkaline lignin [1]. The TGA curves for both the membranes and alkaline lignin have been depicted in **Fig. 4.7**. Based on the decomposition temperature (T_d) and peak derivative temperature (T_p), it can be inferred that the pure PSf membrane (M_0) possessed greater thermostability in comparison with alkaline lignin (T_d and T_p values of 287 and 472 °C, respectively, which are approximately 300 °C higher than those obtained for the alkaline lignin). Only one considerable reduction in weight was apparent for all membranes between 470 and 570 °C. This was attributed to the breakdown of the PSf structure. In this regard, it can be concluded that the PSf/Lignin membranes were as thermally stable as the pure PSf

membrane. Furthermore, the enhanced thermal stability of the hydrophilic PSf/lignin membranes was possibly due to the introduction of strong aromatic chains in grafted polymers along with those found in pure PSf. The mass percent remaining at 800°C (i.e., char yield) was significantly lesser for the PSf/Lignin membranes (29-33.5%) in comparison to the alkaline lignin (38.5%). Char yield in the PSf/lignin membranes augmented with increasing lignin content in the PSf mixed matrix membranes.

The AFM images were used to examine the contours and surface roughness of the developed MMMs. **Fig. 4.8** depicts the 2D and 3D illustrations. The concentration of lignin had an impact on surface roughness, which is evident in **Fig. 4.8**. As a result, the surface roughness of the lignin blend MMMs was more significant for the lignin nanolayer than the pure sample. Lower dark grooves in the 2D illustrations indicate greater surface smoothness for the PSf membranes. For MMMs denoted as M0, M1, M2, and M3, the calculated average roughness (Ra) values were 1.18 nm, 3.26 nm, 3.69 nm, and 4.35 nm, respectively. This phenomenon might be understood from two distinct perspectives. The first refers to the alteration in the membranes' surface pore configuration due to the presence of the lignin nanolayer. The second conveys that the lignin possessing a lower density than the PSf enabled the movement of the lignin nanolayers towards the surface in due course of the phase separation process and subsequent rougher surface development.

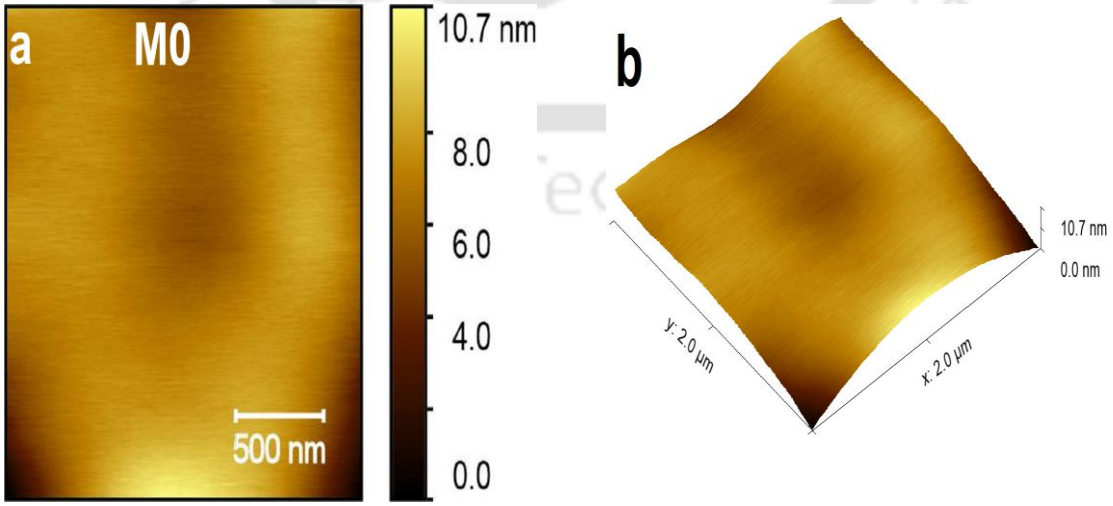

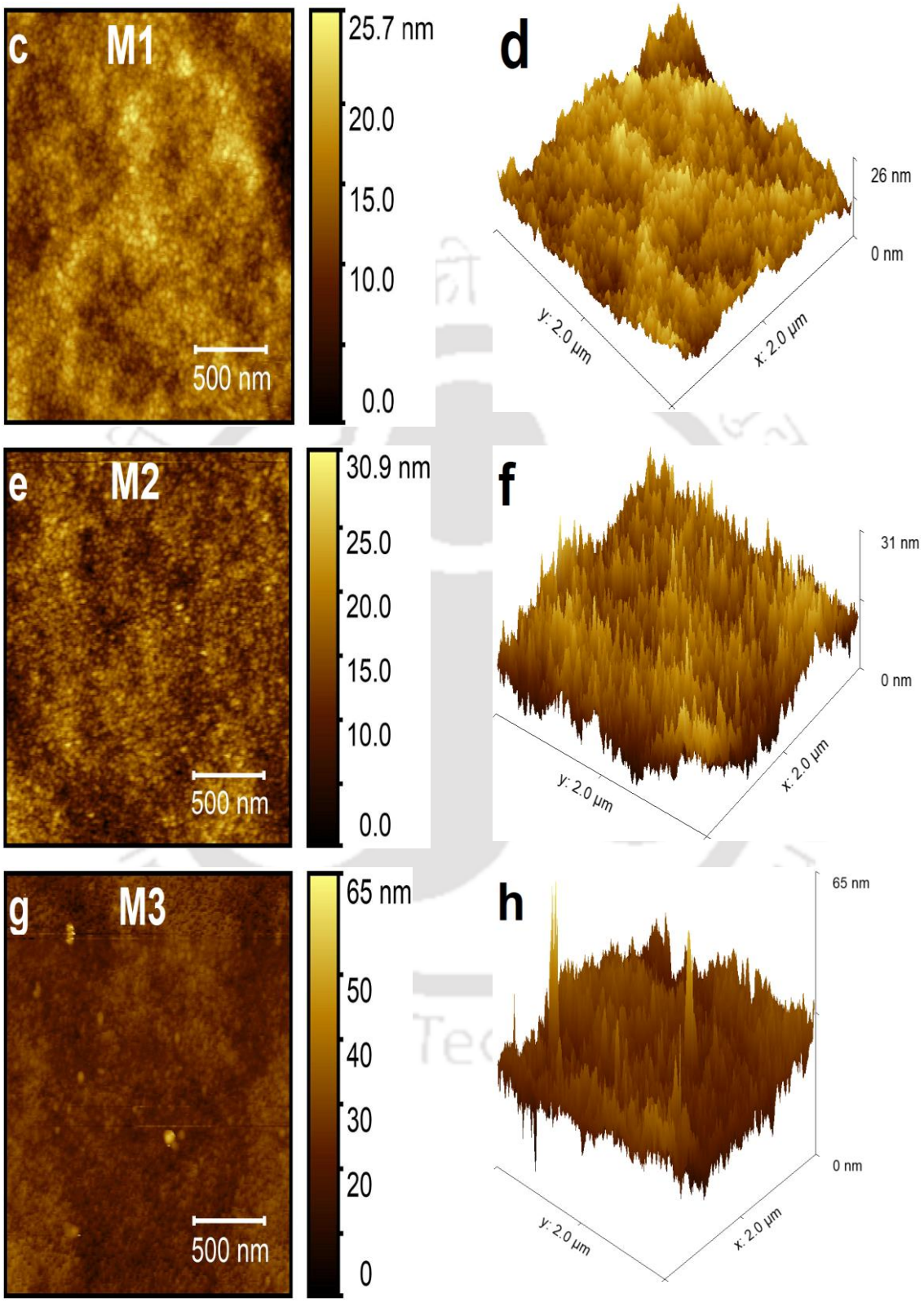

Figure 4.8: 2D (a, c, e, g) and 3D (b, d, f, h) AFM images of the prepared MMMs: (a, b) M0, (c, d) M1, (e, f) M2, (g, h) M3.

M0 (pure PSf membrane), M1 (0.25 wt% PSf/lignin membrane), M2 (0.5 wt% PSf/lignin membrane), and M3 (1 wt% PSf/lignin membrane)

According to AFM image analysis, the addition of lignin to the PSf matrix enables the formation of a large porous surface. This had been hypothesized to influence the MMMs Cr (VI) removal ability positively. Thus, with an expansion in the surface area accessible for the permeation of water, the standard surface roughness may elevate the membrane PWF.

Fig. 4.9 displays the cross-section and surface images of the pure PSf and PSf/lignin membranes. With three distinct morphologies in their cross-sectional structure, all membranes exhibit an asymmetric nature; i.e., the outermost layer possesses a pretty compacted structure, the central layer has sizable macro voids that resemble fingers, and the bottom layer has a sponge-like texture. The high reciprocal diffusivity of water and solvent was a key factor in influencing these structural morphologies [9]. Due to lignin's affinity with different hydrophilic groups and the enhanced rate of mass transfer among solvent and water through phase inversion, the lignin concentrations improved, and the finger-like macro voids evolved and stretched out across a larger thickness [16]. It is intriguing to earn upon the expansion of the overall volume of the sponge-like portion due to enhanced lignin content in the membrane matrix. Such an effect enables an upsurge in the solution viscosity with increased lignin concentration. Therefore, it causes phase separation and slower demixing phenomena [17].

The pure PSf membrane SEM images are shown in **Fig. 4a**. The image depicts that the entire membrane could be seen without any trace of lignin. The lignin started to appear on the membrane surface when lignin was introduced to the membrane casting solution (**Figs. 4.9c, 4.9e, and 4.9g)**. It was evident that the agglomeration tends to increase with an increase in the lignin content in the casting from 0.25 to 1 wt.%. Thus, with

increased lignin content, the particles became more crowded, resulting in probable cluster formations and subsequent clogging of surface pores by the clusters.

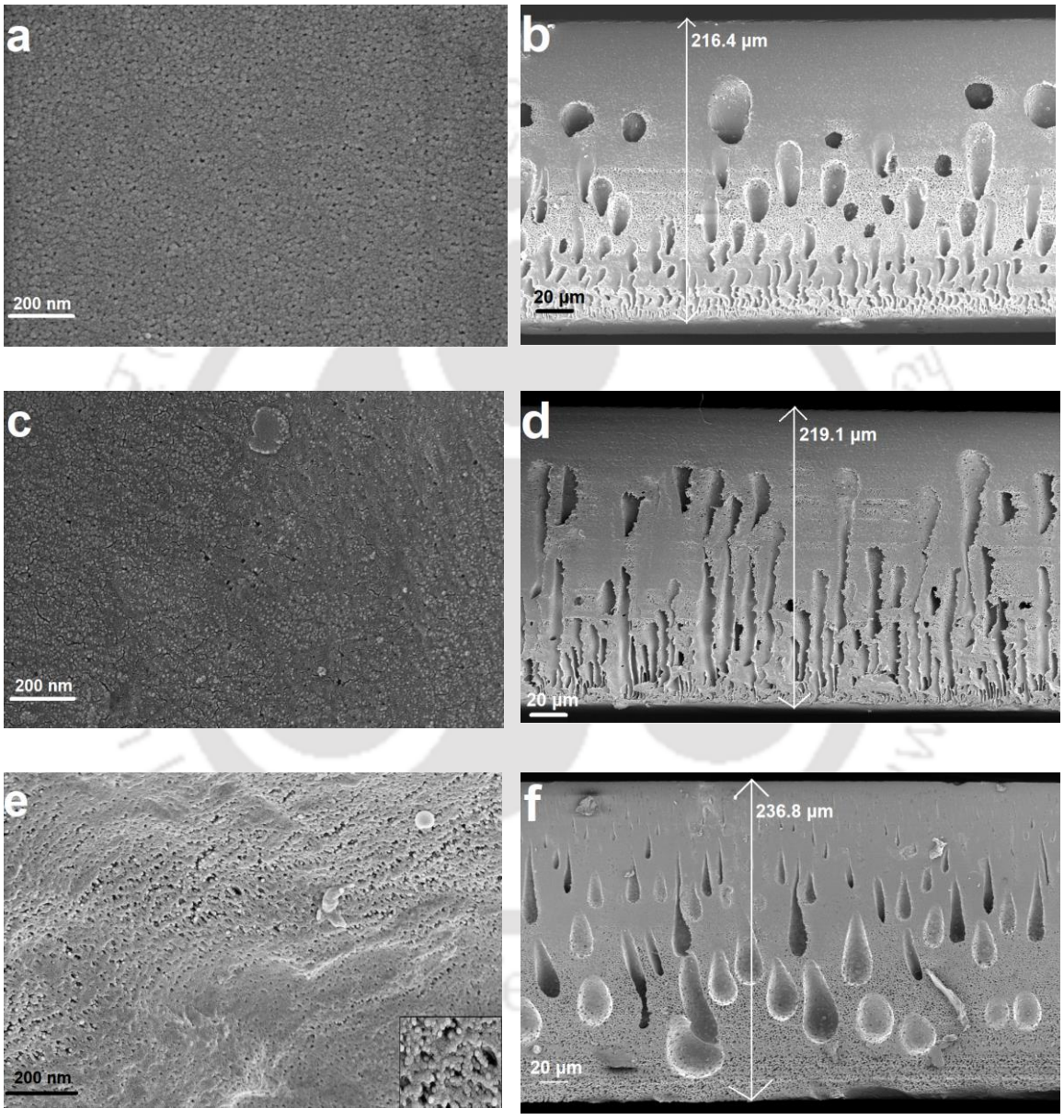

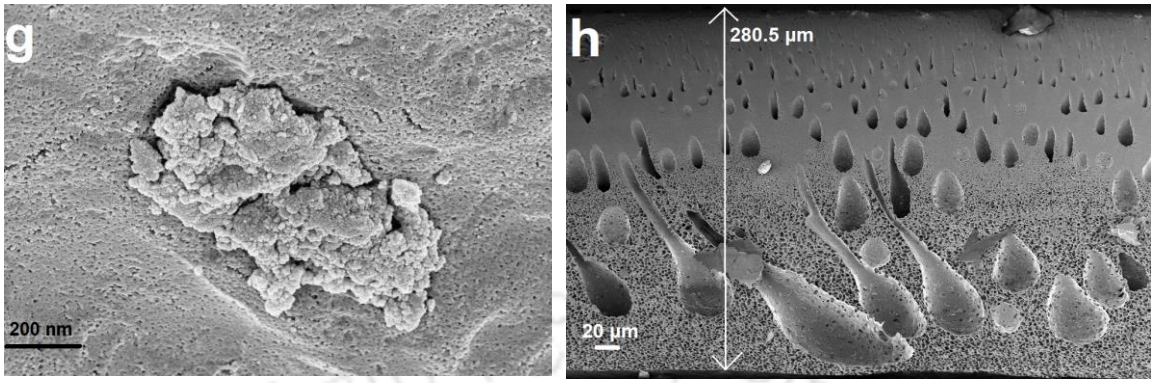

Figure 4.9: Surface (a, c, e, g) and Cross-section (b, d, f, h) SEM images of the prepared MMMs: (a, b) M0, (c, d) M1, (e, f) M2, and (g, h) M3.

In the XPS spectra of synthesized PSf membranes, three prominent peaks at 284 eV, 532 eV, and 168 eV have been ascribed to C 1s, O 1s, and S 2p (**Fig. 4.10a**). The high concentration of carbon in the PSf and lignin polymer is responsible for the C intensity in the manufactured membranes and causes signal amplification. The core level spectra for the O 1s and C 1s peaks of the pure PSf and PSf/lignin membranes in the XPS spectra were further analyzed and displayed in **Figs. 4.10b and 4.10c**. C-C/C-H, C-S, and C-O were each assigned to the PSf C 1s peak segments at binding energies of about 284.6, 285.1, and 286.2 eV. For PSf/lignin membranes, the peak positions marginally shifted towards the lower energy range and ranged respectively about 284.3-284.6, 284.8-285.1, and 259.8-286.1. Through quantitative analysis, it can be inferred that with increasing concentration of lignin, the peak area widened, and peaks became sharper. This has been probably due to existing C–OH, C=O, and COOH functional groups in the PSf/lignin MMM surfaces.

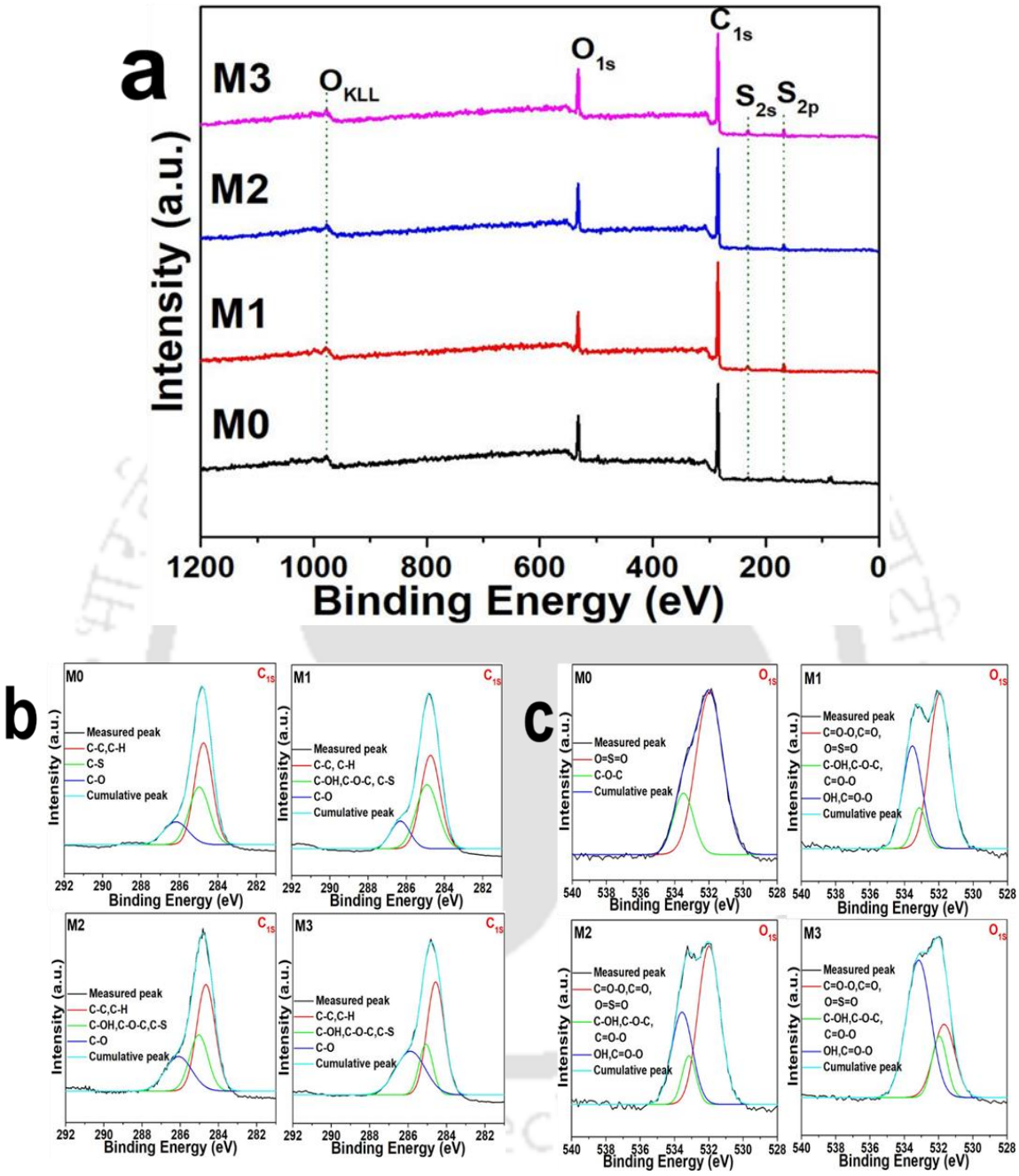

Figure 4.10: (a) The XPS survey spectra, (b) C 1s spectra, (c) O 1s spectra of fabricated membranes.

The C-O-C at 533.4 eV and the O=S=O at 531.9 eV referred to two peaks from the deconvolution of the O 1s in the pure PSf membrane. PSf is a predominant component of the membranes, so the pertinent bands resulted due to the polymer structure. The

appearance of the latest O 1s band at 533.6 eV signified the O-H species. This indicated that the spectra of PSf/lignin and PSf differed significantly. The alcohol units in lignin structures, such as guaiacyl, syringyl, and coniferyl alcohol units, have been responsible for the broad peaks of 533.4-533.6 eV in the lignin/PSf MMMs.

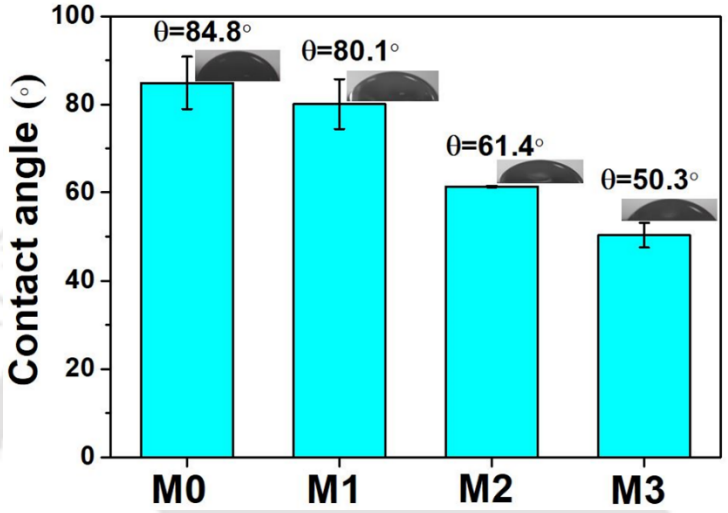

Figure 4.11: The water contact angle of synthesized membranes

Membrane hydrophobicity and hydrophilicity were determined with the static contact angle [18]. **Fig. 4.11** exhibits the outcomes of the wettability analysis of the synthesized membranes. Pure PSf membrane had a water contact angle of around 84.80º, which indicates a marginal hydrophilic characteristic. With increasing lignin concentration up to 1 wt.%, a reducing trend in contact angle was observed for the PSf/lignin MMMs. This trend was due to methoxyl, carboxyl, and other phenolic functional groups that appeared on the membrane surface because of the existing lignin. Such an inference improved the hydrophilicity of the membrane. The hydrophilicity for PSf/lignin MMMs improved for an increase in lignin percentage from 0.25 to 1 wt.%. This could be due to the nanolayer aggregation in the membrane matrix.

According to the findings of the zeta potential measurements conducted at pH 7 (**Table 4.2**), lignin's polyphenolic contents significantly affected the surface charge of the membranes. They could cause the zeta potential of pure PSf to alter from -16± 0.36 mV to -30.7± 0.42 mV (M3). During preliminary studies, it was noticed that developed

membranes had negative charges in the entire evaluated pH range. However, higher negative zeta potential values were observed as pH rises. Because of that, the adsorption amount of positively charged Cr (VI) is expected to increase with pH enhancement in the synthesized MMMs.

Table 4.2: Zeta potential and porosity of fabricated membranes

Membrane	Zeta potential (mV) at pH-7	Porosity (%)
M0	**-16 ± 0.36**	**18.01 ± 1.14**
M1	**-23.7 ± 0.63**	**43.0 ± 0.3**
M2	**-25.4 ± 0.7**	**52.53 ± 0.44**
M3	**-30.7 ± 0.42**	**67.0 ± 0.34**

Based on membrane weight, the porosity (%) was determined. The findings of the porosity assessment values are shown in **Table 4.2**. The addition of synthesized lignin nanolayers enhanced the porosity of the membrane. The hydrophilic character of MMMs was demonstrated with the water absorption findings for the PSf/lignin membranes. These assured a considerable increase in the amount of absorbed water. In this regard, it is important to note that the occurrence of hydrophilic components in the membrane framework altered the cross-sectional layout and porosity. This leads to significantly larger pore sizes. The FESEM images (**Fig. 4.9**) demonstrated these modifications in the membrane structure, and the measured porosity % from the water absorption test (**Table 4.2**) reaffirmed these observations. The rapid interchange among the solvent and non-solvent in the entire phase separation process for the membrane samples having 0.25, 0.5, and 1 wt% lignin resulted in the development of membranes with increased porosity. However, a higher concentration of lignin (1 wt.%) in the M3 membrane caused hydrophilic nanolayer aggregation in the membrane surface. This negatively influenced the membrane property, such as pure water flux.

4.2.3 Membrane Performances

Water flux data measured before and post-removal of Cr(VI) affirmed a sharp decline in water flow. This occurred with the accumulation of Cr molecules on the membrane surface and subsequent pore blockage. After the first cycle of filtration, the flux recovery was between 40-60 %. Also, it was observed that the M0 and M3 had suffered more than the M1 and M2 membranes. This is due to its lesser hydrophilic nature, smaller pore size of the M0 membrane surface, and a larger quantity of negatively charged lignin nanoparticles in the M3 membrane, causing higher Cr adsorption. Flux recovery significantly improved (65-80%) for all membranes after 2nd filtration cycle and affirmed better membrane stabilization. However, the FR % reduced after 3rd filtration cycle as membrane saturation was achieved due to blocked pores and complete utilization of active adsorption sites.

Fig. 4.12 depicts the test conclusions for Cr removal with the membranes in every filtration cycle. In all three filtration cycles, it was observed that the Pure PSf membrane (M0) was able to remove the least Cr (VI) % among all the synthesized MMMs. After the third cycle, the removal was as low as 40%. Over the course of three filtration cycles, an upward trajectory in the removal percentage can be seen for all samples. This is possibly due to the higher thickness, highly porous matrix structure, and utilization of all possible active sites and adsorption surfaces. As expected, the absence of adequate adsorbent functional groups prevented the pure PSf membrane from successfully removing Cr ions. However, the removal percentage of Cr enhanced to 98.75% in the presence of lignin (M3). According to Nassima et al. (2009), with increasing activated lignin concentration, the Cr(VI) removal efficiency increased despite enabling a reduction in the adsorption capacity [19]. Considering that some active sites were left unsaturated in the entire filtration course, the adsorption capacity can be inferred to have reduced. However, with increasing lignin dosage, the absolute number of active sites also enhanced, thereby increasing the overall adsorption efficiency of the membranes. The maximum removal of Cr(VI) was obtained for the M3 membrane, and the removal increased from M0 to M3 due to pore blocking and adsorption of Cr in the active sites

of the lignin matrix. This implies that the removal in these circumstances relies on both the pore size and surface charge of the MMMs.

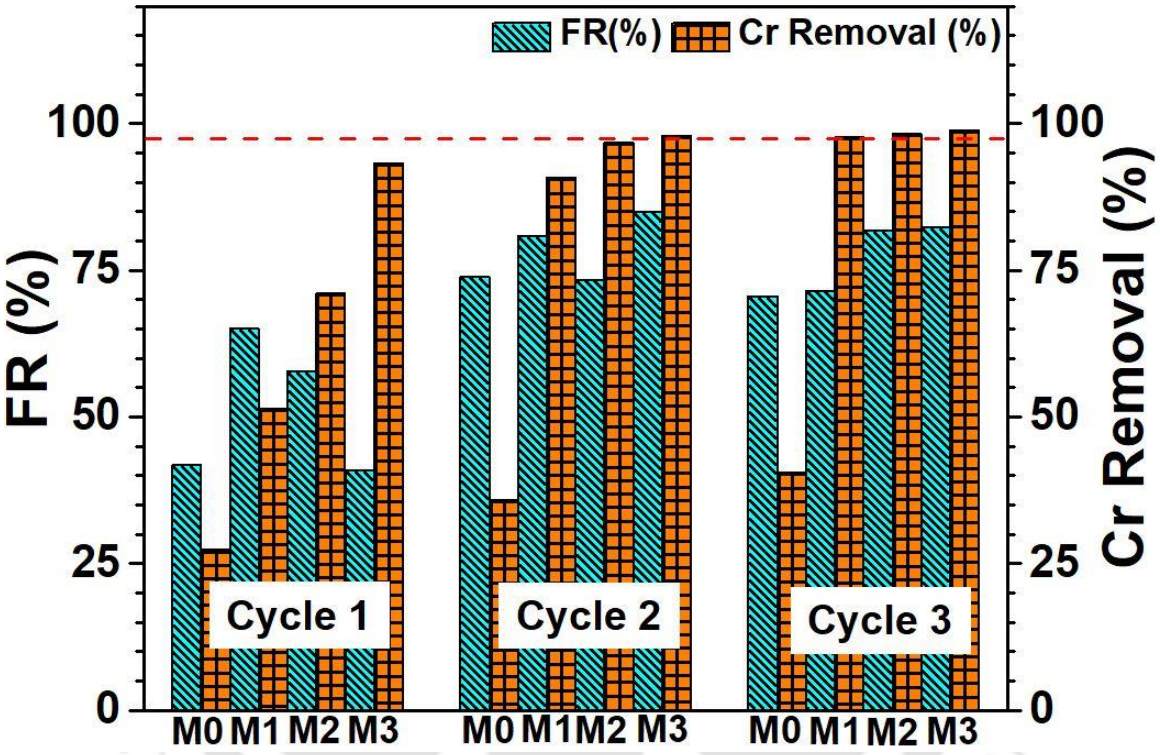

Figure 4.12: Cr removal and Flux recovery (FR) of the membranes during three filtration cycles

Fig. 4.13 depicts the spectrograms obtained from the energy-dispersive X-ray spectroscopy (EDX) analysis of the spent membranes after three filtration cycles. The primary elements, namely, carbon, oxygen, sulfur, and foulant Cr, were analyzed. Carbon and sulfur content gradually decreased with increased concentration of lignin in the PSf matrix (M0>M1>M2>M3). However, the oxygen content increased with

increasing lignin wt.% (M0<M1<M2<M3). This was due to polyphenolic functional groups and alcoholic subunits of lignin on the membrane matrix. All EDX spectra had well-defined peaks of Cr ions. This confirmed that the Cr(VI) ion was bound to the membrane surfaces. Also, the spectrum images of M2 and M3 depict agglomerated lignin lumps that could be seen on the membrane surface. On the EDX spectra of the M3 membrane, a maximum of 3.2 wt% Cr(VI) was observed. This was mainly due to lignin nanoparticle agglomeration. The adsorption phenomena of Cr(VI) onto the active lignin surface were thereby confirmed and corroborated with other membrane performance indices.

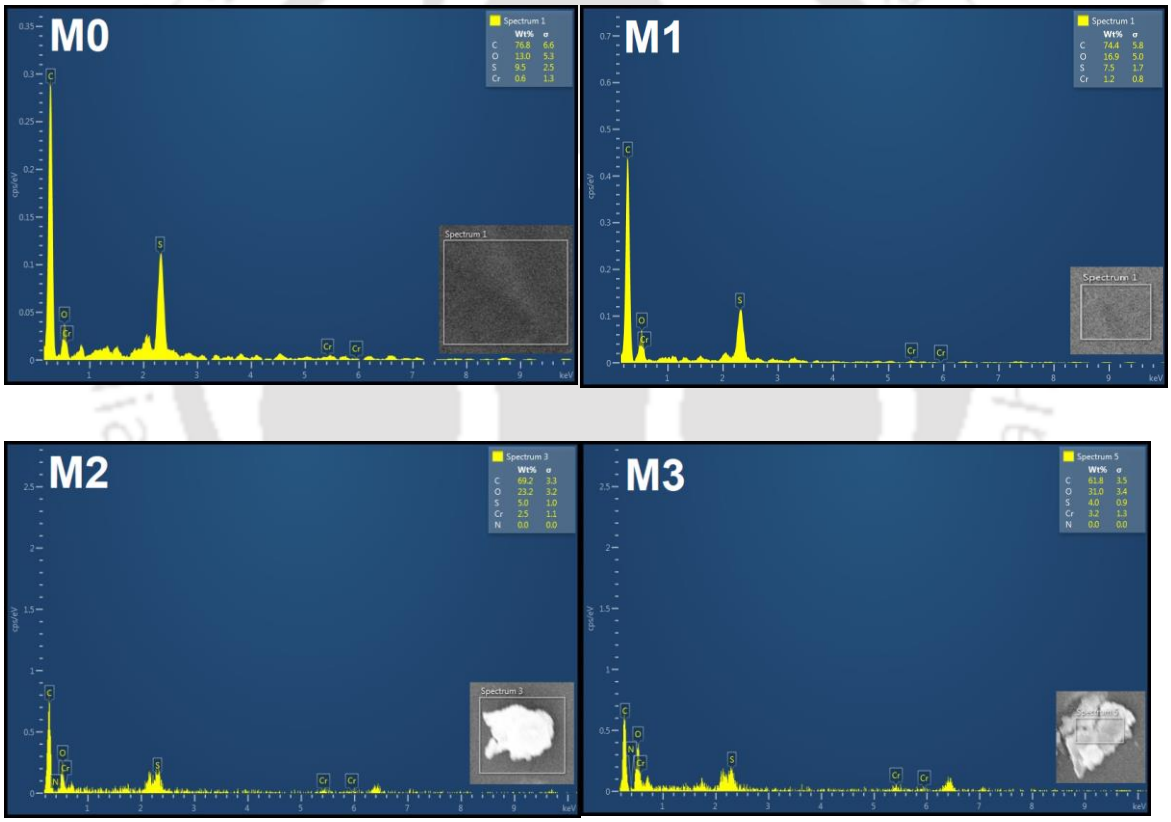

Figure 4.13: The EDX images of synthesized membranes after filtration

The PWF test was performed on the synthesized membranes. **Table 4.3** summarizes the results obtained in the conducted study. The PWF of the pure PSf membrane was the least and thereafter increased for lignin blend membranes due to their enhanced hydrophilicity. The improved PWF was due to the larger pores and the enhanced

porosity in the M1 and M2 membranes. The same thing can be observed in FESEM images (**Fig. 4.9**). On the other hand, dense nanolayer and agglomerates formation can be seen on the M3 membrane surface (**Fig. 4.9g**). This resulted in reduced PWF in comparison with that achieved for the M2 membrane.

Table 4.3: fouling behavior of the membranes

Membrane	PWF (L/m^2h)	TFR%	RFR%	IFR%
M0	**13.89**	**78.18**	**9.07**	**69.11**
M1	**101.01**	**62.47**	**37.48**	**25**
M2	**131.32**	**65.39**	**38.46**	**26.92**
M3	**123.75**	**71.43**	**32.65**	**38.78**

The antifouling study was conducted to analyze the membrane's antifouling behavior toward Cr ions and the possible influence of lignin on its alleviation. The outcomes of the studies are shown in **Table 4.3**, which includes the calculated values of the membrane fouling parameters. Due to the hydrophilicity of MMMs, the surface hydration guaranteed the buildup of a firmly linked water layer. This ensured the pertinent antifouling capabilities of the membranes. On the other hand, the electrostatic pull and adsorption of positively charged Cr(VI) onto the membranes affected the time course of water flux through the membranes. From the M0 to the M1 membrane, the TFR continued to decline. This is because lignin nanoparticles have a significant impact. Through a careful examination of the irreversible and reversible fouling factors and their underlying causes, the pertinent observations can be comprehended. Reversible fouling results due to the deposition of the foulant on the membrane and can be mitigated through a simple wash-off.

On the contrary, irreversible fouling occurred in the membrane pores and could not be retrieved. The addition of lignin positively influenced IFR reduction, resulting in reduced membrane performance. The membrane with a lower IFR corresponds to a higher RFR and better flux recovery. However, the M3 membrane exhibited higher IFR

than other PSf/lignin MMMs. This is due to better sponge-like pore formation in the case largely trapped Cr(VI) into the matrix. Higher negative surface charge and agglomerated lignin lumps enable greater Cr(VI) adsorption, resulting in blocked surface pores of the M3 membrane. The adsorbent nanolayers of lignin impede the passage of the foulants via the membrane surface pores of PSf/lignin MMMs. This assured enhanced reversible fouling in comparison to the pure PSf membrane.

A comparison of the outcome of the membranes synthesized in this study with those reported in the literature was conducted, and **Table 4.4** summarizes the findings. Even after three filtration cycles and an adequate flux, the synthesized membranes continued to remove Cr (VI) in a favorable manner.

Table 4.4: Comparison of membrane performance of this work with other PSf-based membranes

Sl no	Membrane	Filtration condition	PWF (L/m^2h)	Cr (VI) Removal (%)	Ref.
1	Aminated PSf/TiO_2 (0.4 g) composite membrane	Dead-end cell unit (100kPa) at pH 4	12.3	100	[20]
2	One wt.% Amide functionalized carbon nanotube/PSf composite membrane	UF test cell setup (0.49 MPa) at pH 2.6	210	94.2	[21]
3	Preacidified PSf/ diethanolamine membrane	UF setup at pH-7	235.2	100	[22]
4	PSf/PEG/HCl treated ZnO membrane	Dead-end cell (2 bar)	302	80	[23]
5	PSf/PVP/1% TiO_2	Cross-flow filtration unit (69 bar)	75.714	94.045	[24]
6	PSf/SiO2/PDA (polydopamine) membrane	Dead-end filtration apparatus (2 bar) at pH 3	13	94	[25]

7	PSf/3% mMMT (modified montmorillonite clay) MMM	Cross-flow filtration unit (2 bar)	271	95	[26]
8	10% 2-acrylamido-2-methylpropane sulfonic acid (AMPS) grafted PSf hollow fiber membrane	Home-built cross-flow filtration apparatus (4 bar) at pH 9.0	23.8	95.1	[27]
9	2.5% ABA-PVC (4-aminobenzoic acid- polyvinyl chloride)/PSf/TiO_2 (300 mg) composite membrane	Stainless steel dead-end filtration unit (100 kPa) at pH 4	6.5	88	[28]
10	PSf/lignin (1 wt.%) MMM	Rustic dead-end filtration setup (2 bar) at pH 7	123.75	98.7	This work

Membranes must have substantial mechanical strength to serve in several applications that demand sufficient mechanical stress in the membrane. For this purpose, each sample was examined with a Universal testing machine for its mechanical stress parameters. This was addressed to determine the influence of lignin content on the membrane's mechanical characteristics. **Table 4.5** summarizes the outcomes of unidirectional tensile tests for both membrane samples before and after filtration. For an increase in the lignin content to about 1 wt.% in the membranes, tensile strength and elongation % at the breakpoint gradually rose. For pristine membranes, a synergistic behavior was seen for the tensile strength and the elongation at break [29] [30]. The development of sponge-like structures and the advantageous mechanical properties of lignin contributed towards improved mechanical strength. Also, the presence of lignin and its uniform distribution throughout the PSf matrix allowed the membranes to have greater mechanical strength. The abrasion during filtration resulted in greater fragility after filtration and reduced elasticity. Additionally, using HCl as a cleaning agent in the backwashing process would have caused degradation in the PSf structure. Membranes were subjected to mechanical stress, chemical exposure, and fouling throughout the filtering process, all of which caused them to lose tensile strength and elasticity. The membranes had experienced swelling, fouling, and degradation, which had a detrimental impact on their mechanical characteristics [31][32]. After filtration, the

elongation% at the breakpoint decreased, suggesting less flexibility and elongation capacity of the used membranes as a result of the drop in tensile strength, which showed reduced resistance to stress.

Table 4.5: Mechanical properties of the fabricated membranes before and after filtration

Membrane	Before filtration		After filtration	
	Tensile (MPa)	Elongation (%)	Tensile (MPa)	Elongation (%)
M0	**4.55 ± 0.45**	**18.1 ± 1.62**	**4.77 ± 0.33**	**16.85 ± 0.67**
M1	**5.48 ± 0.16**	**24.25 ± 2.91**	**4.14 ± 0.12**	**18.3 ± 0.28**
M2	**5.6 ± 0.27**	**27.15 ± 0.90**	**4.85 ± 1.02**	**21.95 ± 3.88**
M3	**5.76 ± 0.28**	**29.0 ± 0.73**	**5.29 ± 0.21**	**27.2 ± 1.85**

4.3 Cost Analysis

The affordability of membrane technology is the feature that makes it industrially competitive. The price of typical polymeric membranes for industrial-scale operations ranges between $50 to $200 per m^2 [33]. To conceptually determine the overall expenditure of the materials needed for the fabrication of 1 wt% PSf/lignin mixed matrix membrane of 1 m^2 surface area, conceptual cost estimation was conducted [34]. To do so, 68 USD was required for a 1 m^2 membrane area. The membrane required 239 mL NMP, 58.5 g PSf, and 3 g alkaline lignin. However, the data presented in this work inspired optimism regarding long-term reliability. The projected membrane cost was predicted to be quite close to the stated figure. Also, given its superior performance, the membrane can be regarded as a cost-effective membrane.

4.4 Summary

This work provided a simple and useful method for enhancing the PSf membrane characteristics by incorporating alkaline lignin. Such membranes have a greater ability to regenerate. Amorphous lignin extracted from Ravenna grass possessed a negative zeta potential value of -22.3 mV at a pH of 7. The lignin fillers doping into the PSf

matrix increased its zeta potential value (from -15.1 mV up to -30.1 mV) and the hydrophilicity of the membranes. Phenolic functional groups of lignin bound onto the PSf polymer matrix and enhanced the mechanical strength and thermal stability of PSf/lignin membranes. Morphological changes were confirmed by SEM and AFM images, where the addition of 1 wt% lignin enhanced the membrane thickness by 64.1 µm, and surface roughness was increased by 270% compared to pure PSf membrane. The synthesized membranes were examined through FTIR and XPS, and the analyses affirmed the successful blending of lignin into the PSf matrix. PSf/lignin MMMs produced the most impressive results in terms of PWF and Cr removal. The contact angle data demonstrated that when the lignin weight % in the membrane matrix increased, the hydrophilicity of the membranes increased as well, leading to improved PWF. The Cr (VI) removal primarily depended upon the membrane charge and the porous matrix framework. The M3 membrane with a 67% porous structure and a surface charge of -30.7 mV achieved a removal efficiency of 98.75 % after 3rd filtration cycle.

In terms of overall performance, considering removal efficiency (98.5%) and antifouling behavior (26.9% IFR) after three filtration cycles, the M2 membrane (0.5 wt.% lignin) could be inferred to have a very promising outcome. It can be concluded that the incorporation of lignin improved the membrane function and morphology. Additionally, due to their propensity to regenerate, the fabricated lignin/PSf membranes could be deployed repetitively to remove positively charged heavy metal ions. Such a principle was crucial to reduce membrane fouling and extend membrane lifespan. For the remediation of Cr(VI) and other heavy metals from wastewater, this work offers very useful insights and can serve as a benchmark for the development of extremely effective PSf/lignin MMMs from inexpensive and waste material sources and with an easy synthesis process. Future studies can also be devoted to multi-heavy metal removal and real wastewater systems.

References

[1] S. Dhara, N. S. Samanta, R. Uppaluri, and M. K. Purkait, "High-purity alkaline lignin extraction from Saccharum ravannae and optimization of lignin recovery through response surface methodology," *Int. J. Biol. Macromol.*, vol. 234, p. 123594, 2023, doi: https://doi.org/10.1016/j.ijbiomac.2023.123594.

[2] A. Alkhouzaam and H. Qiblawey, "Synergetic effects of dodecylamine-functionalized graphene oxide nanoparticles on antifouling and antibacterial properties of polysulfone ultrafiltration membranes," *J. Water Process Eng.*, vol. 42, p. 102120, Aug. 2021, doi: 10.1016/j.jwpe.2021.102120.

[3] N. S. Samanta, S. Banerjee, P. Mondal, Anweshan, U. Bora, and M. K. Purkait, "Preparation and characterization of zeolite from waste Linz-Donawitz (LD) process slag of steel industry for removal of Fe3+ from drinking water," *Adv. Powder Technol.*, vol. 32, no. 9, pp. 3372–3387, 2021, doi: https://doi.org/10.1016/j.apt.2021.07.023.

[4] C. Bhattacharya, N. Maiti, B. M. Mandal, and S. N. Bhattacharyya, "Thermodynamic characterization of miscible blends from very similar polymers by inverse gas chromatography. The poly(ethyl acrylate)-poly(vinyl propionate) system," *Macromolecules*, vol. 22, no. 10, pp. 4062–4068, Oct. 1989, doi: 10.1021/ma00200a043.

[5] E. Pregi, D. Kun, V. Vu, and B. Pukánszky, "Structure evolution in poly(ethylene-co-vinyl alcohol)/lignin blends: Effect of interactions and composition," *Eur. Polym. J.*, vol. 111, pp. 74–81, 2019, doi: https://doi.org/10.1016/j.eurpolymj.2018.11.040.

[6] H. Ni, S. Ren, G. Fang, and Y. Ma, "Determination of Alkali Lignin Solubility Parameters by Inverse Gas Chromatography and Hansen Solubility Parameters," *BioResources*, vol. 11, Mar. 2016, doi: 10.15376/biores.11.2.4353-4368.

[7] N. S. Samanta, P. P. Das, P. Mondal, U. Bora, and M. K. Purkait, "Physico-chemical and adsorption study of hydrothermally treated zeolite A and FAU-type zeolite X prepared from LD (Linz–Donawitz) slag of the steel industry," *Int. J. Environ. Anal. Chem.*, pp. 1–23, May 2022, doi: 10.1080/03067319.2022.2079082.

[8] P. V. Chai, "Evaluation of Iron oxide decorated on graphene oxide (FE3O4 / GO) nanohybrid incorporated in PSF membrane at different molar ratios for Congo red rejection Jurnal Teknologi E VALUATION OF I RON O XIDE D ECORATED ON," no. January, 2017, doi: 10.11113/jt.v79.10440.

[9] H. Namdar, A. Akbari, R. Yegani, and H. Roghani-Mamaqani, "Influence of aspartic acid functionalized graphene oxide presence in polyvinylchloride mixed matrix membranes on chromium removal from aqueous feed containing humic acid," *J. Environ. Chem. Eng.*, vol. 9, no. 1, p. 104685, 2021, doi: https://doi.org/10.1016/j.jece.2020.104685.

[10] D. Dong, A. L. Fricke, B. M. Moudgil, and H. Johnson, "Electrokinetic study of kraft lignin," *Tappi J.*, vol. 79, no. 7, pp. 191–197, 1996.

[11] D. Rana, B. M. Mandal, and S. N. Bhattacharyya, "Miscibility and phase diagrams of poly(phenyl acrylate) and poly(styrene-co-acrylonitrile) blends," *Polymer (Guildf).*, vol. 34, no. 7, pp. 1454–1459, 1993, doi: https://doi.org/10.1016/0032-3861(93)90861-4.

[12] P. Pedrosa, J. A. Pomposo, E. Calahorra, and M. Cortazar, "On the glass transition behavior, interaction energies, and hydrogen-bonding strengths of binary poly(p-vinylphenol)/polyether blends," *Macromolecules*, vol. 27, no. 1, pp. 102–109, Jan. 1994, doi: 10.1021/ma00079a016.

[13] M. U. M. Junaidi, C. P. Leo, A. L. Ahmad, S. N. M. Kamal, and T. L. Chew, "Carbon dioxide separation using asymmetric polysulfone mixed matrix membranes incorporated with SAPO-34 zeolite," *Fuel Process. Technol.*, vol. 118, pp. 125–132, 2014, doi: https://doi.org/10.1016/j.fuproc.2013.08.009.

[14] D. Nasirian, I. Salahshoori, M. Sadeghi, N. Rashidi, and M. Davidson, "Investigation of the gas permeability properties from polysulfone/polyethylene glycol composite membrane," *Polym. Bull.*, vol. 77, Oct. 2020, doi: 10.1007/s00289-019-03031-3.

[15] M. U. M. Junaidi and R. Rohani, "Diamine Modified Polysulfone and P-84 Symmetric Membranes for Hydrogen/Carbon Dioxide Separation," *Int. J. Appl. Eng. Res.*, vol. 14, pp. 2883–2889, Jul. 2019.

[16] N. F. Ishak, N. A. Hashim, and M. H. D. Othman, "Antifouling properties of hollow fibre alumina membrane incorporated with graphene oxide frameworks," *J. Environ. Chem. Eng.*, vol. 8, no. 4, p. 104059, 2020, doi: https://doi.org/10.1016/j.jece.2020.104059.

[17] Y. Li, S. Huang, S. Zhou, A. G. Fane, Y. Zhang, and S. Zhao, "Enhancing water permeability and fouling resistance of polyvinylidene fluoride membranes with carboxylated nanodiamonds," *J. Memb. Sci.*, vol. 556, pp. 154–163, 2018, doi: https://doi.org/10.1016/j.memsci.2018.04.004.

[18] Maria, M. Farooq, W. Ahmad, and F. Subhan, "Fabrication of rGO-CuO and/or Ag2O Nanoparticles Incorporated Polyvinyl Acetate Based Mixed Matrix Membranes for the Removal of Cr6+ from Anti-corrosive Paint Industrial Wastewater," *J. Environ. Chem. Eng.*, vol. 9, p. 105151, Feb. 2021, doi: 10.1016/j.jece.2021.105151.

[19] T. Nassima and A. Moussa, "Chromium (VI) adsorption onto activated kraft lignin produced from alfa grass (Stipa tenacissima)," *BioResources*, vol. 4, May 2009.

[20] M. S. Jyothi, V. Nayak, M. Padaki, R. Geetha Balakrishna, and K. Soontarapa, "Aminated polysulfone/TiO2 composite membranes for an effective removal of Cr(VI)," *Chem. Eng. J.*, vol. 283, pp. 1494–1505, 2016, doi:

https://doi.org/10.1016/j.cej.2015.08.116.

[21] P. Shah and C. N. Murthy, "Studies on the porosity control of MWCNT/polysulfone composite membrane and its effect on metal removal," *J. Memb. Sci.*, vol. 437, pp. 90–98, 2013, doi: https://doi.org/10.1016/j.memsci.2013.02.042.

[22] Z.-Q. Huang, W. Cai, and Z. Zhang, "Modification and acidification of polysulfone as effective strategies to enhance adsorptive ability of chromium (VI) and separation properties of ultrafiltration membrane," *J. Appl. Polym. Sci.*, vol. 139, no. 19, p. 52127, May 2022, doi: https://doi.org/10.1002/app.52127.

[23] P. Mahajan-Tatpate, S. Dhume, and Y. Chendake, "Recovery of chromium using membrane containing charged material," *IOP Conf. Ser. Mater. Sci. Eng.*, vol. 1146, no. 1, p. 12022, 2021, doi: 10.1088/1757-899X/1146/1/012022.

[24] L. Jacob, T. Moses, S. Joseph, L. Varghese, and S. Nalinakshan, "Study on the Effective Removal of Chromium VI via Polysulfone/TiO2 Nanocomposite Membranes and Its Antifouling Property," 2019, pp. 157–166.

[25] S. Habibi, A. Nematollahzadeh, and S. A. Mousavi, "Nano-scale modification of polysulfone membrane matrix and the surface for the separation of chromium ions from water," *Chem. Eng. J.*, vol. 267, pp. 306–316, 2015, doi: https://doi.org/10.1016/j.cej.2015.01.047.

[26] L. Jacob, S. Joseph, and L. A. Varghese, "Polysulfone/MMT Mixed Matrix Membranes for Hexavalent Chromium Removal from Wastewater," *Arab. J. Sci. Eng.*, vol. 45, no. 9, pp. 7611–7620, 2020, doi: 10.1007/s13369-020-04711-3.

[27] H. Xu, J. Wei, and X. Wang, "Nanofiltration hollow fiber membranes with high charge density prepared by simultaneous electron beam radiation-induced graft polymerization for removal of Cr(VI)," *Desalination*, vol. 346, pp. 122–130, 2014, doi: https://doi.org/10.1016/j.desal.2014.05.017.

[28] V. Nayak, K. Soontarapa, R. G. Balakrishna, M. Padaki, V. Y. Zadorozhnyy, and S. D. Kaloshkin, "Influence of TiO2 charge and BSA-metal ion complexation on retention of Cr (VI) in ultrafiltration process," *J. Alloys Compd.*, vol. 832, p. 153986, 2020, doi: https://doi.org/10.1016/j.jallcom.2020.153986.

[29] D. Rana, H. L. Kim, H. Kwag, and S. Choe, "Hybrid blends of similar ethylene 1-octene copolymers," *Polymer (Guildf).*, vol. 41, no. 19, pp. 7067–7082, 2000, doi: https://doi.org/10.1016/S0032-3861(00)00066-5.

[30] D. Rana, C. H. Lee, K. Cho, B. H. Lee, and S. Choe, "Thermal and mechanical properties for binary blends of metallocene polyethylene with conventional polyolefins," *J. Appl. Polym. Sci.*, vol. 69, no. 12, pp. 2441–2450, Sep. 1998, doi: https://doi.org/10.1002/(SICI)1097-4628(19980919)69:12<2441::AID-APP15>3.0.CO;2-#.

[31] D. Rana, K. Cho, T. Woo, B. H. Lee, and S. Choe, "Blends of ethylene 1-octene

copolymer synthesized by Ziegler–Natta and metallocene catalysts. I. Thermal and mechanical properties," *J. Appl. Polym. Sci.*, vol. 74, no. 5, pp. 1169–1177, Oct. 1999, doi: https://doi.org/10.1002/(SICI)1097-4628(19991031)74:5<1169::AID-APP13>3.0.CO;2-W.

[32] D. Rana *et al.*, "Blends of ethylene 1-octene copolymer synthesized by Ziegler–Natta and metallocene catalysts. II. Rheology and morphological behaviors," *J. Appl. Polym. Sci.*, vol. 76, no. 13, pp. 1950–1964, Jun. 2000, doi: https://doi.org/10.1002/(SICI)1097-4628(20000624)76:13<1950::AID-APP13>3.0.CO;2-8.

[33] B. K. Nandi, R. Uppaluri, and M. K. Purkait, "Preparation and characterization of low cost ceramic membranes for micro-filtration applications," *Appl. Clay Sci.*, vol. 42, no. 1, pp. 102–110, 2008, doi: https://doi.org/10.1016/j.clay.2007.12.001.

[34] I. Das, S. Das, R. Dixit, and M. M. Ghangrekar, "Goethite supplemented natural clay ceramic as an alternative proton exchange membrane and its application in microbial fuel cell," *Ionics (Kiel).*, vol. 26, no. 6, pp. 3061–3072, 2020, doi: 10.1007/s11581-020-03472-1.

Chapter 5

Preparation and characterization of PSf-GO-alkaline lignin ultrafiltration composite membrane for Pb^{2+} and Eosin Y dye removal

The detailed experimental method of lignin extraction and the GO synthesis process is discussed in this chapter. Lignin/graphene oxide incorporated polysulfone composite membranes were fabricated using the phase inversion method and PEG 6000 as a pore-forming agent. A series of analyses were conducted to assess the physicochemical characteristics of the nanofillers and the resultant membranes. Filtration operations were carried out using an aqueous solution containing both lead (Pb) and Eosin Y dye. A study on the adsorption of $Pb2^{+}$ ions in an aqueous solution was conducted using the optimized lignin/GO membrane. The adsorption process was investigated through Langmuir and Freundlich isotherm analyses. The background, state-of-the-art literature, and scope of this work are reported in Chapter 1, Section 1.1.3, 1.3.4, and Section 1.4.4, respectively. This research has been formally recognized in the Separation and Purification Technology journal.

5.1 Materials and Methods

5.1.1 Chemicals

Sodium Nitrate (99%), Potassium Permanganate (98.5%), Manganese (II) sulfate (99%), Hydrogen peroxide (30%), Potassium hydroxide flakes (84%), Nitric acid (70%), Sulfuric acid (98%), Polysulfone beads, N-Methyl-2-Pyrrolidone (99.5%), Hydrochloric acid (38%), and Lead nitrate [Pb $(NO_3)_2$] (99%) were procured from Merck Life Science. Eosin Y (88%) was purchased from Nice Chemicals, India. Synthetic-grade graphite powder with a particle size of 325 mesh was supplied by SRL, India.

5.1.2 Lignin extraction from Ravenna grass

The optimized conditions from previous work were used to extract alkaline lignin from Ravenna grass biomass (RGB) [1]. Dry RGB was ground and sieved using a sieve of 150 mesh size. 6.41 wt% (w/v) of sieved biomass was then suspended into 2.4 % (w/v) KOH solution and pre-treated at 100℃ oil baths for 177 minutes. After pre-treatment, the solution was filtered with Grade 1 Whatman filter paper and a vacuum filtration setup. 6M HNO_3 solution was dropwise added into the filtrate to precipitate the lignin. At around pH 2, alkaline lignin coagulated in the solvent. The resulting semi-solidified liquid was centrifuged at 10000 rpm to separate the solid lignin fraction. Additionally, the solid residue was washed with warm water and centrifuged again to remove the remaining acid residue from the resultant lignin fraction. Solid lignin residues were further suspended in 20% (v/v) H_2SO_4 solution and autoclaved at 121℃ for one h. This step was performed to remove the remaining sugars and other impurities from the lignin sample. After autoclaving, the solution was filtered, and the retentate solid alkaline lignin residues were washed with deionized water. This was followed by oven drying.

5.1.3 Graphene oxide (GO) synthesis

Graphene oxide sheets were synthesized from graphite powder and via the method given by Sontakke and Purkait (2020) [2]. Initially, 2g of graphite and 1g of sodium nitrate ($NaNO_3$) were mixed in a cold-water bath (4°C) and stirred for 15 minutes after adding 50ml of 98% H_2SO_4. 6g of potassium permanganate ($KMnO_4$) was gradually introduced to prevent exothermic reactions and maintain the temperature below 20°C. After 45 minutes at room temperature, the mixture thickened into a dark brown paste. The mixture was subsequently subjected to heating on a hot plate at a temperature of 100°C for a duration of 45 minutes. Subsequently, it was diluted by incorporating 200 mL of deionized water, followed by the gradual addition of 10 mL of 30% hydrogen peroxide (H_2O_2) to convert any remaining potassium permanganate ($KMnO_4$) into soluble manganese sulfate ($MnSO_4$). Furthermore, 250mL 0.1 N HCl solution was mixed with the obtained suspension [3]. Following centrifugation at approximately 10,000 rpm for 15 minutes, the supernatant was discarded until a neutral pH was reached. Thereby, a viscous brown layer of pure graphene oxide (GO) above the oxidation by-products was

realized. The GO layer was isolated by rinsing it with warm water and underwent freeze-drying for 12 hours. Thereafter, it was then placed in a desiccator for storage.

5.1.4 Lignin and GO characterization

The morphology of lignin and GO particles was analyzed using a Sigma 300 (Zeiss, Germany) Field emission scanning electron microscope (FESEM). The samples were gold coated before analysis at 3 Kv and different magnifications. The corresponding phases of the alkaline lignin and GO powder substances were evaluated using the JEOL 2100F (Japan) Field emission transmission electron microscopy (FETEM) apparatus. To determine the surface charge of Lignin and GO particles, a 1 mg/mL solution in water was made, and the aqueous solutions were sonicated at 50 Hz for 30 minutes prior to the analysis. The Litesizer 500 device (Maker- Anton Paar, Austria) was subsequently utilized to determine the Zeta potential of Lignin and GO nanoparticles.

The ATR-FTIR spectra were obtained with an optimum resolution of 0.5 cm^{-1} utilizing FTIR analysis in a Spectrum two-PerkinElmer instrument (Singapore) and for a scanning spectral range of 4000-400 cm^{-1}. A TG209 F1 NETZSCH TGA instrument was used to obtain the thermal degradation graph of lignin and GO across the 25-800°C temperature range and with a 10°C/min heating rate. The crystallinity properties of both samples were studied through a Smartlab 9KW Powder XRD system (Rigaku Technologies, Japan). The surface area, pore volume, and pore diameters of the samples were determined with Autosorb-IQ MP Surface Area and pore size analyzer (Quantachrome, USA).

5.1.5 Membranes fabrication

The phase inversion method was used to fabricate the PSF-based lignin/GO composite membranes. In this procedure, a homogeneous polymer solution is demixed by immersion in a non-solvent bath. Accordingly, an effective procedure known as immersion precipitation phase inversion was adopted in this work. First, synthesized GO and lignin nanoparticles (0-1.5 wt.% of PSf) were added to the NMP solvent and homogenized with sonication (50 Hz and 120 Watts) for 30 minutes. Following sonication, PSf beads and PEG 6000 were dissolved in the homogenous solution. The resultant mixture underwent heating and stirring at 65°C for 4 hours at 150 rpm on a hot plate-magnetic stirrer. This

process ensured the complete dissolution of PSf beads, thereby forming a thick and uniform casting solution. The casting solution was kept at 60 °C in a hot air oven for six hours for degassing.

Following degassing, the casting solution was manually cast on a clean glass plate and with a casting knife. The effective membrane casting area measured 11 cm in width and 21 cm in length, and the casting knife was positioned 350 µm above the glass plate. To ensure thorough solidification and solvent removal, the newly fabricated membrane on the glass plate was solidified through immersion in a deionized water bath for 24 hours. The membranes were then allowed to air dry at ambient temperature. To fabricate alternate lignin/GO composite membranes, the concentrations of alkaline lignin and GO were adjusted. Further details on the components and their respective proportions in each membrane formulation have been detailed in **Table 5.1**.

Table 5.1: Composition of fabricated membranes

Membrane	PSF (g)	NMP (g)	PEG 6000 (g)	Lignin (mg)	GO (mg)	Total Wt. (g)
LGM0	1.2	10.2	0.6	0.0	0.0	12
LGM1	1.2	10.182	0.6	18	0.0	12
LGM 2	1.2	10.182	0.6	0.0	18	12
LGM 3	1.2	10.182	0.6	9	9	12
LGM4	1.2	10.182	0.6	12	6	12
LGM 5	1.2	10.182	0.6	6	12	12

5.1.6 Membrane characterization

Surface roughness analysis of the membranes was carried out with an Atomic Force Microscope (AFM) (Cypher S, manufactured by Oxford Instruments in the United Kingdom). On the top layer of the magnetic metal plate, small rectangular membranes were cut and affixed with carbon tape. Following that, the imaging was performed.

A Zeiss FESEM Gemini 300 was used to examine the membrane cross-sections, while a Zeiss FESEM Sigma 300 was used to assess the surface structures of the synthesized membranes. Prior to the assessment, all specimens were gold-coated. Cross-sectional pictures were acquired at 700x magnification, and surface depictions were taken at 100kx magnification. In all assessments, the extra high-tension (EHT) voltage was specified as 5 kV.

The surface composition and chemical state of the membrane components were analyzed using X-ray photoelectron spectroscopy. A PHI 5000 Versa Probe III Photoelectron Spectrometer (ULVAC-PHI, Inc., Japan) was used to investigate the membranes. Survey spectra (1200 to 2 eV) were taken at 1.0 eV intervals and for 200 eV pass energy. The high-resolution spectra of C1S and O1S were obtained using 55 eV pass energy at 0.05 eV intervals in the 281-292 eV and 525-540 eV regions.

The zeta potential of the fabricated membranes was determined using the Anton Paar Litesizer 500 instrument. The membranes were sliced into bite-sized pieces and soaked in pH 7 deionized water. Subsequently, the samples were set aside for 12 hours. Sonication for 30 minutes was done prior to the assessment.

Following the gravimetric technique, the following expression was used to calculate the porosity (ε) of the synthesized membranes.

$$\varepsilon = (\omega 1 - \omega 2)/(A \times l \times \rho) \quad (1)$$

In the given equation, ω1 and ω2 correspond to wet and dry membrane weight (g). A represents the effective membrane area (cm^2), l stands for the membrane thickness (cm), and water density (0.998 g/cm^3) is represented as ρ.

The water contact angle on the membrane surface was assessed through the implementation of the sessile drop procedure. For this, initially, the membranes were trimmed to the desired dimensions. Subsequently, both ends of the membrane samples were secured to a transparent slide using tape. Following this, a minuscule droplet of deionized water was carefully dispensed onto the dry membrane surface with a micro syringe. The resultant water contact angle micrograph was captured and analyzed using Holmarc's contact angle meter (Model No: HO-ED-M-01).

The evaluation of membrane elongation and tensile strength at the point of rupture, both before and after three filtration cycles, was conducted using a 5KN electromechanical universal testing machine (UTM) (Z005TNProline, manufactured by Zwick Roell in Austria). To perform the mechanical analysis, each sample was divided into rectangular pieces, and the assessment was carried out at a speed of 5 mm/min.

5.1.7 Membrane filtration

Firstly, 1598 mg lead nitrate was added into 1000 mL of deionized water to realize the 1000 ppm Pb^{2+} stock solution. Similarly, 1g of dye was dissolved in 1000 ml of deionized water to realize the 1000 ppm stock solution of Eosin Y. The stock solutions were further diluted to the desired concentrations for filtration. The Pb^{2+} and Eosin Y separation processes were carried out using a self-assembled dead-end filtration apparatus. The fabricated membrane was encased within the filtration device, perched on a hole-perforated stainless-steel sheet, and the membrane filtrations were performed under 2 bar pressure. A mix of 10 ppm Eosin Y dye and 2 ppm Pb^{2+} solution was prepared for filtration. The pure water flux (PWF) was measured prior to the filtration study. Initially, a 3-bar pressure was maintained for 30 min to prevent compaction-related influences. At a 2-bar pressure, the PWF was determined and represented as J_i ($L/m^2.h$) with the following equation.

$$J = \frac{V}{A.\Delta t} \quad (2)$$

In the above expression, V (L) represents the collected permeate volume over a sampling period, A denotes the effective filtration area (m^2), and Δt (h) stands for the time span. Upon assessing the permeate water flux (PWF), the performance evaluation of custom-manufactured membranes over three filtration/regeneration cycles was conducted. Each cycle entailed the filtration of a solution comprising 2 ppm of Pb^{2+} and 10 ppm of Eosin Y for 120 minutes at pH 7 and at a constant trans-membrane pressure of 2 bar. Subsequently, membranes were subjected to backwashing with aqueous HCl solution (pH-3) for 15 minutes to regenerate the fouled membranes. Post the third filtration cycle, the PWF of the membrane was denoted as J_f. Subsequently, the PWF of the membrane

after backwashing was represented as J_r. Leveraging J_i, J_f, and J_r, the fouling parameters of the membranes were computed with the subsequent equations [4].

$$FR = J_r/J_i \quad (3)$$

$$TFR = (J_i - J_f)/J_i \quad (4)$$

$$RFR = (J_r - J_f)/J_i \quad (5)$$

$$IFR = (J_i - J_r)/J_i \quad (6)$$

where FR TFR, RFR, and IFR are flux recovery, total fouling ratio, reversible fouling ratio, and irreversible fouling ratio, respectively. The membrane rejection percentages for Eosin Y and Pb^{2+} removal were determined with the following expressions:

$$Eosin\ Y\ Rejection\ (\%) = \frac{{C_i}^E - {C_f}^E}{{C_i}^E} \times 100 \quad (7)$$

$$Pb^{2+} Removal\ (\%) = \frac{{C_i}^P - {C^P}_p}{{C_i}^P} \times 100 \quad (8)$$

where C_i^E and C_f^E are the initial and final concentrations of Eosin Y, measured by using a UV–vis spectrophotometer (SHIMADZU UV-1900), and C_i^P and C_p^P are the concentrations of Pb^{2+}, measured by Atomic absorption spectroscopy (AAS, SHIMADZU AA-6880), in the feed and permeate streams, respectively.

5.1.8 Pb^{2+} Adsorption Study

The most efficient membrane from the membrane filtration test regarding lead removal was selected to study further Pb^{2+} adsorption on the Lignin/GO composite membrane. Batch analyses were carried out to assess the Pb^{2+} adsorbing behavior of the Lignin/GO composite membrane. For this purpose, 20-100 ppm lead solution was prepared, and the pH of the solutions was brought to a value of 7 by employing 0.1 M HCl and 0.1 M NaOH aqueous solutions. For batch adsorption tests, approximately 100 mg of membrane fragments were introduced into a glass beaker filled with 100 mL of Pb^{2+} solutions.

Subsequently, the beakers were positioned on a magnetic stirrer and agitated at room temperature with a rotation speed set at 300 rpm for a duration of 24 hours.

The extent of Pb^{2+} removal throughout the adsorption process was expressed as "% adsorption." This was determined by using the following relationship, which involves the initial Pb^{2+} concentration in the sample (C_i) and the concentration after adsorption (C_e) in mg/L

$$\% \, Absorption = \frac{C_i - C_e}{C_i} \times 100 \quad (9)$$

Using the values of Ci, Ce, sample volume (V), and membrane mass (m), the adsorption capacity at equilibrium (q_e) was computed by implementing the following expression.

$$q_e = \frac{(C_i - C_e) \times V}{m} \quad (10)$$

The Langmuir adsorption isotherm was determined using the following equation [5].

$$\frac{C_e}{q_e} = \frac{C_e}{q_m} + \frac{1}{q_m K_b} \quad (11)$$

In the equation, Ce represents the final concentration of Pb in the water, measured in mg/L, and q_e signifies the amount of Pb ions adsorbed on the adsorbent, measured in mg/g. Furthermore, q_m denotes the maximum adsorption capacity in mg/g, and K_b is the Langmuir constant associated with adsorption energy.

The following relationship was used to investigate the Freundlich adsorption isotherm [6].

$$log q_e = log K_F + \frac{1}{n} log C_e \quad (12)$$

Here, n represents the adsorption intensity, and K_F stands for the Freundlich constant, which pertains to multilayer adsorption and is indicative of bond strength.

5.2 Results and discussion

5.2.1 Characterization of extracted Lignin and Synthesized GO

FESEM and TEM images were used to analyze the surface morphologies of the lignin nanoparticles and GO sheets **(Fig. 5.1 a-f)**. The alkaline lignin particles exhibited a wide range of particle sizes and displayed a spherical shape, with sizes ranging from 39 nm to 1.3 μm **(Fig. 5.1a)**. The average sizes of alkali lignin nanoparticles were found to be 183 ± 102 nm (SEM). Some agglomerates also comprised small lignin spheres with smooth surfaces, and the average agglomerate size was 794 ± 272 nm. The result was also evidenced by TEM images (**Fig. 5.1c**), in which most particles were spherical in shape but had better dispersibility. The average particle size of lignin nanoparticles measured from TEM images was 84 ± 25 nm. The resultant particle sizes are small because the lignin particles were dissolved in DMSO solvent and drop-casted before FETEM analysis. Accordingly, lignin nanoparticles were well dissolved and dispersed evenly.

The SEM images of the synthesized GO sheets **(Fig. 5.1b)** represent a layered and wrinkled sheet-like two-dimensional structure of graphene oxide, which is relatively large, and the frame is like a thin screen. These thin sheets of GO are closely associated with each other. The TEM image **(Fig. 5.1d)** confirms the correct and successful synthesis of GO nanostructure, which has a distinctive wrinkled and crumpled appearance. The GO is relatively thin and has an apparent translucent structure. The selected area electron diffraction (SAED) method was used to characterize the crystallographic structure of the Lignin **(Fig. 5.1e)** and GO sheet **(Fig. 5.1f)**.

A white ring-shaped pattern in the SAED analysis of lignin confirms the amorphous nature of the lignin particles. The SAED pattern of the GO sheet displayed a distinct set of hexagonal diffraction patterns characterized by sharp and well-defined diffraction spots [7].

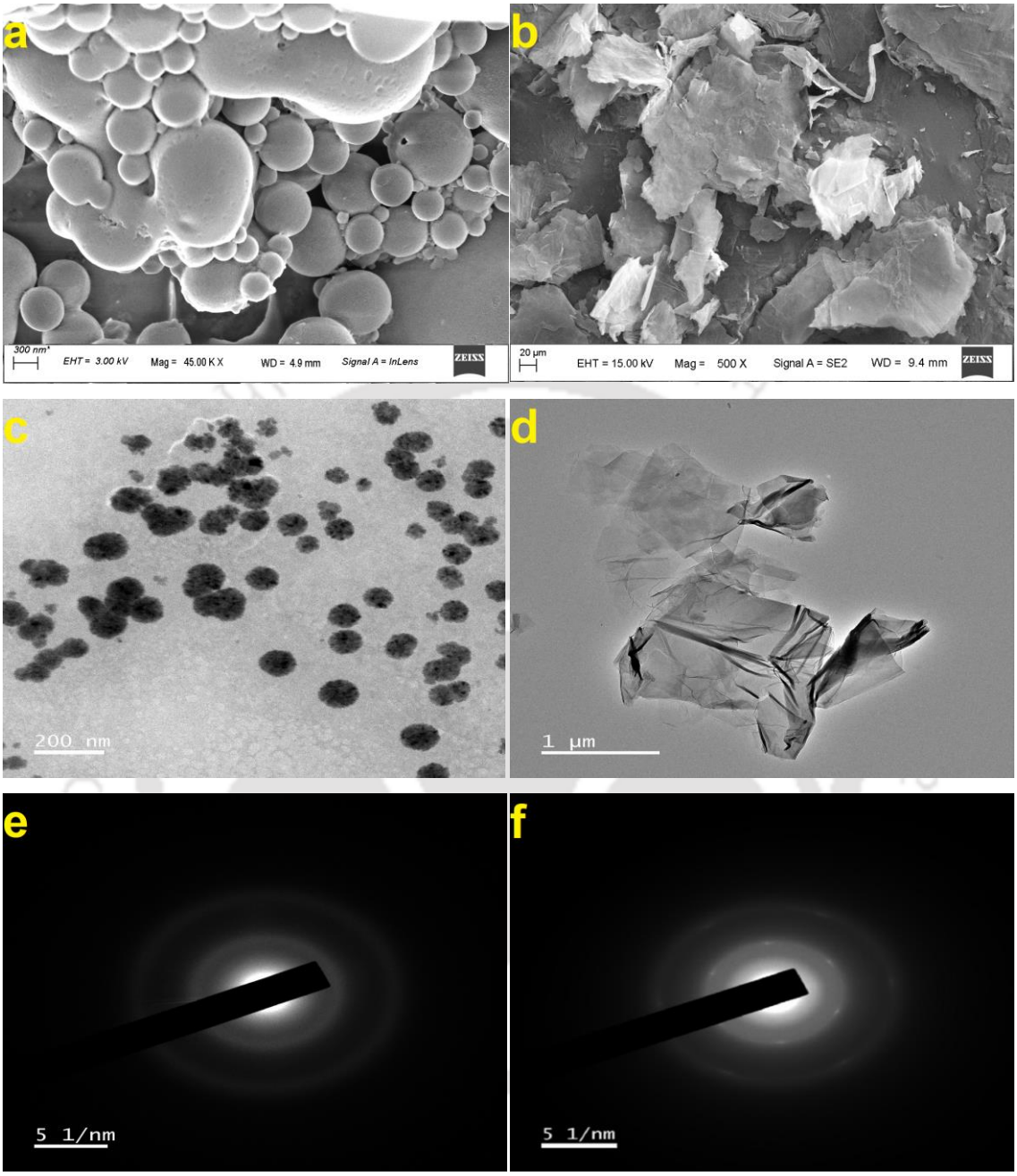

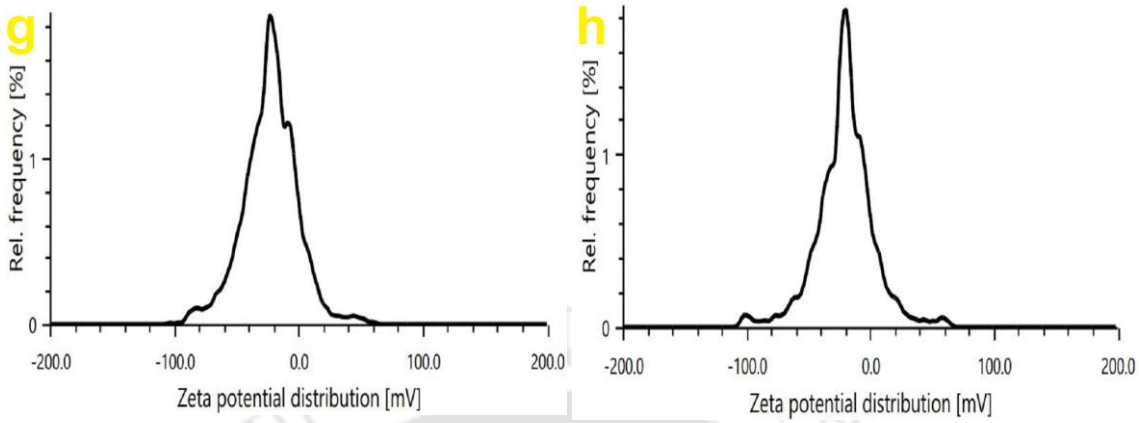

Figure 5.1: SEM images (a, b), TEM images (c, d), SAED pattern (e, f), and ζ potential distribution curve (g, h) of lignin (a, c, e, g) and GO sheets (b, d, f, h).

The ζ potential of both alkaline Lignin and GO was assessed in a neutral pH aqueous solution. The average ζ potential value for the extracted lignin was measured at -25.3 mV. This value can be attributed to the ionization of phenolic functional groups that are present on the surfaces of the particles, including COOH, -OH, -and C=O, which tend to disperse in the aqueous environment. Conversely, GO exhibited a ζ potential of approximately -24.9 mV at neutral pH, generally considered sufficient to promote mutual repulsion among GO particles. This resulted in the formation of a stable aqueous dispersion [8].

The FTIR spectrum in **Figure 5.2a** was utilized to investigate the functional groups present on the lignin nanoparticles and GO sheets. Both lignin and the GO spectrum exhibit distinctive absorption bands associated with various oxygen-containing groups. The stretching vibration of C-OH (hydroxyl) can be seen for both lignin (3300 cm^{-1}) and GO (3425 cm^{-1}) with marginally different peak positions. Because of absorbed water molecules and alcohol groups, this is overlaid with the OH stretch of carboxylic acid [9]. The stretching vibrations of C-H bonds in methylene and methyl groups are responsible for the infrared peaks at 2850 cm^{-1} and 2925 cm^{-1} in both samples. The characteristic GO peaks were observed at 1735, 1618, 1390, 1154, and 1044 cm^{-1}, attributed to the stretching vibration of C=O, C=C, C-OH, and C-O (epoxy and alkoxy) groups [10]. These distinctive peaks validated the synthesis of GO [8].

The stretching vibration of C=O in the acetyl and p-coumaroyl groups in lignin was primarily associated with the peak at 1656 cm^{-1}. Additionally, the stretching vibrations of C=C and the benzene ring stretching of the lignin aromatic skeleton were observed at 1597 cm^{-1} and 1510 cm^{-1} [1]. The indistinct peak at 1368 cm^{-1} was attributed to the presence of phenolic OH and aliphatic C-H groups in methyl groups, while a pronounced vibration at 1214 cm^{-1} was associated with the stretching of C-C, C-O, and C=O bonds in lignin subunits. The deformation of aromatic C–H bonds at 1033 cm^{-1} is a complex vibration related to stretching C–O, C–C bonds, and bending C–OH groups in polysaccharides. The 1118 cm^{-1} band corresponds to the deformations of C-O bonds in secondary alcohols and the in-plane deformation of aromatic C-H in the guaiacyl ring. At 822 cm^{-1}, the peak is linked to the out-of-plane deformation of C-H bonds in the syringyl subunit of lignin [11].

XRD analyses were performed to assess the structures of the extracted lignin nanoparticles and the synthesized GO sheets. The X-ray diffraction plots are presented in **Fig. 5.2b**. The XRD pattern of the lignin sample displays an obscure and widened peak positioned at $2\theta = 21.5°$, demonstrating the amorphous characteristic of lignin. Conversely, the primary distinctive diffraction peak in the synthesized graphene oxide (GO) manifested at $2\theta = 10.82°$ (001), indicating a 0.82 nm d-spacing [12]. The bigger interlayer spacing observed in GO is possibly due to the formation of oxygen-containing functional groups that are consequential from graphite oxidation. Furthermore, the diffraction peak at approximately $2\theta = 42.58°$ (100) in the XRD plot suggests the presence of turbostratic disorder in GO [13].

Thermal analysis of the extracted alkaline lignin and synthesized GO was accomplished using the TGA method. The TGA curves for both the Lignin and GO are presented in **Fig. 5.2c**. Lignin undergoes a two-step thermal degradation process.

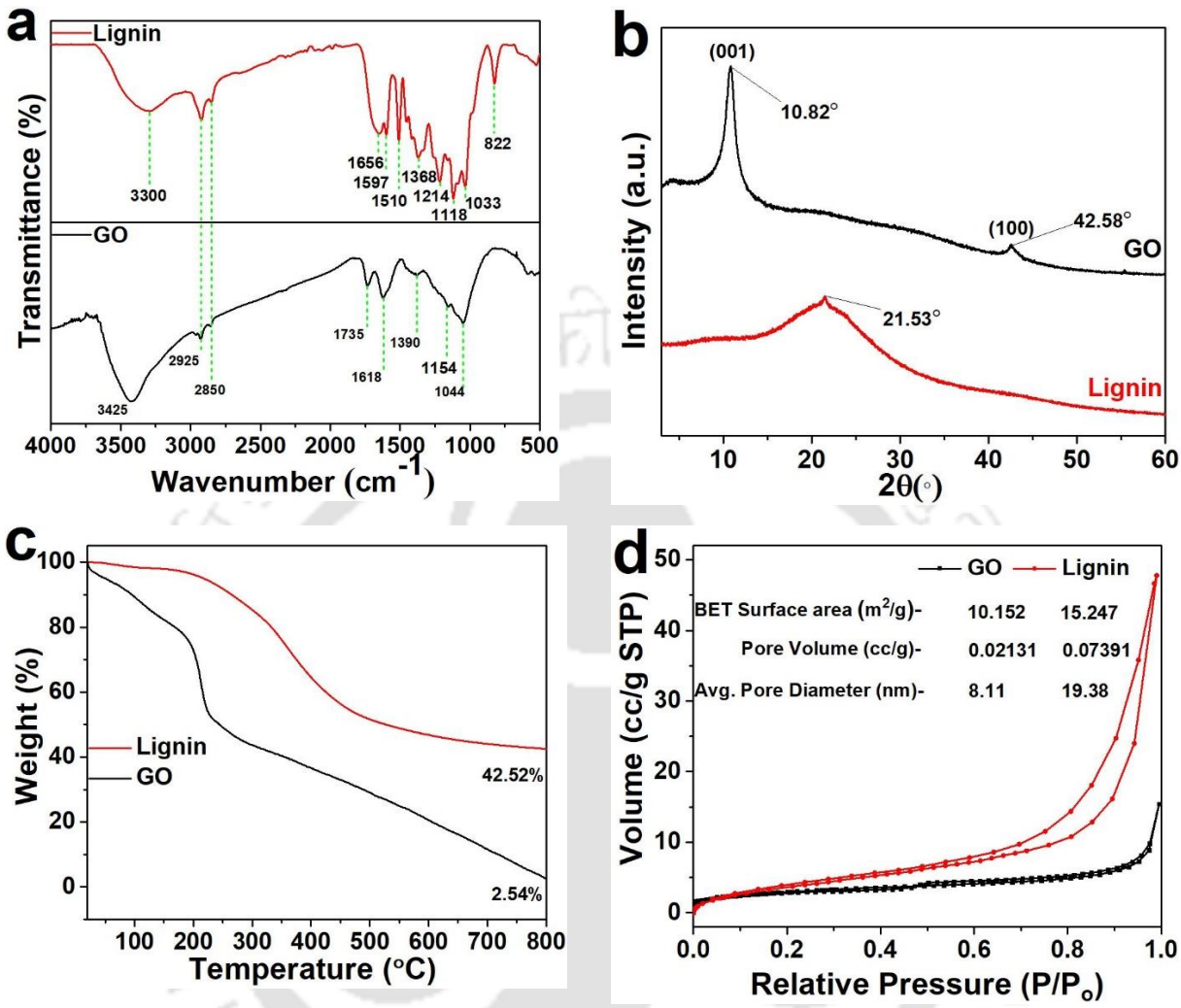

Figure 5.2: ATR-FTIR spectra (a), XRD spectra (b), TGA spectra (c), and BET surface area (d) of Lignin and GO sheets.

The first step involves the gradual degradation of lignin in the temperature range of 180°C to approximately 500°C, resulting in char residue formation. The second step involves the oxidation of the char residue occurring at temperatures above 500°C [14]. The residue consisting of 42.52% char is carbon-based and degrades slowly, which can provide superior thermal degradation properties to the polymeric membranes. Conversely, GO exhibits thermal instability, manifesting in three distinct stages of weight loss. The first stage, occurring between 25°C and 140°C, results in a mass loss of approximately 17% and is attributed to the removal of physically adsorbed water present on the surface and between the layers of GO. In the second stage, around 240°C, a more substantial weight

loss (approximately 34%) is observed, which can be attributed to the pyrolysis of unstable oxygen-containing functional groups. The final stage, from 275°C to 800°C, involves removing phenolic groups and decomposing sp3 hybridized carbon atoms at defective sites within the GO structure, causing a significant weight loss (approximately 44%) [15].

Surface area pore size and average pore volume of lignin and synthesized GO were determined by employing BET analysis. The results of porosity studies and the N_2adsorption–desorption isotherms of Lignin and GO are plotted in **Fig. 5.2d**. The explicit hysteresis loops observed at high pressures are a distinctive feature of the isotherms for both material types, providing confirmation of the significant role played by mesopores in their porosity. Significant distinctions in the pore diameter, volume, and surface area were identified by shifts in the isotherm shape and the quantity of nitrogen adsorbed. Due to its formation through solvent evaporation and being a thick film, GO may not be considered a genuine porous material, and this could result in partially obstructed channels. The specific surface area of lignin was approximately 15 m^2/g, while the specific surface area of GO was roughly 10 m^2/g. The International Union of Pure and Applied Chemistry (IUPAC) provides a pore classification based on size, categorizing them as micropores (width below 2 nm), mesopores (width between 2 and 50 nm), and macropores (width exceeding 50 nm). Lignin and GO are both mesoporous in nature and possess an average pore size of 19.38 nm and 8.11 nm, respectively.

5.2.2 Synthesized membrane characterizations

In the surface and the cross-sectional analysis of the control membrane **(Figure 5.3a, 5.3b)** and of those modified through the addition of lignin nanoparticles and GO nanosheets **(Figure 5.3c-5.3l)**, it can be observed that the introduction of nanofillers could significantly impact the membrane morphology and surface properties. The doping of PEG 6000 in the casting solution has a crowding effect in the membrane environment. This, in turn, reduced non-specific interactions between the membrane and nanoparticles and thereby resulted in increased porosity. The membrane without doping (LGM0) of lignin and GO had dense membrane morphology, smoother membrane surface, significantly fewer surface pores, and a suboptimal dispersion, which might produce

inadequate flow and confined retention. The nanocomposite membranes containing 1.5 wt.% lignin nanoparticles **(Fig. 5.3c)** showed an increased number of pores, and these pores became more elongated by connecting the surface pores. This leads to higher surface porosity. The fissure-like pores on the surface of LGM1 are due to the dispersing of the hydrophilic lignin nanoparticles integrated into the seemingly hydrophobic PSf matrix, preventing polymer chains from joining during phase separation. These characteristics can result in increased flux while retaining contaminants. The presence of lignin nanofillers in the solution affected the viscosity and the rate of phase separation during the precipitation process. This resulted in a thicker and more porous LGM1 membrane **(Fig. 5.3d)**.

The presence of GO nanosheets had varying effects on the morphology of the polymeric membranes. In **Fig. 5.3e,** it is evident that the membrane infused with 1.5 wt.% GO (LGM2) did not exhibit greater porosity than LGM1. Thus, such surface configuration can guarantee a greater retention of the contaminant. Nanosheets were also observable on the membrane surface, predominantly as agglomerates. This contributes to an enhancement in hydrophilicity, owing to the highly hydrophilic nature of GO. The cross-sectional image **(Fig. 5.3f)** of LGM2 showed the micro void structures in the membrane matrix, and the spongy portion completely disappeared. This resulted in reduced membrane thickness.

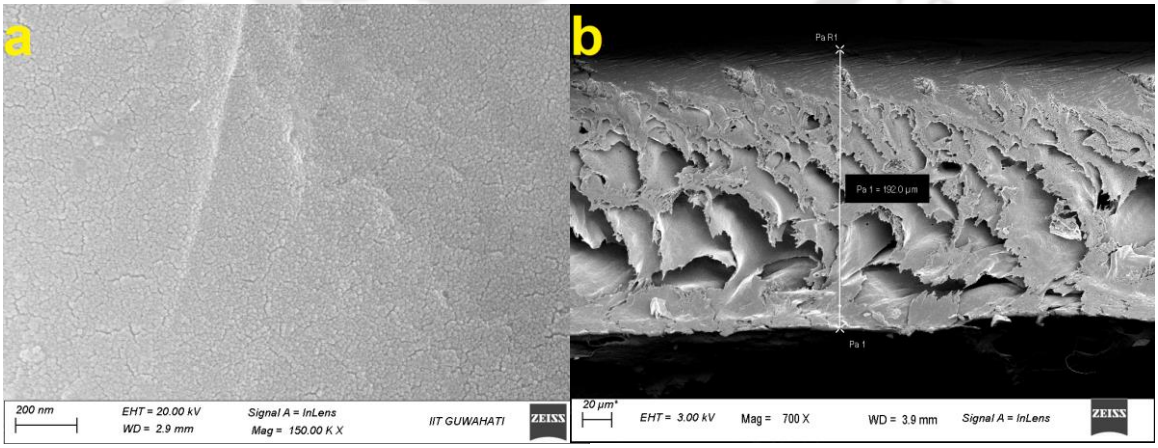

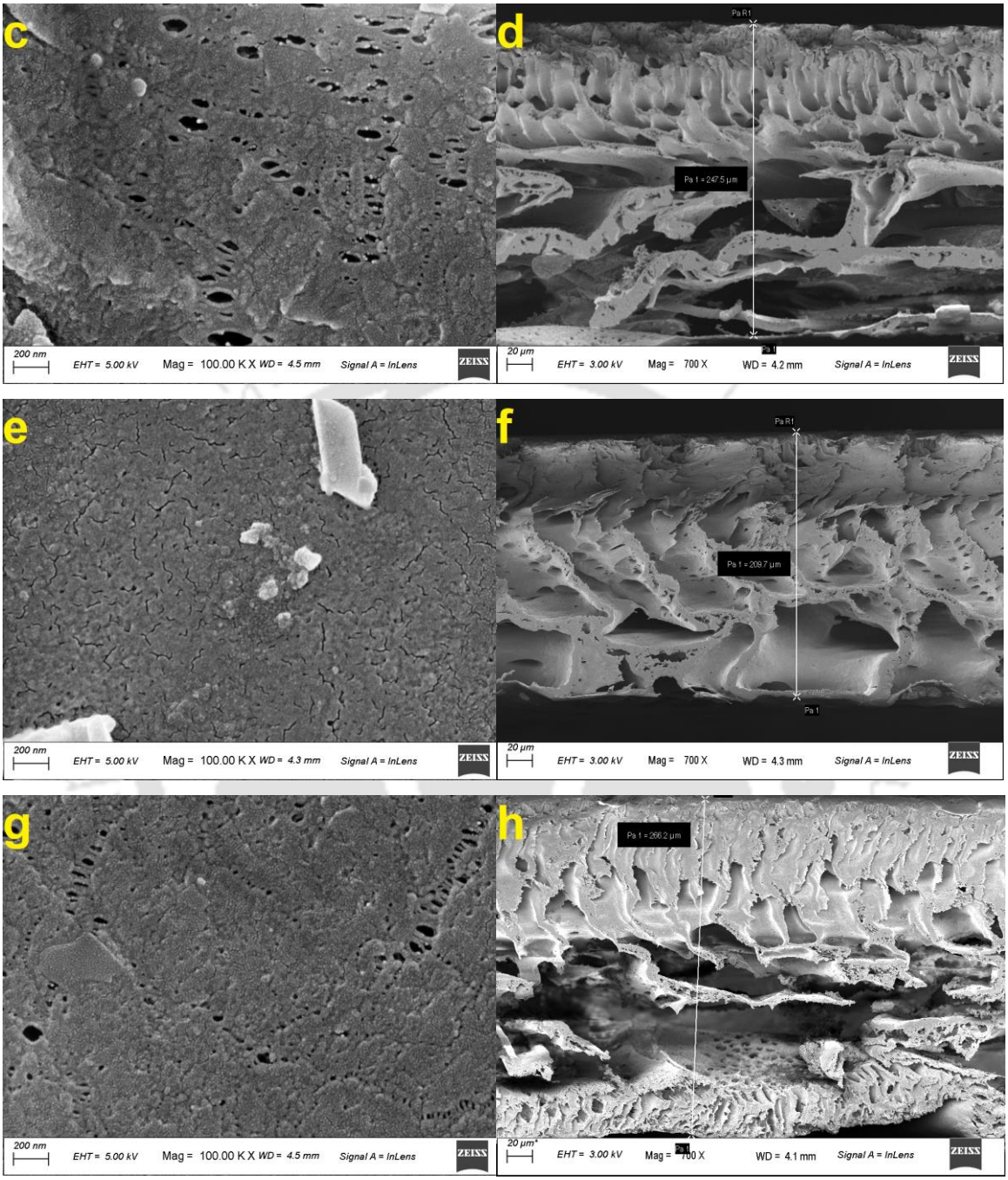

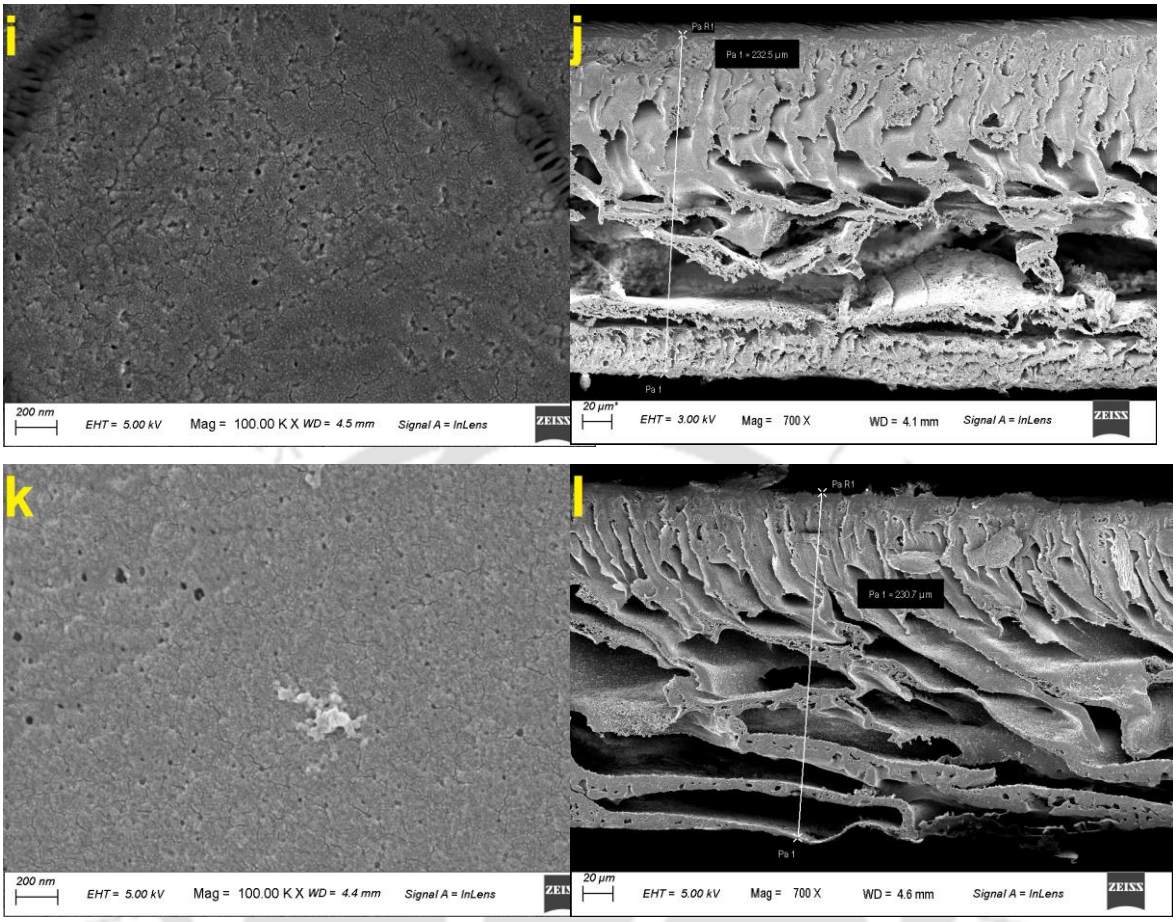

Figure 5.3: Membrane surface (a, c, e, g, i and k), and cross-sectional (b, d, f, h, j and l) SEM images of LGM0 (a, b), LGM1 (c, d), LGM2 (e, f), LGM3 (g, h), LGM4 (i, j) and LGM5 (k, l) membranes.

In both LGM3 (with 0.75 wt.% lignin and 0.75 wt.% GO) and LGM4 (with 1 wt.% lignin and 0.5 wt.% GO) membranes, a comparable cross-sectional image (**Fig. 5.3f and 5.3h**) revealed three distinct morphological regions. The upper layer exhibited vertical finger-like channels with dense walls, the middle layer featured open microvoids, and the bottom layer displayed a highly porous structure. In contrast, in LGM5 (with 0.5 wt.% lignin and 1 wt.% GO), the middle layer and the porous bottom layer fused to form horizontal cavities characterized by slender, dense walls (**Fig 5.3l**). The surface morphology of these three membranes is shaped by the varying concentrations of Lignin and GO within the casting solution (**Fig. 5.3g, 5.3i, 5.3k**). The distinctive characteristics are a result of the unique interplay between these components during the membrane fabrication process.

Notably, the porosity of these three membranes falls below that of LGM1 but surpasses that of LGM2. This difference in porosity levels can be attributed to the nuanced combinations and concentrations of Lignin and GO in the respective casting solutions. Thereby, they influence the overall membrane structure and properties.

AFM images of the membrane's top surface in both 2D and 3D representations are illustrated in **Fig. 5.4**. The bright portions show the highest points, and the dark parts show the troughs or pores of the constructed membranes. In general, the concentration of nanoparticles plays a crucial role in determining the final membrane morphology and its hydrophilicity. As depicted in **Fig. 5.4**, it is evident that surface roughness was influenced by the concentration of nanolayers. Consequently, the presence of nanolayers resulted in increased surface roughness of the membranes compared to the control PSf membrane (LGM0). Incorporating lignin into the membrane (LGM1) increases the surface roughness. Due to its irregular surface features, when incorporated into the membrane, it can create a slightly rougher surface compared to LGM0. GO, on the other hand, is a 2D nanomaterial with a relatively smooth and planar structure. Adding GO to the membrane increased the surface roughness compared to pure PSf. However, it was not as effective as lignin for roughness enhancement.

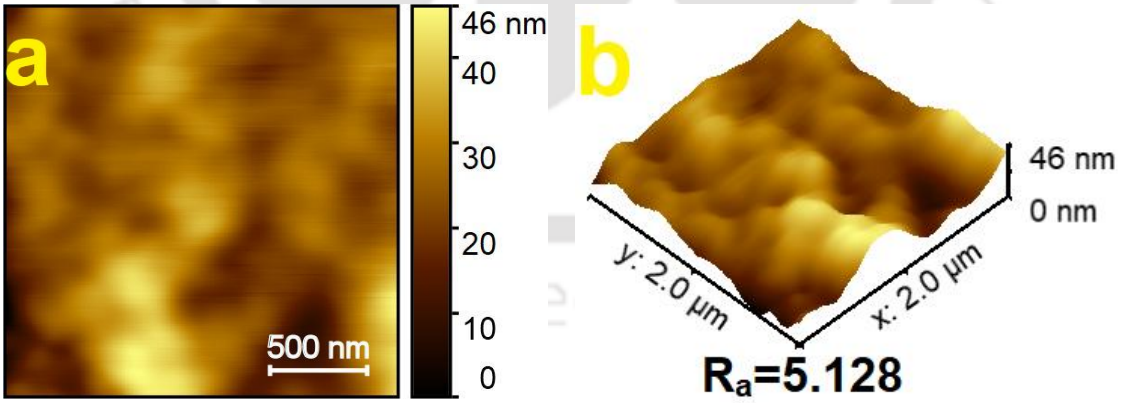

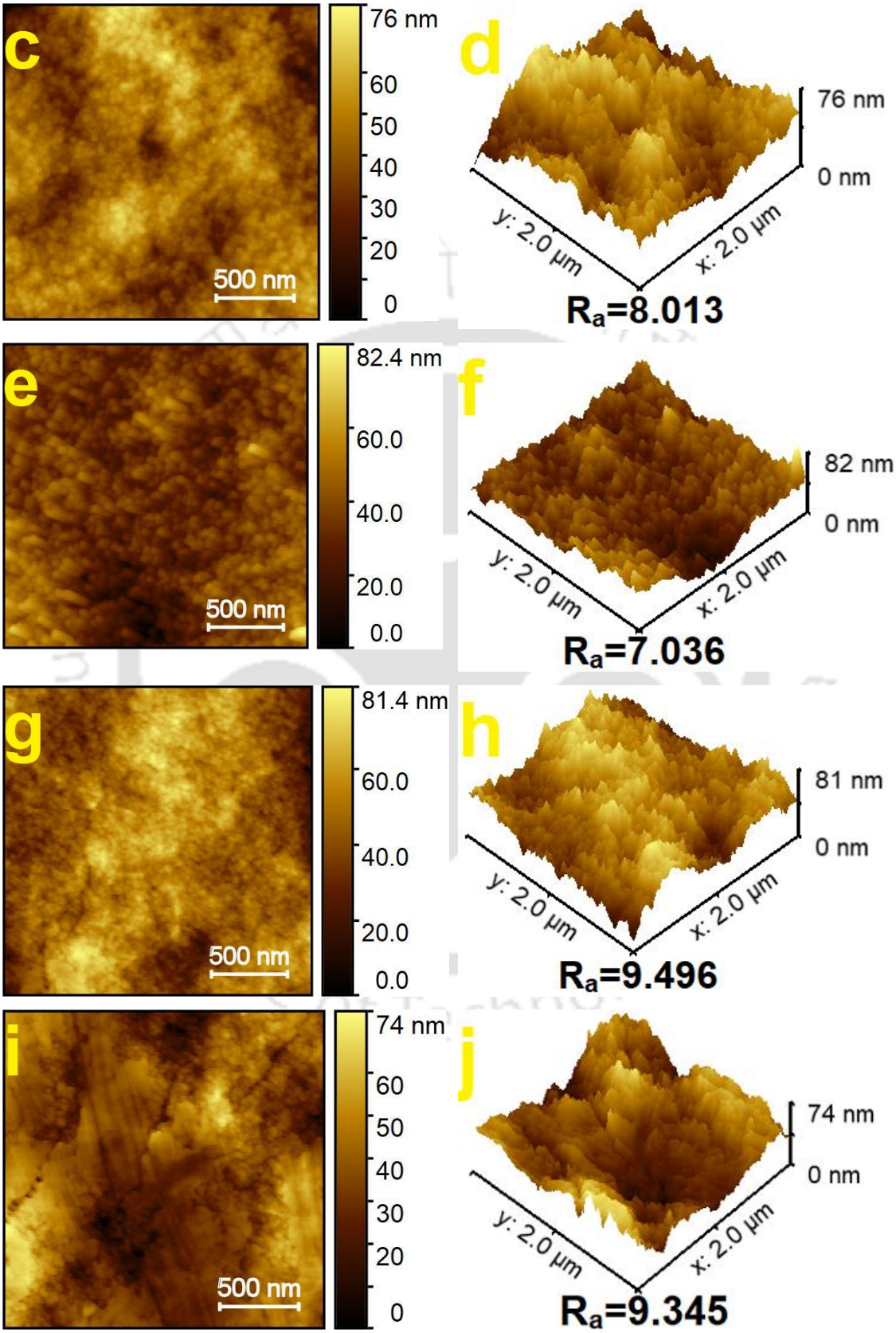

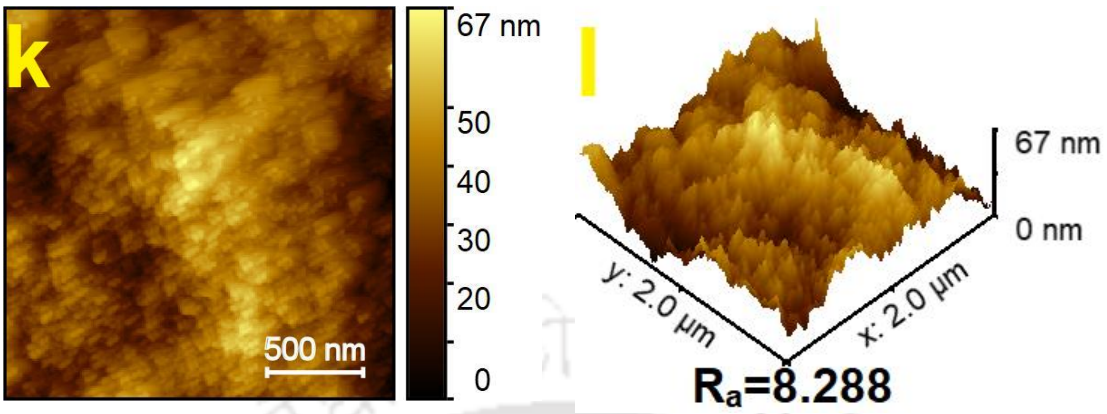

Figure 5.4: 2D (a, c, e, g, i and k) and 3D (b, d, f, h, j, and l) AFM images of LGM0 (a, b), LGM1 (c, d), LGM2 (e, f), LGM3 (g, h), LGM4 (i, j) and LGM5 (k, l) membranes.

The simultaneous incorporation of Lignin and GO in the membrane matrix resulted in a surface roughness that is slightly higher than the only lignin-incorporated membrane (**Fig. 5.4g-5.4l**). Both components could introduce additional structural complexity and thereby lead to increased roughness. The highest surface roughness is observed when both lignin and GO are present in equal proportions (LGM3). This could be due to the synergistic effect of the integration of lignin's irregular structure with GO's planar structure. For the case of the LGM5 membrane, the dominant effect might be from the GO, which is known to have a smoother surface. As a result, the roughness is marginally lower than that of the lignin-dominant membrane (LGM4).

XPS was employed to analyze alterations in the chemical composition of the membrane surfaces. **Fig. 5.5** displays the survey spectrum of the samples along with the higher-resolution spectra focused on the C 1s and O 1s regions. In **Fig. 5.5a**, a comprehensive range of standard XPS spectra for the membranes has been presented. Each of the membranes displayed consistent components, encompassing carbon, oxygen, and sulfur. **Figures 5.5b and 5.5c** showcase the core-level spectra for C 1s and O 1s, respectively, along with the results of the spectral fitting. The asymmetrical C 1s peak observed in the controlled PSf membrane (LGM0) is deconvoluted into three distinct peaks at 284.8, 285.86, and 286.46 eV. These correspond to C–C/C–H, C–S, and C–O-C/C-OH, respectively. The intensity of the C–O-C/C-OH peak in the blend membranes is notably enhanced compared to the control membrane. This enhancement is attributed to the

presence of functional groups from lignin and GO. An extra peak falling within the range of 287.4-287.7 eV was observed in LGM1 (1.28% of spectra) and LGM2 (0.85% of spectra). Thereby, it signified the existence of carbonyl functional groups originating from lignin and GO on the membrane's surface. The introduction of both Lignin and GO into the same membrane (LGM 3-5) resulted in mutual interference of their functional groups within the C 1s spectra. These interactions, arising from the coexistence of multiple components, give rise to complex signal interactions, which have the potential to mask or modify the characteristic peak associated with carbonyl groups.

Within the O 1s core level spectra of controlled PSf membrane (LGM0), the peak components situated at 531.8 and 532.5 eV were attributed to O=S=O and C–O–C, respectively. The relative area percentages of these peaks were 52.56% and 47.44%, respectively. Nevertheless, in the modified membranes, the ratio of these peaks showed noticeable variations due to the grafting of lignin nanoparticles and GO nanosheets onto the membrane matrix. These nanofillers introduced carbonyl and hydroxyl groups and thereby introduced a peak between 532.9-533.5 eV, which led to distinct changes in the O 1s spectra.

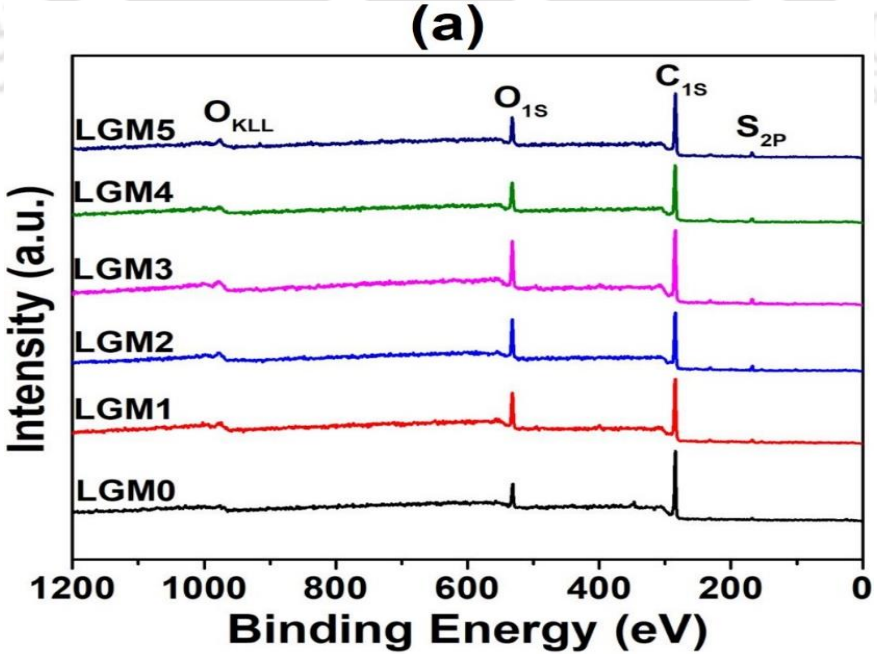

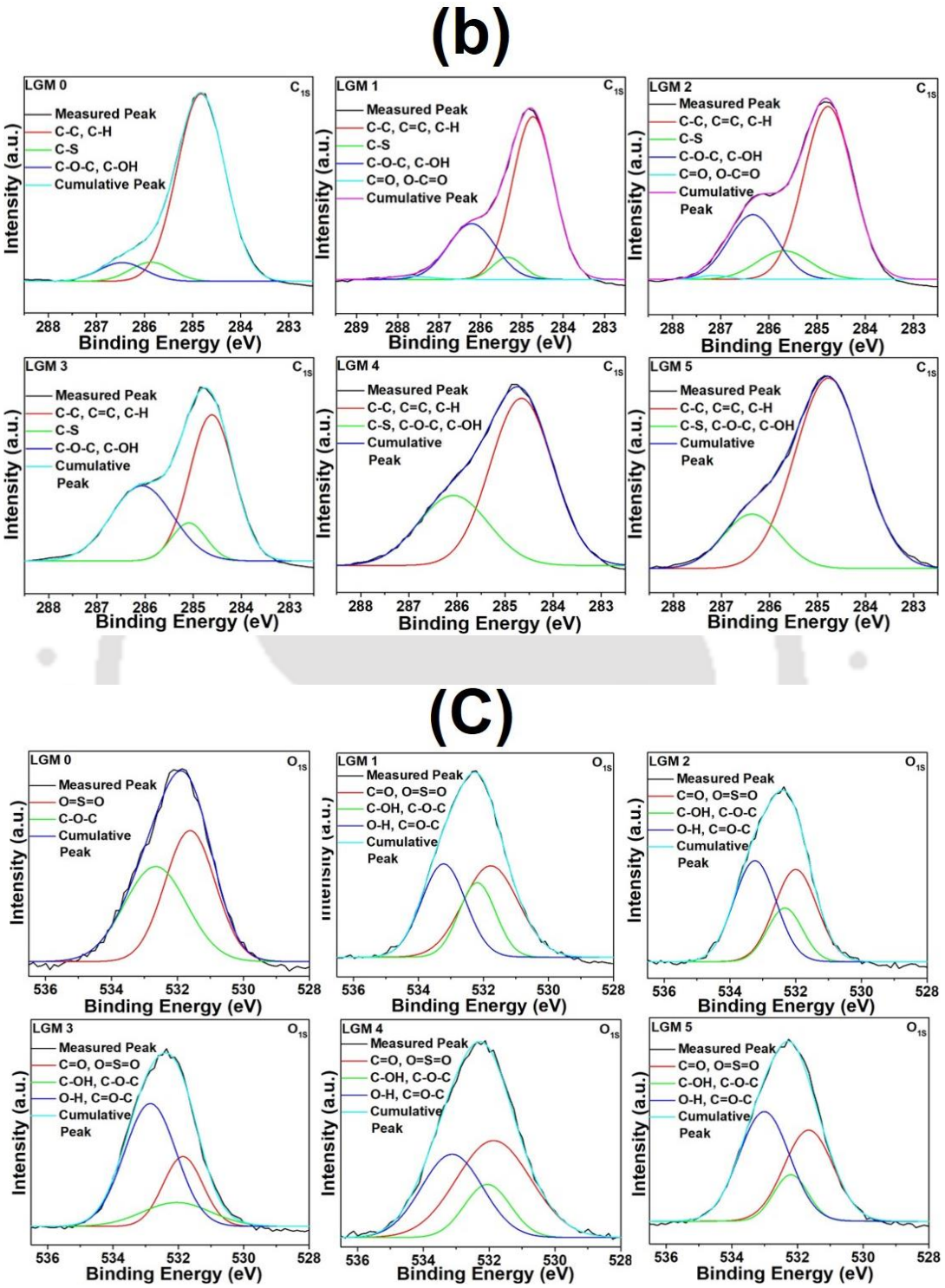

Figure 5.5: (a) XPS survey spectra, (b) C 1s spectra, and (c) the O 1s spectra of synthesized immaculate membranes

The zeta potential measurements of the various membranes are summarized in **Table 5.2**. The controlled PSf membrane (LGM0) exhibits a characteristic trend commonly seen in uncharged polymeric materials that did not undergo further modifications. Notably, the presence of hydroxide ions stemming from the self-ionization of water leads to a negative surface charge on the membrane. Lignin and GO are rich in oxygen-containing functional groups, such as carboxyl and hydroxyl groups, which carry negative charges. When lignin (LGM1) and GO (LGM2) were blended with the PSf matrix, these anionic functional groups became part of the membrane's surface chemistry. The presence of these anionic groups on the membrane surface led to a negative surface charge. The observed increase in the surface charge of the PSf membrane when both lignin and GO (LGM 3-5) are mixed can be attributed to the combined influence of these materials on the surface properties of the membrane. The grafting or attachment of lignin and GO nanosheets can lead to a more uniform and extensive coverage of the membrane surface with these functional groups. Also, both lignin and GO led to synergistic interactions that enhanced the surface charge. As a result, the membrane surface became more negatively charged due to the accumulation of anionic groups.

Table 5.2: ζ potential, Porosity, and PWF of synthesized membranes

Membrane	ζ potential (mV)	Porosity (%)	Pure water flux (L/m^2h)
LGM0	-15.6±0.7	36.9±4.7	74.27
LGM1	-28.2±0.4	82.4±6.2	297
LGM2	-27.5±0.2	40.7±3.4	116.71
LGM3	-39.4±0.7	67.1±6.1	193.11
LGM4	-38.6±0.3	73.5±4.4	243.19
LGM5	-37.9±0.4	52.3±5.1	154.06

Porosity analysis is of significant importance as it directly correlates with a membrane's capability for rejection and permeation flux. Generally, a membrane's porosity is contingent on the rate of mass transfer between the solvent and non-solvent phases during

the inversion phase. The results of porosity and pure water flux measurements for membranes containing different percentages of Lignin and GO (held constant at 1.5 wt.%) are summarized in **Table 5.2**. Notably, an increase in membrane porosity was observed for the LGM1 membrane in comparison to the LGM0 membrane. Such an increase can be attributed to the presence of hydrophilic functional groups in lignin nanofillers, which promote the development of pores by speeding the exchange of solvent and non-solvent phases [4].

However, upon comparison of the porosity of lignin-modified membranes to GO-modified membranes (LGM2), it is evident that the former exhibits significantly higher porosity. Such a difference can be attributed to the tendency of GO nanosheets to agglomerate, limiting their dispersion and exfoliation. This, in turn, hinders the achievement of enhanced porosity. Furthermore, the higher concentration of GO (1.5 wt.%) tends to increase the viscosity of the casting solution and thereby slows down the exchange between the non-solvent and solvent phases. This ultimately leads to a decrease in the membrane porosity [16]. It is worth mentioning that nanocomposite membranes (LGM3-5) with a greater GO wt.% had reduced porosity.

Additionally, the 1.5 wt% GO and 1.5 wt.% lignin-integrated membranes showed an increased trend in PWF compared to the controlled PSf membrane sample. This rise in PWF is probably caused by increased hydrophilicity as well as increasing surface porosity, which is made possible by the incorporation of nanolayers. Nevertheless, when lignin and GO were mixed in the membrane, there was a considerable drop in PWF. The synergistic impact of the nanolayers in the composite membrane samples can be attributable to this decrease.

The hydrophilic characteristics and surface wettability of the membranes were assessed using a water contact angle measurement, and the findings are shown in **Fig. 5.6**. PSf membranes are widely criticized for their poor hydrophilicity [4]. However, the addition of PEG 6000 has been shown to reduce the contact angle of PSf membranes. With the addition of Lignin and GO nanofillers, the water contact angle of the membranes decreases even more. Such a reduction in contact angle indicates that these nanofillers

cause the membranes to become even more hydrophilic. Graphene oxide (GO) is more hydrophilic than lignin due to its structural and chemical characteristics. Consequently, a membrane containing GO is expected to exhibit a reduced contact angle compared to a membrane incorporating lignin.

For the case of membranes LGM 3-5, the introduction of GO and lignin nanofillers into the membrane matrix leads to an observed increase in surface roughness. As a general trend, the enhanced surface roughness of a membrane corresponds to higher contact angles. This correlation is consistent with the elevated contact angles found in the membranes incorporating lignin and GO (LGM 3-5). Furthermore, it's worth noting that the contact angles exhibited variations depending on the concentration of GO and lignin within the membrane matrix.

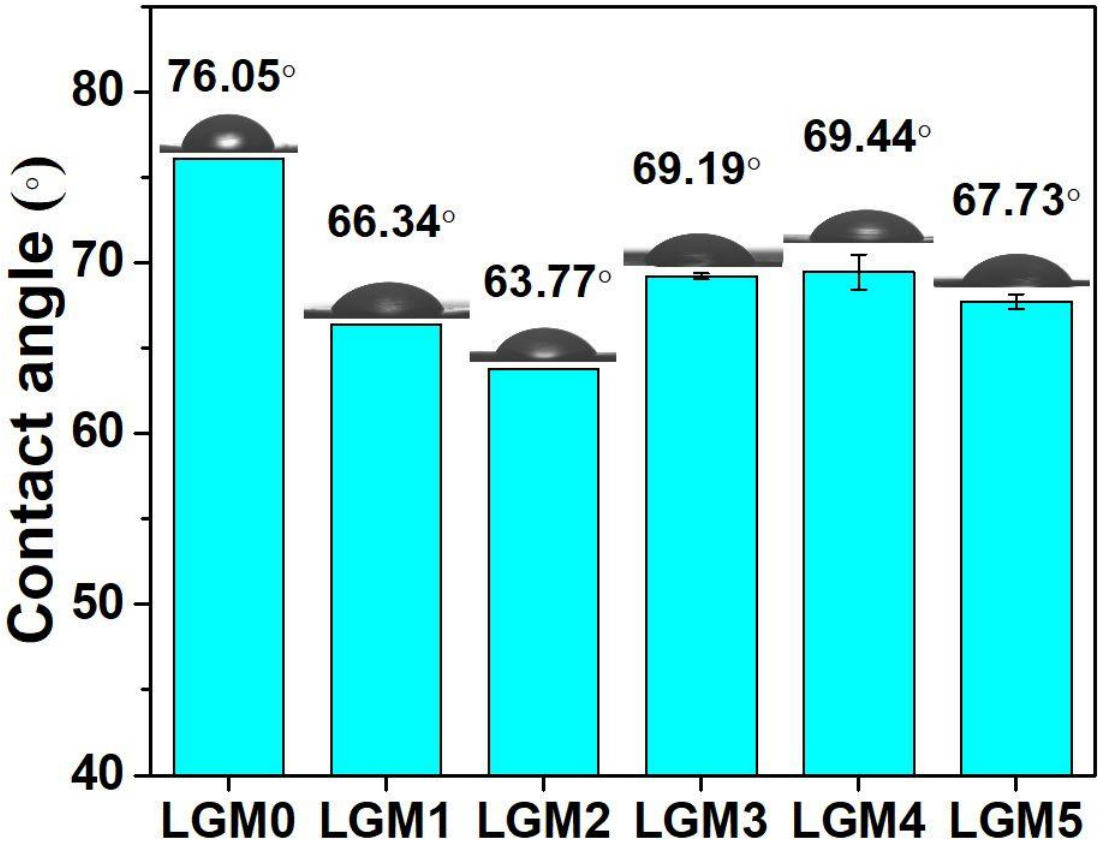

Figure 5.6: Water contact angles of controlled and Lignin/GO-modified membranes

5.2.3 Membrane Performance

Figure 5.7 illustrates the flux decline patterns of the membranes used over three filtration/regeneration cycles. The results depicted in **Fig. 5.7** highlight the suitability of nanocomposite membranes for effectively removing Pb^{2+} ions in the presence of Eosin Y dye. Lignin-GO integrated membranes outperformed the remaining membrane samples over three filtration/regeneration cycles. Throughout each filtration cycle, a consistent trend emerged, revealing a gradual decline in water flux over time. To address this decline and restore optimal flux levels after each filtration cycle, a backwashing procedure was implemented with the aqueous HCl solution. This HCl treatment effectively revitalized water flux for the subsequent filtration cycle. The transition in flux levels between these cycles was influenced by the duration of the filtration process.

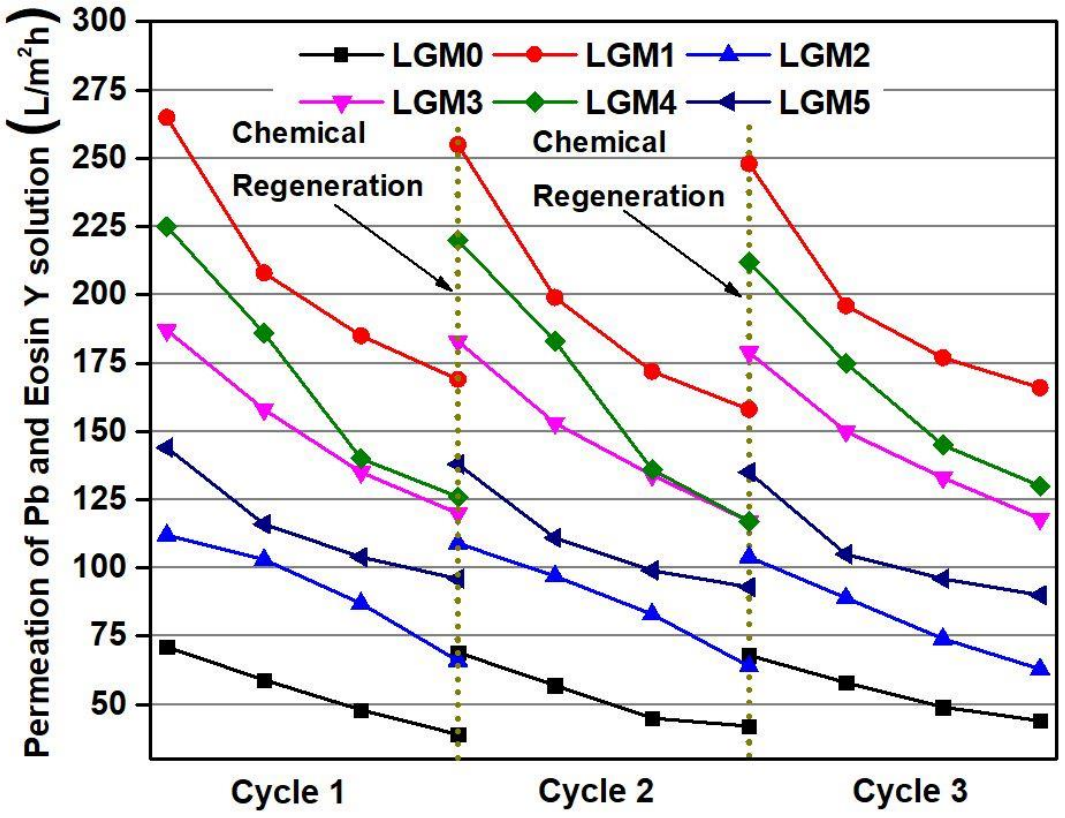

Figure 5.7: Changes in flux during three filtration/regeneration cycles

A careful examination of the graphical representation of the data showcased the ability of HCl-based cleaning to restore the initial water flux of each membrane. The Pb^{2+} ions

adsorbed by the functional groups of Lignin and GO are replaced by H^+ ions released by HCl during regeneration. Accordingly, they rejuvenated the membrane adsorption sites. Notably, following HCl cleaning, membranes LGM0, LGM1, and LGM4 exhibited a remarkable and rapid increase in water flux during 3rd cycle in comparison to their performance during the initial two filtration cycles. Such a significant alteration in flux levels strongly indicated the possibility of membrane damage or an alteration of surface properties caused by the HCl treatment. Moreover, as filtration cycles progressed, it was evident that, as the cycles neared completion, the final flux levels experienced a decline. Consequently, it can be concluded that HCl-based regeneration was not 100% effective in removing all the foulants from the membrane surfaces.

The removal and rejection percentage of Pb^{2+} and Eosin Y dye through all the membrane samples through the filtration/regeneration process are given in **Fig. 5.8**. The LGM0 membrane displays a declining trend during three filtration/regeneration cycles, which might be attributed to the irreversible fouling caused by the presence of Eosin Y and Pb ions. In the first filtration cycle, the nanocomposite membranes (LGM1-LGM5) effectively removed Pb^{2+} and the negatively charged dye. The negative surface charge of lignin and GO played a role in enhancing the rejection of negatively charged Eosin Y due to electrostatic repulsion. The removal of Pb^{2+} and rejection of Eosin Y were good because the active adsorption sites in the membrane matrix and the negative surface charge of nanofillers helped prevent the passage of negative Eosin Y dye through the membrane. The concurrent presence of Eosin Y and Pb ions had a similar impact on the results. This simultaneous presence yielded two positive effects on membrane filtration: (1) the electrostatic interaction between Pb ions, Eosin Y molecules, and adsorbent nanolayers and (2) the development of relatively large Pb-Eosin Y complexes in the feed, which restrict the passage of Pb^{2+} through the membrane pores. The membranes containing lignin, GO, and Lignin/Go mixture experienced the adsorption phenomenon of Pb^{2+} ions, which leads to more reversible fouling.

After the first cycle, the regeneration process cleans the membrane, removing fouling from the membrane surface and reactivating adsorption sites, preparing it for the next filtration cycle. After regeneration, the membranes exhibited even better removal and

rejection of Pb^{2+} and the Eosin Y dye. The lignin and GO nanofillers with negative zeta potential values might have reactivated and interacted more effectively with the contaminants and further enhanced the removal percentage. The reduction in water flux during the second filtration cycle indicates the presence of irreversible pore blockages. These blockages not only impede the flow of water but are also responsible for the physical adsorption of Pb^{2+} ions. During the third cycle, a decrease in the removal of Pb^{2+} and rejection of Eosin dye was observed. Despite regeneration, some foulant accumulation on the membrane surface over multiple cycles leads to decreased removal and rejection. The active sites on the membrane may have become saturated with Pb^{2+} ions and dye molecules, reducing their capacity to adsorb or reject further.

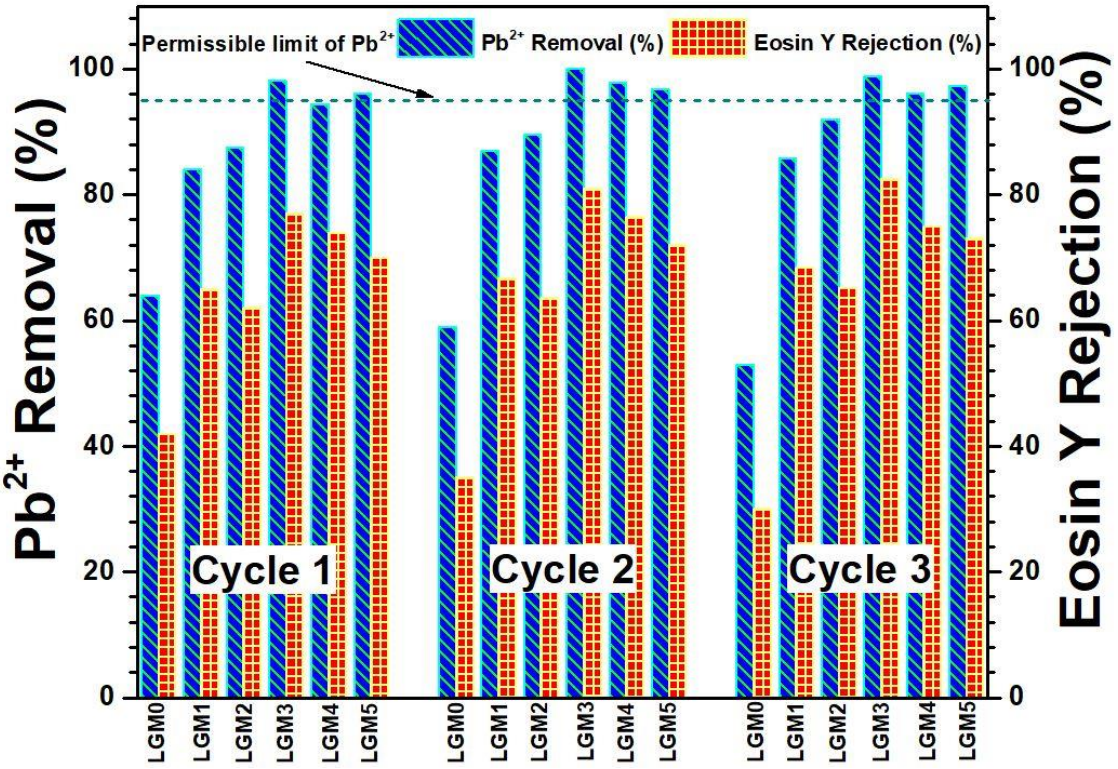

Figure 5.8: Pb^{2+} removal and Eosin Y rejection through the synthesized membranes during three filtration cycles

A complete removal (100%) of Pb^{2+} ions and 81% rejection of Eosin Y was observed for the LGM3 membrane during 2nd filtration cycle. Lignin and GO may synergistically affect the adsorption and rejection of Pb^{2+} metal ions and negatively charged Eosin dye. The performance differences in the removal of Pb^{2+} ions and the rejection of Eosin Y in membranes with different lignin-to-GO ratios are influenced by the balance of lignin's surface area and charge and GO's adsorption properties. In the LGM4 membrane with more lignin content, the membrane might be less hydrophilic and may not effectively repel negatively charged Eosin Y molecules. The higher lignin content might limit the electrostatic repulsion. The increased lignin content might also result in fewer available adsorption sites for Pb^{2+} and thereby reduce the removal efficiency. On the other hand, with more GO, the LGM5 membrane may become more hydrophilic. This reduces its ability to adsorb heavy metal ions. Higher GO concentration leads to a reduction in the available surface area for lignin. This, in turn, may decrease the efficiency of lignin's adsorption and charge-based removal capabilities.

To advocate the rejection of Eosin Y and the adsorption of Pb^{2+} on the membrane surface during filtration, EDX analysis was conducted. **Fig. 5.9** depicts the EDX spectrograms of the spent membranes after three filtration cycles. Carbon and oxygen are the predominant elements found in the lignin, GO, PSf, polyethylene glycol (PEG), and Eosin Y. Sulfur is specifically present in the PSf matrix. Eosin Y dye is characterized by the presence of bromine and sodium as distinctive elements. To conduct a comprehensive elemental analysis, carbon, oxygen, sulfur, and the foulants, namely lead (Pb), bromine (Br), and sodium (Na) were investigated using EDX.

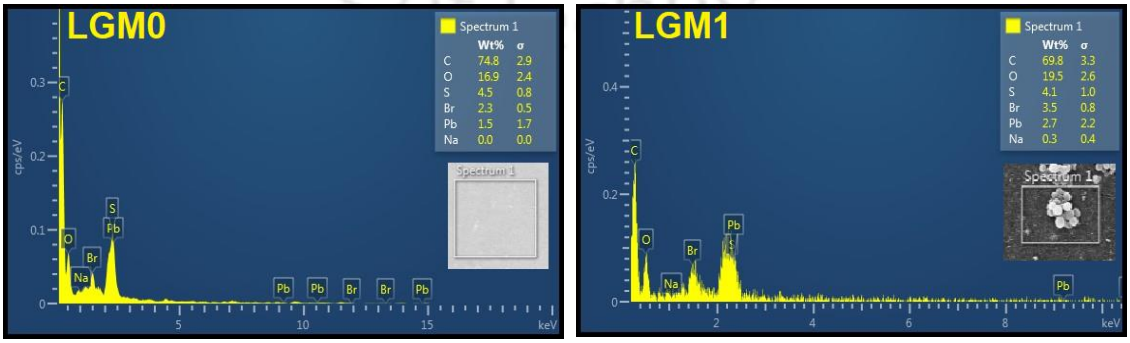

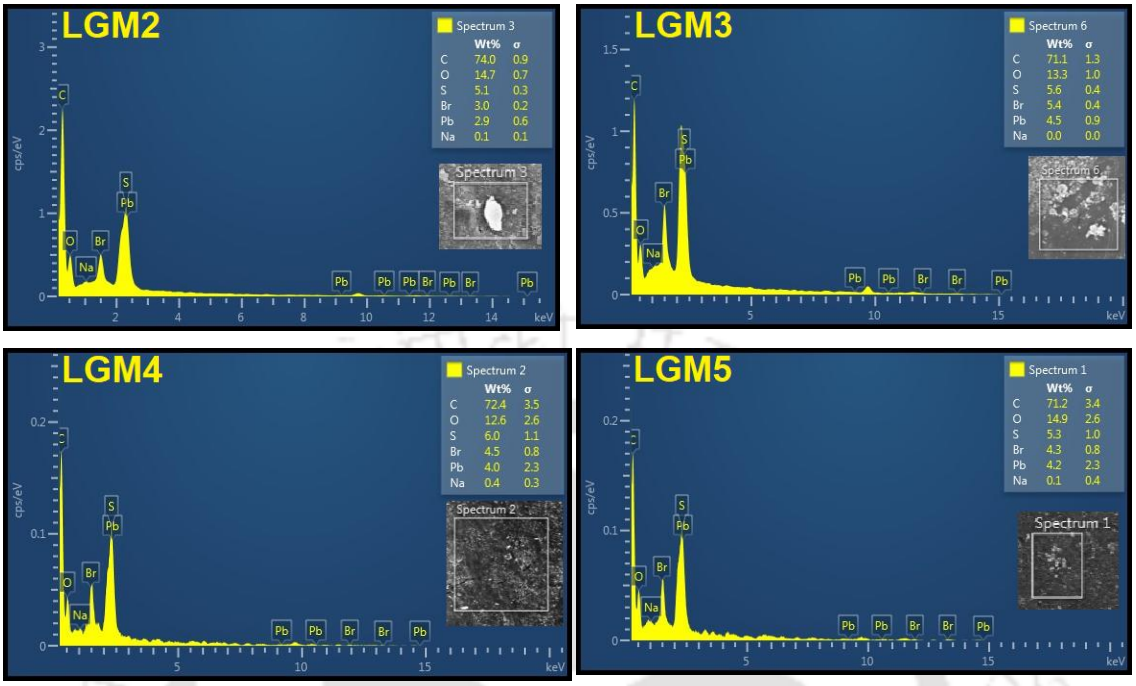

Figure 5.9: SEM-EDX analysis of the synthesized membranes after 3 filtration cycles

In the spectrograms, the weight percentage of sodium (Na) is notably low in comparison to bromine or is even completely absent. This observation suggests that the Eosin Y dye underwent deprotonation during the filtration process, leading to the release of sodium ions (Na^{+}). Consequently, the deprotonated Eosin Y molecule was associated with the positively charged lead (Pb^{2+}) ions and thereby formed a complex on the surface of the membrane. All EDX spectra had well-defined peaks of Pb ions. In the LGM3 spectra, a maximum of 4.5 weight percent (wt.%) of lead (Pb) and 5.4 wt.% of bromine (Br) was observed. These significant findings are attributed to the highest surface charge and optimal membrane porosity of LGM3. The results derived from the EDX spectra were in good agreement with the filtration cycle data obtained through Atomic Absorption Spectroscopy (AAS) and UV spectroscopy. This alignment reaffirmed the accuracy and reliability of the results.

The percentage of FR, TFR, RFR, and IFR) after three filtration and regeneration cycles was calculated to assess the membranes' fouling resistance. The corresponding findings are displayed in **Table 5.3**. The introduction of Lignin (LGM1) and GO (LGM2) nanolayers has proven to be beneficial due to their regenerative properties. This resulted

in a positive impact on the reduction of IFR (irreversible fouling ratio), which is primarily responsible for diminishing membrane efficiency. Lower IFR values equate to greater RFR (reversible fouling ratio) and FR (flux recovery) values. The total fouling ratio (TFR) of the LGM1 and LGM2 membranes, on the other hand, increased. The regeneration properties of GO and lignin, which help lower IFR, are also capable of introducing additional fouling steps and interactions, which are responsible for this rise in TFR. The fouling processes include Eosin Y precipitation, Pb^{2+} adsorption, concentration polarization, and chemical interactions between nanofillers and contaminants. Even with significant improvements in FR and RFR, these further fouling mechanisms help account for the noted rise in TFR.

Table 5.3: Membrane fouling characteristics

Membrane	FR%	TFR%	RFR%	IFR%
LGM0	74.86	42.1	16.96	25.13
LGM1	82.93	44.78	27.71	17.07
LGM2	87.39	46.87	34.27	12.6
LGM3	88.55	39.93	28.48	11.45
LGM4	83.47	48.18	31.66	16.52
LGM5	85.03	43.52	28.56	14.96

The ζ potential of a membrane surface is critical in determining membrane performance. It sensibly alters characteristics such as total fouling ratio (TFR), reversible fouling ratio, flux recovery, and irreversible fouling ratio. The LGM3 membrane's exceptionally high zeta potential value allows it to efficiently reject Eosin Y dye, resulting in less fouling and, as a result, a lower TFR. The repelling action between the LGM3 membrane surface and foulants minimizes TFR and the irreversible fouling ratio. The heightened negative zeta potential of LGM3 increased the repulsion effect and potentially contributed to better flux recovery (FR) through the prevention of foulants adherence to the membrane surface. The distinctive zeta potential characteristics of the LGM3 membrane highlight its ability

to minimize fouling and improve its overall performance, particularly in terms of TFR and FR.

The filtration outcomes achieved in this study have been meticulously juxtaposed with the most recent advancements in membrane-based filtration for removing Pb^{2+} ion removal, and the membrane adsorption techniques were applied to Eosin Y dye. The detailed comparative analysis and findings are thoughtfully compiled and presented in **Table 5.4**. They provide a comprehensive overview of the study's results, insights, and performance in relation to these two distinct but crucial removal processes.

Table 5.4: Literature comparison of this work

S. no	Membrane	Operating setup	PWF (L/m^2h)	Contaminant	Removal /rejection (%)	Ref.
1	CaAlg/PAN-UiO-66-$(COOH)_2$ TFNC (thin film nanofibrous composite) membrane (UiO-66-$(COOH)_2$: PAN=2)	Using a dead-end filtration system (M8010, Millipore, USA)- at 0.1 MPa	50	Pb^{2+}	≥90%	[17]
2	NaX zeolite (0.9 %)/ PES (Polyethersulfone) ultrafiltration mixed matrix membrane	Cross-flow system- at 1.6 bar	88.05	Pb^{2+}	97%	[18]
3	Commercial anion exchange membrane BI (quaternized poly	Adsorption study- 0.15 g membrane in 50mg/mL Eosin Y solution	NA	Eosin Y	88%	[19]

	2,6-dimethyl-1,4-phenylene oxide and polyvinyl alcohol).	(tap water) for 60 minutes (1st cycle)				
4	N,Pd codoped TiO_2 (7%) /PSf membrane	The photocatalytic degradation- 3 cm × 3 cm membrane in 100 mL of 100 PPM EY solution under visible light irradiation for 4 h	NA	Eosin Y	97%	[20]
5	Lignin (0.75%)-GO (0.75%) / PSf composite membrane	Dead-end filtration setup- at 2 bar for 120 minutes (2nd cycle)	193.11	Pb^{2+} Eosin Y	100% 81%	This work

Table 5.5 presents the tensile strength and elongation percentage at the rupture point for the fabricated membranes before and after filtration. Adding PEG 6000 to the PSf membrane acted as a plasticizer and henceforth increased the free volume between the polymer chains. This increased free volume allowed the PSf polymer chains to move more freely and rendered the membrane with greater flexibility. As a result, the membrane was largely susceptible to deformation. This reduced its mechanical strength. In a prior study in which PEG 6000 was not incorporated into the PSf matrix, the tensile strength was measured at 4.55 ± 0.45 MPa, and the elongation percentage was 18.1 ± 1.62%. However, in the present study, with the inclusion of PEG 6000, the tensile strength decreased to 0.91 ± 0.13 MPa, while the elongation percentage increased to 22.51 ± 2.17% [4].

Table 5.5: Tensile attributes of the membranes prior to and following filtration

Membrane	Before filtration		After filtration	
	Tensile (MPa)	Elongation (%)	Tensile (MPa)	Elongation (%)
LGM0	0.91 ± 0.13	22.51 ± 2.17	0.89 ± 0.08	11.6 ± 0.44
LGM1	2.41 ± 0.23	36.35 ± 1.74	1.50 ± 0.12	10.14 ± 1.57
LGM2	1.31 ± 0.09	15.56 ± 0.43	0.98 ± 0.06	5.71 ± 0.52
LGM3	2.09 ±0.14	25.50 ±1.46	1.36 ± 0.17	10.81 ± 1.22
LGM4	2.33 ± 0.21	42.39 ± 4.81	1.43 ±0.21	9.63 ± 3.57
LGM5	2.06 ±0.06	16.25 ±1.69	1.15 ±0.09	11.58 ± 1.96

Lignin and graphene oxide are both utilized to enhance the mechanical properties of membranes. As a natural polymer, lignin establishes robust intermolecular interactions with the polymer chains within the PSf matrix. This resulted in improved mechanical strength. Conversely, as a synthetic material, graphene oxide does not create as effective physical entanglements with the PSf polymer matrix. Furthermore, its inherent stiffness can sometimes render the membrane to have greater brittleness and reduced tensile strength. After performing filtration cycles, the tensile strength and elongation percentage reduced as backwashing with hydrochloric acid (HCl) led to the breakdown of the polymeric membrane structure. The post-filtration surface morphology of the used LGM3 membrane was examined, and the results are displayed in **Fig. 5.10**. During the filtering process, the membranes were subjected to an array of demanding circumstances, including mechanical stress, chemical exposure, and fouling. These cumulative components resulted in a significant decrease in the tensile strength and elasticity of the membranes.

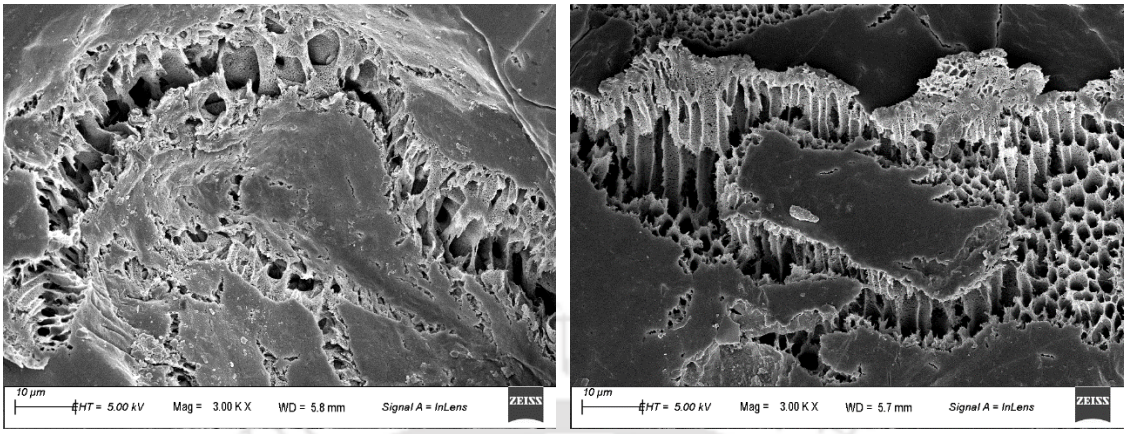

Figure 5.10: Surface morphology of spent LGM3 membrane

5.2.4 Adsorption study

The adsorption investigation of Pb^{2+} onto the LGM3 membrane was conducted due to its superior performance in the filtration process. The experimental data was employed to fit Langmuir and Freundlich isotherm models. **Table 5.6** displays the calculated parameters derived from these models, providing insights into adsorption. **Fig. 5.11** shows the plot for Langmuir and Freundlich isotherms. The correlation coefficient values (R^2) obtained indicate that both Langmuir and Freundlich models offer a superior fit for describing the experimental data. The Langmuir isotherm graph showed that the maximum adsorption capacity was 71.32 mg/g, while the Langmuir constant value was 0.102 (K_b).

Table 5.6: Adsorption isotherm models for adsorption Pb^{2+} on LGM3 membrane

Parameters	Langmuir Isotherm	Freundlich Isotherm
R^2	0.977	0.994
K_b	0.102	-
q_m (mg/g)	71.32	-
K_F	-	12.08
n	-	2.29

The Freundlich adsorption isotherm offered insights into the heterogeneity of the

adsorption process. The value of 1/n (indicates favorability in the range $0.1 < 1/n < 1$) was 0.435, which confirmed a favorable adsorption process. The value of n determines the affinity of the process, with $n < 1$ indicating chemisorption and $n > 1$ suggesting physisorption. The Freundlich model yields an n value of 2.29, indicating physisorption has occurred. Therefore, the Freundlich model is the best to describe the adsorption data. The results from both Langmuir and Freundlich models suggest that the adsorption of Pb^{2+} onto the LGM3 membrane matrix involves a complex mechanism, encompassing both monolayer and heterogeneous surface conditions.

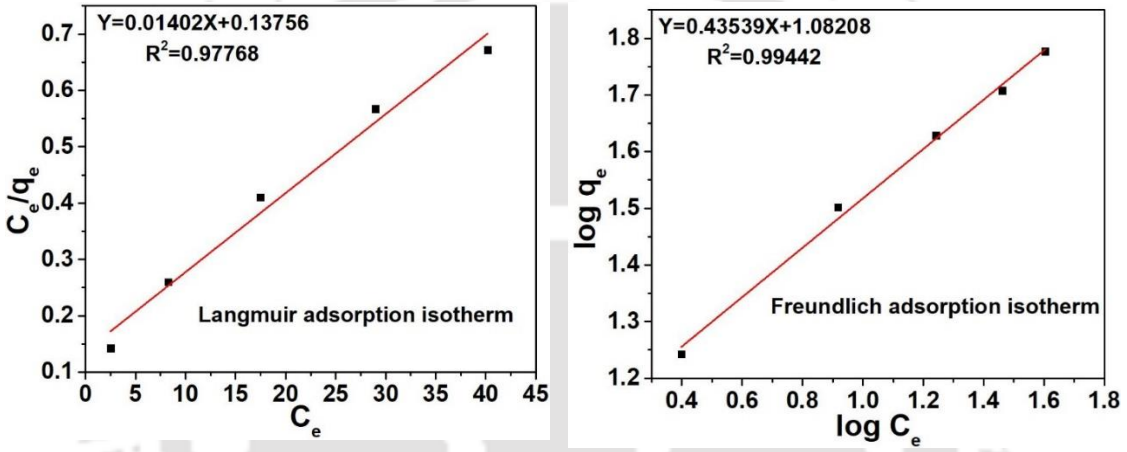

Figure 5.11: Langmuir and Freundlich isotherm plots

5.3 Cost Analysis

The cost-effectiveness of membrane technology is a crucial factor that enhances its competitiveness in industrial applications. Polymeric membranes designed for large-scale operations are generally priced within the range of $50 to $200 per square meter [4]. **Table 5.7** presents a comprehensive lab-scale cost analysis for producing an optimized composite membrane using lignin and graphene oxide (GO). Lignin and graphene oxide (GO) were synthesized rather than purchased commercially. Thus, the approach significantly reduced the cost of these nanofillers. The estimated cost for the synthesis of lignin and GO was 7.4 INR per gram and 18.41 INR per gram, respectively. The total cost

estimate for producing a 1 square meter LGM3 membrane is 55.16 dollars, and its favorable performance characteristics affirm it to be a cost-effective membrane.

Table 5.7: Cost analysis of optimized synthesized membrane per m^2

Part A- Material Cost				
Sl. No.	**Material used**	**Amount taken**	**Unit Rate**	**Price (INR)**
1	Lignin	300 mg	Rs. 7.4/g	2.22
2	GO	300 mg	18.41/g	5.52
3	PEG 6000	20 g	Rs. 492 /500g	19.68
4	NMP	339.4 g	Rs. 1624 /500 mL	1067.13
5	Polysulfone	40 g	Rs. 21522.9/250 g	3443.66
		Total Material Cost (A)		**₹ 4538.21**

Part B- Power consumption					
Sl. No.	**Instrument used**	**Power Rating (Watt)**	**Power unit price (INR)**	**Power consumption (Unit)**	**Price (INR)**
1	Ultrasonic Sonicator bath	120		0.06	0.35
2	Hot plate magnetic stirrer	1170	Rs. 5.96/Unit	4.68	27.89
3	Hot air oven	750		4.5	26.82

	Total power expenses (B)	**₹ 55.06**
	Net cost for membrane fabrication per m^2 (A+B)	**₹ 4593.27**
	The synthesis cost per 1m^2 membrane ($)	**55.16 $**

5.4 Summary

This study presented a straightforward and pragmatic method for enhancing the characteristics of PSf membranes while also introducing regenerative capabilities by incorporating lignin and GO fillers. The performance of the membranes was assessed while filtering a solution containing both Eosin Y dye and lead (Pb). Correspondingly, this study offered reasonable insights into the significance of surface characteristics, hydrophilicity, and porosity in influencing dye rejection, heavy metal removal, and antifouling properties. The membrane, with the equivalent weight percentage (0.75 wt.%) of lignin and GO (LGM3), exhibited the most superior performance in terms of permeation, rejection of Eosin Y dye, removal of lead (Pb), and flux recovery over the course of three filtration and regeneration cycles. The simultaneous existence of Eosin Y and Pb had a favorable impact on membrane filtration efficiency due to the development of significant Eosin-Pb complexes via electrostatic interaction. The adsorption investigation of lead (Pb) on the LGM3 membrane demonstrated noticeable adsorption activity. Upon comparing two isotherm models, it was evident that the adsorption isotherm data was accurately described by both the Langmuir and Freundlich models, emphasizing the occurrence of multilayer physisorption. The findings collectively indicate that Lignin/GO composite membranes exhibit notable efficiency and environmental friendliness in heavy metal and anionic dye removal. Given their cost-effectiveness and utilization of biowaste, these membranes are likely to garner broader acceptance for various applications.

References

[1] S. Dhara, N. S. Samanta, R. Uppaluri, and M. K. Purkait, "High-purity alkaline lignin extraction from Saccharum ravannae and optimization of lignin recovery through response surface methodology," *Int. J. Biol. Macromol.*, vol. 234, p. 123594, 2023, doi: https://doi.org/10.1016/j.ijbiomac.2023.123594.

[2] A. D. Sontakke and M. K. Purkait, "Fabrication of ultrasound-mediated tunable graphene oxide nanoscrolls," *Ultrason. Sonochem.*, vol. 63, p. 104976, 2020, doi: https://doi.org/10.1016/j.ultsonch.2020.104976.

[3] A. D. Sontakke, A. Bhattacharjee, R. Fopase, L. M. Pandey, and M. K. Purkait, "One-pot, sustainable and room temperature synthesis of graphene oxide-impregnated iron-based metal-organic framework (GO/MIL-100(Fe)) nanocarriers for anticancer drug delivery systems," *J. Mater. Sci.*, vol. 57, no. 40, pp. 19019–19049, 2022, doi: 10.1007/s10853-022-07773-w.

[4] S. Dhara, N. Shekhar Samanta, P. P. Das, R. V. S. Uppaluri, and M. K. Purkait, "Ravenna Grass-Extracted Alkaline Lignin-Based Polysulfone Mixed Matrix Membrane (MMM) for Aqueous Cr(VI) Removal," *ACS Appl. Polym. Mater.*, Jul. 2023, doi: 10.1021/acsapm.3c00999.

[5] W. Ahmad *et al.*, "Utilization of Tires Waste-Derived Magnetic-Activated Carbon for the Removal of Hexavalent Chromium from Wastewater," *Materials (Basel).*, vol. 14, p. 34, Dec. 2020, doi: 10.3390/ma14010034.

[6] K. Mastor *et al.*, "Application of Freundlich and Temkin Isotherm to Study the Removal of Pb(II) Via Adsorption on Activated Carbon Equipped Polysulfone Membrane," *Int. J. Eng. Technol.*, vol. 7, pp. 91–93, Jan. 2018.

[7] P. Dash, T. K. Rout, and S. K. Biswal, "Study on the Preparation of GO and RGO by Chemical and Mechanical Exfoliation of Natural Graphite for the Aluminum Industry," *J. Sustain. Metall.*, vol. 6, no. 1, pp. 26–33, 2020, doi: 10.1007/s40831-019-00251-9.

[8] F. Baskoro *et al.*, "Graphene oxide-cation interaction: Inter-layer spacing and zeta potential changes in response to various salt solutions," *J. Memb. Sci.*, vol. 554, pp. 253–263, 2018, doi: https://doi.org/10.1016/j.memsci.2018.03.006.

[9] A. D. Sontakke and M. K. Purkait, "A brief review on graphene oxide Nanoscrolls: Structure, Synthesis, characterization and scope of applications," *Chem. Eng. J.*, vol. 420, p. 129914, 2021, doi: https://doi.org/10.1016/j.cej.2021.129914.

[10] A. D. Sontakke, S. Tiwari, and M. K. Purkait, "A comprehensive review on graphene oxide-based nanocarriers: Synthesis, functionalization and biomedical applications," *FlatChem*, vol. 38, p. 100484, 2023, doi: https://doi.org/10.1016/j.flatc.2023.100484.

[11] Y. Horikawa, S. Hirano, A. Mihashi, Y. Kobayashi, S. Zhai, and J. Sugiyama,

"Prediction of Lignin Contents from Infrared Spectroscopy: Chemical Digestion and Lignin/Biomass Ratios of Cryptomeria japonica," *Appl. Biochem. Biotechnol.*, vol. 188, no. 4, pp. 1066–1076, 2019, doi: 10.1007/s12010-019-02965-8.

[12] A. D. Sontakke, R. Fopase, L. M. Pandey, and M. K. Purkait, "Development of graphene oxide nanoscrolls imparted nano-delivery system for the sustained release of gallic acid," *Appl. Nanosci.*, vol. 12, no. 9, pp. 2733–2751, 2022, doi: 10.1007/s13204-022-02582-8.

[13] T. F. Emiru and D. W. Ayele, "Controlled synthesis, characterization and reduction of graphene oxide: A convenient method for large scale production," *Egypt. J. Basic Appl. Sci.*, vol. 4, no. 1, pp. 74–79, 2017, doi: https://doi.org/10.1016/j.ejbas.2016.11.002.

[14] P. Purnama and S.-H. Kim, "Biodegradable blends of stereocomplex polylactide and lignin by supercritical carbon dioxide-solvent system," *Macromol. Res.*, vol. 22, Sep. 2014, doi: 10.1007/s13233-014-2004-2.

[15] H. Abdali and A. Ajji, "Preparation of Electrospun Nanocomposite Nanofibers of Polyaniline/Poly(methyl methacrylate) with Amino-Functionalized Graphene," *Polymers (Basel).*, vol. 9, p. 453, Sep. 2017, doi: 10.3390/polym9090453.

[16] H. Namdar, A. Akbari, R. Yegani, and H. Roghani-Mamaqani, "Influence of aspartic acid functionalized graphene oxide presence in polyvinylchloride mixed matrix membranes on chromium removal from aqueous feed containing humic acid," *J. Environ. Chem. Eng.*, vol. 9, no. 1, p. 104685, 2021, doi: https://doi.org/10.1016/j.jece.2020.104685.

[17] T. Zhang, P. Li, S. Ding, and X. Wang, "High-performance TFNC membrane with adsorption assisted for removal of Pb(II) and other contaminants," *J. Hazard. Mater.*, vol. 424, p. 127742, 2022, doi: https://doi.org/10.1016/j.jhazmat.2021.127742.

[18] H. Alfalahy and S. Al-Jubouri, "Preparation and application of polyethersulfone ultrafiltration membrane incorporating NaX zeolite for lead ions removal from aqueous solutions," *Desalin. Water Treat.*, vol. 248, Mar. 2022, doi: 10.5004/dwt.2022.28072.

[19] K. Parveen, S. Zafar, M. Khan, R. Anwer, and A. Shanableh, "Removal of eosin yellow from wastewaters by the commercial anion exchange membrane BI," *Desalin. Water Treat.*, vol. 287, pp. 245–253, Apr. 2023, doi: 10.5004/dwt.2023.29368.

[20] A. T. Kuvarega, N. Khumalo, D. Dlamini, and B. B. Mamba, "Polysulfone/N,Pd co-doped TiO2 composite membranes for photocatalytic dye degradation," *Sep. Purif. Technol.*, vol. 191, pp. 122–133, 2018, doi: https://doi.org/10.1016/j.seppur.2017.07.064.

Chapter 6

Conclusions and Scope for Future Work

This chapter states the main conclusions drawn from each objective and the possible scope for further research in sections 6.1 and 6.2.

6.1 Conclusions

The bioethanol was produced from *Saccharum ravennae* biomass using hydrochemical pretreatment and surfactant–assisted enzymatic hydrolysis. Also, high-purity alkaline lignin was extracted from the biomass. The extraction process was optimized through the response surface methodology that targeted the optimality of solid loading, alkali concentration, and reaction time-independent variables. The extracted lignin was used as an additive for the synthesis of a PSf-based mixed matrix membrane that was targeted for Cr(VI) removal from water. The purified form of the extracted lignin was further used for PSf membrane modification along with graphene oxide (GO) for lead (Pb) and Eosin Y dye removal from water systems. For each fulfilled objective of the Ph.D. thesis, both subjective and objective conclusions have been stated as follows:

Studies on the chemical pretreatment and surfactant-mediated enzymatic hydrolysis of Saccharum ravennae grass biomass for enhanced sugar and bioethanol yield

- The acid-alkali system (2% H_2SO_4 followed by 2% NaOH) pretreatment (10% solid loading, 121^oC, and 60 min reaction time) proved to be effective for complete hemicellulose removal and maximum delignification (92.07%). However, it resulted in a lower solid recovery (24.74%).
- The alkali treatment (2.0 % (w/v) NaOH, 60 minutes, 121°C, and 10% (w/v) solid loading) exhibited superior performance in terms of various parameters, such as the excellent combination of solid recovery (43.66%), delignification (87.71%), and hemicellulose retention (25.93 ± 0.64%).

- SDS and CTAB induce cellulase unfolding and increase particle size through electrostatic interactions, with SDS causing vesicle formation and CTAB causing folding. Surfactant vesicles, influenced by ζ potential, create a destabilization region affecting cellulase immobilization. In contrast, the non-ionic surfactant Tween 20 does not significantly alter cellulase properties.
- Pretreatments, particularly acid-alkali (AC-AL), enhance the enzymatic hydrolysis of *S. ravennae* biomass by effectively removing hemicellulose and minimizing lignin interference. This results in significantly higher sugar yields, with AC-AL achieving complete hemicellulose removal and exclusive glucose synthesis, demonstrating the efficacy of the pretreatment method in facilitating efficient enzymatic conversion.
- SDS addition during enzymatic hydrolysis decreases sugar yields in both raw and pretreated biomass. Concentrations above the CMC lead to cooperative binding with cellulase, causing electrostatic repulsion, structural damage, and reduced enzyme activity. Despite higher glucose yields in the presence of SDS for AL biomass compared to AC-AL biomass, the overall sugar yield is lower due to the stronger interaction of SDS with cellulase.
- CTAB in enzymatic hydrolysis negatively affects sugar yields due to electrostatic interactions with cellulase, reducing β-glucosidase activity and increasing cellobiose concentration. While CTAB initially improves glucose yield in samples with higher lignin content, prolonged hydrolysis results in reduced yields due to ruptured hydrogen bonds and decreased hydrophobic interaction, influencing both glucose and xylose production.
- The AL and AC-AL processes based on enzymatic hydrolysis (0.1 M sodium citrate buffer, 5% (w/v) biomass, 4.8 pH, 50 °C, 72 h and 110 rpm, 1.5% (v/v) Cellulase enzyme from *Trichoderma reesei* and Tween 20 (0.2 g/g of biomass) for the case with surfactant) of RGB and without any surfactant ensured maximum sugar yields of 602 mg/g and 624 mg/g, respectively. For AL and AC-AL treated RGB cases, the highest sugar yields were achieved with the addition of Tween 20 and measured about 816 mg/g and 646.2 mg/g, respectively.

- The maximum enhancement in enzymatic digestibility of cellulose and hemicellulose with Tween 20 was about 16% and 34%, respectively.

The addition of Tween 20 ascertained 0.249 g and 0.318 g of ethanol per 1 g of AL, and AC-AL treated RGB with *Saccharomyces cerevisiae* as the fermenting organism (SHF operating condition of, with 5% (v/v) S. cerevisiae pre-inoculated solution, 72 h, 35° C and 110 rpm).

KOH pretreatment based high purity alkaline lignin extraction from Saccharum ravennae grass and its characterization

- Higher KOH concentration, longer reaction time, and lower solid loading reduce solid recovery in lignocellulosic biomass pretreatment, while increased KOH concentration, prolonged reaction time, and optimal 10% solid loading enhance lignin recovery in *Saccharum ravennae* grass biomass. All these observations infer upon complex variable interactions for the optimality of desired response variables.
- The CCD-RSM predicted a maximum lignin recovery of 15.38 g/100g of raw biomass (R^2= 0.9828) at optimal process conditions of 2.4% KOH, 6.41% solid loading, and 176.57 minutes duration. Experimentally 15.81±0.32 g/100g lignin recovery was obtained, and thereby confirmed the model-predicted value.
- Maximum purity of 93.7 % was achieved for the extracted lignin at the operating condition of 3% KOH, 10% solid loading, and 125 minutes of reaction time.
- The KOH pretreatment enhanced lignin quality, exhibiting higher total phenolic content and superior functional groups in comparison to commercial lignin. Relevant alterations in alkaline concentration, solid loading, and reaction time are responsible for such varied characteristics.
- The Total Phenolic content (TPC) varied from 20.61- 54.44 wt% in the extracted lignin samples, which is significantly higher than that of commercial alkaline lignin (CL) (11.85%).
- The SEM image analysis conveyed that the KOH pretreatment induced significant degradation of the fiber framework, and thereby ascertained morphological alterations in the cell wall, increased cellulose surface area, and the separation of

lignin. Further, the extracted lignin exhibited a smaller and more uniform particle size distribution in comparison with the commercial lignin.

- The thermo-decomposition stages of alkali lignin revealed through thermal analysis, indicate early-stage weight loss related to water and volatile evaporation, followed by severe lignin degradation (200–500 °C) involving ether bond cleavage, side-chain oxidation, and dehydrogenation. The final stage (>500 °C) resulted in C-C bond breakdown and char formation with distinct char contents in commercial (CL) and extracted (EL) alkali lignins attributed to the G/S unit ratio and initial degraded lignin fractions.

- ^{1}H and ^{13}C NMR analyses revealed structural differences between extracted and commercial alkaline lignin. Signals in ^{1}H NMR spectra indicated the breakdown of β-O-4 ether bonds, while ^{13}C NMR spectra showed prevalent signals for S, G, and H units in the aromatic region. The higher intensity of signals in extracted lignin suggested a higher number of functional groups, correlating with its higher total phenolic content. Peaks in ^{13}C NMR spectra identified carbonyl groups, aliphatic COOR, and lignin-forming units, highlighting distinctive features in extracted lignin.

Preparation and characterization of mixed matrix membrane for Cr(VI) removal with the alkaline lignin extracted from Ravenna grass

- The computed Flory-Huggins Interaction Parameter (χ) value of 0.34 affirmed a favorable interaction between polysulfone (PSf) and alkaline lignin. Thereby, the parameter conveyed increased miscibility and potentially enhanced characteristics in the blended solution of PSf and lignin.
- The presence of lignin altered the cross-sectional layout and porosity of the membranes. Water absorption tests and porosity measurements confirmed increased water absorption and thereby, membranes with larger pore sizes have been obtained for blended solutions with higher lignin concentrations.

- Cross-sectional images revealed an asymmetric structure with compacted outer layers, finger-like macro voids, and a sponge-like bottom layer. Lignin addition influenced the overall volume of the sponge-like portion, influencing their potential applications, particularly in water treatment processes involving Cr (VI) removal.
- Enhanced and optimal Cr (VI) removal was achieved through the incorporation of alkaline lignin extracted from Ravenna (*Saccharum ravennae*) grass in the PSf mixed matrix membrane.
- The lignin altered the surface charge of the PSf membrane from -15.1 mV to -30.1 mV. Also, the hydrophilicity, porosity, and pure water flux enhanced for PSf/lignin membranes.
- A Cr (VI) removal of 98.75% was achieved after 3rd filtration cycle with the M3 (lignin 1 wt.%) membrane.
- For the M0 membrane, the irreversible fouling index was 69.11%. This reduced to 25%, 26.92%, and 38.78 % for M1, M2 and M3, respectively.
- The incorporation of 1 wt.% lignin in the PSf membrane enhanced its tensile strength (MPa) and elongation properties (%) from 4.55 ± 0.45 MPa, and 18.1 ± 1.62% to 5.76 ± 0.28 MPa, and 29.0 ± 0.73%, respectively.
- The fabrication cost of a 1 m^2 M3 membrane was estimated to be $68.

Preparation and characterization of PSf-GO-alkaline lignin ultrafiltration composite membrane for Pb^{2+} and Eosin Y dye removal

- The Ravenna grass extracted purified lignin and synthesized graphene oxide was incorporated into the PSf membrane matrix to successfully realize ultrafiltration membranes.
- The incorporation of lignin and GO enhanced the regenerative capabilities, porosity, PWF, hydrophilicity, and Zeta potential of the composite membranes.
- The LGM3 membrane, with the equivalent weight percentage (0.75 wt.%) of lignin and GO, exhibited the most superior performance in terms of permeation, rejection of Eosin Y dye, removal of lead (Pb), and flux recovery in due course of the three filtration and regeneration cycles.

- The Zeta potential of the membranes reduced from -15.6±0.7 mV (for LGM0) to -39.4±0.7 mV (LGM3 membrane).
- The Porosity and PWF of the membranes increased from 36.9±4.7% and 74.27 L/m^2h (for LGM0 membrane) to 67.1±6.1% and 193.11 L/m^2h (for LGM3 membrane), respectively.
- The prepared membranes were evaluated for filtration performance of Pb^{2+} and Eosin Y dye mixture. After the second filtration cycle, the LGM3 membrane removed 100% Pb^{2+} and 81% Eosin Y.
- The Pb adsorption study on the LGM3 membrane demonstrated noticeable adsorption activity. The adsorption isotherm data was accurately described for both the Langmuir and Freundlich models and thereby conveyed the occurrence of multilayer physisorption. The maximum adsorption capacity for Pb^{2+} was 71.32 mg/g
- The fabrication cost of 1 m^2 LGM3 membrane was estimated to be 55.16 $.

6.2 Future Work

Considering the findings reported in Chapters 2 to 5, the following have been suggested to be few directions in which future research work can be addressed in the mentioned areas of research:

Fermentation based bio-ethanol production from elephant grass biomass

- The fermentation study shall target microorganisms that facilitate pentose sugar fermentation to the relevant hydrolysates.
- A techno-economic analysis of the entire process.

Alkaline lignin applications

- Application of alkaline lignin in environmental remediations and organic chemical developments.
- Recovery of cellulose from delignified biomass waste and preparation of cellulose nanocrystals and their utilization in environmental applications.

PSf-Lignin membranes and their applications

- Further doping-based improvement in the membrane surface properties in the perspective of better removal efficiency of the targeted heavy metals.
- Application of lignin in hydrogel development for applications such as contaminants removal and oil-water separation.

PSf-GO-Lignin composite membranes and their applications

- Further modification and improvement of the developed membranes for industrial-scale application.
- Application of lignin as adsorbent and catalysts.

Appendices

Appendix A: Calibration curves for the determination of sugars, ethanol concentrations

HPLC system for chromatographic separations. Equipped with RI detector (Model No.: Prominence HPLC System; Make: M/s Shimadzu, Singapore) operated with the colum temperature of 60 ℃ with 0.6 mL/min flow rate and aqueous 0.01M H_2SO_4 solution as mobile phase. A calibration curve needs to be generated to quantify the sugar concentration in hydrolysates and the ethanol concentration in fermented media. Sugar concentrations that closely matched those in the biomass were chosen in order to create the standard calibration curves.

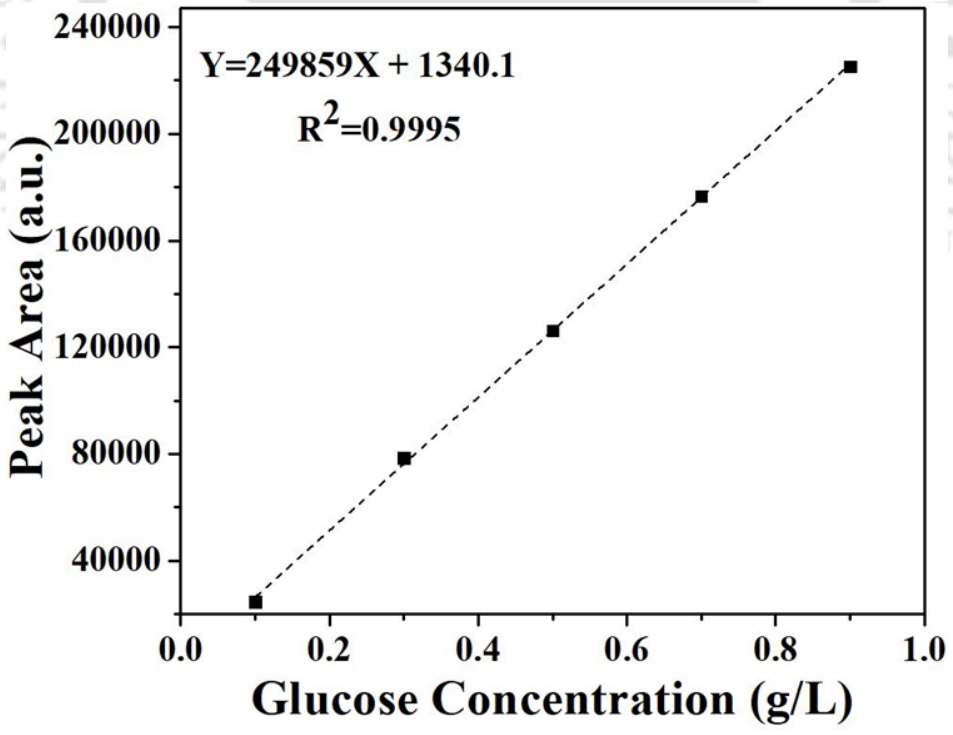

Fig. A1: Calibration curve for the determination of glucose in biomass and hydrolysates.

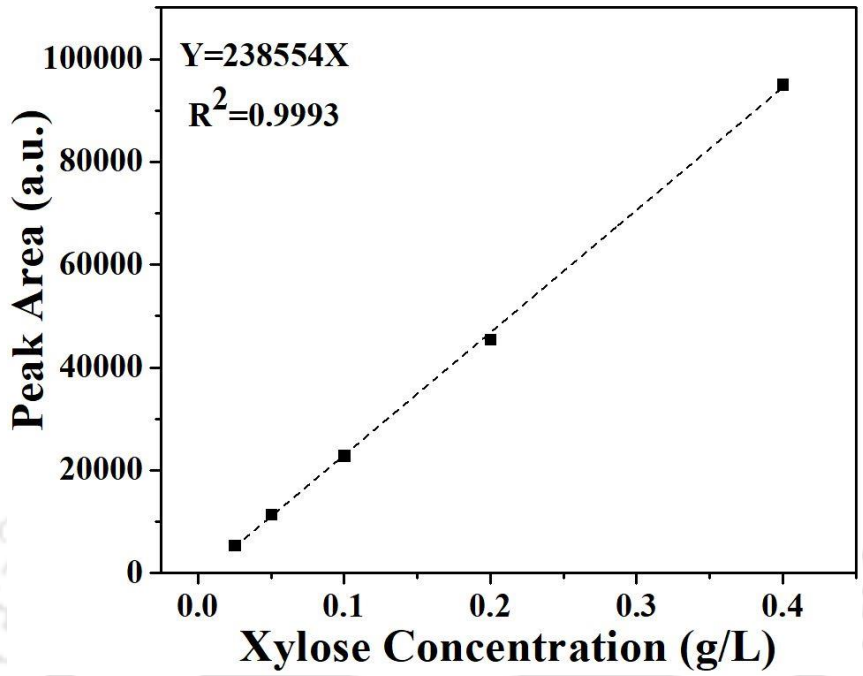

Fig. A2: Calibration curve for the determination of xylose in biomass and hydrolysates.

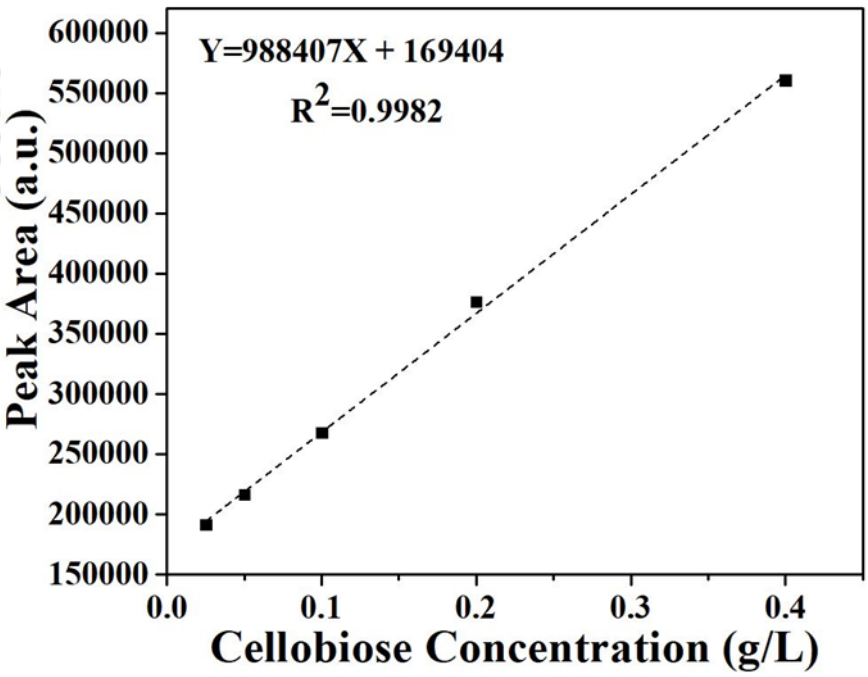

Fig. A3: Calibration curve for the determination of cellobiose in biomass and hydrolysates.

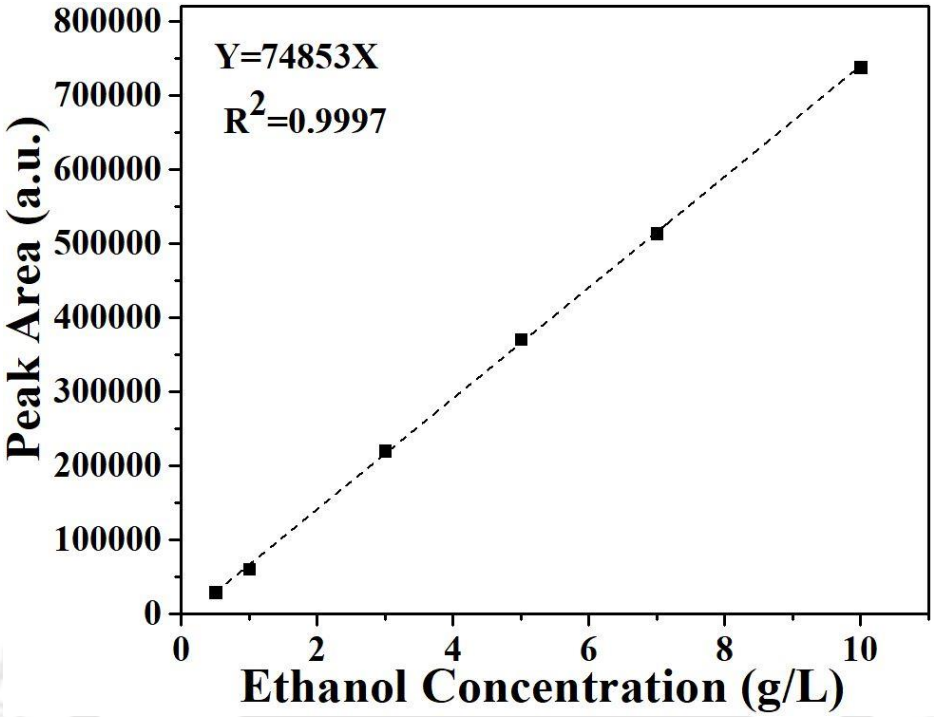

Fig. A4: Calibration curve for the determination of produced ethanol in fermented media.

Appendix B: Calibration curves for the determination of total phenolic content in lignin samples and Eosin Y in filtrate solutions

The determination of gallic acid was conducted using a UV–vis spectrophotometer (Shimadzu UV-2600, Singapore), while Eosin Y quantification was performed with Shimadzu UV-1900. The total phenolic content (TPC) in lignin samples was assessed by quantifying gallic acid equivalents, and the TPC was expressed as a percentage of gallic acid. The calibration curves for gallic acid and Eosin Y dye, recorded at 750 nm and 517 nm, respectively, are presented in Figures A5 and A6.

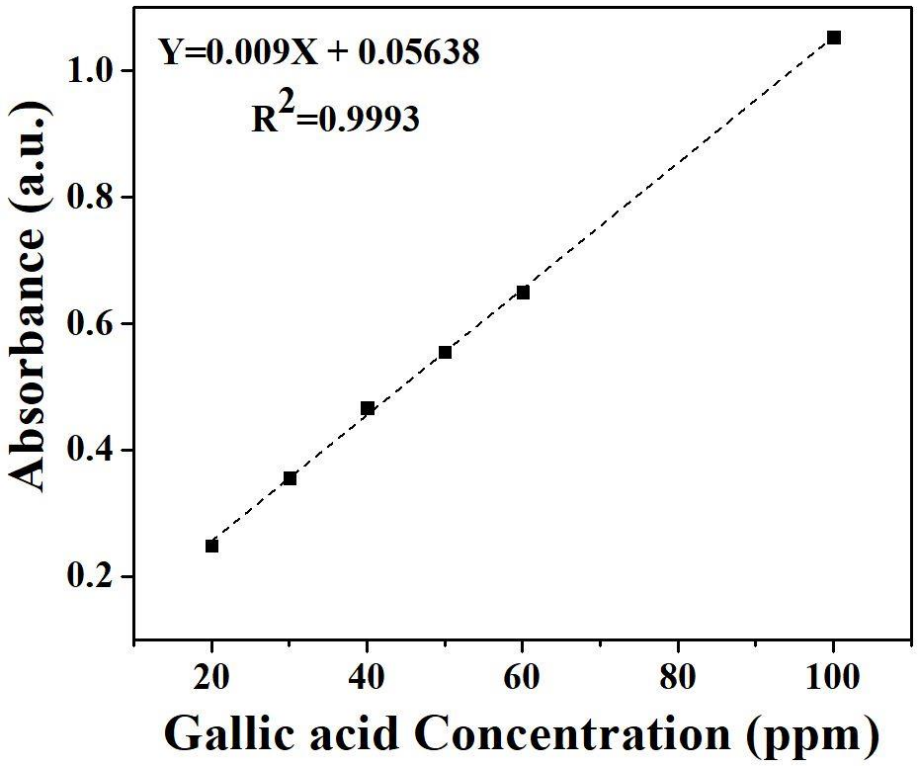

Fig. A5: Calibration curve for the determination of total phenolic content of the extracted lignin samples.

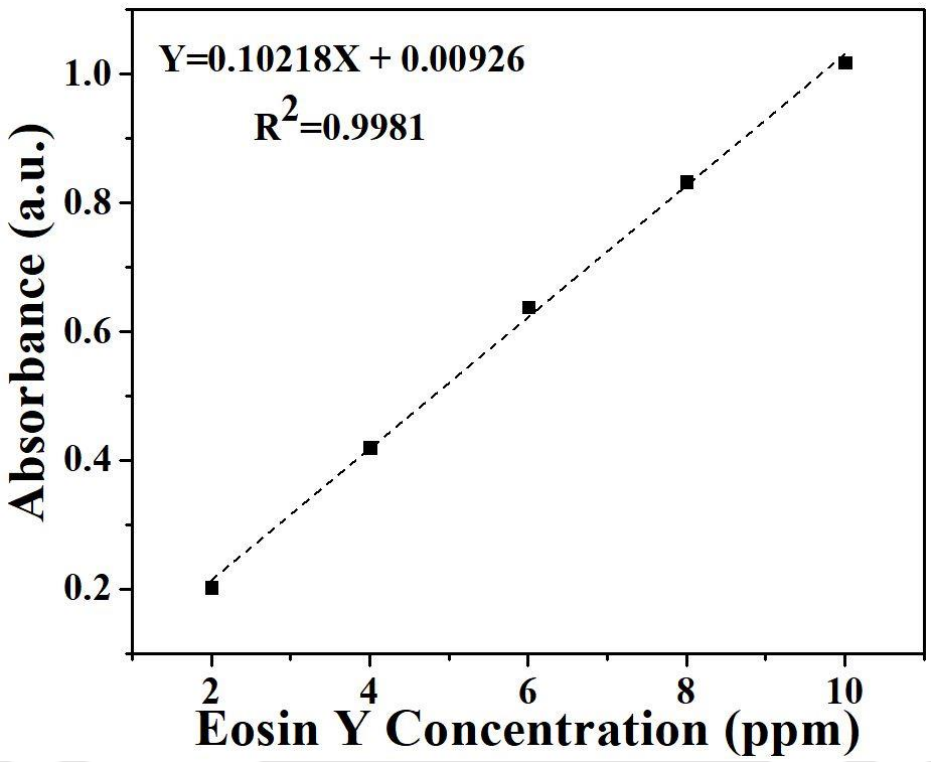

Fig. A6: Calibration curve for the determination of Eosin Y concentration in the feed and filtrate solutions.

Appendix C: Calibration curve for the determination of Cr and Pb in feed and solutions

The analysis utilized Atomic Absorption Spectroscopy (AA240-Varian, Netherlands) for Chromium (Cr) determination at a wavelength of 357.9 nm, while Atomic Absorption Spectroscopy (SHIMADZU AA-6880) was employed for Lead (Pb) detection at a wavelength of 217 nm. Calibration curves were constructed to establish a basis for quantification and serve as supplementary databases for determining concentrations in both the feed and filtrate solutions.

Figures A7 and A8 depict the calibration curves derived from measured absorbances corresponding to varying concentrations of Cr and Pb in synthetic contaminated water systems. These curves demonstrate a linear relationship, indicating that the absorbance of the samples proportionally varies with the concentrations of the studied heavy metal ions.

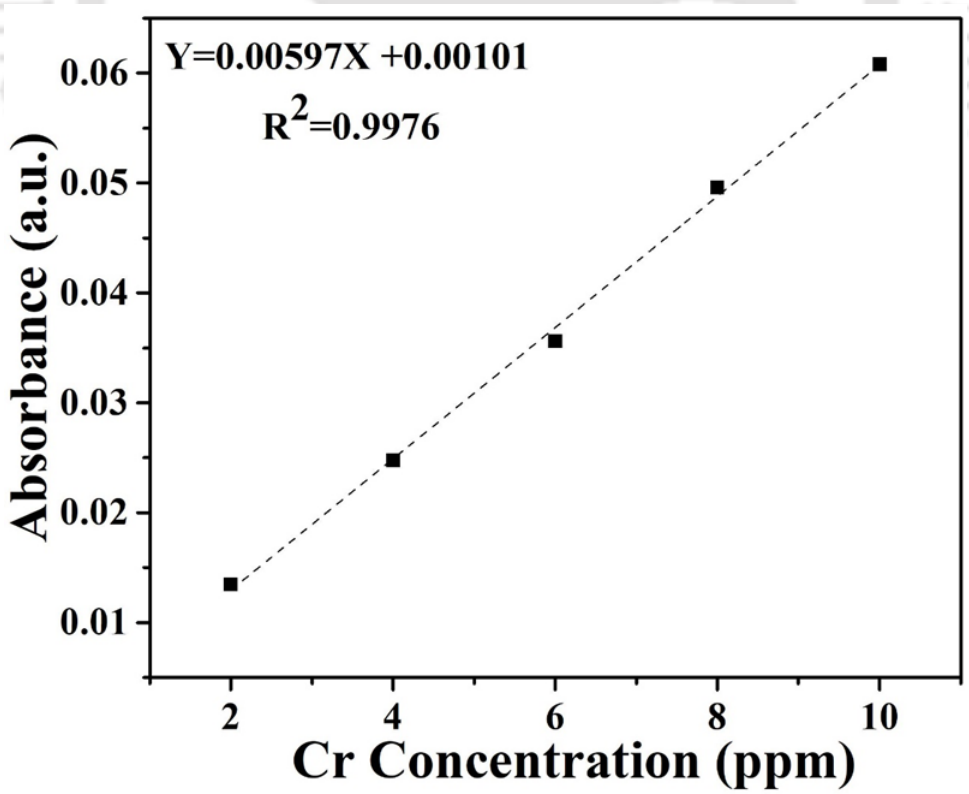

Fig. A7: Calibration curve for the determination of Cr in feed and filtrate solution.

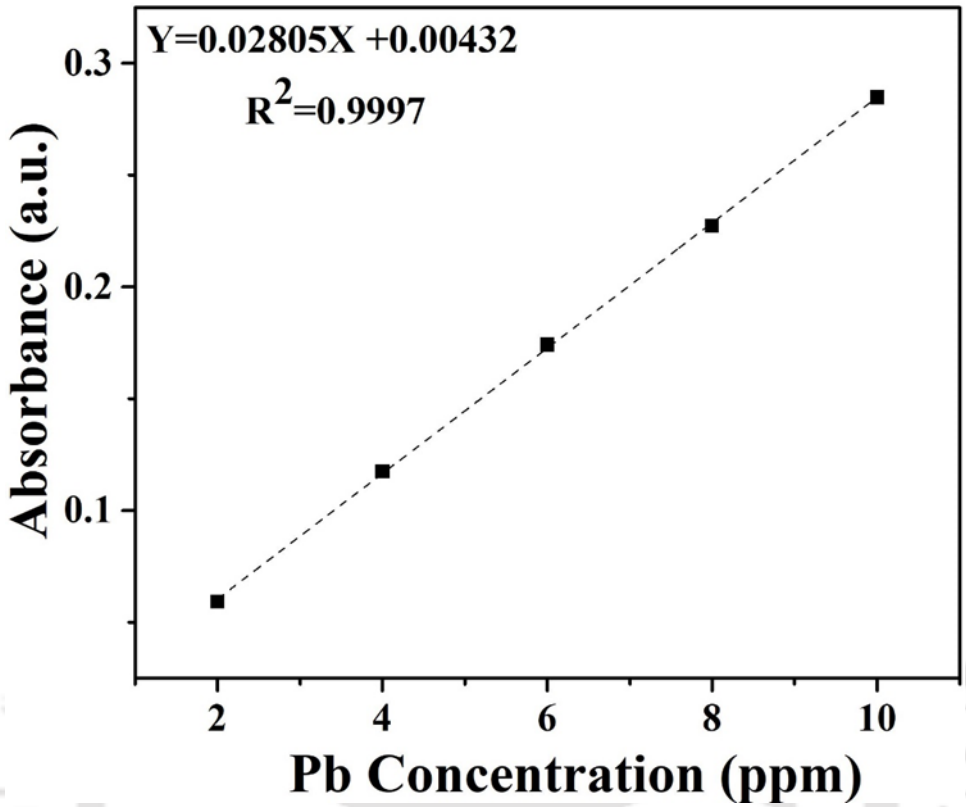

Fig. A8: Calibration curve for the determination of Pb in feed and filtrate solution.

Appendix D: Sample calculations to evaluate cost of Extracted lignin and synthesized GO

The following sections summarize sample calculations associated to the determination of the cost associated with lignin extraction and the synthesis of graphene oxide (GO).

A. Lab scale extraction of alkaline lignin

S. No	Raw material	Amount used	Price (INR)	Instrument used	Unit	Electric charge/ Unit (INR)	Price (INR)
1.	KOH pallets	234 g	201	Oil bath	1.2		7.15
				Centrifuge	0.25		1.5
2.	HNO_3 (69%)	162mL	149			5.96	
				Vacuum filtration	0.5		3.0
3.	H_2SO_4 (98%)	196mL	147.8	Hot air oven	18.1		107.87
				Autoclave	5		29.8
4.	DI Water	24 L	93.6				
		(A)Total=	591.4			(B) Total=	149.32
Overall cost for pure lignin extraction= (A+B) = 740.72 INR/ 100 grams							

B. Lab scale GO synthesis

S. No	Raw material	Amount used	Price (INR)	Instrument used	Unit	Electric charge/ Unit (INR)	Price (INR)
1.	Synthetic Graphite	53.45 g	40.41	Hot plate magnetic stirrer	1.846	5.96	11.01
2.	$NaNO_3$	26.72 g	19.24	Centrifuge	0.272		1.62
3.	$KMnO_4$	160.35 g	234.43	Fridge dryer	18		107.28
4.	H_2SO_4 (98%)	1336.25 mL	1007.53				
5.	H_2O_2 (30%)	267.25g	302.53				
6.	DI Water	26 L	101.40				
7.	HCl (35%)	20 mL	15.56				
		(A)Total=	1721.10			(B) Total=	119.91
Overall cost for GO synthesis= (A+B) = 1841.01 INR/ 100 grams							